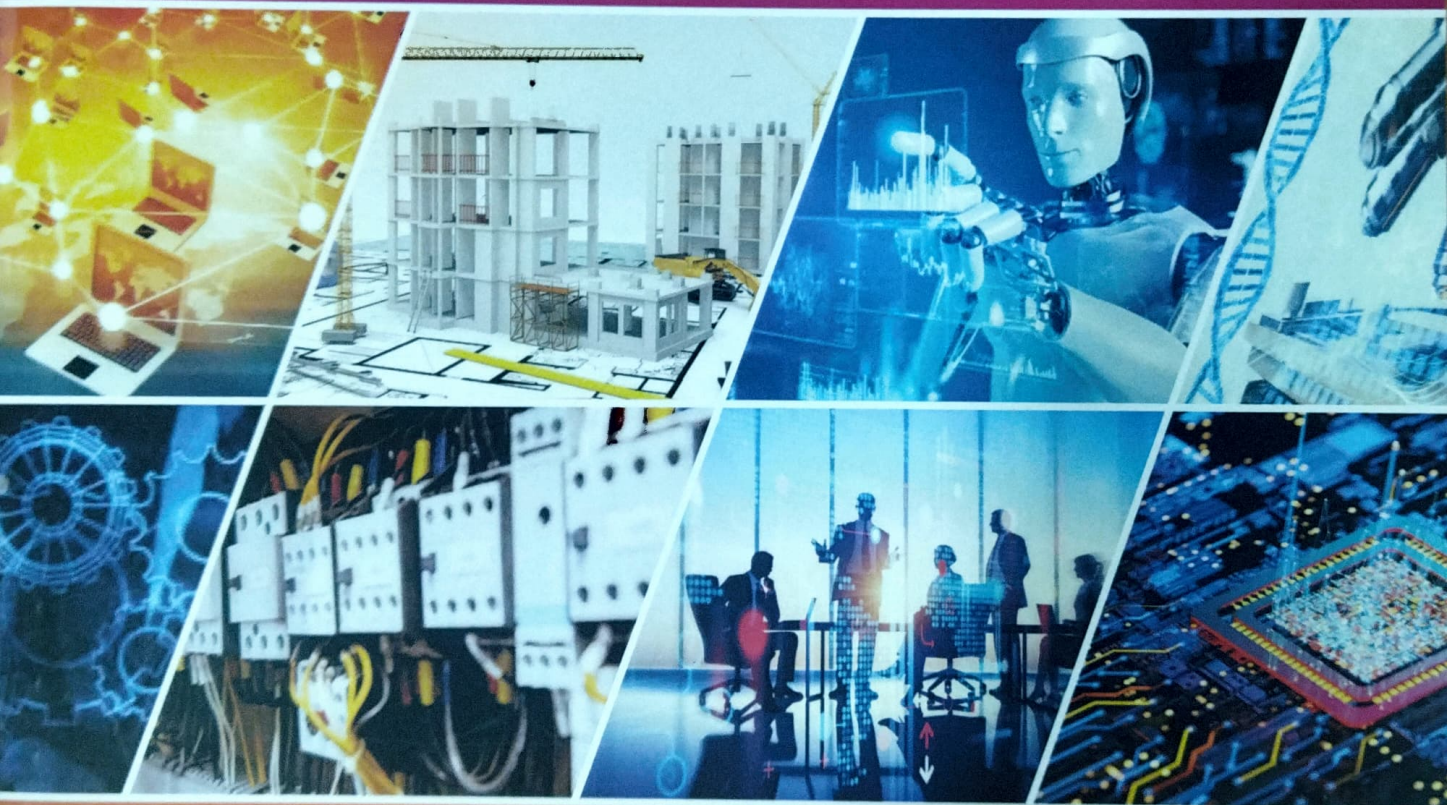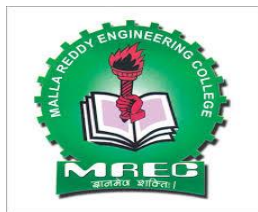# MALLA REDDY ENGINEERING COLLEGE

(Autonomous) - Main Campus

(A UGC Autonomous Institution, Approved by AICTE, New Delhi & Affiliated to JNTUH, Hyderabad).
Accredited by NAAC with 'A++' Grade (Cycle- III),
NIRF Rank Band 101-150, ARIIA Band Performer,
NBA Tier-I Accredited (B.Tech- CE, EEE, ME, ECE & CSE, M.Tech - CSE, EPS, TE)
Maisammaguda, Medchal-Malkajgiri District, Secunderabad– 500100,
Telangana State. www.mrec.ac.in

LIST OF WEB OF SCIENCE JOURNALS IN THE CALENDAR YEAR-2022

MALLA REDDY ENGINEERING COLLEGE (AUTONOMOUS)

(UGC Autonomous Institution, Approved by AICTE, New Delhi & Affiliated to JNTUH, Hyderabad). Accredited by NAAC with 'A++' Grade, Maisammaguda (H), Medchal-Malkajgiri District, Secunderabad, Telangana State – 500100, www.mrec.ac.in

Faculty Research Publication in the Calendar Year - 2022

LIST OF WEB OF SCIENCE JOURNALS

S.No	Department	No.of Journals
1	Civil Engineering	03
2	Electrical and Electronics engineering	10
3	Electronics and Communication Engineering	05
4	Computer Science and Engineering	02
5	CSE-AIML	01
6	Humanities and Science	03
Total		**24**

Sl. No	Title of paper	Name of the author/s	Department of the teacher	Name of journal	Year of publication	ISSN number
1	Analysis of Reinforced Concrete Structures Beams-Columns Joints using Finite Element Modellings	Dr. J. Selwyn Babu	Civil Engg	Indian Journal of Natural Sciences	2/1/2022	0976-0997
2	Neural Network System based on Real time Object Detection and Recognition for Video Surveillance Systems	Dr.B.Sudharshan Reddy	Civil Engg	Indian Journal of Natural Sciences	Dec, 2022	0976 – 0997
3	Mechanical Properties of Steel Fiber Reinforced Geo Polymer Concrete Incorporated with Fly-Ash & GGBS	Dr. J. Selwyn Babu	Civil Engg	Materials Science Forum	Nov, 2022	1662-9752
4	Solar Powered Arduino Based Automatic Drip Irrigation System for Enhancing Agricultural Productivity	Dr. T. Rajesh, V. Suma Deepthi	EEE	Indian Journal of Natural Sciences	Feb, 2022	0976 – 0997
5	Design of Cascaded Multi-Level Inverter for PV Systems	Dr. P. Sarala	EEE	Indian Journal of Natural Sciences	Feb, 2022	0976 – 0997
6	Energy Shaping Control of Grid Connected Parallel Interleaved Converter for Current Reduction	Dr. N. Rajeswaran, Dr. P. Marimuthu	EEE	Indian Journal of Natural Sciences	Feb, 2022	0976 – 0997

7	Maximum Power Point Tracking for Permanent Magnet Synchronous Generator based Wind Park Application	Dr. Ch. Rami Reddy	EEE	International Journal of Renewable Energy Research	June, 2022	1309-0127
8	Improvement of Power Quality in Grid Integrated Smart Grid Using Fractional-Order Fuzzy Logic Controller	D.Chandra Sekhar	EEE	International Journal of Renewable Energy Research	June, 2022	1309-0127
9	Coordinated IPFC and SMES Strategy for Stability Analysis of Renewable Energy Based Contemporary Interconnected Power System with FOPID Controller	Dr. Ch Rami Reddy	EEE	International Journal of Renewable Energy Research	June, 2022	1309-0127
10	COVID-19 Prevention: an IoT - Based Solution for Effective Social Distancing and Contact Tracing	P. Kamalakar, V. Ganesh Kumar	EEE	Indian Journal of Natural Sciences	Aug., 2022	0976 – 0997
11	Smart Agricultural Management System using Big Data Analysis and Internet of Things	Y. Sudha, S. Bharathi	EEE	Indian Journal of Natural Sciences	Oct., 2022	0976 – 0997
12	Neural Network System based on Real time Object Detection and Recognition for Video Surveillance Systems	Dr. D. Raja Reddy, K. Anitha Reddy	EEE	Indian Journal of Natural Sciences	Dec., 2022	0976 – 0997
13	Suppression of Ferranti Effect of Transmission System Using Closed Loop Control of FACTS Devices	Dr. P.V.V. Satyanarayana Dr. Ch. Rami Reddy	EEE	J. Electrical Systems	Dec., 2022	1112-5209
14	An Efficient Transform based Low Rank Tensor Completion to Extreme Visual Recovery	Sunil Kumar Jyothula, Jaya Chandra Prasad Talari	ECE	Indian Journal Of Science And Technology	2022	0974-5645

15	Optimization of Environmental Data to Improve Safety in Coal Mine using Wireless Sensor Networks	Syed Jalal Ahmad, Ahmed MM, Unissa I,	ECE	Indian Journal of Science and Technology	2022	0974-5645
16	MEMS Based Automatic Fall Detection for Aged People	M.Jagadeesh Chandra Prasad Telugu Maddileti	ECE	Indian Journal of Natural Sciences	2022	0976 – 0997
17	Design of a Compact ISM-band Microstrip Slot Antenna for Wireless Sensor Nodes	G S K Gayatri Devi S Krishna Veni T Vidyavathi Syed Jalal Ahmad	ECE	Indian Journal of Science and Technology	2022	0974-5645
18	Driver Drowsiness Alerting System	Telugu Maddileti and M.Jagadeesh Chandra Prasad	ECE	Indian Journal of Natural Sciences	2022	0976 – 0997
19	Dynamic voltage and frequency scalling Technique in cloud computing Environment	Dr.Arun Kumar Kandru	CSE	Telewmatique	22-Aug	1619-1634
20	A Study on Inside Views of Cloud Computing Tools	Dr.Arun Kumar Kandru	CSE	CSAC	2022	2288-601X
21	Emerging challenges in IoT, Blockchain and Data Mining for effective treatment of Covid and flu diseases through Telemedicine process	Dr Manyam Thaile	CSE_AIML	CSAC	2022	2288-601X
22	Review on chemical constituents of Bauhinia species	Dr. M. Vijaya Bhaskar Reddy	Chemistry	Annals of Phytomedicine	2022	2393-9885
23	Bioassay guided fractionation, isolation and synthesis of potent antimicrobial agents from Alpinia galanga (L.) Willd.	Dr. M. Vijaya Bhaskar Reddy	Chemistry	Annals of Phytomedicine	2022	2393-9885

24	Isolation, characterization and structure elucidation of flavonoids from the root bark of Bauhinia variegata L.	Dr. M. Vijaya Bhaskar Reddy	Chemistry	Annals of Phytomedicine	2022	2393-9885

ORIGINAL PAPER

Applying ANN – PSO algorithm to maximize the compressive strength and split tensile strength of blended self curing concrete on the impact of supplementary cementitious materials

C. Vivek Kumar[1] · K. Sargunan[2] · J. S. S. K. Vasa[2] · V. Praveen Jesuraj[3] · A. Punitha[4] · R. Karthikeyan[5]

Abstract

This study was intended to get the optimized Compressive strength and split tensile strength of Blended Self CuringConcrete(BSCC) on the impact of Supplementary Cementitious Materials (SCM's). The experiments were conducted by varying the quantity of Cement, Flyash, Ground Granulated Blast Furnace Slag (GGBFS), Silica Fume and Slump with fixed quantity of Fine aggregate, Coarse aggregate, S.P and Water. Totally 13 different mix proportions were prepared and tested for Compressive Strength (CS) and Split Tensile Strength (STS). Both strengths were calculated for 7, 14 and 28 days. To optimize the compressive strength and split tensile strength, a feed forward Artificial Neural Network (ANN) model was developed, and Particle Swarm Optimization (PSO) algorithm was used by optimizing the weighing factors of the network in the neural power software. Finally, with a root mean square error of 0.008223, 0.006559, and 0.009743 for CS and 0.008905, 0.006999, and 0.008745 for STS, the model was obtained for 7, 14, and 28 days. The percentage contribution of input parameters is also discussed separately for compressive strength and split tensile strength of 7, 14 and 28 days of curing. Finally, the optimized compressive strength and split tensile strength were found to be 42.3552 N/mm^2 and 4.3113 N/mm^2 respectively for 28 days.
.

1 Introduction

Blended cement concrete is a mixture of cement replaced with supplementary cementitious materials with different proportioning mixes based upon the utility of concrete. SCMs like fly ash (FA), silica fume (SF), metakaolin (MK), bentonite, and ground granulated blast-furnace slag (GGBFS) were used to replace cement up to 60% without the need of

alkaline solution in the investigation done by Halit Yazıcı [1]. Due to this SCMs the rheological, durability, and mechanical qualities of concrete can be enhanced by adding up to 40% mineral additive to the mixture and keeps costs down by reducing the amount of cement used in the concrete. Utilising pozzolanic materials and transforming them into useful materials can help conserve the environment while also assisting in the development of high-performance concrete thorough the literature on unary, binary, and triple blended pozzolans which was employed as concrete replacements explained by Athiyamaan [2].

Ternary blended concrete reveals the addition of several pozzolanic materials to the concrete, including cement acting as the primary binding agent. Metakaolin as well as fly ash from power stations are both important ingredients for modern concrete. Increasing the use of SCMs including such fly ash, silica fume, GGBFS, rice husk ash, and metakaolin during concrete production, precedes to the idea of blended cements and concretes. By reorienting the mix design parameters for enhanced structural characteristics of concrete, with an emphasis on regulating OPC content while increasing

✉ C. Vivek Kumar
    vivekkumarcr@gmail.com

1   Civil Engineering, Gokaraju Rangaraju Institute of Engineering and Technology, Hyderabad, India

2   Civil Engineering, Malla Reddy Engineering College, Hyderabad, India

3   Civil Engineering, SSM Institute of Engineering and Technology, Dindigul, India

4   Computer Science & Engineering, Annamalai University, Chidambaram, India

5   Mechanical Engineering, Gokaraju Rangaraju Institute of Engineering and Technology, Hyderabad, India

the overall cementitious material and limiting water content while obtaining chemical admixture for improved workability and compensating concerted hydration using SCMs. Due to the intensified utilization of performance built concrete, concrete incorporating self-curing agents could mean a new range of trend in construction throughout the modern era. For the inclusion of internal or self-curing water in concrete, newer techniques can also be used.

Most researchers suggested using saturated aggregates to perform internal concrete curing using polyethylene glycol PEG 400 mostly as self-curing agent for concrete mixes. Supplementary Cementitious Materials (SCMs) such as Flyash, Ground Granulated Furnace Slag, and Silica Fume improve the stiffness, ductility, and load bearing capability of concrete structures while reducing crack strengthening and dissemination. Thus according to the cement composite philosophy, a new composite material has high structural implementation and exceptional economic advantages can be produced by combining positive synergy with different admixtures. Suryawanshi et al. [3] investigated the incorporation of mineral admixtures to cement concrete enhances the amount of water required for curing, and this requirement can be much higher than those in ordinary Portland cement concrete mixes. Chemical shrinkage happens when there is water shortage for hydration also because inner relative humidity decreases. The key property of hardened concrete, durability, is profoundly affected by curing as it has a significant impact upon its hydration of Portland cement.

Using soft computing techniques, Feizbakhsh et al. [4] investigated the prediction model of compressive strength of self–compacting concrete (SCC). Adaptive neuro–based fuzzy inference method (ANFIS), artificial neural network (ANN), and PSOPC–ANFIS, a combination of particle swarm optimization with passive congregation (PSOPC) and ANFIS, are among the techniques used. Khademi et al. [5] developed three different models of multiple linear regression (MLR), artificial neural network (ANN), and adaptive neuro-fuzzy inference system (ANFIS), trained, and tested in the MATLAB programming environment for forecasting the 28-day compressive strength of concrete for 173 different mix designs, based upon the experimental results. Numerous regression, neural networks (NNT), and ANFIS models are developed, trained, and tested using concrete constituents as input variables in determining the 28-day compressive strength of no-slump concrete (28-CSNSC) by Sohbani et al. [6]. When the results are compared, perhaps the NNT and ANFIS models are more capable of predicting the 28-CSNSC than the conventional regression models suggested.

Nikoo et al. [7] studied about numerous experimental data patterns were used to build models from observations of cylindrical concrete components with different aspects. Uysal [8] researched the forecasting of the loss in compressive strength of SCC, an artificial neural network (ANN)

model based specific formulation had been proposed, which would be defined in terms with cement, mineral additives, aggregates, heating degree, and with or without PP fibres and the analytical model developed with ANN appeared to have a strong prediction capability of CS. Ahmet Raif Boğaa [9] investigated concrete containing GGBFS and CNI, the effects of cure form and curing time were investigated along with compressive strength, splitting tensile strength, and chloride ion permeability were all tested extensively and formulated four-layered artificial neural network approach (ANN) and adaptive neuro-fuzzy inference system (ANFIS). Lingam et.al [10] developed Artificial Neural Networks (ANN) to forecast the compressive strength of HPC comprising binary and quaternary blended mixes. Gulbandilar et al. [11] formulated the prediction models for flexural strength of cement mortars were created using Artificial Neural Networks (ANN) and Adaptive Network-based Fuzzy Inference Systems (ANFIS)with four input parameters Portland cement, GGBFS, WTRP, and sample age and one output parameter flexural strength of cement mortars.

2 Materials and methods

In this investigation, the self curing blended concrete was planned to prepare with the following ingredients such as Cement, Fly ash, Ground Granulated Blast Furnace Slag, Silica Fume, Fine Aggregate, Coarse Aggregate, S.P, Water and Slump. To prepare the SCBC, different quantities of cement, fly ash, ground granulated blast furnace, silica fume, and slump were maintained, while the remainder of the materials were kept constant. Table 1 shows the proportioning of standard self-curing concrete of M30 grade, while Table 2 shows the various mix proportions of Blended Self Curing Concrete for M30 Grade as per IS10262:2019 [12] codal provisions. It should be noted that the slump was measured from the bottom of the mould. Finally compressive and split tensile strength tests were performed on the specimens for seven, fourteen, and twenty-eight days of curing.

From the literature, the factors which are having considerable influence on the performance of Compressive Strength and Split tensile Strength for 7, 14 and 28 dayswere identified. They are (i) Cement (kg/m^3), Fly Ash (kg/m^3) (iii) GGBFS (kg/m^3) and (iv) Silica Fume (kg/m^3) and these factors were controlled during mixing process. A series of trial experiments were undertaken to determine the functional range of the supplementary Cementitious Materials (SCM's). Totally 13 different combinations was mentioned as M1 to M13 in Table 2 of BSCC specimens in Cube and Cylindrical forms were prepared. Each cube mould of the size is 150 × 150 × 150 mm for CS and STS with cylinder 150 mm in diameter and 300 mm long. For each blended mix, in a fresh state, the slump value (in mm) and for a hardened state, the strength

Table 1 Proportioning of Standard Self Cured mix for M30 Concrete (unit expressed as kg/m^3)

Materials	Cement	Fine Aggregate	Coarse Aggregate	PEG 400	Water	Water-Cement Ratio
Quantity	350	744.3	1314.2	2.28	175	0.4

Table 2 Mix proportions of Blended Self Curing Concrete for M30 Grade

Mix	Cement	FlyAsh	GGBFS	SF	Fine Agg	Coarse.Agg	S.P	Water	Slump (mm)
Quantity in kg/m^3									
M1	350	0	0	0	744.3	1314.2	3.5	140	244
M2	227.5	87.5	35	0	744.3	1314.2	3.5	140	255
M3	227.5	0	87.5	35	744.3	1314.2	3.5	140	255
M4	227.5	87.5	0	35	744.3	1314.2	3.5	140	256
M5	227.5	70	52.5	0	744.3	1314.2	3.5	140	251
M6	227.5	0	70	52.5	744.3	1314.2	3.5	140	251
M7	227.5	70	0	52.5	744.3	1314.2	3.5	140	254
M8	227.5	35	0	87.5	744.3	1314.2	3.5	140	252
M9	227.5	35	87.5	0	744.3	1314.2	3.5	140	255
M10	227.5	0	35	87.5	744.3	1314.2	3.5	140	252
M11	227.5	70	0	52.5	744.3	1314.2	3.5	140	248
M12	227.5	70	52	0	744.3	1314.2	3.5	140	251
M13	227.5	70	0	52.5	744.3	1314.2	3.5	140	253

parameters were calculated and noted down. Finally, the characteristic compressive strength and split tensile strength was calculated by using formula shown in Eqs. (1)and (2) [13] respectively.

$$CS\left(\frac{N}{mm^2}\right) = \frac{AppliedLoad\ overCubeSpecimen}{CrossSectionalArea} \quad (1)$$

$$STS\left(\frac{N}{mm^2}\right) = \frac{2*AppliedLoad\ over\ Cylindrical\ Specimen}{\pi *diameter\ of\ cylinder*length\ of\ cylinder} \quad (2)$$

The calculated (experimental) values of compressive strength and split tensile strength for BSCC are displayed in the Table 3 for 7, 14 and 28 days. Figs. 1 and 2 show specimens in Cube and Cylindrical forms of BSCC, whereas Figs. 3 and 4 are the tested specimens of compressive strength and split tensile strength respectively.

3 Developing a model and an optimization

In this investigation, it was planned to optimize the characteristic compressive strength and split tensile strengthfor 7, 14 and 28 days of Blended SCC using SCMs and finding the optimized process parameters after the model was created. Here, the model was created by Artificial Neural Network (ANN) and the model was optimized by Particle

Swarm Optimization (PSA) algorithm. The role played by ANN and PSO in the field of modeling and optimization is discussed below. Figure 5 illustrates the integrated attempt of artificial neural network and particle swarm optimization algorithm.

3.1 Artificial neural network

The ANN methodology outperforms all other model, including linear and exponential regression. Many researchers have supported the use of ANN as a forecasting model because of its exceptional learning algorithm and balancing of input and output associations, including for non-linear and complicated systems [15, 16]. According to Ebrahimpour et al. [17], the ANN methodology has tremendous modelling potential due to its ability to identify the relationships at the core of complex systems. HadiMashhadban et al. [18] investigated whether a neural network could be designed to perform a specific role by changing the values of the connections (weights) between the components. Tavakoli et al. [19] explored into the use of artificial neural networks (ANN) to forecast the mechanical properties and energy dissipation capacity of fibre reinforced self-compacting concrete. They mentioned that now the ANN outcomes are really like the experimental information. To train the data, ANN uses various learning algorithms such as "Fast Propagation," "Batch Back

Table 3 Experimental Results of various Mix Proportions of Blended Self Curing Concrete

Mix	Compressive Strength (N/mm^2)			Split Tensile Strength (N/mm^2)		
	7 days	14 days	28 days	7 days	14 days	28 days
M1	12.48	20.15	31.21	1.34	2.1	3.4
M2	16.04	26.67	41.12	1.48	3.11	4.21
M3	16.79	25.6	38.16	1.54	3	4.18
M4	15.52	25.89	37.85	1.47	2.99	4.13
M5	13.06	24.52	35.21	1.42	2.6	4.03
M6	13.97	22.52	36.76	1.39	2.48	4.1
M7	14.03	20.78	35.07	1.35	2.56	4.19
M8	13.36	21.42	34.25	1.47	2.49	3.94
M9	14.08	20.76	33.53	1.49	2.44	3.91
M10	14.64	23.78	34.86	1.45	2.5	3.86
M11	15.97	25.29	38.95	1.33	2.24	3.54
M12	15.17	23.9	35.29	1.29	2.19	3.68
M13	14.25	21.19	33.93	1.3	2.28	3.79

Fig. 1 Cubical test specimens for compressive strength

Fig. 2 Cylindrical test specimens for split tensile strength

Fig. 3 Cubical tested specimens for compressive strength
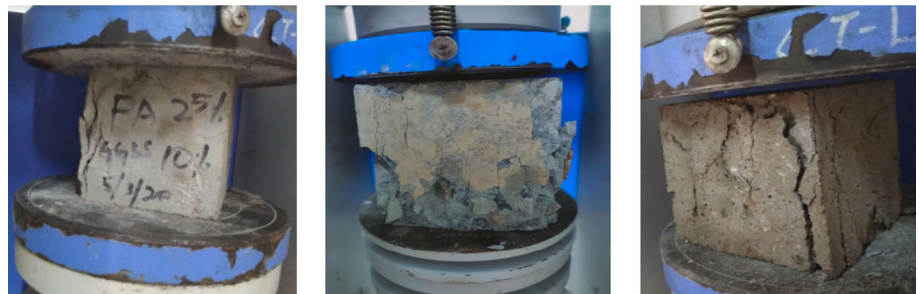
Fig. 4 Cylindrical tested specimens for split tensile strength
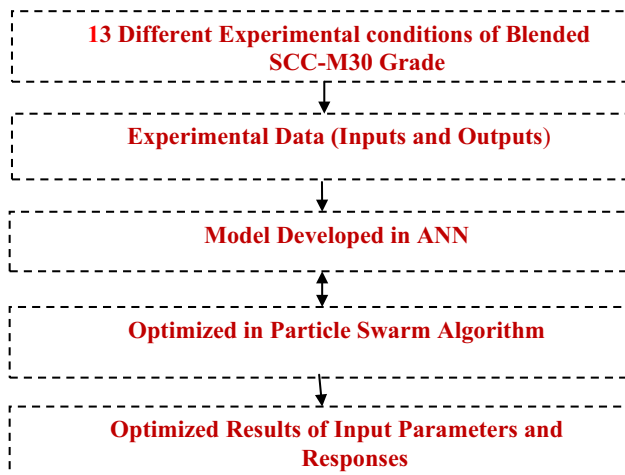
Fig. 5 Flow Chart of Hybrid ANN—PSO [14]

Fig. 6 Configuration of Three-Layered Neural Network

Propagation," "Incremental Back Propagation," and "Levenberg Marquadt." Nonlinear transfer functions such as Linear, Threshold Linear, Bipolar Linear, Gaussian, Tanh, and sigmoid are also included [20].This investigation's programme supports two separate link types: "multilayer regular feed forward" and "multilayer full feed forward." The RMSE divergence was used as a deciding factor as to when to stop training [21].

3.2 Particle swarm optimization

The PSO is a population-based optimization algorithm invented by Eberhart and Kennedy in 1995 and inspired by social behaviour such as bird flocking or fish schooling. In PSO, each particle in dimensional solution space is treated as an individual even amongst the population. The velocity and position of each particle are randomly chosen, and the very first position of each particle is determined using the target functions [22]. Then, amongst these results generated by all particles throughout the populations, gbest is found. The pbest particle is fixed which is based on the gbest. The pbest particle is assigned a velocity and a new population is formed, defining the new (second) position among all particles. Then gbest is discovered among the outcomes of the newly formed population, which is based on the most recent pbest particle. This process is repeated before the stop criterion, either the number of variables or no adjustments in the gbest value, take effect upon this algorithm.

3.3 Solutions of ANN & PSO

CPC-X Neural Power [20] was used to model and optimize the problem in this study. Engineering fields are also aware of the implementation of ANN and PSOA throughout the engineering world [23]. In ANN, the Levenberg Marquadt algorithm and multilayer normal feed forward propagation have been used as learning algorithm and connection type, meanwhile.Both the learning rate and the momentum were set to 0.8. For the hidden layer and output layer, the sigmoid transfer feature has been used. The sigmoid function was found to be the most used function by Muthupriya et al. [24]. There is no standard method for determining the number of neurons in the network's hidden layer; instead, trial and error can be used, which was investigated by Singh et.al [25] and Kennedy et al.[26].

According to Das et al. [27], the number of neurons in the hidden layer can be based on the number of input sources n, and the number of neurons in the hidden layer can vary between n, n/2, 2n, 2n + 1, and 2n + 2. Kutanaei et al. [28] investigated PSOA's ability to model the mechanical properties of fibre reinforced cement sand. Xuesong [29] explained the use of the PSO algorithm to solve the TSP and the experiment results show that the new algorithm is successful for this problem, despite the drawbacks of genetic algorithms such as being easily locked into a local optimum. The total number of hidden layer is 1 and node on the hidden layer is 5. Finally, the model was achieved with the root mean square error of 0.008223, 0.006559 and 0.009743 for CS and 0.008905, 0.006999 and 0.008745 for STS respectively for 7, 14 and 28 days. Figure 6 shows the model which was used in this investigation.
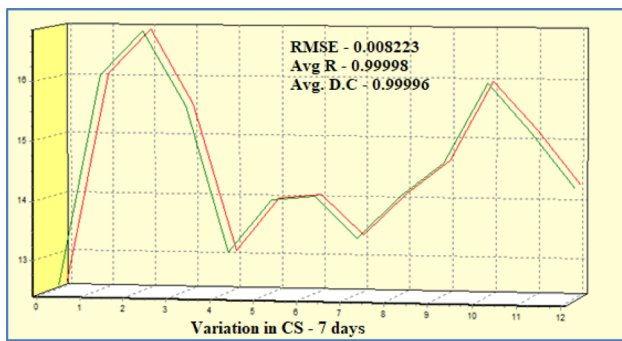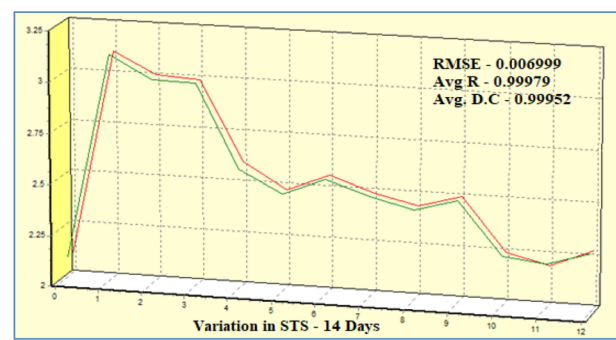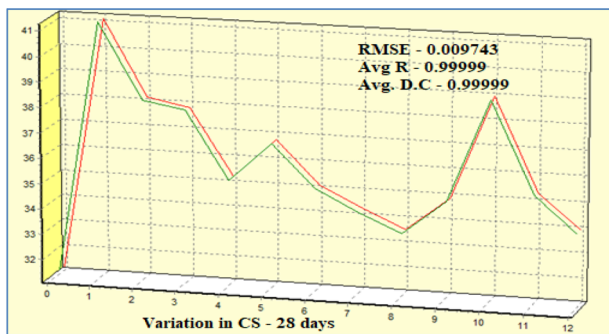
(a) ANN Model for CS – 7 days
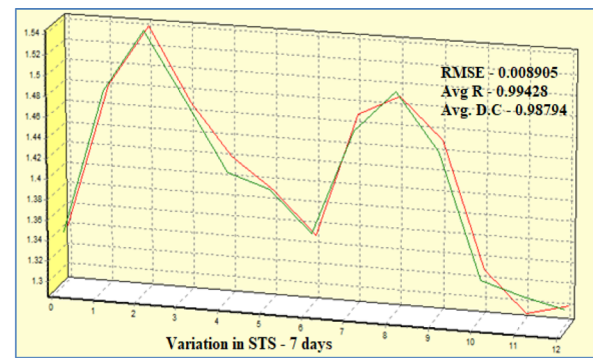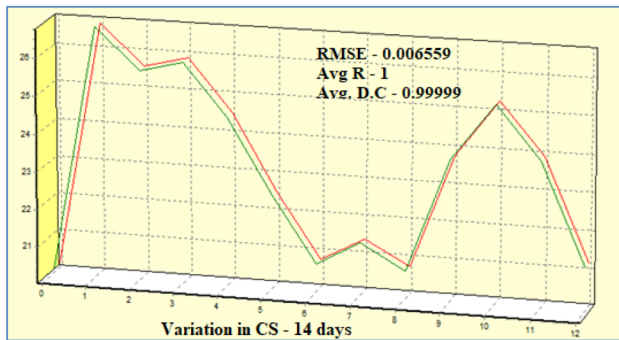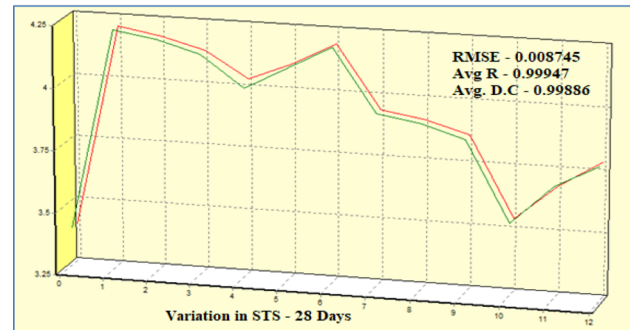

(b) ANN Model for CS – 14 days

(c) ANN Model for CS – 28 days

Fig. 7 **a** ANN Model for CS—7 days. **b** ANN Model for CS—14 days. **c** ANN Model for CS—28 days

(a) ANN Model for STS – 7 days

(b) ANN Model for STS – 14 days

(c) ANN Model for STS – 28 days

Fig. 8 **a** ANN Model for STS—7 days. **b** ANN Model for STS—14 days. **c** ANN Model for STS—28 days

Table 4 ANN Model's Statistical values of CS for different curing days

	7 Days	14 Days	28 Days
RMSE	0.008223	0.006559	0.009743
Avg R	0.99998	1	0.99999
Avg. D.C	0.99996	0.99999	0.99999

Figures 7(a) through (c) and 8(a) through (c) show the results of model created by ANN for CS and STS respectively, whereas Table 4 and 5 show the statistical significance of the model for CS and STS respectively.

To execute the optimization in PSO the following parameters were used [29]. The population size, inertia weight, learning factors such as cognitive factor (C1) and social factor (C2) are 10, 0.1, 2and 2 respectively. Finally, it was observed that the optimized values of Compressive strength are 17.3288, 27.4850 and 42.3553 N/mm^2 for 7, 14 and

Table 5 ANN Model's Statistical values of STS for different curing days

	7 Days	14 Days	28 Days
RMSE	0.008905	0.006999	0.008745
Avg R	0.99428	0.99979	0.99947
Avg. D.C	0.98794	0.99952	0.99886

Table 6 Optimized CS and optimized input values for different curing days

	7 Days	14 Days	28 Days
Compressive strength (N/mm^2)	17.3288	27.4850	42.3553
Cement	240.96	290.0097	229.4345
Fly ash	40.6751	86.0072	87.3342
GGBFS	67.3086	38.7017	2.4941
Silica fume	6.4172	73.4944	1.3895
Slump	253.3402	252.2067	251.1089

Table 7 Optimized STS and optimized input values for different curing days

	7 Days	14 Days	28 Days
Split Tensile Strength (N/mm^2)	1.5713	3.2363	4.3113
Cement	304.3145	319.9055	284.9032
Flyash	66.0441	20.6085	61.2320
GGBFS	59.6020	80.7960	83.9702
Silica fume	33.3184	32.2040	54.7132
Slump	251.3592	254.1756	247.2356

(a) Factors Importance (%) on CS – 7 days

(b) Factors Importance (%) on CS – 14 days

(c) Factors Importance (%) on CS – 28 days

Fig. 9 **a** Factors Importance (%) on CS—7 days. **b** Factors Importance (%) on CS—14 days. **c** Factors Importance (%) on CS—28 days

28 days respectively. Moreover it was found that the optimized values of Split Tensile Strength are 1.5713, 3.2363 and 4.3113 N/mm^2 for 7, 14 and 28 days respectively. Table 6 and 7 show the optimized input parameters for compressive strength and split tensile strength respectively for different curing days.

Figures 9(a) through (c) and 10(a) through (c) show process parameters importance (%) for CS and STS respectively. Whereas Tables 8 and 9 show the importance of each input factor (%) on compressive strength and split tensile strength respectively for different curing days. From the Tables 8 and 9 it can be found that the importance of cement contribution is low irrespective of strength and number of curing days.

As the CS and STS are dependent on the quantity of GGBFS, fly ash, silica fume, and slump and the heat of hydration of concrete, the contribution of GGBFS, fly ash, silica fume, and slump vary in different curing periods (long term and early-age). The CS of concrete mixtures including GGBFS increases when the amount of GGBFS is increased [30]. The presence of GGBFS provides greater early strength, whereas fly ash provides greater strength after a long time of curing. Fly ash particles interact with free lime in the cement to obtain more cementitious material, which improves long-term strength [31]. The type and quantity of cementing material, the water content, the aggregate grading, the existence of entrained air, and using chemical admixtures have a significant impact on the fresh and hardened properties of fly ash-based concrete [32].
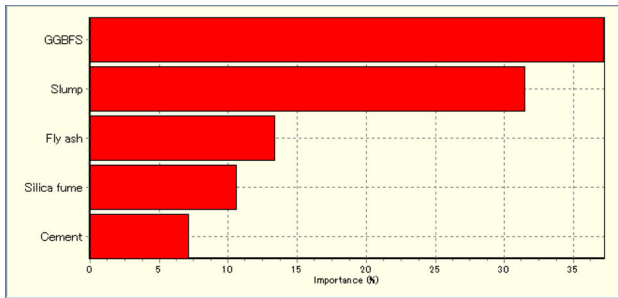
(a) Factors Importance (%) on STS – 7 days
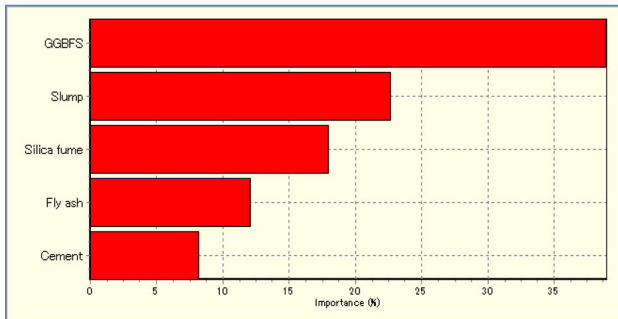
(b) Factors Importance (%) on STS – 14 days
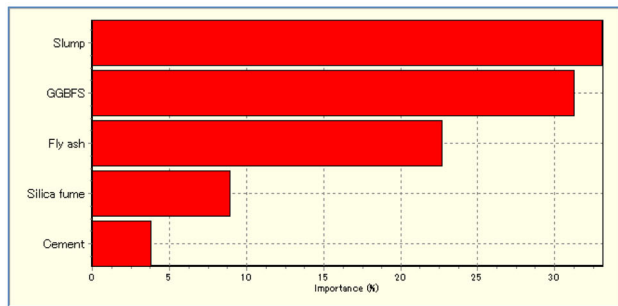
(c) Factors Importance (%) on STS – 28 days

Fig. 10 a Factors Importance (%) on STS—7 days. **b** Factors Importance (%) on STS—14 days. **c** Factors Importance (%) on STS—28 days

4 Conclusions

- The self-curing blended concrete was prepared with the following ingredients such as Cement, Fly ash, Ground Granulated Blast Furnace Slag, Silica Fume, Fine Aggregate, Coarse Aggregate, S.P, Water and Slump.
- Cement, Fly ash, Ground Granulated Blast Furnace, Silica Fume and Slump were maintained with different proportions and the rest of the ingredients were fixed constant.
- The compressive strength and split tensile strength tests were conducted on the respective specimens for three different curing days of 7, 14 and 28.
- The model was constructed between the process factors and output values by artificial neural network. Finally, the model was achieved with the root mean square error of 0.008223, 0.006559 and 0.009743 for CS and 0.008905, 0.006999 and 0.008745 for STS respectively for 7, 14 and 28 days.
- The model trained by ANN was suitably incorporated with the evolutionary computational techniques of particle swarm optimization.
- It was observed that the optimized value of compressive strength is 17.3288, 27.4850 and 42.3553 N/mm^2 for 7, 14 and 28 days respectively. Moreover it was found that the optimized value of split tensile strength is 1.5713, 3.2363 and 4.3113 N/mm^2 for 7, 14 and 28 days respectively.
- The percentage importance was found separately for optimized compressive strength and split tensile strength. It was also found that irrespective of curing days cement has the least importance on compressive strength and split tensile strength.

Table 8 Importance of each input factor in % on CS for different curing days

Parameters	7 Days	Parameters	14 Days	Parameters	28 Days
GGBFS	35.73	Slump	22.27	Slump	28.84
Slump	26.3	GGBFS	22.09	Fly ash	25.24
Silica fume	15.01	Fly ash	20.93	Silica fume	24.95
Fly ash	14.52	Silica fume	19.52	GGBFS	15.87
Cement	8.439	Cement	15.19	Cement	5.106

Table 9 Importance of each input factor in % on STS for different curing days

Parameters	7 Days	Parameters	14 Days	Parameters	28 Days
GGBFS	37.23	GGBFS	38.95	Slump	33.12
Slump	31.55	Slump	22.69	GGBFS	31.29
Fly ash	13.42	Silica fume	18.01	Fly ash	22.76
Silica fume	10.62	Fly ash	12.13	Silica fume	8.98
Cement	7.175	Cement	8.23	Cement	3.85

Declarations

Conflict of interest On behalf of all authors, I hereby disclose that no potential competing interest is involved with this technical paper.

References

1. Yazıcı, H.: The effect of silica fume and high-volume Class C fly ash on mechanical properties, chloride penetration and freeze–thaw resistance of self-compacting concrete. Constr. Build. Mater. **22**(4), 456–462 (2008). https://doi.org/10.1016/j.conbuildmat.2007.01.002

2. Athiyamaan, V.: Admixture-based self-compacted concrete with self-curing concrete techniques a state of art of review. Cleaner Eng. Technol. (2021). https://doi.org/10.1016/j.clet.2021.100250

3. Suryawanshi, N.T., Thakare, S.B., Jain, R.K.: Self-curing possibilities of blended concrete using water soluble polymer. Int. J. Adv. Sci. Technol. **29**(9s), 3829–3835 (2020)

4. Feizbakhsh, A., Khatibinia, M.: A comparative study of Traditional and Intelligence Soft Computing methods for predicting Compressive strength of Self Compacting concretes. Int. J. Optim. Civil Eng. **7**(3), 367–382 (2017)

5. Khademi, F., Akbari, M., Jamal, S.M., Nikoo, M.: Multiple linear regression, artificial neural network, and fuzzy logic prediction of 28 days compressive strength of concrete. Front. Struct. Civil Eng. (2017). https://doi.org/10.1007/s11709-016-0363-9

6. Sobhani, J., Najimi, M., Pourkhorshidi, A.R., Parhizkar, T.: Prediction of the compressive strength of no-slump concrete: a comparative study of regression, neural network and ANFIS models. Constr. Build. Mater. **24**(5), 709–718 (2010)

7. Nikoo, M., Torabian Moghadam, F., Sadowski, L.: Prediction of concrete compressive strength by evolutionary artificial neural networks. Adv. Mater. Sci. Eng. (2015). https://doi.org/10.1155/2015/849126

8. Uysal, M., Tanyildizi, H.: Estimation of compressive strength of self compacting concrete containing polypropylene fiber and mineral additives exposed to high temperature using artificial neural network. Constr. Build. Mater. **27**(1), 404–414 (2012)

9. Boğa, A.R., Öztürk, M., Topcu, I.B.: Using ANN and ANFIS to predict the mechanical and chloride permeability properties of concrete containing GGBFS and CNI. Compos. Part B Eng. **45**(1), 688–696 (2013)

10. Lingam, A., Karthikeya, J.: Prediction of compressive strength for HPC mixes containing different blends using ANN. Comput. Concr. **13**(5), 621–632 (2014)

11. Gulbandilar, E., Kocak, Y.: Application of expert systems in prediction of flexural strength of cement mortars. Comput. Concr. **18**(1), 1–16 (2016)

12. IS 10262: 2019, Concrete mix proportioning—guidelines (2nd Revision), Bereau of Indian Standards, New Delhi

13. Jagannadha Kumar, M.V., Srikanth, M., Jagannadha Rao, K.: Strength characteristics of self-curing concrete. Int. J. Res. Eng. Technol. **1**(1), (2012), ISSN: 2319–1163

14. Karthikeyan, R., Senthil Kumar, V., Punitha, A., Chavan, U.M.: An integrated ANN - GA approach to maximize the material removal rate and to minimize the surface roughness of wire cut EDM on Titanium alloy. Adv. Mater. Process. Technol. (2020). https://doi.org/10.1080/2374068X.2020.1793267

15. Alavala, CR: Fuzzy logic and neural networks: basic concepts and applications. Daryaganj, Delhi: New Age International; (2008)

16. Pilkington, J.L., Prestonb, C., Gomesa, R.L.: Comparison of response surface methodology (RSM) and artificial neural networks (ANN) towards efficient extraction of artemisinin from Artemisia annual. Ind. Crop. Prod. **58**, 15–24 (2014)

17. Ebrahimpour, A., Abd, R.R., Chng, D.H., et al.: A modeling study by response surfacemethodologyandartificial neural network on culture parameters optimization for thermostable lipase production from a newly isolated thermophilic Geobacillus sp. Strain ARM. BioMedCentral **8**, 96 (2008)

18. Mashhadban, H., Kutanaei, S.S., Sayarinejad, M.A.: Prediction and modeling of mechanical properties in fiber reinforced self-compacting concrete using particle swarm optimization algorithm and artificial neural network. Constr. Build. Mater. (2016). https://doi.org/10.1016/j.conbuildmat.2016.05.034

19. Tavakoli, H.R., Omran, O.L., Shiade, M.F., Kutanaei, S.S.: Prediction of combined effects of fibers and nano-silica on the mechanical properties of selfcompacting concrete using artificial neural network. Lat. Am. J. Solids Struct. **11**(11), 1906–1923 (2014)

20. CPC-X Software, Neural Power User Guide (2003) Available: http://www.geocities.com/neuralpower, https://www2.southeastern.edu/Academics/Faculty/pmcdowell/matlab_nnet_help.pdf

21. Awolusi, T.F., Oke, O.L., Akinkurolere, O.O., et al.: Performance comparison of neural networktraining algorithms in the modeling properties of steel fiber reinforced concrete. Heliyon. **5**, e01115 (2019)

22. Bharathi Raja, S., Baskar, N.: Particle swarm optimization technique for determining optimalmachining parameters of different work piece materials in turning operation. Int. J. Adv. Manuf. Technol. **54**, 445–463 (2011)

23. Tavakoli, H.R., Omran, O.L., Kutanaei, S.S., Shiade, M.F.: Prediction of energy absorption capability in fiber reinforced self-compacting concrete containing nano-silica particles using artificial neural network. Lat. Am. J. Solids Struct. **11**(6), 966–979 (2014)

24. Muthupriya, P., Subramanian, K., Vishnuram, B.G.: Prediction of compressive strength and durability of high performance concrete by artificial neural networks. Int. J. Optim. Civil Eng. **1**, 189–209 (2011)

25. Singh, A.K., Singhal, D., Kumar, R.: Machining of aluminum 7075 alloy using EDM process: an ANN validation. Mater. Today (2020). https://doi.org/10.1016/j.matpr.2020.02.591

26. Kennedy, J., Clerc, M.: Standard PSO 2006. . info/ Standard-PSO-2006.c.

27. Das, K., Kumar, K., Barman, T.K., Sahoo, P.: Application of artificial bee colony algorithm for optimization of MRR and surface roughness in EDM of EN31 tool steel, Procedia. Mater. Sci. **6**, 741–751 (2014). https://doi.org/10.1016/j.mspro.2014.07.090

28. Kutanaei, S.S., Choobbasti, A.J.: Prediction of combined effects of fibers and cement on the mechanical properties of sand using particle swarm optimization algorithm. J. Adhes. Sci. Technol. **29**(6), 487–501 (2015)

29. Yan, X., Zhang, C., Luo, W., Li, W., Chen, W., Liu, H.: Solve traveling salesman problem using particle swarm optimization algorithm. Int. J. Comput. Sci. **9**(6), 264 (2012)

30. Samad, S., Shah, A., Limbachiya, M.C.: Strength development characteristics of concrete produced with blended cement using ground granulated blast furnace slag (GGBS) under various curing conditions. Sādhanā **42**, 1203–1213 (2017). https://doi.org/10.1007/s12046-017-0667-z

31. https://www.fhwa.dot.gov/pavement/recycling/fach03.cfm#:~:text=Fly%20ash%20particles%20react%20with,to%20increase%20long%2Dterm%20strength

32. https://www.pci.org/PCI_Docs/Design_Resources/Guides_and_manuals/references/bridge_design_manual

Publisher's Note Springer Nature remains neutral with regard to jurisdictional claims in published maps and institutional affiliations.

RESEARCH ARTICLE

Seismic Analysis of a Reinforced Concrete Structure with and without Shear Wall at Zone-II with Etabs

K. Harshada[1] and MD Thoufik ali[2]*

[1]Assistant Professor, Department of Civil Engineering, Malla Reddy Engineering College, Hyderabad, Telangana, India
[2]PG Scholar, Department of Civil Engineering, Malla Reddy Engineering College, Hyderabad, Telangana, India

*Address for Correspondence
MD Thoufik ali
PG Scholar, Department of Civil Engineering,
Malla Reddy Engineering College,
Hyderabad, Telangana, India
Email: thoufik.ali.23@gmail.com

ABSTRACT

Shear wall systems are one of the most commonly used lateral load resisting strategies in high-rise buildings, and they are also one of the most expensive. The in-plane stiffness and strength of shear walls are high, and this enables them to withstand considerable horizontal stresses while still supporting gravity loads, making them valuable in a wide range of structural engineering applications. Typically, shear walls are seen in high-rise buildings to prevent the structure from collapsing as a result of lateral loads.. Shear walls are primarily flexural elements that are designed to withstand lateral stresses induced by earthquake and other phenomena. The seismic study in this research is based on an 11-story RCC structure in Zone II. There is a wealth of information available to help you design and analyze a shear wall. However, there is little discussion in the literature on where the shear wall should be placed in a multi-story building. The major goal of this work is to find a solution for shear wall placement in multi-story buildings. The construction is an RCC structure in HYDERABAD that is susceptible to seismic loads in zone II. IS 1893 (PART–I):2002 is used to compute an earthquake load utilizing the seismic coefficient technique. ETABS was used to conduct these analyses.

Keywords: Multi-storey, RC structure, seismic analysis, RC with shear wall and without shear wall, ETABS.

INTRODUCTION

As the construction's mass grows, we must choose for heavier sections to counteract the seismic forces, which will increase the structure's mass, resulting in increased seismic forces. Ductility may be simply produced in a enclosed building with suitable reinforcing details, then when the building rises over a certain height, massive sections are necessary to counter forces, making it practically impracticable. Control of lateral displacement caused by lateral forces is currently one of the most important requirements in building RCC structures in seismic zones. The influence of Shear Wall location on lateral displacement and Storey. Drift in RCC Structures was investigated in this thesis.

Why High Rise Buildings?
The increasing urban people expansion with the resulting demand on restricted space has had a significant impact on city residential construction. The high cost of land, the desire to avoid ongoing urban development, and the necessity to protect key agricultural output have all contributed to the increasing trend in residential construction. Local topographical limits kind towering structures the only viable answer for housing demands in some places, such as Hong Kong and Rio de Janeiro.

Structural System in High Rise Building
Columns and walls are the two principal vertical load acting components of tall structures, with the latter serving as shear walls or shear wall cores in assemblies. The supply of everything to divide and enclose space, as well as cores to hold and carry utilities like elevators, would automatically follow the building purpose. Gravity loads and, in some types of constructions, horizontal loads will be transmitted via columns in then unsupported locations.

SHEAR WALLS
In adding to slabs, beams, and columns, shear walls are vertically concerned with elements that can withstand lateral stresses. RCC shear walls have a high in-plane stiffness while resisting huge horizontal weights and supporting gravity masses in the way of the walls' alignment, making them useful in a wide range of structural engineering applications and lowering the danger of Building damage.

SHEAR WALL – FRAME BUILDINGS
Shear Walls

A shear wall is a structural system made up of braced panels that are used to mitigate the effects of lateral loads on a structure. Shear walls are typically constructed to withstand wind and earthquake stresses. Exterior wall lines in wood or steel surround structure necessity be braced according to numerous construction requirements. Shear walls, on the other hand, when positioned in a favorable position, constitute an effective lateral force resisting structure.

DIFFERENT SHAPES OF SHEAR WALLS
The form and placement of the shear wall have an effect on the structural behaviour of the structure when subjected to lateral stresses. A horizontal diaphragm serves to convey lateral loads parallel to the force of the action. Lateral loads are delivered to the shear walls, where they are absorbed by the shear walls, which serve as a horizontal diaphragm. When viewed in relation to the structural elements, the eccentrically positioned core is required to fulfil a variety of activities, including torque, bending, and direct shear. These shear walls are able to withstand horizontal pressures while remaining upright due to their high stiffness as deep beams that react to shear and flexure against overturning. While rectangular cross sections are the most common in structural applications, L- and U-shaped cross sections are also common. Shear walls constructed of thin-walled deep RC shafts around the elevator core of the building should be used to resist seismic effects. It is included in this part to provide information on the shear wall forms that were employed in this project, as seen in Fig. 1.

- U Section
- W Section
- H Section
- T Section

BASIC ASPECTS OF SEISMIC DESIGN

Because earthquakes generate inertia forces proportional to the mass of the structure under construction, the mass of the structure under construction has an influence on seismic design in addition to the stiffness of the structure under construction. As a consequence, it is possible that the structure will need to undergo damage in order to release the energy that has been absorbed by the earthquake. To counteract this effect, the traditional earthquake-resistant design philosophy stipulates those typical constructions must be capable of withstanding any of the following:

a) Mild to moderate shaking that occurs on a regular basis with minimal harm to structural or non-structural components;
b) Moderate shaking with only minimal structural damage and some non-structural damage; and
c) Severe (and sporadic) shaking results in structural damage but no collapse (in order to spare lives and property inside and next to the structure).

Under design wind forces, on the other hand, structural damage is unacceptable. As a result, earthquake resistant design, rather than earthquake-proof design, is used to describe earthquake-resistant construction, as shown fig.2,

SEISMIC ZONES OF INDIA

The seismic zone map has been altered, with just four zones instead of five, based on the intensities suffered by severe prior earthquakes. Zone I was once split into two zones, one of which is now known as Zone II. As a result, only Zones II, III, IV, and V are included in the new zoning system. About Seismic Zoning Map of India. The first seismic zoning map of India was produced in 1935 by the Geological Survey of India (G. S. I.). This map was originally based on the amount of damage experienced by various parts of India as a result of earthquakes, with multiple adjustments made afterwards. This map depicts India's four unique seismic zones, which are color-coded in varying degrees of red. The following are the country's several seismic zones, as seen on the map, shown in fig3,

Zone - II: This is said to be the least active seismic zone.
Zone - III: It is included in the moderate seismic zone.
Zone - IV: This is considered to be the high seismic zone.
Zone - V: It is the highest seismic zone.

Function of Shear wall

To be able to withstand horizontal earthquake forces, shear walls must possess the necessary lateral strength. Shear walls would convey horizontal forces to other components in the load channel below them as soon as their strength was determined to be sufficient. Shear walls provide additional lateral stiffness to a structure, preventing the roof or floor from swaying excessively to one side. Shear walls with appropriate stiffness will prevent the sliding away of floor and roof bordering members once their supports have been removed. Furthermore, structures that are sufficiently robust may absorb less non-functional damage as a result of their construction. Shear walls also offer lateral stiffness, which prevents the ceiling or floor from moving excessively in either direction sideways.

Requirements of Structural Element In High Rise Buildings

As high-rise buildings are built, the wind and seismic forces to which they are subjected become more important considerations in the design and construction of the structures. It is now possible to improve tall building structural systems in order to manage their dynamic responses as a result of the dramatic increase in the maximum height of concrete buildings over the last few decades, which includes the incorporation of more appropriate structural elements such as shear walls and tube structures, as well as improved concrete material qualities used in their

construction. The margins of shear walls are especially sensitive to severe compressive and tensile stresses as a consequence of the massive overturning effects induced by horizontal earthquake pressures, which may cause the wall to collapse. In order for shear walls to be capable of withstanding load reversals while retaining their strength, a certain kind of reinforcement must be employed in the concrete at the end parts of the walls. This is referred to as the "ductile reinforcement strategy" in the technical literature. In construction, boundary components are the terminal elements of a wall that are more constrained in their movement than the remainder of the wall structure. Rather than being employed throughout the frame as a restricting element, transverse reinforcement, similar to that found in the columns of a reinforced concrete frame, is used just in the border components. In certain instances, the thickness of the shear wall in these border components is also increased in order to compensate for the increased loading.

RC Shear Wall

As an alternative to slabs, beams, and columns, they are vertical plate-like reinforced concrete (RC) walls that are often employed in reinforced concrete buildings to give extra structural support in addition to slabs, beams, and columns. Shear walls are made of reinforced concrete (RC), and they have a similar appearance to plate-like walls. These walls are often constructed by beginning at the ground level and ascending to the maximum height of the building in a series of steps. When used in tall constructions, they may be as thin as 150 mm or as thick as 400 mm in thickness, depending on the application and the needs of the structure. A well-known consulting engineer from the United States, Mark Fintel, believes we "can not afford to construct concrete structures meant for severe earthquakes without shear walls." "Concrete buildings intended for severe earthquakes without shear walls" is not an option, he argues. Then he said something like, "We can't afford to create concrete structures that are designed to withstand big earthquakes without including shear walls in the design."In particular, the overturning effects of shear walls are remarkable because they carry significant horizontal earthquake forces to the ground underneath them. Shear walls must be organised in a symmetrical manner in order to prevent the harmful effects of twisting on the structural stability of a building's foundation. Asymmetry in plan along one or both directions is possible, as is symmetrical positioning in plan along one or both directions. It is more advantageous for shear walls to be situated on the external perimeter of a structure than on the inside perimeter of a structure. As a consequence of this configuration, the twisting resistance of the structure is enhanced.RCC shear walls have a high in-plane stiffness while resisting huge horizontal weights and supporting gravity masses in the direction of the walls' orientation, making them useful in a variety of structural engineering applications and lowering the risk of structural damage. Shear walls also provide lateral rigidity to avoid excessive side-sway of the roof or floor above. Shear walls also provide lateral rigidity, preventing excessive side-sway of the roof or floor above. Shear walls come in a variety of shapes and sizes, including rectangular and irregular cores like channel, T, L, barbell, and box. The location of a shear wall in a structure has an impact on the structure's behavior.

Function of Shear Wall

Earthquakes are vibrations that occur under the earth's surface, resulting in the death of people and the destruction of structures. The major goal of the structural systems in the building is to properly transmit gravity loads such as dead load, living load, and snow load. Buildings are susceptible to lateral loads induced by wind, blasting, or earthquakes, which can create significant stresses, sway, or vibration in addition to gravity loads. The combination of sufficient vertical strength and enough stiffness can efficiently withstand lateral forces. hear walls in a structure withstand a mixture of shear, moment, and axial loads resulting from lateral and gravity loads.

Objectives

The objectives are as follows,

1. With the help of the ETABS software, a multi-story structure with a shear wall was analysed.
2. To investigate the behaviour of the structure when the shear wall is placed at various locations.
3. Natural Period, storey shear, storey displacement, and storey drift are all factors that will be investigated and compared in this research.
4. In order to establish the most advantageous site for the construction,
5. Shear walls are used to prevent structures from collapsing due to earthquakes.

LITERATURE REVIEW

[Greifenhagen and Lestuzzi, 2005]

According to the results of the investigation, a squat reinforced shear wall, which was not meant to withstand seismic stimulation, has high strength and deformation capacity under load. The outcomes of a series of static cycle tests performed on a poorly reinforced concrete shear wall of an existing building with the purpose of measuring the deformation capacity of the wall are presented in this paper. Before making any suggestions for earthquake-resistant design, this study will conduct a more realistic seismic assessment of existing shear walls in order to offer better earthquake-resistant design recommendations. A multitude of parameters, including cross section type, reinforcement details and quantity, reinforcing steel characteristics, and boundary conditions, may cause failure modes to manifest themselves, but the most common are as follows:

[Elwood, et-al., 2006]

Using a beam–pillar frame construction, the capabilities of an earthquake-resistant structure are examined in this paper. According to the conclusions of this investigation, a beam pillar construction should be strengthened against earthquake loads by applying compression and tension braces diagonally to it. To test the performance of tension braces with a thickness of 200 mm, connectors and tap bolts are attached to the braces and then released (tap bolts on two perpendicular sides of the connections on the pillar-beam element). As an alternative, we investigate compression braces with the same thickness as the walls, and we find that they are particularly advantageous in such situations since they are simple to install and effective at boosting seismicity. In order to prevent any possible difficulties that may occur during the demolition and subsequent rebuilding of the structure for reinforcement, the major goal of this inquiry was to identify them. According to the findings of this research, tensile braces are efficient whether they are employed globally or just as a last option.

METHODOLOGY

Vibrations caused by earthquakes produce inertia forces in the structure. As a result, a structure must be capable of securely transmitting the horizontal and vertical inertia forces created by the superstructure to the earth via the foundation. Seismic codes will help a designer construct a structure that will be safe for its intended use. There are a variety of approaches for analyzing structures for earthquakes; two of them are discussed below. The approach used to assess the seismic behavior of regular and irregular structures with and without shear walls. There are two types of G+11 Storey building geometry: regular buildings with and without shear walls, and irregular buildings with and without shear walls. ETABS 2016 is used to model and evaluate the buildings. The equivalent static approach and the response spectrum method are used to analyze structures. According to the IS: 1893-2002(Part 1) code of practice, models are used for zone factor V and soil type II (Medium). Maximum displacement, stiffness, and storey drift are among the characteristics evaluated in the study.

a   A thorough analysis of the literature to gain a better understanding of seismic evaluation of building structures and to determine the most effective and efficient placement of shear walls inside the structure.
b   Creating a model of a forty-story structure. Shear walls with apertures are given at the central core and at the centre of each side of the exterior perimeter.
c   Checking the building's design for dead load, live load, and seismic load in accordance with Indian standards.
d   Using linear static dynamic analysis, i.e., Response Spectrum Analysis, to analyze the building.
e   Interpreting the findings and drawing inferences.

The following approaches may be used to model a shear wall: -CAD (computer-aided design)
1.   Using the equivalence frame approach,
2.   The braced frame approach is also known as

3. The finite element approach is a kind of numerical analysis. The shear wall is modelled in ETAB, utilising the Finite Element Method and Surface Meshing to get the desired results.

Load Conditions
1. The dead load criterion for all of the models is one kilonewton per metre.
2. In all cases, the live load criterion is 3KN/M for all of the various types.
3. In accordance with IS 1893 (PART 1):2002, the lateral load is the seismic load that is applied to the mass centre of the building.

MODELLING AND ANALYSIS PROGRAM

MODELING
Four distinct types of infill materials are considered in this study: traditional brick, cement concrete block, hollow block, and light weight brick. The computer software ETABS-2009 was used to develop and evaluate the building models using various types of infill materials, and the results were compared.

Material Specifications
Table: 2 Specifications of Materials

Analysis
The building is being analysed with the help of the programme ETABS. ETABS was responsible for the creation of the models. The programme makes use of a variety of RC shear wall cross sections, including the box type, the L type, and the cross type, and these cross sections are placed in various positions, including the perimeter, the corner, and the centre.

METHODS OF ANALYSIS
When a structure is subjected to earthquake ground motion, earthquake response analysis is an art form that employs dynamics and a mathematical model of the structure to simulate the structure's behavior.To do the proper analysis, precise modelling of the behaviour of the materials, components, and connections to the structure will be necessary. Taking into consideration the study's purpose, the number of degrees of freedom should be properly calculated in the model. Given that each node has its own displacement, a three-dimensional model may be used to simulate any kind of behaviour. Because of the difficulties associated with modelling, verification, and numerical calculation, the three-dimensional model has not yet been included in the most sophisticated design methodologies. This research was carried out with the help of the ETABS 2006 software package.

Frame analysis
The appropriate sort of member requirements are used to define three-dimensional (3D) beam or column components in this study. Each node has six degrees of freedom (Ux, Uy, Uz, Rx, Ry, Rz).

Seismic method of analysis
Following the selection of a structural model, it is possible to conduct an analysis to determine the presence of seismically induced forces in a structure. It is the present emphasis of the study to conduct linear static analysis or a similar kind of static analysis for regular structures with limited height.

ETABS INTRODUCTION
Extended 3D (Three-Dimensional) Analysis of Building Systems (ETABS) is a term that refers to the increased 3D (Three-Dimensional) Analysis of Buildings (ETA This is done using finite element software and the stiffness matrix. The analysis and design are carried out in accordance with Indian standards to ensure that all of the checks are met. Finally, a data base for diverse structural reactions is created. TABS Software: Structural analysis and building design

are made easier with the revolutionary new ETABS software package, which is the most complete software solution available today. This version of ETABS lacks comparable 3D modelling and visualisation tools, as well as quick linear and nonlinear analytical power, complex and comprehensive design capabilities for a wide range of materials, and incisive graphic presentations, reports, and schematic drawings. Direct conversion of CAD drawings into ETABS models is possible. The examination of the G+6 Building exposed to loads is the primary focus of this paper. The methods for structural analysis that we will offer in this study were developed using software (ETABS).

ETABS is a structural and seismic engineering programmed developed by Computer and Structural Inc (CSI). The world's tallest structure, the Burj Khalifa, was also planned and assessed using this software.

The following are some of the reasons we picked ETABS:

◎ Easy to use interface,

◎ Confirmation with the Indian Standard Codes

◎ Versatile nature of solving any type of problem,

◎ Accuracy of the solution

MODELLING IN ETABS

53D View of the Building in ETABS

RESULTS

Storey displacement, storey drift, Natural period, and storey shear are the results of the study, which are produced for all models in both lateral directions (X and Y). For multistory building with bare frame model at various positions of shear wall, results are obtained and graphs are generated.

STOREY DISPLACEMENT

Table: 3 Storey Displacement (mm) , Graph1:Storey Displacement (mm)

Story Drift

Table: 4 Storey Drift (m), Graph2:Storey Drift (m)

STOREY SHEAR

Table: 5 Storey Drift (m), Graph3:Storey Drift (m)

CONCLUSIONS

The current investigation aims to determine the impact of a shear wall on a structure in an earthquake-prone zone. For all models, the load combination 1.5DL+1.5EQX is shown to be the most essential. ETABS was used to conduct the investigation. According on the findings of the study, the following conclusions may be drawn.

1. All models show that when the storey height rises, the displacements increase.
2. Storey displacement is lower for structures with shear walls at corners than for structures with shear walls in the middle and structures without shear walls. As a result, it is possible to construct a shear wall at the corners.
3. In comparison to structures with shear walls in the middle, structures with shear walls at the corners yield greater values. As a result, shear walls at corners are a viable option.
4. It is clear from the preceding observations that constructions with shear walls at corners perform better than other structure.

REFERENCES

1. Choi, I. R., & Park, H. G. "Ductility and energy dissipation capacity of Friction joint-dominated steel plate walls". Journal of structural engineering, vol no.134, No.9, pp 1495-1507, 2008

2. Greifenhagen, C., &Lestuzzi, P. "Static cyclic tests on lightly reinforced concrete shear walls". Engineering Structures, vol no.27, No.11, pp 1703-1712, June 2005] Kitada, Y., Nishikawa, T., Takiguchi, K., & Maekawa, K. "Ultimate strength of reinforce concrete shear walls under multi-axes seismic loads". Nuclear engineering and design, vol.no.237, no.12, pp 1307-1314, October 2007

3. Matamoros, A. B., & Elwood, K. (Eds.). (2006). "Beam-Pillar structure capacity and shear strength of reinforced concrete members under cyclic loading". San Francisco, California. American Concrete Institute. vol.no.9, No.2, pp 24-28, October 2004

4. Su, R. K. L., & Wong, S. M. "Seismic behaviour of slender reinforced concrete shear walls under high axial load ratio". Engineering Structures, vol.no.29, No.8, pp 1957-1965, Feburary 2007

5. Vetr, M. G., Shirali, N. M., &Ghamari, A. "Seismic resistance of hybrid shear wall (HSW) systems". Journal of Constructional Steel Research, vol.no.116, No. 2, pp 247-270, January 2016.

6. Wang, M., Shi, Y., Xu, J., Yang, W., & Li, Y. "Experimental and numerical study of unstiffened steel plate shear wall structures". Journal of Constructional Steel Research, vol.no.112, No.1, pp 373-386, June 2015

Table : 1 Details of building

Number of storeys	11
Story Height	3m
Size of Beam	30X60
Size of column	50X50
Slab thickness	15cm
Support condition	Fixed
Thickness External wall	20cm
Grade of steel	Fe-415
Grade of concrete for Beam	M 25
Grade of concrete for column	M 30
Response Reduction Factor	5
Importance Factor	1
Soil condition	Medium
Type of soil	II
Zone	II
Zone Factor	0.36

Table 2. Specifications of Materials

Material Specifications	
Grade of concrete M 30	$f_{ck}=30N/mm^2$
Grade of Steel	$f_y=415N/mm^2$
Density of concrete	$\Gamma_c=25N/mm^2$
Density of brick walls concrete	$\Gamma_{brick}=20N/mm^2$

Harshada and Thoufik ali

Table: 3 Storey Displacement (mm)

Storey No	With Shear Wall	Without Shear Wall
Storey 11	71.9	36.9
Storey 10	68.6	32.8
Storey 9	64.3	28.6
Storey 8	58.7	24.3
Storey 7	51.8	20
Storey 6	43.9	15.8
Storey 5	35.3	11.9
Storey 4	26.3	8.3
Storey 3	17.4	5.1
Storey 2	9.2	2.6
Storey 1	2.8	0.9
Base	0	0

Table : 4 Storey Drift (m)

Storey No	With Shear Wall	Without Shear Wall
Storey 11	0.001073	0.001381
Storey 10	0.001446	0.001424
Storey 9	0.001882	0.001439
Storey 8	0.002291	0.001429
Storey 7	0.002627	0.001391
Storey 6	0.002867	0.001317
Storey 5	0.002992	0.001202
Storey 4	0.002968	0.001044
Storey 3	0.00273	0.000845
Storey 2	0.002145	0.000611
Storey 1	0.000939	0.000284
Base	0	0

Table: 5 Storey Drift (m)

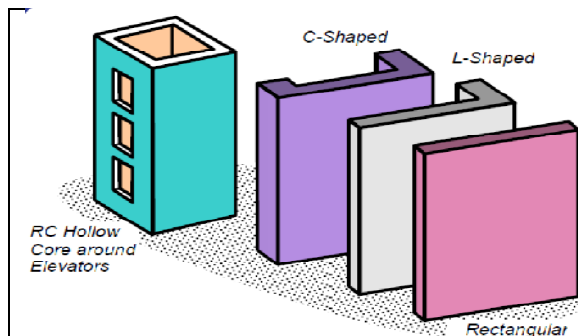| Storey No	With Shear Wall	Without Shear Wall
Storey 11	178.8791	430.9792
Storey 10	455.3334	1104.997
Storey 9	679.2614	1650.951
Storey 8	856.1922	2082.323
Storey 7	991.6548	2412.591
Storey 6	1091.178	2655.238
Storey 5	1160.292	2823.742
Storey 4	1204.525	2931.585
Storey 3	1229.406	2992.247
Storey 2	1240.464	3019.207
Storey 1	1241.01	3020.701
Base	0	0

Harshada and Thoufik ali

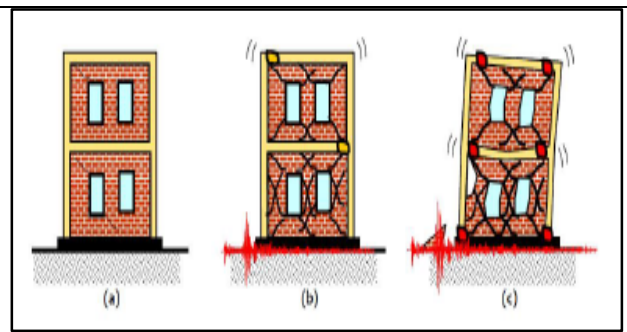**Fig. 1. Various Types of Shear Walls**

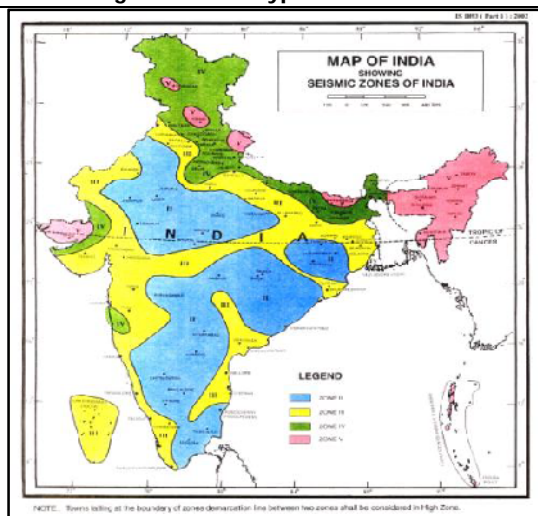**Fig. 2 Earthquake-Resistant philosophy for building**

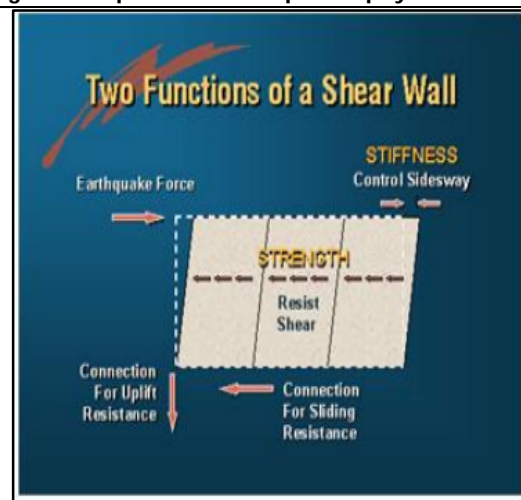**Fig. 3. Modified seismic zones of INDIA (IS 1893-PART 1 2002)**
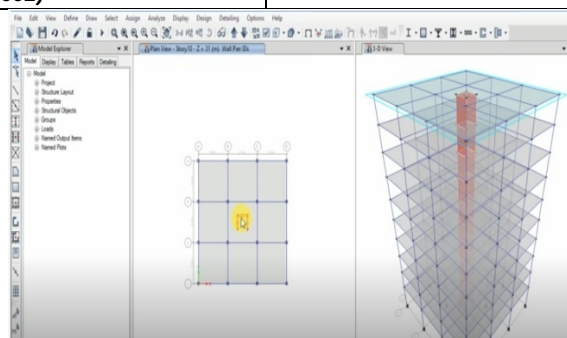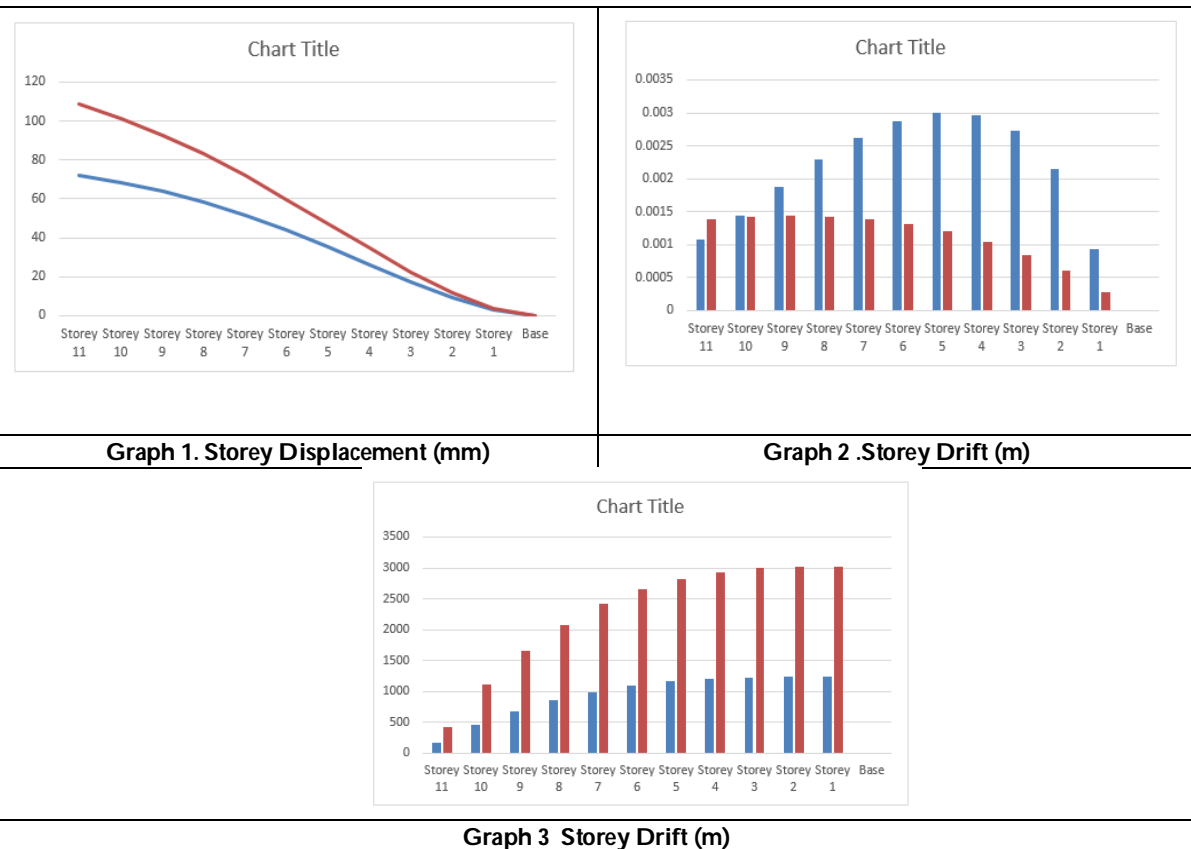

Fig-4: Function of Shear Wall

Fig. 5. 3D View of the Building in ETABS

Harshada and Thoufik ali

Graph 1. Storey Displacement (mm)

Graph 2 .Storey Drift (m)

Graph 3 Storey Drift (m)

45844

RESEARCH ARTICLE

Performance of Hybrid Columns Subjected to Axial, Eccentric and Cyclic Loading

T. Ram Prasanna Kumar Reddy[1] and Mohammed Bilal Badr[2]*

[1]Assistant Professor, Department of Civil Engineering, Malla Reddy Engineering College, Hyderabad, India

[2]PG Scholar, Department of Civil Engineering, Malla Reddy Engineering College, Hyderabad, India.

*Address for Correspondence
Mohammed Bilal Badr,
PG Scholar,
Department of Civil Engineering,
Malla Reddy Engineering College,
Hyderabad, India.
Email: mhbadr.ce@gmail.com

ABSTRACT

This study deals with the analytical study that investigate the performance of concrete encased hybrid column without reinforcement subjected to axial, eccentric and cyclic loading. The column made up of steel, concrete, and fiber reinforced polymer (FRP). Eight columns of different cross-sectional shape were studied under axial and eccentric loading. Finite element model (FEM) were developed for performing the analysis. Load deflection characteristics, deformation, and ductility of the column were investigated. The result indicate that outer square and inner circular shaped columns have more load carrying capacity. Cyclic analysis was performed for best model. Then the best model is considered for further parametric study. Use of High Strength Concrete (HSC), Radius of inner tube, and hybrid FRP tube are the parameters studied. Cyclic analysis is performed and energy dissipation capacity is studied.

Keywords: Column; Cyclic analysis, Ductility, Energy Dissipation Capacity, Fiber reinforced polymer (FRP), Finite element model (FEM), High Strength Concrete (HSC), Hybrid column.

INTRODUCTION

As a result of the increased need for improved execution at lower prices, there has been an increase in research directed towards enhancing the mechanical behaviour and seismic execution of columns. Diverse column types have been subjected to a number of investigations to better understand their seismic behaviour. Composite elements, also known as hybrid elements, are structural components that are constructed from two or more distinct types of materials. It is the fact that the features of each fabric may be merged to generate a single unit that performs better overall than its partitioned constituent parts that is the most advantageous aspect of hybrid components. According

45931

to industry experts, a steel-concrete composite frame might be the most widely used hybrid component frame in development right now. Concrete, as a material, performs well in compression, but it performs poorly in tension. Steel is very strong under tension, even when just a tiny quantity of it is employed. Steel-concrete hybrid components combine the compressive strength of concrete with the tensile resistance of steel, resulting in a structurally strong and lightweight unit that is often used in multi-story buildings and bridges.

Due to the great strength of composite columns while having a small cross-sectional area, it will be possible to maximise the amount of usable floor space available for usage. Several different types of composite columns are available, with the most often used being a hollow section steel tube that has been packed with concrete, or an associate degree open steel section that has been encased in concrete. Adding concrete to the steel section increases the compression resistance of the steel, which helps to keep the steel from buckling under compression. Because of its fire resistance, the column may be left uncovered or just lightly shielded if necessary.

The most often seen hollow sections are rectangular and circular in shape. However, rectangular sections are advantageous in that they have flat sides that are suitable for finish plate beam-to-column connections. Fin plates, on the other hand, will be used for rectangular and circular forms. In a vast amount of research on the axial compressive behaviour of FRP-wrapped columns, it has been shown that the external confinement of existing concrete columns by fibre reinforced polymer (FRP) composites is an excellent way of enhancing column ductility. The issues associated with traditional building materials are alleviated by using fibreglass reinforced plastic (FRP). The use of fibre reinforced plastic (FRP) increases the flexural and shear strength. The use of fibre reinforced polymer (FRP) composites to externally restrict existing concrete columns has been shown to be a successful approach for increasing column ductility and extending column life.

OBJECTIVES ANDSCOPE

The Objective of this study is to investigate the behavior of hybrid columns subjected to axial, eccentric and cyclic loading. Hybrid Column is made of an inner tube and outer tube. Concrete is sandwiched between the tubes. Study deals with the comparative study between conventional column and hybrid columns of different shapes, different strength of concrete, radius of inner tube and hybrid FRP. Study includes the load carrying capacity, cyclic behavior, ductility and energy dissipation capacity of columns. Also study the behavior of columns under eccentric loading. This study is to investigate the best shape and material for inner and outer tube. Software used in the study is ANSYS 16.1

METHODOLOGY

A literature survey should be carried out by referring to and reading papers and journals published in the field of study in order to get detailed topic knowledge. Model selection and associated data gathering that will help in the completion of the task, such as validation model detail collecting, earthquake data collection, and so on, must be completed before the work can be completed. A software study is a vital phase in this project; one needs to complete a software study in order to get familiar with the software tools. This aids in the elimination of any and all potential mistakes that may arise throughout the modeling and analysis process. The validation model is being modelled. Validation is accomplished by the use of an RCC column with FRP wrap. The validation process is a critical step in ensuring the accuracy of the final product. It also helps in the evaluation of the product quality received from the software application. Validation should be carried out using the same software as that which is being used to prepare the project study.

The validation process is a critical step in ensuring the accuracy of the final product. It also helps in the evaluation of the product quality received from the software application. Validation should be carried out using the same software as that which is being used to prepare the project study.

Ram Prasanna Kumar Reddy and Mohammed Bilal Badr

SOFTWARE STUDY

ANSYS, Inc. is a publicly traded American corporation with its headquarters in Canonsburg, Pennsylvania. It is a software company that produces and offers engineering simulation software. Designing items and semiconductors using ANSYS software is also possible. The program me may also be used to build simulations that test a product's durability, temperature distribution, fluid motions, and electromagnetic characteristics.

STEPS INVOLVED IN STRUCTURALANALYSIS

The following steps are involved in this structural analysis.

➢ Creation of geometry
➢ Real constants and cross-section properties
➢ Selection of element type
➢ Meshing
➢ Selection of material and properties
➢ Define loads and displacements
➢ Reviewing results
➢ Verify of results

VALIDATIONS

DETAILS OF THE STRUCTUREANALYSED

The column selected for validating the software is 150x150x1000 mm size. The column has eight numbers of 10 mm diameter bars. FRP wrap is provided outside the column. 10 mm clear cover is provided. Lateral ties provided only in two positions. Pushover analysis was performed. Aramid FRP is used for providing outside wrap to the column. Modelling and Analysis were done using ANSYS16.1.

Finite element modeling was done for the RC column with FRP wrap outside. Pushover analysis was performed on this column. And the results were obtained as follows (Table 1). The deformation of the RC column with FRP wrap outside is shown in Figure 3. Buckling is characterized by a sudden sideways deflection of a structural member.
The column shows signs of worldwide buckling. According to the pushover study of the RCC column with FRP wrap performed in ANSYS 16.1, the column has a load carrying capacity of 61.382 k N, which is higher than the load carrying capability found in the validated journal, which was 58 k N. It seems that the result acquired from ANSYS is comparable to the result obtained from the validating journal. The experiment's outcome is only 5.83 percent accurate.

MODELLING AND ANALYSIS

Over the last two decades, the use of fibre-reinforced polymer (FRP) reinforcement to strengthen structures has grown more prevalent. Hybrid FRP-concrete-steel columns are a new kind of hybrid column that is being developed. According to the findings of this investigation, the hybrid column outperformed the traditional RCC column with a FRP wrap. The form of the inner and outer tubes, the presence of high-strength concrete inside and outside the inner tube, the radius of the inner tube, and the presence of a hybrid FRP tube were all considered in the analysis of the hybrid column.

The column was exposed to axial, eccentric, and cyclic loads throughout the experiment. The material characteristics of concrete, steel, and fiber-reinforced plastic (FRP) are listed in Table 2. The element type 20 noded solid 186 is used in the FE modeling process. It is a non-linear analysis, as the name implies. The concrete has multilinear characteristics. Bilinearity is a feature of both fibreglass reinforced plastic and steel.

Axial Loading

Different shaped columns are modeled and analysed under axial loading condition. Different material used for inside and outside tubes. Outside FRP and inside steel tubes and vice versa. The dimension of inner and outer tube is

taken in accordance with the dimension of conventional column and steel table. he compression or tension force exerted on a member is referred to as the axial force. When an axial force is applied via the centroid of a part, this is referred to as concentric loading. Eccentric loading is a term used to describe when a force does not act via the centroid. Due to the fact that the load is located a distance away from the centroid, eccentric loading results in the generation of a moment in a beam.

Eccentric Loading
An eccentric load is applied to the model that performs the best out of all the models. Upon completion of the study, it can be determined that the outer square FRP and inner circular steel column models are the best when applying axial load (later discussed in chapter 6). Eccentricity is measured at 10%, 25%, 50%, and 90% deviations from the centre of the column. Biaxial loading is applied to a column when the eccentricity is measured in both directions (with respect to both axes) of the column (x and y axes). Figure 5.depicts this, with the eccentrically laden column at 90% eccentricity. The inner tube is reinforced with high-strength concrete both inside and outside. The outside tube is made of fibreglass, while the inner tube is made of steel. Steel fibres are added to M40 concrete to provide it with high strength, which amounts to 1.5 percent. M65 concrete is considered to have normal strength. HSC has a yield strength of 43543.08 N/mm2 and is a high-strength material.

Cyclic Loading
Cyclic loading is described as the continuous and repetitive application of a load (fluctuating stresses, strains, pressures, tensions, and so on) on a material or on a structural component that causes deterioration of the material and eventually leads to fatigue of the material or structural component. Cyclic loading causes materials to degrade as a result of fatigue, and this occurs at lower loads and for a shorter period of time than would be anticipated otherwise. Cyclic loading is applied to the columns which have best shape. As per FEMA350 cyclic protocol cyclic loading is given at 0.375%, 0.75%, 1%, 2%, 3%, 4%, 5%, 6%, 8% and 10% drift ratio.

RESULTS AND DISCUSSIONS

PERFORMANCE OF DIFFERENT SHAPEDCOLUMNS
Results from the analysis discussed in this chapter, Maximum load and deflections of each column is discussed here. Also, ductility, deformation of columns, energy dissipation capacity are discussed. Ductility of column calculated from load deformation From this it can conclude that Load carrying capacity is more for outer square FRP and inner circular steel column. It has minimum deflection. Eccentric loading is applied on this column and the results are given in Table4.

Ductility of conventional column = 1.52
Ductility of hybrid column=2.64
Outer square FRP inner circular steel column is more ductile than conventional column. From the hysteresis curve it is clear that outer square FRP inner circular steel column has more ductile behavior. For further parametric study the outer square FRP inner circular steel hybrid column is considered.

PERFORMANCE OF HYBRID COLUMN FILLED WITHHSC
Load and deformation of hybrid columns filled with HSC inside the tube and outside the tube are given in Table 5. HSC in outer tube take more load. The deformation of two models is almost same. For better results, the HSC should give outside the inner tube. Ductility of Column =2.71 At 10% drift the specimen reaches a load value of 200 kN and displacement of 40mm. When unloading the column, it reaches to 15 mm. Its strain recovery is 62.5%. Energy dissipation capacity is good for the column. The column is ductile in nature. It is very clear from the hysteresis curve.

PERFORMANCE OF COLUMNWITH M A X I M U M INNER TUBERADIUS

Radius of inner tube increases, the confinement increases. As a result, load carrying capacity increased with minimum deformation.

Load   = 6795.6 kN
Deformation   = 22.025mm

From Figure 9 it is clear that the column is subjected to global buckling. It is due to the presence of FRP and steel. Concrete takes the load and fails. Then the load transferred to the steel tube. Steel tube has yielding property. The buckling is occur due to the yielding of steel. FRP enhance the tensile property. There is no crushing due to the presence of FRP. Maximum deformation occurs at outer tube.

Load and deflection of Hybrid column with maximum inner tube radius when subjected to eccentric load is given in Table 6. Ductility is also improved for this column. It is due to the presence of steel tube and FRP tube. FRP enhance the tensile property. From hysteresis curve it can be concluded that the column ductile in nature.

Ductility of the column   =2.72

At 10% drift the specimen reaches a load value of 900 kN and displacement of 100mm. When unloading the column, it reaches to 55 mm. Its strain recovery is 45%. The column has better energy dissipation capacity.

PERFORMANCE OF COLUMNS MADE OF HYBRID FRPTUBE

Carbon and Aramid FRP used for making hybrid FRP tube. Load and deflection of the model subjected to axial loading is given below.

Load   = 7489.3 kN
Deformation= 20.019mm

Maximum deformation occurs on outer FRP tube. The column subjected to global buckling. Load deformation curve for hybrid FRP tube column is given in Figure 6.13. AFRP and CFRP are high strength fibers. They have high modulus of elasticity. Therefore, the column take more load with minimum deflection. Among all models, hybrid column with outer hybrid FRP tube has better performance.

Ductility of the column   =2.58

Ductility of the column is more than conventional one. The use of FRP enhance the ductility.

At 10% drift the specimen reaches a load value of 400 kN and displacement of 80mm. When unloading the column it reaches to 20 mm. Its strain recovery is 75%. The column with hybrid FRP tube have better energy dissipation capacity. It has more strain recovery capacity than all models. It shows good hysteresis behavior and it possess better ductility.

CONCLUSION

Performance of Hybrid Column Subjected to Axial, Eccentric and Cyclic Loading has been conducted in this study. Analytical study is performed in ANSYS 16.1 software. Nonlinear analysis is performed to understand the behavior of the hybrid column under various parameters. Four different parameters are considered in this study. Shape of inner tube and outer tube, High Strength Concrete (HSC) in inner tube and outer tube, Radius of inner tube and Hybrid FRP tube. Load deformation capacity, ductility, failure type, energy dissipation capacity were analysed in this study. The results were compared with conventional column which has a FRP wrap outside the column.

- ➢ From the parametric study it is clear that, best shape of hybrid column which has an outer tube and inner tube with sand witched concrete is outer square and inner circular. It has more load carrying capacity than conventional column. It shows good hysteris is behaviour and ductility.

- ➢ When HSC is filled in inner steel tube and HSC filled in Outer FRP tube, the two models shows increase in load carrying capacity. Hybrid column with HSC in outer tube shows more load carrying capacity than HSC in inner tube. The HSC mixes typically have an increased modulus of elasticity, which increase the stability and reduces deflections. HSC increases the load carrying capacity by 2.64% than above model. It has good ductility and hysteris is behaviour.

- ➢ When radius of inner tube is in cresed to maximum, the confinement of the concrete increased which results into better load carrying capacity. It shows 2.86% more load carrying capacity than hybrid column with outer square FRP inner circular steel tube.

- ➢ Use of Hybrid FRP outer tube enhance the load carrying capacity and shows good hysteris is behaviourr and ductility. AFRP and CFRP are high strength fibers. AFRP has high modulus of elasticity and high abrasion resistance. CFRP also enhance the shear strength. This model has very good load carrying capacity and better strain recovery than all models.

- ➢ Confinement provided by the FRP tube also improve the axial load-carrying capacity

- ➢ Ductility of all proposed models will have almost same value. Ductility of proposed columns is greater than conventional column. The ductile behaviour is due to the presence of FRP tube.

- ➢ When column subjected to axial load, it shows good load carrying capacity. And also for eccentric load it exhibit good characteristics. Among them Hybrid Column with Hybrid FRP tube has better performance.

- ➢ Applying Cyclic load to these columns, all specimens show good hysteresis behaviour and delivered a similar trend of energy dissipation capacity. In case of strain recovery, the specimen with hybrid FRP outer tube has more strain recovery.

- ➢ From this study, a best model can be predict. Outer square hybrid FRP tube and inner circular steel with maximum radius hybrid column encased with HSC.

REFERENCES

1. Amir Mirmiran, Mohsen Shahawy, and Hazem Thomas Beitleman, (2001), Slenderness Limit For Hybrid FRP-Concrete Columns, *J. Compos. Constr.* ,Vol 5, Issue 1, P26-34.
2. Amir Mirmiran, Mohsen Shahawy and Hazem El Echary, (1999), Acoustic Emission Monitoring Of Hybrid FRP Concrete Columns, *J. Eng. Mech.*, Vol. 125, Issue 8, P899-905.
3. B. Zhang, J. G. Teng, and T. Yu, (2017) Compressive Behavior of Double Skin Tubular Columns with High-Strength Concrete and a Filament-Wound FRP Tube , *J. Compos. Constr.*, Vol. 21, Issue 5, P 1-15.10.1061/(ASCE)CC.1943-5614.0000800.
4. Chris P. Pantelides, Michael E. Gibbons*et.al.* (2013), Axial Load Behavior of Concrete Columns Confined with GFRP Spirals, *J. Compos. Constr.*, Vol. 17, Issue 3, P 305-313.
5. MaheswaranChellapandian, ShanmugamSuriyaPrakash*et. al.* (2019), Experimental and Numerical Studies on Effectiveness of Hybrid FRP Strengthening on Behavior of RC Columns under High Eccentric Compression, *J. Bridge Eng,* Volume: 24 Issue: 6, P 1-15. 10.1061/(ASCE)BE.1943-5592.0001420.
6. MaheswaranChellapandian, ShanmugamSuriyaPrakash*et.al.*, (2019), Experimental Investigation of the effectiveness of Hybrid FRP- Strengthened RC Columns on Axial Compression- Bending Interaction Behavior, *J. Compos. Constr.*, Vol. 23, Issue 4, P 1-16.10.1061/(ASCE)CC.1943-5614.0000952
7. M. M. Correia, F. Nunes *et. al.* (2013), Buckling Behavior and Failure of Hybrid Fiber- Reinforced Polymer Pultruded Short Columns, *J. Compos. Constr.*, Vol. 17,Issue 4, P 463-475.10.1061/(ASCE)CC.1943-5614.0000339.
8. Omar I. Abdelkarim and Mohamed A. ElGawady, (2014), Behavior of Hybrid FRP-Concrete-Steel Double Skin Tubular Column Subjected to Cyclic Axial Compression, *Structures Congress.*, P1002-1013.

9. Omar I. Abdelkarim and Mohamed A. ElGawady, (2014), Analytical and Finite Element Modeling of FRP-Concrete-Steel Double-Skin Tubular Columns, *J. Bridge Eng.,* Vol. 20, Issue 18.10.1061/(ASCE)BE.1943-5592.0000700.
10. PedramZohrevand, and Amir Mirmiran (2012), Cyclic Behavior of Hybrid Column made of Ultra High Performance Concrete and Fiber Reinforced Polymers. *J. Compos. Constr.,* Vol. 16, Issue 1, P 91-99.10.1061/(ASCE)CC.1943-5614.0000234.

Table 1. Results of Finite Element Analysis

LOAD CARRYING CAPACITY		
Actual Value (from journal) (kN)	**Obtained Value (from ANSYS) (kN)**	**Error(%)**
58	61.382	5.83

Table 2. Properties fibers

Fiber	Nominal thickness(mm)	Tensile strength (MPa)	Ultimate Tensile Strain	Elastic modulus (GPa)
Carbon	0.117	3626	1.44	251
Aramid	0.200	2663	2.12	125.7

Table 3. Load and Deformation

MATERIAL	SHAPE	LOAD (kN)	DEFORMATION (mm)
OUTER FRP INNER STEEL	Both square	5154.5	21.16
	Out square in circle	6606.3	21.02
	Out circle in square	5329.2	21.59
	Both circle	5240	17.95
OUTER STEEL INNER FRP	Both square	2873.2	54.44
	Out square in circle	4103.4	22.16
	Out circle in square	3501.6	19.41
	Both circle	3490	19.40

Table 4. Load and deformation when subjected to eccentric loading

Eccentricity (%)	10	25	50	90
Load (kN)	2837	2525	2172	1123
Deformation(mm)	72.58	77.01	91.96	135.73

Table 5. Load and Deformation

|	LOAD (kN)	Deformation (mm)
HSC in inner tube	6663.4	21.023
HSC in outer tube	6780.7	21.024

Table 6. Load and Deformation of Hybrid Column with Maximum Inner Tube Radius Subjected to Eccentric Loading

Eccentricity (%)	10	25	50	90
Load (kN)	3154.5	2868.5	2469.9	2056.6
Deformation(mm)	69.56	75.96	104.95	120.24

Ram Prasanna Kumar Reddy and Mohammed Bilal Badr

Table 7. Load and Deformation of Hybrid Column with Hybrid FRP Outer Tube Subjected to Eccentric Loading

Eccentricity (%)	10	25	50	90
Load (kN)	4584.5	4183.1	3687.9	2879.4
Deformation(mm)	65.28	72.78	102.91	118.7
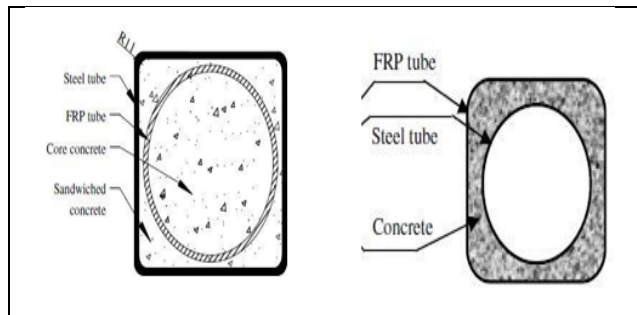
Figure 1. Cross-section layout of SCFC

Figure 2. ANSYS Software window
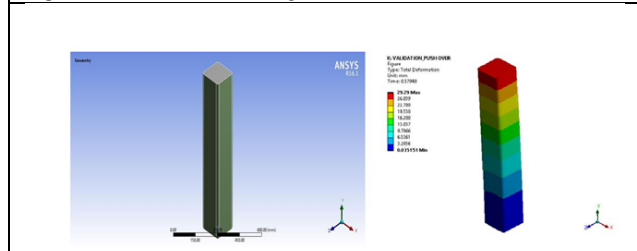
Figure 3. Isometric view of the model with Total Deformation
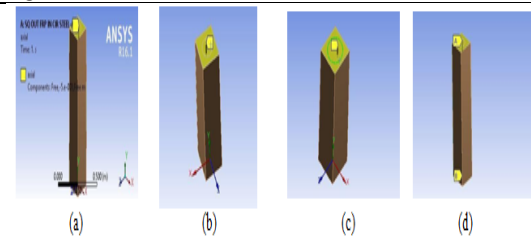
Figure 4. axial loadings (a) Inner and outer tube (b) HSC in column (c) Radius of Inner Tubes (d) Hybrid FRP tubes
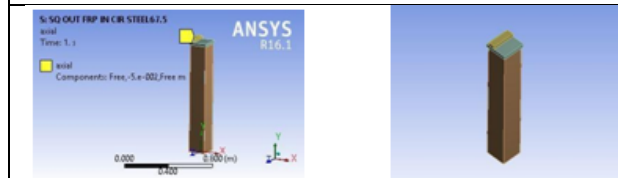
Figure 5.Eccentric loading on column at 90% and 50% eccentricity
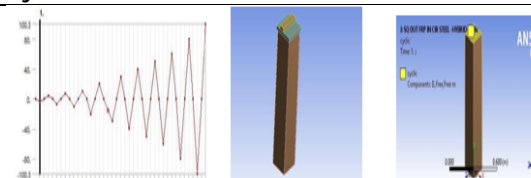
Figure 6. (a) Inner and outer tube (b) Radius of Inner Tubes (c) Hybrid FRP tubes
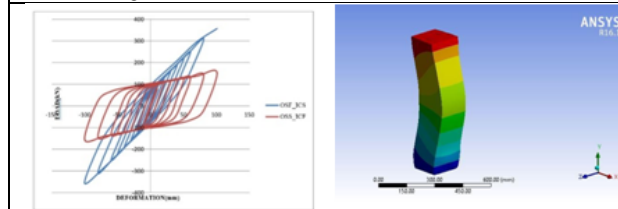
Figure 7. (a) Hysteresis loop for outer square inner circular columns (b)Deformation of column
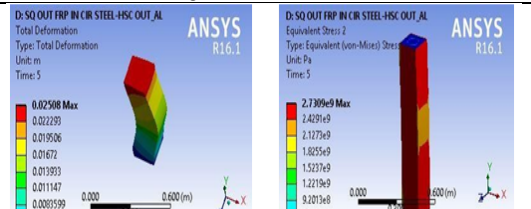
Figure 8. (a) Deformation of Hybrid Column with HSC in Outside Tube (b) Stress on Hybrid Column

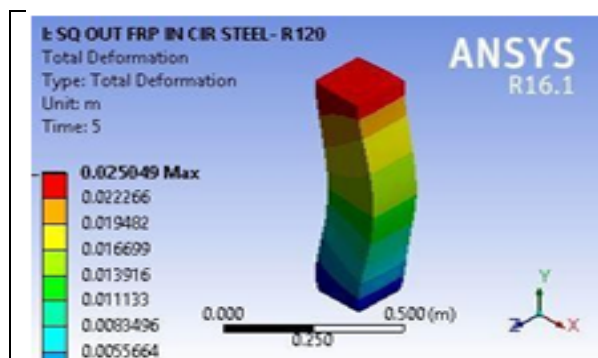**Ram Prasanna Kumar Reddy and Mohammed Bilal Badr**
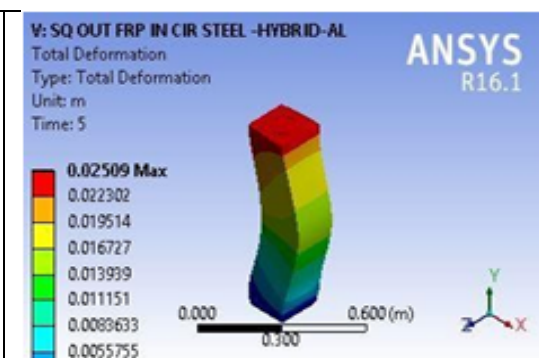

Figure 9. Deformation of column

Figure 10. Deformation of column

RESEARCH ARTICLE

Analysis of Reinforced Concrete Structures Beams-Columns Joints using Finite Element Modellings

J.Selwyn Babu[1], Santhosh Varma[2]* and J.Rex[1]

[1]Assistant Professor, Department of Civil Engineering, Malla Reedy Engineering College, Hyderabad, Telangana , India.
[2]PG Scholar, Department of Civil Engineering, Malla Reedy Engineering College, Hyderabad, Telangana , India.

*Address for Correspondence
Santhosh Varma
PG Scholar, Department of Civil Engineering,
Malla Reedy Engineering College,
Hyderabad, Telangana , India.
Email: santhoshvarma369@gmail.com.

ABSTRACT

Various structures in many nations, including Portugal, were not completely installed for earthquake protection in recent past. As a result, buildings constructed in the 1960s using RC Beam-Column Joints used less reinforcing steel than those constructed in line with more current standards. As a result, determining the soundness of ancient RC Beam-Column joints is critical in determining the future requirement for retrofitting and the intervention's goals. As a result, a building is deemed typical of the stock constructed in the 1960s in Lisbon, Portugal, in order to place a value on contemporary modelling methods for the assessment of existing jerry-made RC Beam-Column joints. SAP 2000 is utilised to determine the important joints of the structure. Pushover analysis is done since it is an ancient structure that needs restoration. Push the structure till it reaches its maximum capacity to disfigure, as the name suggests. It aids in comprehending the disfigurement and breaking of a structure in the case of an earthquake, as well as providing reasonable knowledge of building deformation and the creation of plastic hinges in the structure. The structure is then modelled in STAAD. Pro in accordance with IS requirements. The structure was simulated in order to determine the forces on the circular beam column joints based on the SAP 2000 analysis. Finally, crucial beam-column junctions are rectified using a retrofit technique such as FRP wrapping in Abaqus, and graphs are displayed to show that if the retrofitting had been done sooner, the beam-column joint failure might have been avoided.

Keywords: RC Beam-Column joint, Staad pro, Sap2000, Abaqus, FRP wrapping, FEM.

38479

Selwyn Babu *et al.,*

INTRODUCTION

Earthquakes have the potential to cause the collapse of reinforced concrete structures, as well as the loss of lives and valuable property. The vast majority of structures constructed throughout the world in accordance with non-seismic standards of practise are incapable of withstanding even small earthquake stress. It is essential that the reinforced concrete structure has sufficient lateral resistance strength to prevent brittle fracture in seismic conditions. Because dismantling and rebuilding such RC buildings is so expensive, it may be more cost-effective to upgrade the main structural components in order to ensure the building's and people's safety in the first place. There may be non-ductile reinforcing components at the beam-column joint region, with inadequate or no shear reinforcement, as well as short anchor lengths of bottom steel bars that run down the longitudinal beam in these early RC structures. Furthermore, because of the strong beam design, the joint may be capable of withstanding considerable resistance. When a bond slide or joint shear failure occurs, the overall strength of the structure is significantly decreased.

Details of Building
The proposed site is an eight-story structure (ground floor +seven storys), with measurements of 36.80m in X-directions and 10.85m in Y-direction. The structure stands at a height of 27m. The structure was planned and constructed in the 2020s

Objective of the projects
Through the use of a pushover analysis on both the beam and the column, the researchers hope to discover the critical beam-column junction in this investigation. A critical beam-column junction is investigated using the finite element method in this research, which involves the application of total deformation and stress to the junction. It is therefore necessary to adjust the joints in order to compare the behaviour of different joints in terms of total deformation and stress distribution. The pushover research was carried out with the assistance of the SAP2000 software. ABAQUS version 6.13 is utilised to do the Finite Element Analysis, in addition to the other software.

Forces acting on a Beam Column Joint
The pattern of forces acting on a joint is dictated by the configuration of the joint as well as the kinds of loads pushing on the joint. Loads acting on the three types of joints are investigated in terms of stresses and the fracture patterns that occur as a consequence of these stress and fracture patterns. The forces acting on an internal joint as a result of gravity loading are shown in Figure 2. a. formalised Loads from the beam ends, as well as axial stresses from the columns, may be transmitted directly via the joint. When lateral (or seismic) loading occurs, the equilibrating forces from beams and columns cause diagonal tensile and compressive stresses to develop inside the joint, as shown in Fig. 2. (b). Fractures occur perpendicular to the stress diagonal A-B of the joint and at the joint's faces, where the beams act as a frame for the joint. Unlike tension ties, compression struts are shown with dashed lines, while tension ties are depicted with solid lines. The use of transverse reinforcements to bridge the plane of failure and resist diagonal tensile forces is necessary due to the weakness of concrete under tension.

FRP Composites
Since the mid-1980s, fibre-reinforced polymer reinforcing systems have been used to strengthen weak concrete structural components and to restore damaged or deteriorated concrete structures, mostly in the construction industry. Composites were first utilised in RC bridges as flexural strengthening materials and as confining reinforcement in RC columns, and they have since become more popular. Since the inception of the research, the range of possible applications has expanded to include beams, slabs, columns, shear walls, chimneys, vaults, domes, and trusses, among other things.

Selwyn Babu *et al.,*

The term composite material (also known as composite) refers to a well-balanced combination of two or more elements that results in a product that is more efficient than the sum of its parts. Composite materials are used in a variety of applications. One of the components is the reinforcing or fibre phase (which provides strength), while the other is the matrix phase (in which the fibres are embedded). Through its shear transfer capability, the matrix acts as a binder, keeping the fibres in place and contributing to the structural integrity of the composite material in general. The matrix also has the additional function of protecting the fibre from the external environment in which the composite is placed. Continuous fibres are used in FRP products for structural engineering since they are endlessly long and therefore are referred to as continuous fibres. Fibre-reinforced polymers get their name from the fact that these fibres are used in relatively large quantities (ranging from 20 to 60% of the total volume of the polymer resin) to reinforce the polymer resin (FRP). When two distinct materials are mixed, the outcome is a component that has enhanced strength, stiffness, and toughness over and beyond the properties of the individual materials used in the construction. Fibrous fibres such as glass, carbon, aramid, and boron are the most common types of fibres used to create strong sheets and fabrics, and they are also the most expensive.

BEAM-COLUMNJOINT

A beam-column junction is the place where beams and columns of a reinforced concrete construction are connected. Due to the passage of a high number of forces between them (i.e. beams and columns), they are important areas in a reinforced concrete moment resistant frame. The standard design practice does not include a design assessment for beam-column joints. However, the collapse of similar frameworks during previous earthquakes throughout the globe has shown the significance of joint stresses. Shear at the joints leads to the structure collapsing. Only in the last several decades has detailed research into the joints for such structures been conducted. The fundamental criterion for a junction in a reinforced concrete structure to function well is:

- A joint's service load performance should be comparable to that of the member it joins.
- The strength of a joint should be equal to or higher than the strength of the most unfavourable load combination that the adjacent component can bear, repeated as many times as necessary to ensure that the joint is strong.
- he structure's strength should not be determined by the joint's strength, and its behaviour should not impede the growth of the neighbouring member's full-strength capability.

Types of Joints in a Frame

- Interior Beam-Column Junction — An interior joint is one that connects four beams to a single column.
- Exterior Beam-Column Connection – An exterior joint is formed when three perpendicular beams are joined to the vertical face of a single column.
- Corner Beam-Column Joint – Corner joints are the joints that can be seen on the frame's corner edges and are formed by the joining of two beams and two columns. When two beams meet at a corner junction, the vertical face of a single column becomes the connecting point.

FINITEELEMENTANALYSIS

Certain engineering problems cannot be solved analytically owing to the unpredictability of material properties, limit conditions, and the structure itself. This is especially true for structural issues. In engineering, the Finite Element Method, also known as Finite Element Analysis, is a method for finding approximate solutions to a wide range of boundary value or field value problems that may be solved numerically. In its most basic form, FEM divides or displays the structure into small finite components, which are then combined to form the final structure. There are a number of subdomains in the issue domain as a result of this division. Overall, this is a hypothesised technique, and the final findings must be widely known before it can be implemented successfully. Whenever it comes to the analysis of systems, finite element modelling (FEM) is a reliable technique for estimating the displacements, stresses, and traces in a structure under a collection of masses. Using the Finite Element Method, elliptic fractional differential situations are transformed into hard and fast arithmetical standards that are difficult to answer. Initial value problems involving an illustrated or hyperbolic differential condition, as well as the underlying circumstances, cannot be fully resolved using the finite detail method (other than the restriction conditions). When dealing with

38481

parabolic or hyperbolic differential equations, time is one of the independent variables. The Finite Element Method and the Finite Difference Method are needed in order to provide a solution to a preliminary fee issue.

METHODOLOGY

➢ Finding critical beam-column joints. SAP2000
➢ Modelling of joint and carrying out the required rectification process. ABAQUS
➢ Determining the forces in the critical beam column joints. STAAD PRO

SAP-2000
In the initial phase, the structure was modelled and built in SAP 2000, with Pushover Analysis used to identify key beam-column intersections. SAP2000 is a powerful structural design programme that may be used to investigate and plan an auxiliary structure. It is possible to exhibit fundamental and advanced frameworks in a natural protest-based displaying condition that simplifies and reorganises the engineering process. The frameworks can range from 2D to 3D and from simple to intricate geometry, and they can be dissected, composed, and advanced using this method. The major joints of the construction are identified with the help of SAP 2000. Because it is an ancient structure in need of renovation, a pushover analysis is performed.

STAAD. Pro
STAAD. Using the Pro software package, you may conduct traditional first order static analysis, 2nd order p-delta analysis, geometric nonlinear analysis, Pushover analysis (Static-Nonlinear Analysis), and buckling analysis, to name a few applications. It may be utilised in combination with a variety of dynamic analysis methods, such as modal extraction, time history analysis, and response spectrum analysis, among others Thedimensions ofmembers usedin the structure are as follows:

Columns sizes
700 mm X 300 mm
500 mm X 250 mm
400 mm X 250 mm
300 mm X 250 mm
Beams sizes
650 mm X 250 mm
650 mm X 300 mm

M30 concrete was utilized in the construction of the structure. Fe415 steel was utilized in the construction. The results are acquired in STAAD. Pro, and the crucial beam column joints are modeled in ABAQUS with the forces taken into account, and the results are observed.

ABAQUS
Under transient loads, a finite-element analyser uses an explicit integration technique to solve extremely nonlinear systems with many complicated connections. The fundamental task of ABAQUS is to design and assess the building structure's essential beam-column joints. The SAP 2000 results are utilised to replicate the real joint deflections and forces. ABAQUS is primarily used for beam-column joint analysis due to its Finite Element modelling, which produces more accurate results than other software and also has the ability to provide more detail about the model developed.

RESULTS

SAP2000 RESULTS
The modelling of the structure is completed, and the section attributes of the sections are established. Following the application of various load instances and various load combinations, the result is produced in the three axes ("+x," "-y," and "+y," respectively), which are the crucial joints.
The figure below shows the result received after applying the Dead Load on the system.

STAAD PRO RESULTS
According to the SAP2000 , there are 9 important nodes along various push axes.

ABAQUSRESULTS
The fundamental task of ABAQUS is to design and assess the building structures essential beam-column joints. The SAP2000 and STAAD PRO results. It was used to model actual joint deflection and forces. Using the table above, we can compare stress and displacement values with and without FRP Wrapping, and we can also compare with and without FRP Wrapping. Below are graphs that show the stress and displacement reductions that happened as a consequence of the rectification process. Node of Critical Importance-A node of critical importance is a node that has a lot of (B,2,4). The beam column joint is wrapped in FRP and rectangle meshing is performed, enhancing the beam column joint's strength and load bearing capacity and thereby correcting it.

As can be observed in the two tables above, the stress and displacement values obtained with and without FRP Wrapping are similar in both directions. The table that show how the rectification process reduces the amount of stress and displacements that occur as a consequence of the operation clearly illustrate how the rectification process reduces the amount of stress and displacements that occur as a consequence of the operation.
Critical Node–(C,2,8)

Fig 10 After analysis, the Critical Node (C,2,8) The same section is cut for further steps; the section is zoomed in view of the points chosen. The same section is cut out after the FRP Wrapping is applied; the section is zoomed in on the cut-out section; FRP Wrapped Beam Column Joint after FRP Wrapping; FRP Wrapped Beam Column Joint after FRP Wrapping; FRP Wrapped Beam Column Joint after FRP Wrapping; FRP Wrapped Beam Column Joint after FRP Wrapping; FRP Wrapped Beam Column Joint after FRP Wrapping; FRP Wrapped Beam Column Joint after FRP Wrapping. The stress and displacement values are shown in the table above with and without FRP Wrapping, as well as with and without FRP Wrapping. In the following graphs, the stress and displacement reductions that occurred as a result of the rectification procedure are shown in more detail.

CONCLUSION

➢ If the beam-column joint had been modified and repaired in a timely manner, the failure of the beam-column joint could have been avoided. The loads on the structure were more than the members' bearing capacity, resulting in the condition known as "weak column, strong beam."

➢ The use of Carbon Fiber Reinforced Polymer, or CFRP, in the construction of the members reduced stresses on them by about 10% on average, which is a considerable improvement over the members' prior state of construction.

➢ The displacement values of non-retrofitted members were reduced by roughly 10-15% when compared to CFRP-wrapped members.

➢ Carbon Fiber Reinforced Polymer, or CFRP, is also a cost-effective option since the mass required per beam-column joint is quite low, and the stress and displacement values are reduced very well when compared to retrofitting procedures.

➢ When the building was modified with CFRP, it would have avoided a "Soft Storey" collapse that occurred on the ground and first levels. This will result in a low-cost facility that will be available for usage in the future.

REFERENCES

1. "Experimental Investigation on Seismic Behavior of Eccentric Reinforced Concrete Beam-Column-SlabConnections", *ACIStructural Journal*, vol. 105, no. 2, 2008.
2. A.GhobarahandA.Said,"Shearstrengtheningofbeam-columnjoints", *EngineeringStructures*,vol. 24, no. 7, pp. 881-888, 2002.
3. P.Panjwani and D. DUBEY, "Study of Reinforced Concrete Beam-Column Joint", *InternationalJournalof Engineering Research*, vol. 4, no. 6, pp.321-324, 2015.
4. S.V.Chaudhari, K. K.A.Mukane and M. M.A.Chakrabarti, "Comparative Study on Exterior RCCBeamColumnJointSubjectedtoMonotonicLoading", *InternationalJournalofComputerApplications*,vol. 102, no. 3, pp. 35-40, 2014.
5. A.GHOBARAH∗andA.SAID†,"SEISMICREHABILITATIONOFBEAM-COLUMNJOINTS USING FRP LAMINATES", *Journal of Earthquake Engineering*, vol. 5, no. 1, pp. 113-129, 2001.
6. A.Kwan,"ImprovedWide-Column-FrameAnalogyforShear/CoreWallAnalysis",*JournalofStructuralEngineering*, vol. 119, no. 2, pp. 420-437, 1993.
7. Z.Su,T.HanandS.Sun,"NonlinearStaticPushoverAnalysisforShearWallStructuresinSAP2000Program", *Applied Mechanics and Materials*, vol. 470, pp.1007-1010, 2013.
8. J. Saravanan and G. Kumaran, "Joint shear strength of FRP reinforced concrete beam-columnjoints",*Open Engineering*, vol. 1, no. 1, 2011.
9. Hemidine,"NumericalinvestigationonexteriorreinforcedconcreteBeam-Columnjointstrengthened by composite fiber reinforced polymer (CFRP)", *International Journal of the PhysicalSciences*,vol. 6, no. 28, 2011.
10. "Retrofitting of Reinforced Beam-Column Joints Using Hybrid Laminates", *International JournalofScienceand Research(IJSR)*, vol. 5, no.4, pp.2301-2304, 2016.

Table 1: STAAD. Pro employs the following load combinations, which are listed in the following table:

Load combination No.	Multiplying factor of Loads				
	DL	LL	WL(+Z)	WL(-Z)	TH
1	1.5	1.5	0	0	0
2	1.2	1.2	1.2	0	0
3	1.2	1.2	0	1.2	0
4	1.2	1.2	-1.2	0	0
5	1.2	1.2	0	-1.2	0
6	1.2	1.2	0	0	1.2
7	1.2	1.2	0	0	-1.2
8	1.5	0	1.5	0	0
9	1.5	0	0	1.5	0
10	1.5	0	-1.5	0	0
11	1.5	0	0	-1.5	0
12	1.5	0	0	0	1.5
13	1.5	0	0	0	-1.5
14	0.9	0	0	0	1.5
15	0.9	0	0	0	-1.5

DL: Dead Load, LL: Live Load, WL: Wind Load

Selwyn Babu *et al.,*

Table: 2 Critical Node Points and Reinforcement Details

Node No.	Location	Connected Members	Reinforcement
1	A,2,2	B-63	Top:3# 16Ø; Bottom: 3# 16Ø; Stirrups; 2legged 6Ø;@300mm c/c
		B-79	Top:3# 16Ø; Bottom: 3# 16Ø; Stirrups; 2legged 6Ø;@300mm c/c
		B-80	Top:3# 16Ø; Bottom: 3# 16Ø; Stirrups; 2legged 6Ø;@300mm c/c
		B-101	Top:3# 16Ø; Bottom: 3# 16Ø; Stirrups; 2legged 6Ø;@300mm c/c
		C-92	Main:6# 25Ø; Ties:6Ø @250mm c/c
		C-145	Main:6# 25Ø; Ties:6Ø @250mm c/c
2	A,2,3	B-116	Top:3# 16Ø; Bottom: 3# 16Ø; Stirrups; 2legged 6Ø;@300mm c/c
		B-132	Top:3# 16Ø; Bottom: 3# 16Ø; Stirrups; 2legged 6Ø;@300mm c/c
		B-133	Top:3# 16Ø; Bottom: 3# 16Ø; Stirrups; 2legged 6Ø;@300mm c/c
		B154	Top:3# 16Ø; Bottom: 3# 16Ø; Stirrups; 2legged 6Ø;@300mm c/c
		C-145	Main:6# 25Ø; Ties:6Ø @250mm c/c
		C-198	Main:6# 25Ø; Ties:6Ø @250mm c/c
3	B,2,2	B-59	Top:3# 16Ø; Bottom: 3# 16Ø; Stirrups; 2legged 6Ø;@300mm c/c
		B-73	Top:3# 16Ø; Bottom: 3# 16Ø; Stirrups; 2legged 6Ø;@300mm c/c
		B-99	Top:3# 16Ø; Bottom: 3# 16Ø; Stirrups; 2legged 6Ø;@300mm c/c
		C-88	Main:6# 25Ø; Ties:6Ø @250mm c/c
		C-141	Main:6# 25Ø; Ties:6Ø @250mm c/c
4	C,2,2	B-60	Top:3# 16Ø; Bottom: 3# 16Ø; Stirrups; 2legged 6Ø;@300mm c/c
		B-74	Top:3# 16Ø; Bottom: 3# 16Ø; Stirrups; 2legged 6Ø;@300mm c/c
		B-75	Top:3# 16Ø; Bottom: 3# 16Ø; Stirrups; 2legged 6Ø;@300mm c/c
		B-100	Top:3# 16Ø; Bottom: 3# 16Ø; Stirrups; 2legged 6Ø;@300mm c/c
		C-89	Main:6# 25Ø; Ties:6Ø @250mm c/c
		C-142	Main:6# 25Ø; Ties:6Ø @250mm c/c
5	B,2,3	B-112	Top:3# 16Ø; Bottom: 3# 16Ø; Stirrups; 2legged 6Ø;@300mm c/c
		B-126	Top:3# 16Ø; Bottom: 3# 16Ø; Stirrups; 2legged 6Ø;@300mm c/c
		B-152	Top:3# 16Ø; Bottom: 3# 16Ø; Stirrups; 2legged 6Ø;@300mm c/c
		C-141	Main:6# 25Ø; Ties:6Ø @250mm c/c
		C-124	Main:6# 25Ø; Ties:6Ø @250mm c/c
6	C,2,3	B-113	Top:3# 16Ø; Bottom: 3# 16Ø; Stirrups; 2legged 6Ø;@300mm c/c
		B-127	Top:3# 16Ø; Bottom: 3# 16Ø; Stirrups; 2legged 6Ø;@300mm c/c
		B-128	Top:3# 16Ø; Bottom: 3# 16Ø; Stirrups; 2legged 6Ø;@300mm c/c
		B-153	Top:3# 16Ø; Bottom: 3# 16Ø; Stirrups; 2legged 6Ø;@300mm c/c
		C-142	Main:6# 25Ø; Ties:6Ø @250mm c/c
		C-195	Main:6# 25Ø; Ties:6Ø @250mm c/c
7	B,2,4	B-165	Top:3# 16Ø; Bottom: 3# 16Ø; Stirrups; 2legged 6Ø;@300mm c/c
		B-179	Top:3# 16Ø; Bottom: 3# 16Ø; Stirrups; 2legged 6Ø;@300mm c/c

Selwyn Babu *et al.*,

		B-205	Top:3# 16Ø; Bottom: 3# 16Ø; Stirrups; 2legged 6Ø;@300mm c/c
		C-194	Main:6# 25Ø; Ties:6Ø @250mm c/c
		C-247	Main:6# 25Ø; Ties:6Ø @250mm c/c
8	A,2,8	B-375	Top:3# 16Ø; Bottom: 3# 16Ø; Stirrups; 2legged 6Ø;@300mm c/c
		B-376	Top:3# 16Ø; Bottom: 3# 16Ø; Stirrups; 2legged 6Ø;@300mm c/c
		B-389	Top:3# 16Ø; Bottom: 3# 16Ø; Stirrups; 2legged 6Ø;@300mm c/c
		C-390	Main:6# 25Ø; Ties:6Ø @250mm c/c
		C-405	Main:6# 25Ø; Ties:6Ø @250mm c/c
9	C,2,8	B-378	Top:3# 16Ø; Bottom: 3# 16Ø; Stirrups; 2legged 6Ø;@300mm c/c
		B-392	Top:3# 16Ø; Bottom: 3# 16Ø; Stirrups; 2legged 6Ø;@300mm c/c
		B-393	Top:3# 16Ø; Bottom: 3# 16Ø; Stirrups; 2legged 6Ø;@300mm c/c
		B-418	Top:3# 16Ø; Bottom: 3# 16Ø; Stirrups; 2legged 6Ø;@300mm c/c
		C-407	Main:6# 25Ø; Ties:6Ø @250mm c/c
		C-412	Main:6# 25Ø; Ties:6Ø @250mm c/c

Table 3:Results of FRP wrapping details with Abaqus

S.no	STANDARD		FRP	
	STRESS (N)	DISPLACEMENT (mm)	STRESS-FRP (N)	DISPLACEMENT- FRP(mm)
1	371.882	6.174	371.975	6.046
2	372.459	6.162	370.503	6.058
3	379.508	6.097	361.714	6.017
4	371.466	6.068	370.907	6.013
5	369.326	6.042	368.732	6.009
6	368.732	6.026	366.587	6.017
7	364.153	6.026	363.199	6.011
8	364.345	6.038	363.038	5.999
9	366.828	6.054	364.768	5.991
10	369.211	6.070	368.897	5.983
11	371.377	6.099	371.021	5.986
12	378.330	6.127	366.350	5.991
13	379.892	6.194	361.215	6.032
14	372.152	6.027	361.215	6.021

FRP: Fibre-Reinforced Polymer

Table 4: Results of Cut section of FRP wrapping details with Abaqus

S.no	STANDARD		FRP	
	STRESS (N)	DISPLACEMENT (mm)	STRESS-FRP (N)	DISPLACEMENT-FRP(mm)
1	782.997	-2.974	781.720	-2.895
2	794.351	-2.967	770.675	-2.898
3	800.803	-2.955	765.462	-2.896
4	792.800	-2.946	799.332	-2.898
5	798.074	-2.939	769.233	-2.901
6	780.088	-2.933	779.979	-2.904
7	777.459	-2.927	777.263	-2.909

8	777.233	-2.922	777.473	-2.914
9	780.102	-2.917	779.945	-2.919
10	788.641	-2.925	774.774	-2.913
11	797.177	-2.933	769.874	-2.910
12	791.177	-2.941	780.414	-2.908
13	799.161	-2.953	767.175	-2.910
14	783.124	-2.960	781.562	-2.907

FRP: Fibre-Reinforced Polymer

Table 5: Results of final Analysis of FRP wrapping details with Abaqus

S.No	STANDARD		FRP	
	STRESS (N)	DISPLACEMENT (mm)	STRESS-FRP(N)	DISPLACEMENT-FRP(mm)
1	899.087	1.296	899.794	1.276
2	899.087	1.297	898.013	1.278
3	913.016	1.300	897.863	1.279
4	915.673	1.302	901.161	1.282
5	920.905	1.304	905.012	1.284
6	922.049	1.306	907.838	1.286
7	922.173	1.308	909.072	1.288
8	921.822	1.311	909.164	1.290
9	919.197	1.313	908.118	1.293
10	916.590	1.316	905.490	1.295
11	913.917	1.319	901.818	1.298
12	907.798	1.321	898.443	1.301
13	899.328	1.324	898.193	1.304
14	897.559	1.328	899.730	1.306

FRP: Fibre-Reinforced Polymer

| **Fig 1:Existing Building** | **Fig 2:Interiorjoint of RC Beam-Column** |
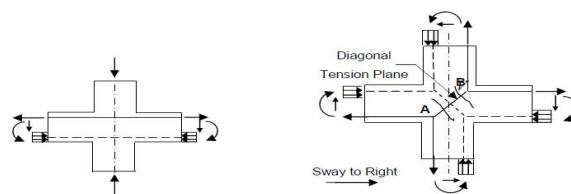
Selwyn Babu *et al.,*
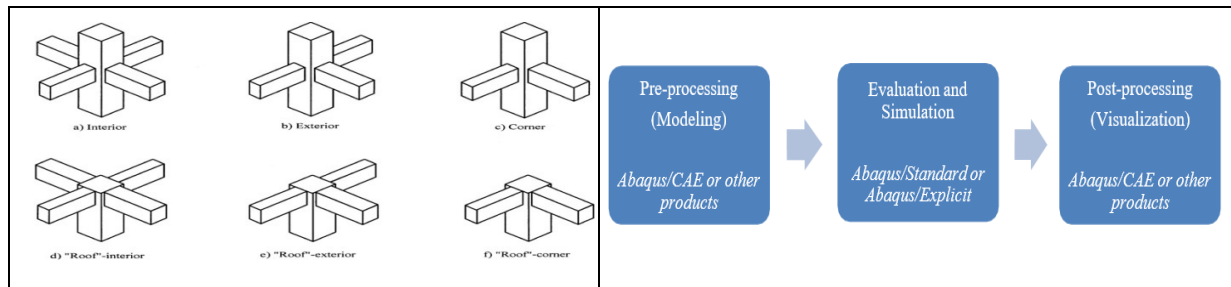
Fig 3: Beam - column joints in frames come in a variety of shapes and sizes.

Fig 4: ABAQUS software order of use
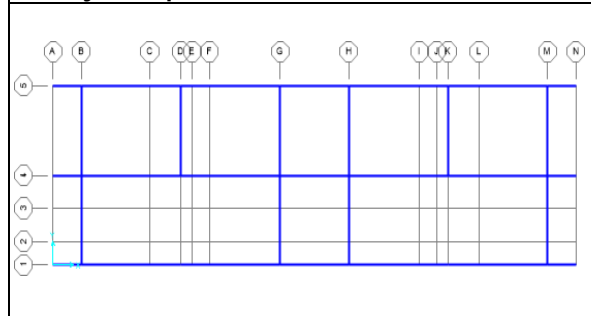
Fig 5: 3D view of the structure
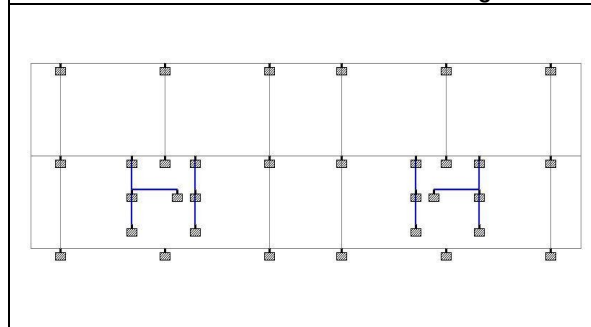
Fig 6 : STAAD. Pro Shear walls and other structural components may be seen in a 3D generated picture of the structure.
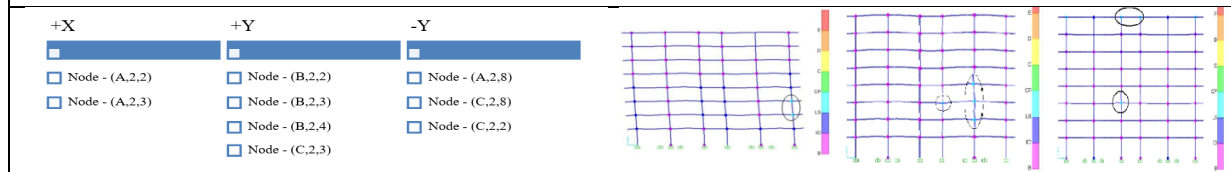
Fig 7:Critical Nodes

Selwyn Babu *et al.,*
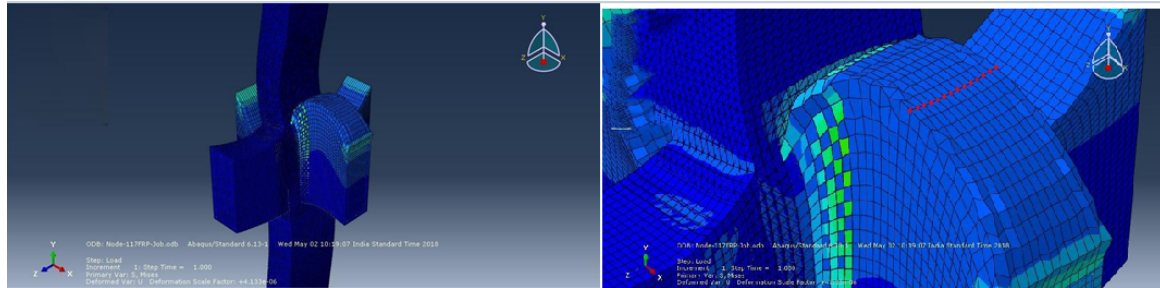
Fig. 8. Deformation after FRP Wrapping with zoomed
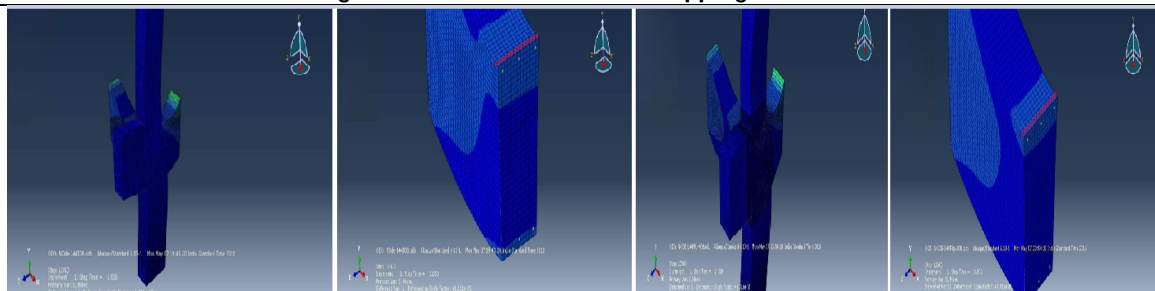
Fig 9: Node of Critical Importance (B,2,4) FRP, after an analysis and a zoomed-in image of the locations selected, Beam Column Joint with Wrapped Beam and After Correction, Zooming in on the Spots.
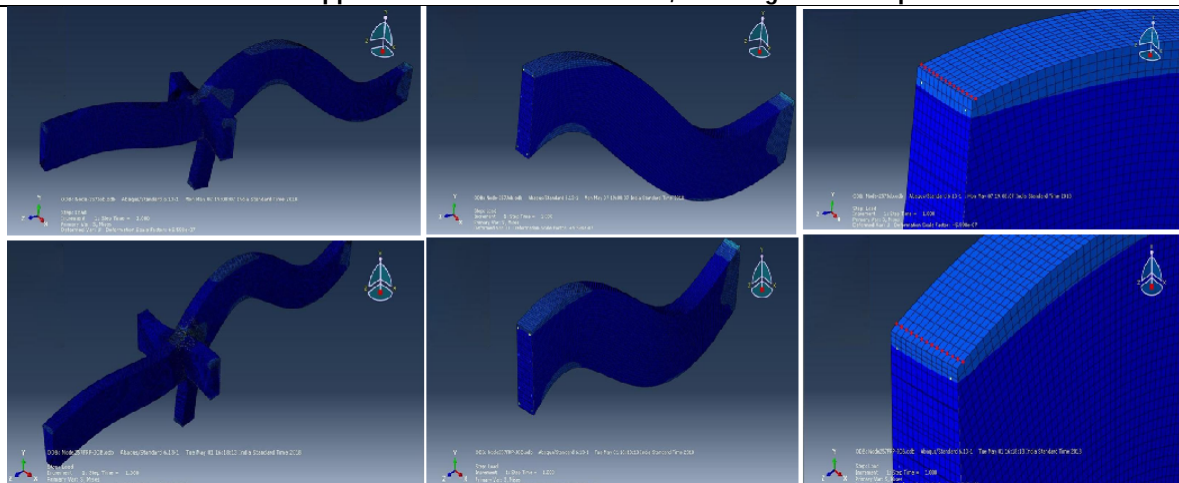
Fig 10 After analysis, the Critical Node (C,2,8) The same section is cut for further steps; the section is zoomed in view of the points chosen. The same section is cut out after the FRP Wrapping is applied; the section is zoomed in on the cut-out section;FRP Wrapped Beam Column Joint after FRP Wrapping; FRP Wrapped Beam Column Joint after FRP Wrapping; FRP Wrapped Beam Column Joint after FRP Wrapping; FRP Wrapped Beam Column Joint after FRP Wrapping; FRP Wrapped Beam Column Joint after FRP Wrapping; FRP Wrapped Beam Column Joint after FRP Wrapping.

RESEARCH ARTICLE

Solar Powered Arduino Based Automatic Drip Irrigation System for Enhancing Agricultural Productivity

T.Rajesh[1], V.Suma Deepthi[1] and P. Sindhuja[2]*

[1]Department of EEE, Malla Reddy Engineering College, Hyderabad, India.
[2]PG Scholar, Department of EEE, Malla Reddy Engineering College, Hyderabad, India.

*Address for Correspondence
P. Sindhuja
PG Scholar, Department of EEE,
Malla Reddy Engineering College,
Hyderabad, India.
Email: pskssindhuja@gmail.com

ABSTRACT

The paper proposes to use an automatic irrigation system based on Arduino boards, soil moisture sensors, float switches and solar panels. The automatic irrigation system senses the soil moisture content and automatically switches the solenoid valve. The top water level is monitored by a float switch detector. The power required by the entire system is generated by solar panels. It also automatically controls the water level in the water tank. This system is suitable for all climatic conditions. This project proposes the use of an automatic irrigation system based on an Arduino board, a soil moisture sensor, a float switch and a solar panel. This automatic irrigation system detects the moisture content of the soil and automatically switches solenoid valves, a float switch sensor monitors the overhead water level, and the power required for the entire system is generated by solar panels. It also automatically controls the water level in the water tank. Whenever a valve opens or closes, the Global System for Mobile Communications (GSM) module sends a message. The project fully supports farmers, provides water on demand, deploys renewable energy, minimizes manpower, saves space, reduces costs, and maintains user-friendliness.

Keywords: Solar panel, Automated drip Irrigation system, Arduino board, Soil moisture sensors, float switch.

INTRODUCTION

Irrigation is the process by which water flows through the soil to cultivate dry plants. There are many irrigation methods, and the most important function of irrigation is to provide water for plants. The water should be evenly distributed on the soil, which seems to be good for yield and growth. There are few irrigation methods. Surface irrigation: The surface irrigation method is one of the oldest methods and has been followed by developers for many years. Now it is also imitated by farmers. In this system, there is a small amount of water around the farmland to keep it moist and enter the soil. If it causes the cultivated land to be flooded, it is either a boundary well or fertilizer irrigation. This process is still valid. The water level is controlled by equipment that is usually inserted into the ground and applied, and rm is not necessarily defined. Unless it's unavoidable, don't use abbreviations in titles or titles. In most rice fields, the rice fields are sometimes poured to the ground by humans.

Drip Irrigation

Drip Irrigation is also called trickle irrigation. It is a system in which water flows out of the water to all bases. In these systems, water is pumped out of the root zone. This pattern increases the growth of all seeds and plants, and it is the most efficient method of irrigation. In this way the water can be divided into pipes, emitters, pipes and fittings. It is much better than watering it. Figure 1 shows the drainage process.

Sprinkler Irrigation

In this method, the irrigation canal is anchored to the paddy field at different points in the soil and can be circulated by spraying too much water. High -pressure nozzles and nozzle tubes are placed on a moving platform and connected to a source. The spray can be placed on a mobile platform and connected to the water through a hose. The voyage sweepers are a system with automatic moving wheels. When the pipe is injured by the drum carried by the irrigation water, the shower is pulled across the field. When the seeding returns to the roller, the system dies. This type of system is known as an irrigation hose and is used for dust removal, irrigation and sewage treatment.

Solar Energy

Solar energy is renewable. The sun needs energy. Sunlight has an output of large amounts of heat that can be converted into energy and is called solar energy. The light is converted into electricity, with the help of a solar plain or directly shown using voltaic acid (PV), or intense solar energy (PDC). The daytime PDC converts sunlight into electricity, namely through contact lenses or glasses and tracking to absorb large amounts of sunlight from the photoelectric [1-6].

Benefits of solar energy

a) Photovoltaic systems have less noise.
b) A small amount of solar energy to the solar panels placed on the roof reduces space.
c) Solar power is an easy connection service. This reduces interference.
d) PV generators are available in all sizes to suit the needs of some.

Automatic Irrigation

Automatic irrigation system is very quiet and goes all the way from this system once installed in the culture soil. It can operate on its own and also does not require a permanent human. There are a lot of used losses here that seem really unwieldy. It is difficult to implement. There are three types of automatic categories. Here it is: The advantage of this system is that the operator can till and irrigate well. The microcontroller 8051 is programmed to receive a signal from the sensing material. An op amp, a moving comparator that connects sensors [7-8]. The humidity characteristic is transmitted by the microcontroller. The Fig.3 shows the Automatic Irrigation system

Rajesh *et al.*,

Irrigation system based on GSM

It is difficult for farmers to irrigate due to lack of manpower, expensive labour cost and water shortage. In order to minimize this problem, a new system using GSM technology was developed. In the GSM-based automatic irrigation system, we use the GSM module to identify the operation of the cultivated land through SMS [9-11]. Fig.5 shows the Irrigation system based on GSM

PROBLEM DESCRIPTION

The energy of the sun is absorbed by the solar system. Solar models use the light energy of the sun's rays (sunlight) to generate electricity through solar products. Solar panels are used in our thesis. Drip irrigation is one of the irrigation methods to control the flow of water, which is applied directly to the roots of many plants. Water dripping from the surface of the roots helps to reduce soil erosion, provides even water flow and reduces water contamination. Drip irrigation is a big part of our project. Hussein and Li Xue [6] investigated the drip irrigation system. In the current situation, drip irrigation systems are being used to improve water utilization. It sucks in groundwater. Manual operating system. It helps our farmers. This generation uses drip irrigation because the water level is very low. So farmers use drip irrigation systems. But farmers with low incomes are spending more water. So it will help small farmers and reduce water waste. C. Automation The technology that allows a device, process or system to operate an automated system is called automation.

The current irrigation system has some shortcomings, that is, soil erosion, water instability, water interference, and interference with the inspection of plants and water levels in the reservoir are required. To overcome these problems, the system is not used in conjunction with drip irrigation or irrigation. It is also an automatic generator to fill the water tank.

METHODOLOGY AND OPERATION OF PROPOSED METHOD

Sensor-Based Valve Operating System

Sensors are devices that detect changes in the environment and send information to the processor. Different types of sensors are commonly used in different applications. All these sensors are used to measure one of the physical properties such as temperature, resistance, capacitance and heat transfer. The different types of sensors are listed below.

Temperature Sensor

- Proximity Sensor
- IR Sensor (Infrared Sensor) Pressure Sensor
- Light Sensor
- Ultrasonic Sensor
- Smoke, Gas and Alcohol Sensor
- Touch Sensor
- Humidity Sensor
- Flow and Level Sensor

Soil moisture sensor

The soil humidity sensor is a type of humidity sensor. Soil moisture sensors are used to indirectly measure the moisture present in the soil by measuring the condition of the soil. The soil moisture sensor has two probes. Both are used to measure the amount of water in it. The two probes allow water to pass through the soil, and then obtain the resistance value depending on the type of soil to measure the water content. The earth has more water; the earth carries more electricity and reduces resistance, so the water level is higher. Dry soils are low in water content and electrical inequality. The sensor works according to this principle for ground moisture. C. Solenoid Valve Solenoid valve is often used to control the flow of fluid through electricity. The solenoid valve operates after power or exercise or is also known as a cut -off that allows fluid to flow. The actuator is an electromagnet. When the suitcase is powered, the magnetic field pulls the plunger toward the spring. Similarly, when the power goes out, the plunger will return to its original position under spring operation.

38814

They are available in five types
- Pilot valve
- Direct valve
- 2-way valve
- 3-way valve
- 4-way valve

Arduino UNO
Arduino UNO board is an open-source microcontroller board based on Microchip ATmega328P microcontroller, developed by Arduino.cc. The board includes analog and digital input/output pins for connecting various boards and other circuits [12-13].

Automatic Tank Water Flow System
A Float switch is a type of water level meter, a machine that detects the water level in the tank. The button can be used to control with instrument, pump, alarm. In these systems, a float unit is used to measure the water level in the tank. When the water is below the indicated level, the body moves to the tank. As the tide reaches higher, the motor changes.

Advantages and Applications
Water waste is a major problem in field agriculture and horticulture. So this kind of automatic drip irrigation with solar energy system will help reduce water waste in agriculture and maintain the water needed for planting trees and crops [14-15].
i)Automatic drip irrigation system is used to automatically develop water supply. Roadside tree planting system.
ii) This automatic drip irrigation system will reduce the manpower required to supply water to the plants.
iii) This automatic drip irrigation system will reduce the total time required to water the garden or field.

CONCLUSION AND FUTURE SCOPE
This negative voltage generator is made up of an Arduino board, solenoid valve, humidity sensor and solar panel. This negative voltage sensor understands the moisture content of the ground and turns on the solenoid valve immediately and the power supplied by the battery and the battery can be used by the sun. Erosion floats are used to control water levels. GSM standard mail delivery, each time the locker is turned on and OFF. With the whole generator is the reduction of erosion, the provision of water without water, no need to do, small space required, humid place in all places no electricity used. The old model is designed for automatic water jet. Using the same strategy, water leaks can be created easily. Check the water tank, just draw the water tank from the well or drinking water.

REFERENCES

1. Moriarty and P. Michael, "Solar receiver-based power generation system." U.S. Patent No. 6,668,555,2017.
2. F. A. Costello, J. L. Manniso, A., J. DiPinto, and G. W. Smith, "Solar Heating System," U.S. Patent No. 4,055,163. Washington, DC: U.S. Patent and Trademark Office,1977.
3. V. Raghunathan, A. Kansal, Hsu and B. Jasonetal, "Design Consideration For Solar Energy Harvesting Wireless Embedded System" In Proceeding of the 4th international symposium on Information processing in sensor networks, (pp. 64), IEEE Press,2015.
4. Jr. Northrup and L. Leonard, "Compound lens solar energy system" U.S. Patent No. 4,022,186,1977.
5. Saeed Mohammed Wazeda and Ben Richard Hughesa, "A review of sustainable solar irrigation systems for Sub-Saharan Africa," Renewable and sustainable Energy reviews, pp 81, 1206-1225,2018.

Rajesh *et al.*,

6. *T.Rajesh*, K.S.Tamilselvan, A.Vijayalakshmi,Ch.Narendra Kumar,K.Anitha Reddy, Oct 2020, 'Design and implementation of an automatic solar tracking system for a monocrystalline silicon material panel using MPPT algorithm' Materials Today: Proceedings, 2021,45,pp.1783-1789.

7. *K.Tiwin Kumar, M. Muthamizh Balan, T.Rajesh* 'Automatic Monitoring and Yield Predictions in Agriculture using Intelligent Techniques' International Journal of Research and Analytical Reviews (IJAR), Volume 6, Issue 1, March 2019,pp 467-471

8. *T.Rajesh, K.Tiwin Kumar, M. Muthamizh Balan* 2019 'E Agriculture based on AI and IOT' International Journal for Research in Applied Science & Engineering Technology (IJRASET), vol 7, Issue II, Feb 2019, pp. 343-347 DOI: 10.22214/ijraset.2019.2038

9. *T.Rajesh, R.Rahul, M.Malligarjun, M.Suvathi*, 2017 'Home Automation using Smart phone Application', International Journal of Advanced Research in Science Engineering and Technology (IJARSET), Vol 4, Issue. 3, pp. 3546-3553

10. *T.Rajesh, R.Rahul, M.Malligarjun, M.Suvathi,*2017 'Design of an Efficient Home Automation using Smart phone Application' , International Journal of Applied Science Engineering & Management (IJASEM), vol 3, no. 2, pp. 19-30

11. S. Anwaarullah, & S. V. Altaf, "RTOS based home automation system using Android" international journal of advanced Trends in computer science and engineering, 2(1), 480-484,2013.

12. R. Gayathri, E. Roshith, B. S. Roshini, S. Murugan, & S. Priya, "Implementation of Arduino based Enhanced Fingerprint Biometric System for Secured Data Exchange". International Journal of Computational Intelligence Research 13.8 , 2113-2123,2017.

13. C. McNally, "Arduino based wireless power meter," MS design project, Cornell University, Ithaca, NY,2010.

14. Shaikh Abdullah, Al MamunHossain and Wang Lixue, "Contemporary Perspective of Drip Irrigation: A Review of Water Saving Crop Production" A Review of Saving Crop Production,2018.

15. S. Postel, P. Polak, F. Gonzales, & J. Keller, "Drip irrigation for small farmers: A new initiative to alleviate hunger and poverty,"Water International, 26(1), 3-13,2001.
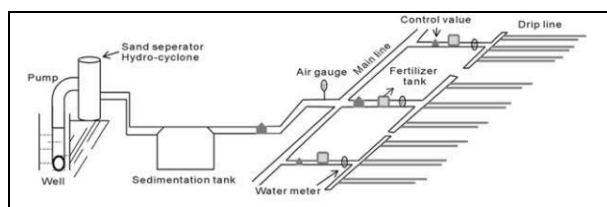
Fig.1 Drip Irrigation system
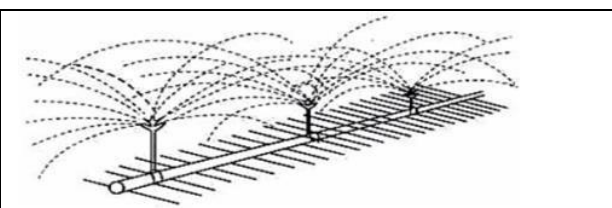
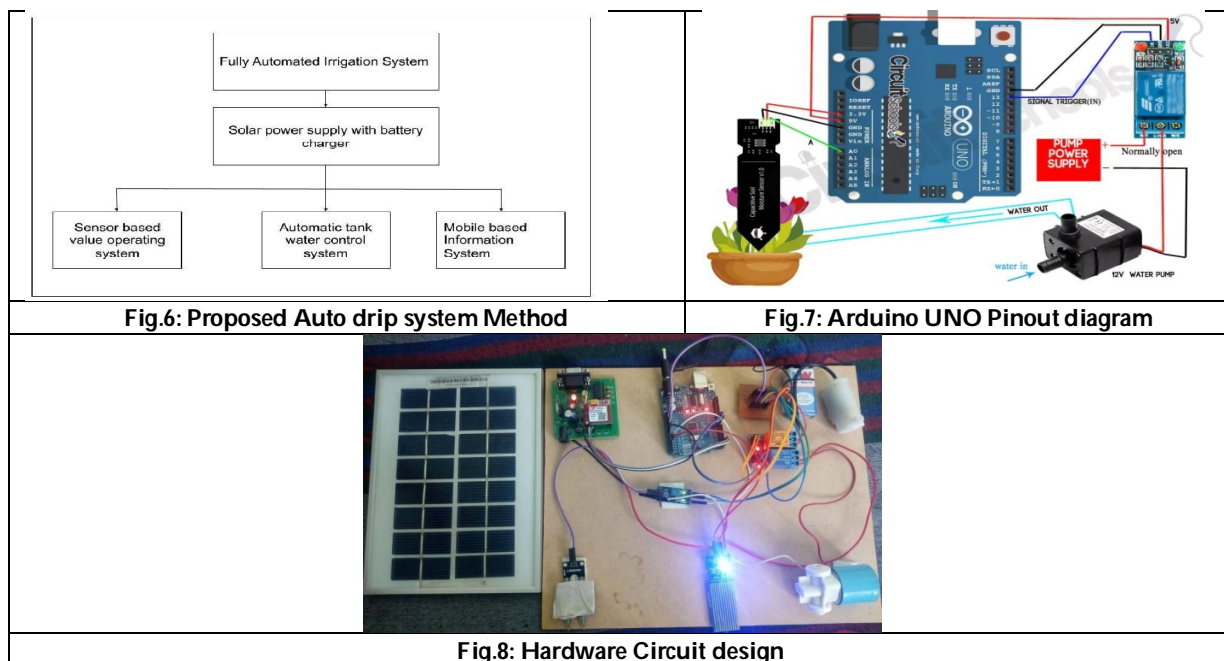**Fig.2 Sprinkler irrigation system**
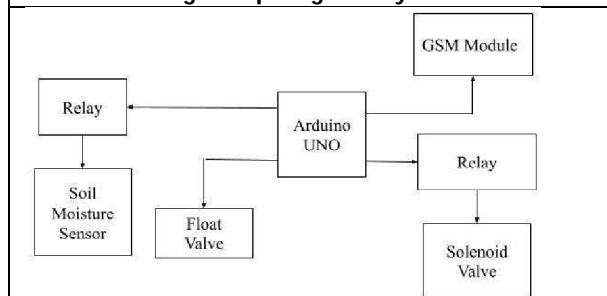
Fig.3: Automatic irrigation system
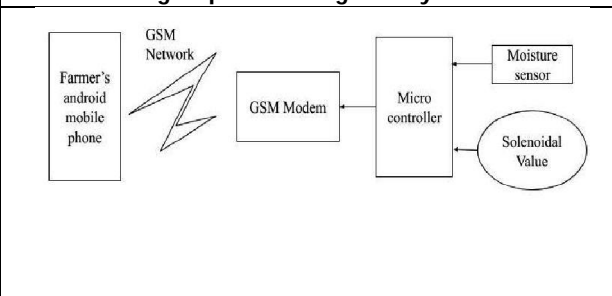
Fig.5: Irrigation system based on GSM

Rajesh *et al*.,

Fig.6: Proposed Auto drip system Method

Fig.7: Arduino UNO Pinout diagram

Fig.8: Hardware Circuit design

38817

RESEARCH ARTICLE

Design of Cascaded Multi-Level Inverter for PV Systems

P.Sarala[1] and J.Indu[2]*

[1]Department of EEE, Malla Reddy Engineering College, Maisammaguda, Hyderabad, India.
[2]PG Scholar, Department of EEE, Malla Reddy Engineering College, Maisammaguda, Hyderabad, India.

*****Address for Correspondence**
J.Indu
PG Scholar,
Department of EEE,
Malla Reddy Engineering College,
Maisammaguda, Hyderabad, India.
Email: indujulakanti9@gmail.com

ABSTRACT

This paper presents the enhanced CMLI (Cascaded Multi-Level Inverter) system for reducing the leakage current. This system is very efficient and secure. The proposed method also provides low switching and power losses, in addition to the reduced switch count.The proposed architecture optimizes high frequency transforms using the suggested PWM method in terminal voltages and in common-mode voltages. Only one carrier signal is needed for all $2m+1$ working levels for the PWM technique described. The planned CMLI's grid current has a Total Harmonic Distortion (THD) that satisfies the IEEE 1547 standard. The article presents a detailed examination of the proposed CMLI utilizing the switching function idea, along with simulation results.

Keywords: Inverter, THD, Optimization, PWM

INTRODUCTION

The advantages of multilevel inverter topologies, such as high performance, low switch count, lightweight and reduced area, are gaining momentum. The galvanic isolation between the PV array and the power output is destroyed when the transformer is disconnected. The leakage current increases, endangering the security of PV systems, when galvanic insulation is removed. As a result, various safety regulations were introduced for PV systems to regulate the value or quantity of the flow of leakage current in photovoltaic systems [1-2]. Apart from reducing the leakage currents, high-quality power generation is now being used from solar systems to the grid. The multilevel inverters (MLI) in transformational PV systems have been implemented in response to this necessity. Many topologies or MLI setups [3] were presented in the literature to decrease the leakage in transformer less PV systems. The leakage current is reduced using two ways under these settings [4]. The first method is to continue the common-mode voltage, and the second is to keep a low level of high-frequency transitions of terminals and

common-mode voltages. A standardized, transformer less PV MLI with fewer electronic components is necessary in order to attain high performance and better objectives, as stated in the previous discussion. The switching and conduction losses of PV MLI should also be ensured by the use of less conductivity switches during zero voltage.Furthermore, it should be able to expand to a larger number of levels. This paper provides a technique to minimize leakage in transformers using lower MLIs. An essay also addresses the proposed MLI pulse width modulation (PWM) technique. The switching function is utilized for PV and common-mode voltages analysis.This research has developed the proposed PWM approach, eliminating changes in the terminal voltage and CMV in high-frequency voltage. The proposed Cascaded multi-level inverter (CMLI) has numerous unique characteristics:

1) The architecture employs eight switches to provide five output voltage levels.
2) Only one switch and one diode are active when the voltage is zero.
3) Four switches are operated in the suggested topology at a low change frequency, reducing the loss of switching.
4) The common-mode voltage is unaffected by the dead band in the PWM method.
5) The suggested inverter may be simply cascaded to reach output levels of more than five levels.

OPERATION OF PROPOSED CASCADED FIVE-LEVEL MLI

Figure 1 shows the schematic circuit layout for the proposed PV system CMLI. The default setup includes two converters (Conv-1 and Conv-2). Conv-1 is a two half-bridge converter (Sx1 and Sx2) that operates together. The Conv-2 is made up of six switches and a highly efficient and dependable inverter design. (Sx3 to Sx8). Conv-2 has six switches, four of which (Sx3 to Sx6) make up an H-bridge circuit. Conv-2's last two switches, Sx7 and Sx8, are bi-directional switches. The voltage levels of VPV and VPV/2 are generated by the switches in the Conv-1. The VPV voltage is on the terminal n when changing on Sx1 with terminal Z. When switch Sx2 is switched on, the terminal n achieves the voltage VPV/2. The switches Sx1 and Sx2 are mutually beneficial. The voltage levels produced in the terminal n of Conv-1 are received as an input. The Conv-2 provides positive, negative and no corresponding input voltage levels for the whole load (voltage between terminals n and z). The multiple SX7 and Sx8 switches provide a freewheeling route during zero voltage. The grid, as described in the Fig, is linked with the CMLI output in five levels via an LCL filter. It consists of induction Li on the inverter, reproduction Cf on the grid side and Induction Lake on the grid side. The shunt channel of the filter's Rd damper resistor is used. The resistance Rac denotes grid-side resistance, whereas the resistance Rg denotes ground-path resistance. Instantaneous grid voltage is denoted by the variable vac. The parasitic capability in a PV system produces a resonant circuit with filter inductance [4-5]. The parasite resistance and inductance are displayed as dotted lines in the PV system parameters Rp and Cp. The i_o, i_c and iac variable indicate the five-level CMLI voltage source and the current going to the grid via the filter shunt branch. The present i_{ce} variable is due to parasite capacity the power output from the PV array to the surface.

Four pairs of additional (Sx1, Sx2) switches (Sx3, SX4), (Sx5, Sx6) and (Sx7, and SX8) are available in the proposed MLI architecture. Further controls are only used for the two switches pairs (Sx1, Sx2) to lower leakage currents (Sx7, Sx8). The PV and grid source insulation during zero voltage is simplified by avoiding complementing actions for other switch pairs. If a zero-voltage configuration of four switches on the H-bridge is switched off, the pv source is separated from the grid. The bi-directional switches Sx7 and Sx8 provide a unlimited accessroute for the inductor current during the turn-off phase of a half - cycle. This operation reduces the leakage current that passes via the parasitic capacitance.

$$v_{uz} = \left(S_1 S_3 + 0.5 S_2 S_3 - \frac{1}{\left(S_3 + S_4\right)} + \frac{1}{\left(S_3 + S_4\right)\left(S_1 + S_2\right)} \right) V_{PV}$$

$$v_{vz} = \left(S_1 S_5 + 0.5 S_2 S_5 - \frac{1}{\left(S_5 + S_6\right)} + \frac{1}{\left(S_5 + S_6\right)\left(S_1 + S_2\right)} \right) V_{PV} \qquad \text{-----(1)}$$

where Sa, (a=1, 2, 3,...) is the switch Sxa's switching state, which may be either 1 (stands for turn-ON) or 0 (stands for turn-OFF). All switches for the equivalent inverter output pressure vuv are presented in Table 1. The Sx1 and Sx2, half-bridges, operate at a low frequency of switching. The Sx2 control is always switched on in the zero states during the voltage transition from level 0 to VPV/2 to reduce unnecessary frequency change. Similarly, throughout the voltage change from level 0 to VPV, the switch Sx1 is maintained switched on. During the positive halving center of the output voltage transformer the inverter interface (Sx3, Sx6) performs at a high frequency and is maintained on an OFF level during a negative half cycle. The second Sx4 inverter pairing, Sx5, established by a similar procedure, runs in the negative half cycle, at higher switching frequency. During the half of the input cycles, the Sx7 and Sx8 controls will be turned on. The elimination of complementary action on switches pairs (Sx3, Sx4) and (Sx5, Sx6) allowed switches to be turned off fully in each half of the voltage UV output cycle. As a consequence, the suggested system has lower switching losses, resulting in a highly efficient and dependable inverter design that may lead to greater efficiency.

PROPOSED PWM STRATEGY ALONG WITH GENERALIZED STRATEGY FOR MINIMIZATION OFTHELEAKAGE CURRENT

The suggested PWM technique's functioning is described using the provided five-level CMLI. The proposed PWM approach decreases high-frequency transitions in the VXG and CMLI 5-level terminal voltages. Every proposed action can be taken by converting from VPV to VPV/VPV/2 rather than changing from VPV to VPV/2. The PV system is isolated from the skillet during the zero voltage or during the phase available of the switching cycle. During the negative voltage condition, the PV array and grid are disconnected, similar to the inverter system described in [6-7]. The size of a comparison wave vmod is reduced to 50 per cent of the original value when the switching between levels VPV and 0. is transformed. The above operation is usually done to accommodate the VPV value of PV voltage. The value of V_{mod} will change when the instantaneous size of the modulative wave V_{mod} reaches the value of ma/2, where ma is the modulation index. The output voltage includes the default stage in all its switching phases once the required change is integrated. The v_{ref} modified modified reference waveform expression is provided in (3).

$$v_{ref\_modified} = \begin{cases} v_{mod} & for \quad 0 \leq |v_{mod}| < \dfrac{m_a}{2} & from \quad \dfrac{V_{PV}}{2} to \ 0 \\ \dfrac{v_{mod}}{2} & for \quad \dfrac{m_a}{2} \leq |v_{mod}| < m_a & from \quad V_{PV} to \quad 0 \end{cases} \quad ---- \quad (2)$$

where, $v_{mod} = m_a \sin\omega t$ gives the magnitude of v_{mod}.

SIMULATION RESULTS

The proposed CMLI of five levels is simulated by utilizing MATLAB/SIMULINK Block POWER SIM to aid in examining the switching function presented in the previous section. The proposed CMLI five-level arrangement uses the PWM method described. The suggested five-level CMLI must create the V_{inv} voltage at a phase inv to deliver the grid's required amount of active power. Figures 3 to 7 illustrate simulated waveforms of the proposed five-level CMLI utilizing the suggested PWM method. The output current of a solar PV panel is shown in Figure 8. The figure clearly demonstrates the existence of zero current state in all current transitions. Figure 5 shows the waveform of the solar panel's terminal voltages. There are voltage spikes at regular intervals, as may be seen in this diagram. The output voltage of the CMLI is shown in Fig.6. The form of the voltage may be seen in this diagram to be a five-leel AC voltage with a magnitude of 500V. Figure 7 depicts the grid current i_{ac}. The current in the grid is essentially sinusoidal. Grid current iac has a Total Harmonic Distortion (THD) of approximately 1.76 percent, which satisfies IEEE 1547 requirements.

CONCLUSION

In this article, a five-tier enhanced CMLI is presented with a lower power frequency to reduce leakage current without transformers in a PV system. The CMLI proposed minimizing the leakage current by preventing the transition from high frequencies from the terminal to the primary signal. The recommended architecture also provides less conduction and a loss of switching to allow the CMLI to operate at a high frequency. In addition, the article includes a solution for the generalized 2m+1 levels CMLI. For the production of 2m+1 levels, the proposed PWM method only needs one carrier wave. The paper also includes the functioning and analysis of terminal and standard-mode voltage by CMLI. The results of the simulation are analyzed in this article. The MPPT algorithm is used with the recommended five-level CMLI to generate maximum power from the PV panels.

REFERENCES

1. Y. Tang, W.Yao, P.C.Lon and F. Bleiberg,"Highly Reliable Transfor merless Photovoltaic Inverters With Leakage Current and Pulsating Power Elimination," IEEE Trans.Ind. Elect.,vol. 63, no.2, pp. 1016-1026, Feb. 2016.
2. W. Li, Y. Gu, H. Luo, W. Cui, X. He and C. Xia, "Topology Review and Derivation Methodology of Single-Phase Transformerless Photovoltaic Inverters for Leakage Current Suppression," IEEE Trans. Ind. Elect., vol. 62, no. 7, pp. 4537-4551, July 2015.
3. J. Ji, W. Wu, Y. He, Z. Lin, F. Bleiberg and H. S. H. Chung, "A Simple Differential Mode EMI Suppressor for the LLCL-Filter-Based Single Phase Grid-Tied Transformerless Inverter," IEEE Trans. Ind. Elect., vol. 62, no. 7, pp. 4141-4147, July 2015.
4. Y. Bae and R. Y. Kim, "Suppression of common-mode voltage using a multicentral photovoltaic inverter topology with synchro nized PWM," IEEE Trans. Ind. Electron., vol. 61, no. 9, pp. 4722–4733, Sep. 2014.
5. N. Vazquez, M. Rosas, C. Hernandez, E. Vazquez, and F. J. Perez-Pinal, "A new common-mode transformerless photovoltaic inverter," IEEE Trans. Ind. Electron., vol. 62, no. 10, pp. 6381–6391, Oct. 2015
6. G. Buticchi, E. Lorenzani, and G. Franceschini, "A five-level single-phasegrid-connected converter for renewable distributed systems," IEEE Trans.Ind. Electron., vol. 60, no. 3, pp. 906–918, Mar. 2013.
7. N. A. Rahim and J. Selvaraj, "Multistring five-level inverter with novel PWM control scheme for PV application," IEEE Trans. Ind.Electron., vol. 57, no. 6, pp. 2111–2123, Jun. 2010.
8. M. Cavalcanti, K. De Oliveira, A. M. de Farias, F. Neves, G. Azevedo, and F. Camboim, "Modulation techniques to eliminate leakage currents in transformerless three-phase photovoltaic systems," IEEE Trans. Ind. Electron., vol. 57, no. 4, pp. 1360–1368, Apr. 2010.
9. L. Zhang, K. Sun, L. Feng, H. Wu, and Y. Xing, "A family of neutral point clamped full-bridge topologies for transformerless photovoltaic grid-tied inverters," IEEE Trans. Power Electron., vol. 28, no. 2, pp. 730–739, Feb. 2013.

Table I Switching States with Their Respective Output Voltage

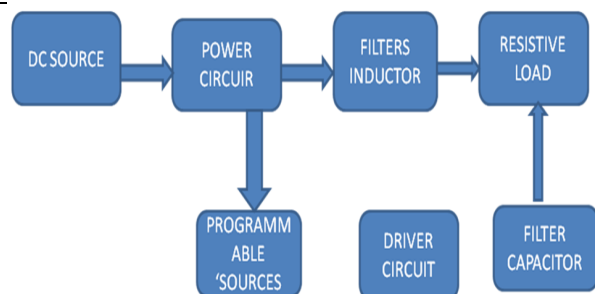| S_{x1}	S_{x2}	S_{x3}	S_{x4}	S_{x5}	S_{x6}	S_{x7}	S_{x8}	V_{uv}
1	0	1	0	0	1	1	0	$+V_{pv}$
0	1	1	0	0	1	1	0	$+V_{pv}/2$
0	1	0	0	0	0	1	0	0
1	0	0	0	0	0	1	0	0
0	1	0	1	1	0	0	1	$-V_{pv}$
1	0	0	1	1	0	0	1	$-V_{pv}/2$

Sarala and Indu

Fig. 1. Proposed five-level grid-connected CMLI with PV and parasitic elements
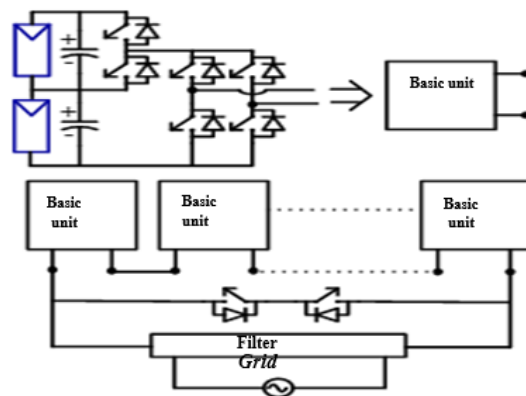

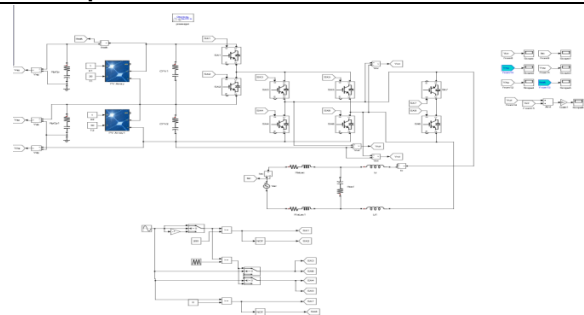**Fig.2. General topology 2m+1 level MLI based on five-level CMLI proposed**
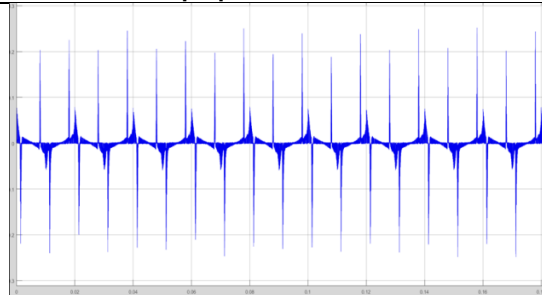

Fig. 3. Simulink model
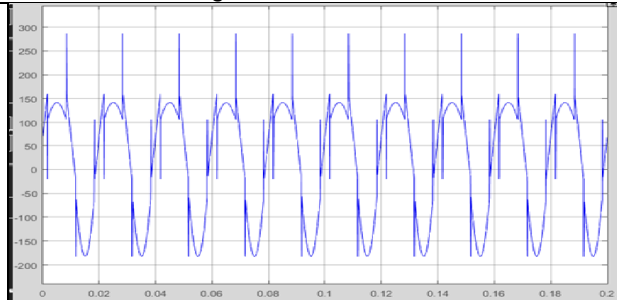

Fig. 4. Solar Current obtained from PV Cell
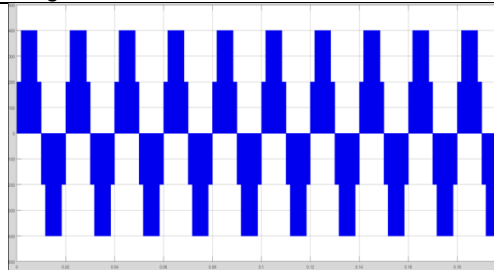

Fig. 5. Output Voltage from solar panel
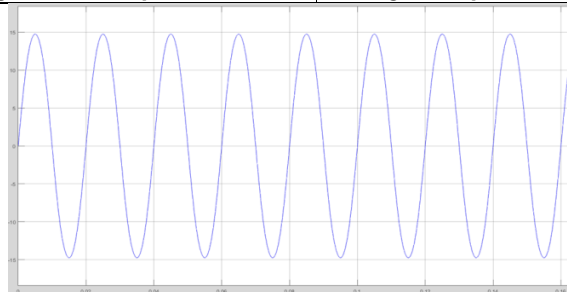

Fig.6. Output voltage of proposed ML Inverter

Fig. 7. Grid current of proposed system

RESEARCH ARTICLE

Energy Shaping Control of Grid Connected Parallel Interleaved Converter for Current Reduction

N. Rajeswaran[1], P. Marimuthu[1] and S.Lavanya[2]*

[1]Department of EEE, Malla Reddy Engineering College, Maisammaguda, Hyderabad, India.
[2]PG Scholar, Department of EEE, Malla Reddy Engineering College, Maisammaguda, Hyderabad, India.

*Address for Correspondence
S.Lavanya
PG Scholar,
Department of EEE,
Malla Reddy Engineering College,
Maisammaguda, Hyderabad, India.
Email: lavanyanani15@gmail.com

ABSTRACT

This paper implements to control a circulating current with low frequencies produced by parallel interleaved converters. The magnetically linked inductors are used for inverters to parallelize in this configuration. The harmonic content in the output voltage is minimized by incorporating carrier interleaving. This consequences in a greater circulating current to flow in the course of the two Voltage Source Converters (VSCs).The mutual inductance of the Coupled Inductors (CI) is competently reduce the components of circulating currents with high frequencies. The components of low frequencies effectively cannot filter by coupled inductors. The coupled inductors are lead to saturation when the circulating currents are very high under uncontrolled due to this the converter have the higher switching losses, and disgrace the overall performances. The delivered active as well as reactive powers to the grid are effectively controlled with this controller and also it decreases the amount of circulating current with the low frequency. The performances of the converter are found by simulation and compared with the performance of Linear Quadratic (LQ) control and classical PI control. The simulation shows a good performance in the proposed method.

Key Words: Voltage Source Inverter, Coupled Inductor, Port Controlled Hamiltonian, Linear Quadratic Control, Proportional Controller, Pulse Width Modulation

INTRODUCTION

The converters have been a lot of pioneering configurations were incorporated to manage the escalating power received from non conventional sources of energy. For such applications, multi-pulse converters, matrix converters and multi-level converters were offered in [1]. Another topology was projected recently based on the parallelization of typical two-level inverters to attain high power converters by coupled inductors [2, 3]. The various offers offered by parallelized inverters are phase shifted by 180∘ to the system; the benefits are size declined of the output filter, multilevel output, and also reduction of Common Mode Voltage in [4, 5]. The acceptable level of circulating currents with lofty frequency components can be shortened by a tolerable choice of coupled inductors in [6]. In [7] proposed the various design procedures of these filtering components. In [8] proposed a reduction of circulating current in the system and common mode voltage by three-level SVM. The PWM techniques were proposed in [9] to diminish the crest value of the circulating current by discriminating harmonic elimination. The PI controllers inputs are identified from the circulating currents from each phase were presented in [10].

The modulating signals added to controller output of only one converter of the two parallelized VSCs and the proposed scheme of modified DPWM were presented in [11]. In [12], the deadbeat control approaches were implemented in order to reduce the amount of circulating currents. The ZSCC was suppressed by a modular two-level interleaved converter with carrier Phase Shifted PWM was presented in [13]. The ES control strategy was implemented in DFIG wind turbine has been presented in [14].

CONTROL METHODOLOGY

The scheme of method for the system MMC with VCM as shown in Fig. 1, it consists of five controllers. The five controllers and their control objectives are: (i) a VSI two–layer controller is used to transfer the amount of power generated into the ac grid, (ii) a leg energy controller is used to control the amount of capacitors energy stored in the SMs in order to make sure the stable operation of the MMC, (iii) a phase - disposition pulse width modulation (PD-PWM) type modulator is used to determines the SMs that need to be switched ON and a voltage balancing algorithm (VBA) to balance the capacitors voltage of the SMs, (iv) a amount of circulating current suppressing controller to suppress the inner circulating currents (v) a VCM controller to reimburse for the difference of voltage during unbalance conditions and both the VCM controller and circulating current suppressing controller are decoupled from the main power stage control. The fig. 2 shows the two layers of VSI controller is wrecked into three blocks: (i) power–to–current transformation (ii) a Phase Locked Loop for synchronization of AC grid and (iii) the conventional control of current in the rotating reference frame of direct quadrature to transfer the amount of power generated into the side of AC grid at an random power factor.

Phase Locked Loop

The synthesizing the information of phase and frequency of the system by using the technique of PLL. The PLL computes the grid phase angle by sensing the grid voltage and projecting the corresponding space vector onto the dq axis. The q component is then forced to be equal to zero ($v_q = 0$) with the help of a PI controller as depicted in fig. 2. By doing so, the dq axis will be rotating at the same speed as the grid angular frequency. This angle is then used to synchronize the dq reference frame for the control of inner current of the system.

Power to Current Transformation

The active power and reactive power references (P$_{ref}$, Q$_{ref}$) are reliant on the load requirement. From dq currents be able to be computed accordingly and this equation is based on the assumption that the PLL is capable to force V$_q$ to zero.

$$P_{ref} = \frac{3}{2}v_d I_d^{ref} \qquad\qquad (1)$$

$$Q_{ref} = -\frac{3}{2}v_d I_d^{ref} \qquad\qquad (2)$$

Inner Current Control

The AC side dynamics of the VSI can be described by the following dynamic phasor relation in the 'abc' reference frame, m_j, v_j and i_j are the three phase AC voltages and currents at the AC terminal respectively, L_s and R_s are the equivalent value of the inductance and the resistance at the VSI side which are defined by the following equations,

$$L_s \frac{di_j}{dt} = -R_s i_j + V_j - v_j \qquad (3)$$

$$L_s = L_f + \frac{L_a}{2} \qquad (4)$$

$$R_s = \frac{R_a}{2} \qquad (5)$$

FLY – BACK CONVERTER

During the operation it has different configuration of Fly-back converter.. From the Fig. 3, the winding of primary of the transformer gets connected when the switch 'S' is 'ON', the input supply with its positive side is connected to the dotted end. The secondary winding connected in series with diode 'D' gets reversed due to the voltage induced in the secondary at the same time. The winding in the primary is able to carry current when turning 'ON' switch 'S', but it blocked the current in the secondary side winding due to the diode reverse biased. This mode of circuit have been denoted here as operation of Mode-1. Fig. (a) Shows the circuit which is current carrying part and Fig. (b) Shows the fly-back circuit during mode-1. The discontinuous flux mode of operation is preferred for enhancing the output voltage. On the other hand, the additional output power can be transferred during continuous mode. The circuit is designed based upon thumb rule for operation of continuous flux mode at the minimum predictable input voltage and at the value of rated output power.

RESULTS AND DISCUSSIONS

The simulation results corresponding to a proposed converter technique is presented and the simulation can be carried out through MATLAB. Fig. 4 depicts that the three phase voltage in the grid side. Fig. 5 shows the current in the grid side. The Fig. 6 depicts the active power of the converter.

CONCLUSION

The coupled inductors can be used to interconnect the conventional two-level inverters in parallel for improvement of rated power of converters connected with grid. The balance of the current delivered by the two converters is feasible without any specific control function of the system. At the same time, it induces disagreeable circulating currents with low frequency which stress on power semi-conductors was increases. In this work, magnetically coupled inductors with interleaved three-phase inverters can be balanced by the proposed technique. The converter is considered as a passive system and it was modeled that meets the requirements of energy shaping control. It required additional sensors to implementation of this algorithm to measure the output currents of the first converter. Consequently the projected control allows enhanced performances and abridged energy losses.
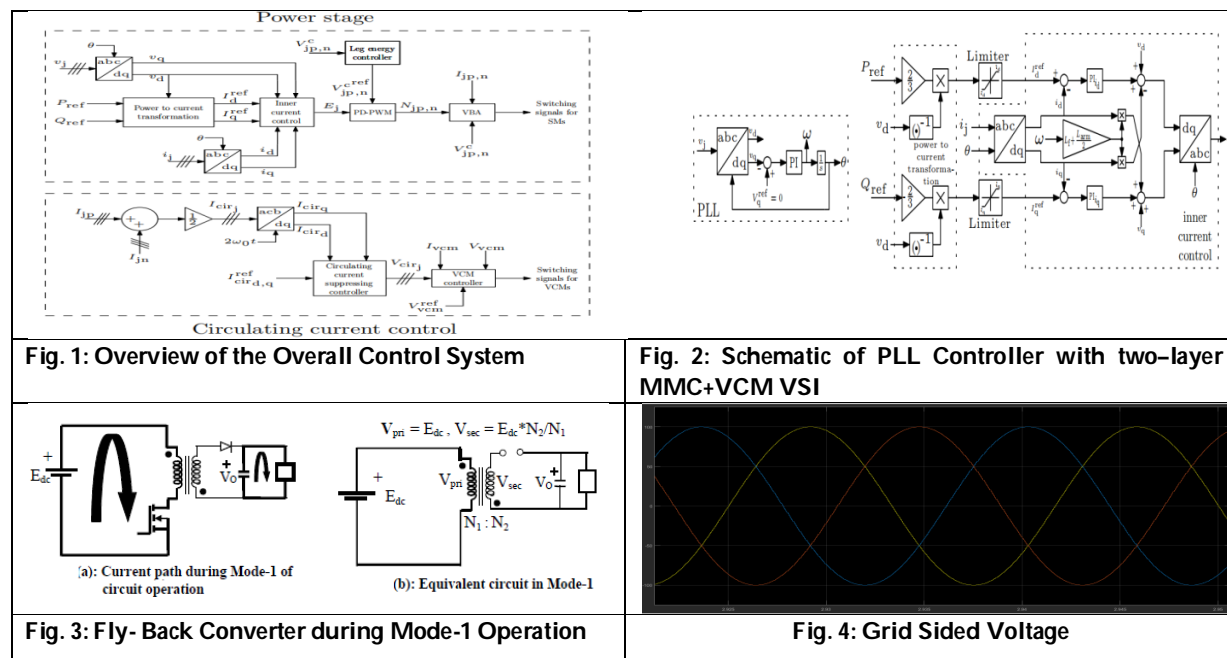
REFERENCES

1. R. Iravani, A. Yazdani, Voltage Sourced-converters in Power Systems. Modeling, Control and Applications, Wiley, New Jersey, 2010 ISBN 978-0-470-52156-4.
2. A. Laka, J.A. Barrena, J. Chivite-Zabalza, M.A. Rodriguez-Vidal, Parallelization of two three-phase converters by using coupled inductors built on a single magnetic core, Przeglad Elektotechnicy 89 (2013) 194–198.
3. A. Laka, J.A. Barrena, J. Chivite-Zabalza, M.A. Rodriguez-Vidal, P. Izurza-Moreno, Isolated double-twin VSC topology using three-phase IPTs for high-power applications, IEEE Trans. Power Electron. 29 (2014) 5761–5769.
4. D. Zhang, F. Wang, R. Burgos, R. Lai, D. Boroyevich, Impact of interleaving on AC passive components of paralleled three-phase voltage source converters, IEEE Trans. Ind. Appl. 46 (2010) 1042–1054.

Rajeswaran *et al.*,

5. G. Gohil, L. Bede, R. Teodorescu, T. Kerekes, F. Blaabjerg, Flux balancing scheme for PD modulated parallel interleaved inverters, IEEE Trans. Power Electron. Vol. 32 (2017) 3442–3457.

6. F. Forest, E. Labouré, T.A. Meynard, V. Smet, Design and comparison of inductors and inter cell transformers for filtering of PWM inverter output, IEEE Trans. Power Electron. 24 (2009) 812–821.

7. F. Ueda, K. Matsui, M. Asao, K. Tsuboi, Parallel-connections of pulse width modulated inverters using current sharing reactors, IEEE Trans. Power Electron. Vol. 10 (1995) 673–679.

8. Z. Quan, Y.W. Li, A three-level space vector modulation scheme for paralleled converters to reduce circulating current and common-mode voltage, IEEE Trans. Power Electron. 32 (2017) 703–714.

9. G. Konstantinou, J. Pou, G.J. Capella, S. Ceballos, V.G. Agelidis, Reducing circulating currents in interleaved converter legs under selective harmonic elimination pulse-width modulation, IEEE International Conference on Industrial Technology (2015).

10. L. Bede, G. Gohil, M. Ciobotaru, T. Kerekes, R. Teodorescu, V.G. Agelidis, Circulating current controller for parallel interleaved converter using PR controllers, 41st Annual Conference of the IEEE Industrial Electronics Society (2015).

11. G. Gohil, R. Maheshwari, L. Bede, T. Kerekes, R. Teodorescu, F. Liserre, F. Blaabjerg, Modified discontinuous PWM for size reduction of the circulating current filter in parallel interleaved converters, IEEE Trans. Ind. Electron. 30 (2015) 3457–3470.

12. Z. Xueguang, Z. Wenjie, C. Jiaming, X. Dianguo, Deadbeat control strategy of circulating currents in parallel connection system of three-phase PWM converter, IEEE Trans. Energy Convers. 29 (2014) 406–417.

13. Z. Quan, Y.W. Li, Suppressing zero-sequence circulating current of modular interleaved three-phase converters using carrier phase shift PWM, IEEE Trans. Ind. Appl. 53 (2017) 3782–3792.

14. X. Lin, Y. Lei, Y. Zhu, A novel superconducting magnetic energy storage system design based on a three-level T-type converter and its energy-shaping control strategy, Electr. Power Syst. Res. 162 (2018) 64–73.

Fig. 1: Overview of the Overall Control System	**Fig. 2: Schematic of PLL Controller with two–layer MMC+VCM VSI**
Fig. 3: Fly- Back Converter during Mode-1 Operation	**Fig. 4: Grid Sided Voltage**

Rajeswaran *et al.,*
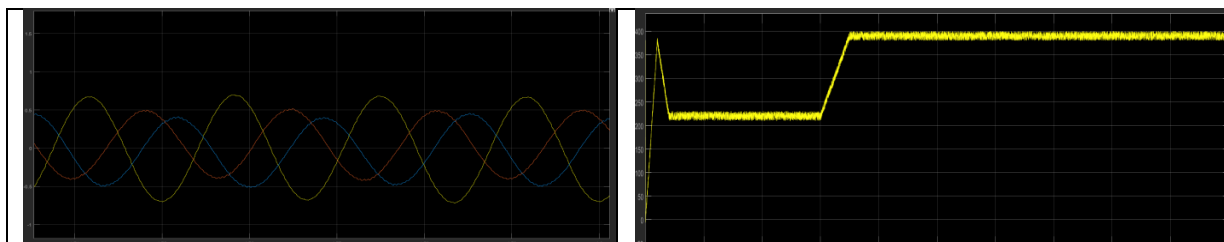
Fig. 5: Grid Sided Current

Fig. 6: Active Power
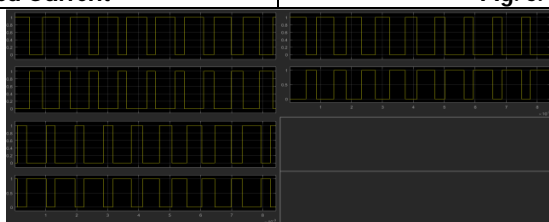
Fig. 7: Gate Pulse

Maximum Power Point Tracking for Permanent Magnet Synchronous Generator based Wind Park Application

R. B. R. Prakash[1‡] iD, P. Srinivasa Varma[1] iD, Ch. Rami Reddy[2] iD, M. Dilip Kumar[3] iD,
A. Giri Prasad[4] iD , E. Shiva Prasad[4] iD

[1]Electrical and Electronics Engineering, Koneru Lakshmaiah Education Foundation, Vaddeswaram, AP, India 522302

[2]Electrical and Electronics Engineering, Malla Reddy Engineering College (A), Secunderabad, Telangana, India 500100

[3]Electrical and Electronics Engineering, St. Peters Engineering College (A), Secunderabad, Telangana, India 500043

[4]Electrical and Electronics Engineering, VNR Vignana Jyothi Institute of Technology (A), Secunderabad, India 500090

(bhanu184@kluniversity.in, pinnivarma@kluniversity.in, crreddy229@mrec.ac.in, manikdilip@gmail.com,

giriprasad_a@vnrvjiet.in, shivaprasad_e@vnrvjiet.in)

‡Corresponding Author: R. B. R. Prakash, bhanu184@kluniversity.in

Abstract- The world's energy consumption is constantly growing, and conventional energy sources may soon be depleted. Wind energy is one such discovered new energy source that is abundant and renewable. However, induction generators require large excitation capacitors and bi-directional power flow controllers. Permanent magnet synchronous generators are now more appropriate for variable speed Direct Driven Wind Power Conversion Systems (DDWPCS). Earlier, a three-stage power conversion for variable ac voltage was done. To reduce these power conversion stages and to overcome the limitations of conventional systems, the Z-Source Inverter (ZSI) based Direct Drive Wind Energy Conversion Systems (DDWECS) is introduced. Mathematical modelling equations are derived for various operating modes of operation using ZSI. In the proposed method Space Vector Pulse Width Modulation (SVPWM) & Modified SVPWM (MSVPWM) methods were compared for shoot through period placement, voltage gain, and Total Harmonic Distortion (THD). The MSVPWM places the shoot through period faster and also it reduces input current THD by 3.6% and output voltage THD by 7.8%. Also, this adds a PWM controller to suppress 3rd order harmonics. To validate the proposed ZSI, simulation is carried out in MATLAB and the results are tabulated.

Nomenclature

DDWPCS	Direct Driven Wind Power Conversion Systems	HCS	Hill climbing search
		HCSC	Hill climbing search control
ZSI	Z-Source Inverter	DFIG	Doubly Fed Induction Generator
PWM	Pulse Width Modulation	MPPT	Maximum Power Point Tracking
SVPWM	Space Vector Pulse Width Modulation	PSO	Particle Swarm Optimization
		VSI	Voltage Source Inverter
MSVPWM	Modified Space Vector Pulse Width Modulation	MBC	Maximum boost control
THD	Total Harmonic Distortion	THI	Third Harmonic Injection
WECS	Wind Energy Conversion System	ρ	Air density
PMSG	Permanent Magnet Synchronous Generator	A	blade area

V_W	wind velocity
P	Power
R	Radius of the turbine blade
C_p	Power coefficient
λ	Tip Speed Ratio
T_e	Electromagnetic Torque
L_m	mutual inductance
i_{qs}	q-axis stator current
i_{ds}	d-axis stator current
i_{qr}	q-axis rotor current
i_{dr}	d-axis rotor current
R_s	Stator Resistance of PMSG
L_s	Inductance of PMSG
E	Generated voltage of PMSG
V_t	terminal voltage of PMSG
i	PMSG stator current
i_q	q-axis stator current of PMSG
i_d	d-axis stator current of PMSG
ψ_q	q- axis flux linkages
ψ_d	d- axis flux linkages
V_c, V_{c1}, V_{c2}	Capacitor voltages
V_L, V_{L1}, V_{L2}	Inductor voltages
V_{DC}	DC Voltage
V_i	Inverter voltage
V_m	peak voltage
V_{ac}	ac output voltage of ZSI
B	Boost factor
G	Voltage gain
M	Modulation index
D, D_0	shoot through duty ratios

1. Introduction

With the ever-increasing demand for electrical energy and our serious concern over environmental pollution, the generation of power from wind is attracting attention. The fixed speed wind energy conversion system requires a gearbox for regulating its speed, terminal voltage and supply frequency. A gearbox system increases the conversion loss and aerodynamic noise and decreases the efficiency. In addition, it requires considerable maintenance. Recent advancements in power electronics equipment have widened the scope for installing the variable speed WECS. Although conventional type induction generator has the advantages of

robust construction and maintenance free operation, it has drawbacks like low power factor and it requires an ac excitation source. Due to the low cost of the permanent magnet materials, the PMSG brings the variable speed WECS into the market for multi megawatt wind turbine applications.

In the literature survey, it has been found that conventional induction generators and alternators are not suitable for WECS, as they suffer from low torque and low efficiency. To overcome this problem direct drive WECS using PMSG is proposed. This scheme does not require any gearbox, it is easy to control, smaller in size and weight, and has much higher efficiency. The three stages of the conventional power converters are subject to more switching stress consequently more switching losses and the corresponding maintenance. Cost effective design of variable speed WECS using PMSG for a speed range of 20 rpm to 200 rpm is presented in [1]. Radial flux PMSG called torus was presented in [2]. Many researchers have discussed three stage of power converter for WECS. The common drawback of these traditional three stage power conversion systems was discussed [3]. To get the constant voltage by adjusting the duty cycle of a boost chopper was presented in [4]. The dead time in the inverter output reduces the power quality of the dc output voltage which requires a large value of LC in the filter, in addition, they are vulnerable to noise [5]. PWM inverter imposes high switching stress on the switching devices [6]. To suppress the above problem, large size LC filters were suggested by them. The problem of a conventional three stage dc-dc-ac conversion system was presented in [7]. They have proposed a high buck boost DC-AC ZSI. [6] Presented a two constant boost control method for ZSI. But they did not take into account the problem of THD. The reference [8] presents a ZSI which greatly enhances the reliability of the inverter. In [9] the modified space vector for ZSI. The shoot through placement in the space vector of zero states is not uniform and hence switching stress is more. A novel 1-φ Z-source multilevel inverter is proposed in [10]. They used the diode clamped topology but this topology increases the complexity of complex circuits. [2] Had discussed the P and O algorithm-based MPPT controller in which the speed is variable in steps and the power utilized by the MPPT is reached. [11] Proposed HCSC method for MPPT controllers of WECS. [12] Described a method to solve the tracking speed versus control efficiency problem by HCS. The design of a wind turbine system with the usage of DFIG as the power generating system which can be operated in grid-connected mode or in grid disconnected mode is presented in [13].

A grid connected qZSI Photovoltaic power system is presented in [14]. They have designed a DC link voltage controller and AC side power controller for improving the performance of qZSI-based photovoltaic systems. A modified NLMS-based control algorithm is designed to control the distributed generation system feeding three phase nonlinear loads. The control algorithm extracts the fundamental weight components with reduced oscillations from the load current [14]. To extract maximum power for a

hybrid solar-wind renewable energy system using the PSO for standalone applications is presented in [15]. Maximum power extraction based on PSO works to achieve optimal power on HRES by adjusting the duty cycle for the boost converter for each energy source system based on current and voltage measurements.

But the authors have not considered frequency variations of DC link voltage concerning photovoltaic voltage variations and also the DC link voltage controller requires a complex control algorithm. A qZSI derived from the traditional ZSI is presented in [15]. The qZSI features a wide range of voltage gain which is suitable for applications in photovoltaic systems. To enhance the performance of qZSI, the authors have proposed design guidelines for boost control methods. Even in that case, the efficiency is not improved and the cost of qZSI is not reduced when compared with traditional ZSI. To circumvent the limitations of the traditional ZSI, qZSIs was proposed [18]. It reduces passive component ratings and improves input profiles. The consistent DC makes qZSI suitable for PV applications [18]. Advanced dc-dc converter improvement techniques such as Switch Capacitor (SC), Switch Inductor (SL) and hybrid SC/SL technology have been disclosed recently to increase the boost factor of the traditional ZSI. So ZSI and Switch inductor are combined to produce a high boost factor. This includes constant current from the input DC source, reduced component ratings, and improved dependability [20]. In the last decade, the fixed-speed wind energy conversion system has given way to variable-speed systems due to their poor energy extraction, mechanical stress on moving parts and poor power quality. Mechanical stress and aerodynamic noise have been minimized by these variable-speed devices [21]. They can be regulated to allow the turbine to work in a wide range of wind velocities at its optimum power coefficient, obtaining greater wind energy collection with instant response to wind velocities and load changes [21], [22] and energy capture from the wind. The gearless wind system also allows optimum energy yield and minimal costs to be achieved, as reported by [23-26]. According to the electric machine design principles, the wind energy conversion system at fluctuating speeds requires a very bulky generator with a large number of poles [27]. Fig. 1 shows the wind turbine generator with and without gearbox topology. To be easily mounted at the top of the tower and directly connected to the wind turbine, the type of generator for this application must be compact and lightweight.
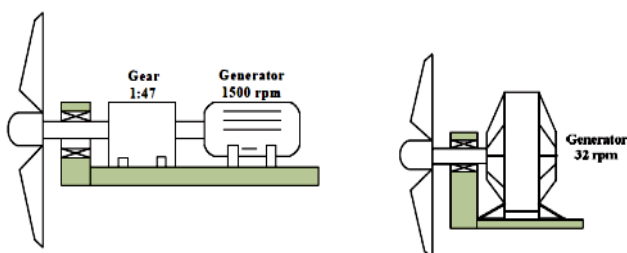

Fig. 1. Types of wind turbine generators (a) With gearbox and (b) Without a gearbox

This work deals with DDWECS. For direct-driven generator needs a very low-speed operation to match the wind turbine speed and at the same time, to produce electricity in a normal frequency range [28]. The recent development in power electronic devices and its control strategy over energy-efficient DDWECS has aroused interest in using PMSG in small and medium DDWECS. There are three phases in traditional to achieving the required voltage and frequency, power conversion systems interface circuits such as the rectifier, dc-dc boost chopper and PWM inverter [28]. VSI and the PWM are commonly used in WECS to get AC, but it has the disadvantages of needing a dc to dc boost chopper to get a constant dc voltage of higher amplitude [29]. Conventional three stages of power conversion require bulky DC link inductor and capacitor, Electrical decoupling between the generator and the grid is provided by the intermediate DC connection [31]. Therefore, the compensation of accumulated kinetic energy in a wind turbine requires a separate controller. The use of PMSG has been documented in some literature. The proposed ZSI [32] and the traditional DDWECS overcome the limitations of PWM-VSI. It is a single stage dc-ac converter buck-boost and thus its performance is improved over the conventional WECS [33-35]. With this ZSI the boost chopper is removed without any change in the objectives. [35] Presented the ZSI enables short circuits through every phase leg and thus improves the efficiency of the system.

The main contributions and novelty of this work can be summarized as follows:

- The ZSI is proposed as a power conditioner in DDWECS to reduce the number of power conversion stages to two as against three in the conventional system.

- The ZSI features buck-boost capability due to an extra shoot-through state created in the zero state of the typical inverter pulse width modulation. The shoot-through condition is used to enhance the input voltage. The shoot-through pulse width is adjusted as per the PMG generated voltage level to maintain constant load voltage.

- The presented study emphasizes investigating the two PWM control methods such as carrier-based third harmonics control and modified space vector PWM are employed to analyze the performance of the Z-source inverter. The two independent control variables such as shoot-through duty ratio and modulation index are suitably adjusted to get the required voltage and power.

- To improve the system performance, sensor less MPPT controller is incorporated into the system is introduced to avoid conventional sensors. Using this scheme the generator speed required for the existing wind velocity to generate maximum power is predicted.

Text in the paper is presented as follows: Section II describes the proposed ZSI based DDWECS and also gives the

operating modes of the proposed system, Section III describes the control strategy of the proposed converter, Section IV and Section V discusses the performance analysis and presents the results of simulation and discussion for various inputs and outputs of the proposed MPPT controller with ZSI conditions of the proposed converter concerning voltage gain, switching stress, input, output and THD. Lastly, section VI presents the conclusions.

2. Proposed ZSi Based Ddwecs

Using three stages of power conversion, the power conversion was done earlier to obtain variable ac voltage at variable frequency. DDWECS-based ZSI is implemented to

reduce the power conversion stages and to overcome the limitations of traditional systems. With the assistance of mathematical equations, the ZSI's operating modes with DDWECS are addressed. It gives and describes in detail the mathematical equations for boost factor, voltage gain and switching stress. The two-stage power conversion method by integrating the ZSI for DDWECS is shown in Fig. 2. Here, without any change in aims, the ZSI replaces the buck raise chopper. The ZSI enables the short circuit to increase system reliability at every stage leg. Fig. 3 shows the full circuit of the proposed WECS with ZSI. The PMSG output is fed through its stator inductances and resistances and then to the rectifier [11]. The rectifier serves as the DC supply and its output is given as input to the ZSI.
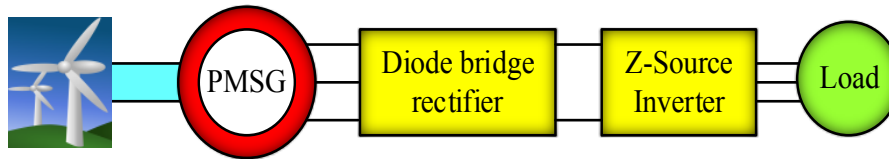
Fig. 2.DDWECS with two stage power conversion
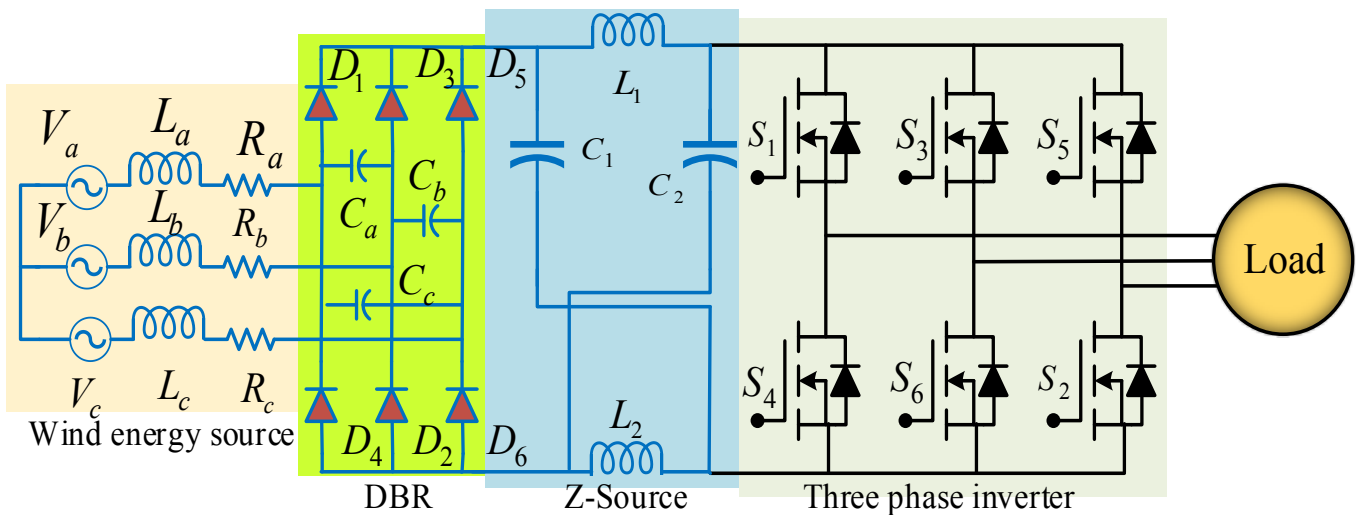
Fig. 3. PMSG with Z-Source inverter and rectifier

Any VSI can be operated in eight different switching modes, out of which six are said as active states and the remaining two are termed as zero states or modes. As here ZSI is integrated, it offers one more additional state of operation; the ninth state is named as shoot-through zero state. In these operating states two switches on the same limb or any two legs made ON, it causes the load terminals to short circuit. This ninth state 'shoot-through zero state', adds a buck boost special provision to the inverter [11]. Switching intervals of the ZSI are shown in Table 1. Here the appreciable objective of the ZSI is its actions to generate any desired output voltage based on the grid code requirements [12]. Modeling and analysis of the proposed converter are discussed in the next section.

A. Modeling of Wind Turbine and PMSG

The wind turbine and permanent magnet generator mathematical equations are generated, modeled and simulated in MATLAB.

A.1. Wind Tturbine Model

The wind is just air moving, air has mass despite its low density. The kinetic energy of wind is related to the mass times the square of the wind velocity. The mass of air traveling in time is the combination of air density (ρ), blade area (A) and wind velocity (V_W).

The kinetic energy in the region

$$ P = \rho A V_W^3 $$

The amount of energy collected by a wind turbine is provided by the

$$P = 0.5\pi R^2 V_W^3 \rho C_P$$

Where

ρ = Air density

R = Radius of the turbine blade (m)

V_w = Wind velocity (m/s)

C_p = Power coefficient

The C_p curve will be approximated analytically using Eq. (1) CP has a theoretical top value of 0.59, although in practice it ranges from 0.2 to 0.4.

$$C_P = \frac{16}{27}\lambda\left[\lambda + \frac{1.32 + \left(\frac{\lambda-8}{20}\right)^2}{\beta^{2/3}}\right] - \frac{0.57\lambda^2}{\frac{C_1}{C_d}\left[\lambda + \frac{1}{2\beta}\right]} \quad (1)$$

Fig 3. shows a basic way to represent a wind turbine. eq shows the generating torque in an arbitrary reference frame (2).

$$T_e = \left(\frac{3}{2}\right)*\left(\frac{P}{2}\right)*L_m\left[i_{qs}i_{dr} - i_{qr}i_{ds}\right]$$

(2)

A.2. Permanent Magnet Synchronous Generator

An accurate machine model is required to predict PMSG steady state and transient behavior. The model should find the machine's dynamic reaction. The dynamic model accounts for changes in voltage, current, stator frequency, and torque. It is generated utilizing a two-phase machine on the direct and quadrant axis.

$$E = V_t + iR_s$$

$$V_t = L_s\frac{di}{dt} - iR_s$$

$$V_t = \lambda\psi - iR_s$$

The d and q axis voltages are as follows.

$$V_q = -R_s i_q + \frac{d}{dt}\psi_q$$

$$V_d = -R_s i_d + \frac{d}{dt}\psi_d$$

Eq. (3) gives the electromagnetic torque in the rotor reference

$$T_e = \left(\frac{3}{2}\right)*\left(\frac{P}{2}\right)*\left[\psi_d i_q - \psi_q i_d\right]$$

(3)

Where P= Number of poles

B. Operating Modes of Proposed ZSI

The proposed system operates in three different modes as follows.

Mode-1: Fig. 4 demonstrates ZSI's equivalent circuit for operation in mode-1. In one of the two traditional zero states, the inverter bridge operates and short-circuits either the upper or lower three devices. It, therefore, functions as an open circuit perceived from the network of Z-source. The PMSG phases a and b are linked via the two diodes to the impedance network. Diodes D1 and D6 are in series with capacitor Ca.
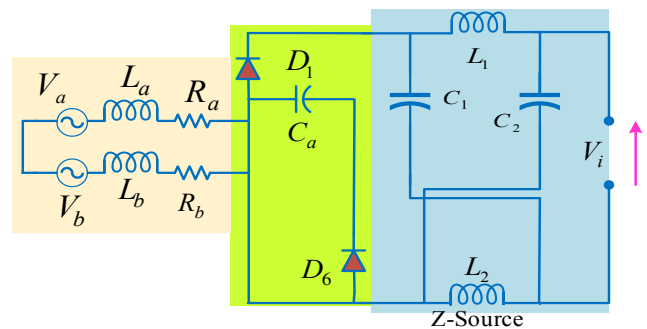
Fig. 4. Equivalent circuit of ZSI for mode-1

Mode-2: The ZSI equivalent circuit in shot through service is shown in Fig. 5. In this mode, both diodes are OFF due to higher voltages in inductors, separating the dc connection from the ac line. The PMSG is thus disconnected from the load. In any switching cycle during the traditional zero states created by the PWM control, this shoot-through mode can be used. Based on the appropriate boost factor, the shoot through time or shoot-through duty cycle is calculated using Eq. (13).
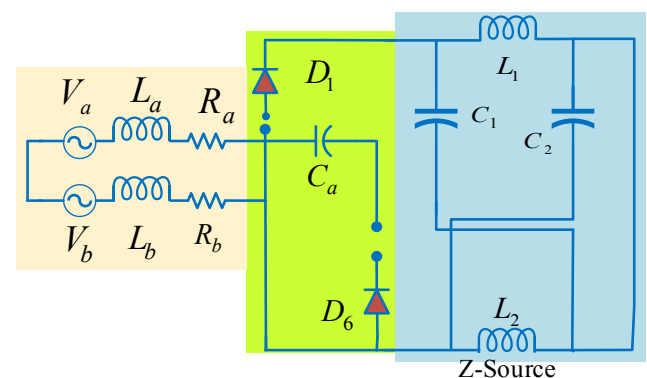

Fig. 5. Equivalent circuit of ZSI for mode-2

From the Fig. 5 the voltage across capacitor is Eq. (4)

$$V_{C1} = V_{C2} = V_C \quad (4)$$

The voltage across inductor Eq. (5)

$$V_{L1} = V_{L2} = V_L \quad (5)$$

When the shoot-through period (T_0) is accommodated during the switching period T, the capacitor and the inductor voltages are equal as in Eq. (6).

$$V_L = V_C \tag{6}$$

The voltage input to the Z- source circuit is given as Eq. (7)

$$V_{DC} = 2V_C \tag{7}$$

The voltage across Inverter Bridge is of Eq. (8)

$$V_i = 0 \tag{8}$$

Mode-3: Fig. 6 shows the ZSI equivalent circuit in typical active state operation. In this mode, an inverter bridge can be run in each of the six historically active states. The voltage during this state is impressed by the load.
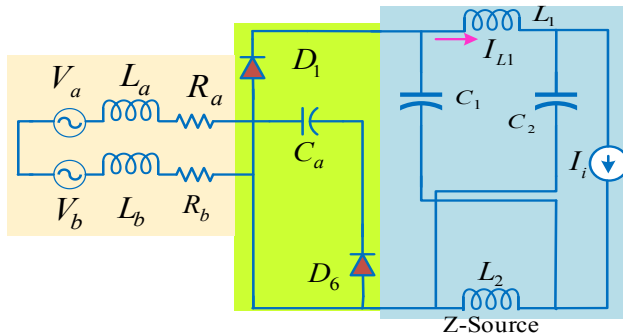
Fig. 6. Equivalent circuit of ZSI for mode-3

The voltage across the inverter when the active time (T_1) is accommodated within the switching period (T) is given by Eq. (9)

$$V_i = V_{DC} - V_C \tag{9}$$

The voltage acquired after input of the Z-source circuit to the inverter bridge is Eq. (10)

$$V_i = 2V_C - V_{DC} \tag{10}$$

The average voltage over the one switching time (T) across the inductor is equal to zero as in Eq. (11).

$$V_L = 0 \tag{11}$$

The input voltage for the inverter circuit is expressed as Eq. (12)

$$V_i = B\frac{V_{DC}}{2} \tag{12}$$

Where,

B is Boost factor and is give by, $B = \dfrac{1}{1 - 2D_0}$

D_0 is the shoot through duty ratio, $D = \dfrac{T_0}{T}$

Rectifier output voltage is given by Eq. (13)

$$V_{DC} = \frac{3\sqrt{3}}{\pi} V_m \tag{13}$$

Eq.(9) can be rewritten as Eq. (14)

$$V_i = \frac{3\sqrt{3}}{2\pi} V_m B \tag{14}$$

The rms output voltage of the ZSI can be expressed as Eq. (15)

$$V_{ac} = \frac{3\sqrt{6}}{2\pi} V_m G \tag{15}$$

where G is voltage gain

Implementation of PWM Schemes for ZSI

The same PWM algorithms for VSI may be utilized for ZSI with minor adjustments. The shoot-through period distribution in the switching waveforms of the standard PWM concept controls the output voltage of ZSI [8]. The controllable ac output voltage, voltage stress across switching devices, and the harmonic profile of the ac output characteristics are all dependent on how the control algorithm inserts the shoot-through period. Several control strategies have been proposed in recent years. There are two main types of MBC: THIPWM and MSVPWM. Fig. 7 displays the maximum boost control PWM technique with THI control. In this PWM method, the three-phase reference voltages are injected with a 1/6th harmonic component of the fundamental component. The R phase V_r peaks at 3/2 M, while the Y phase V_y peaks at -3/2 M. Thus, two straight lines, V_p and V_n, regulate the shot through time with 16% third harmonic injection. The shoot-through pulses' amplitude and breadth vary with PMSG voltage fluctuations.

The maximum shoot through duty ratio obtained by this scheme can be written below

$$D_0 = \frac{2\pi - 3\sqrt{3}\pi}{2\pi}$$

Important expressions in this PWM method are given below:

Voltage Gain, $\qquad G = M\left(\dfrac{1}{1 - 2D_0}\right)$

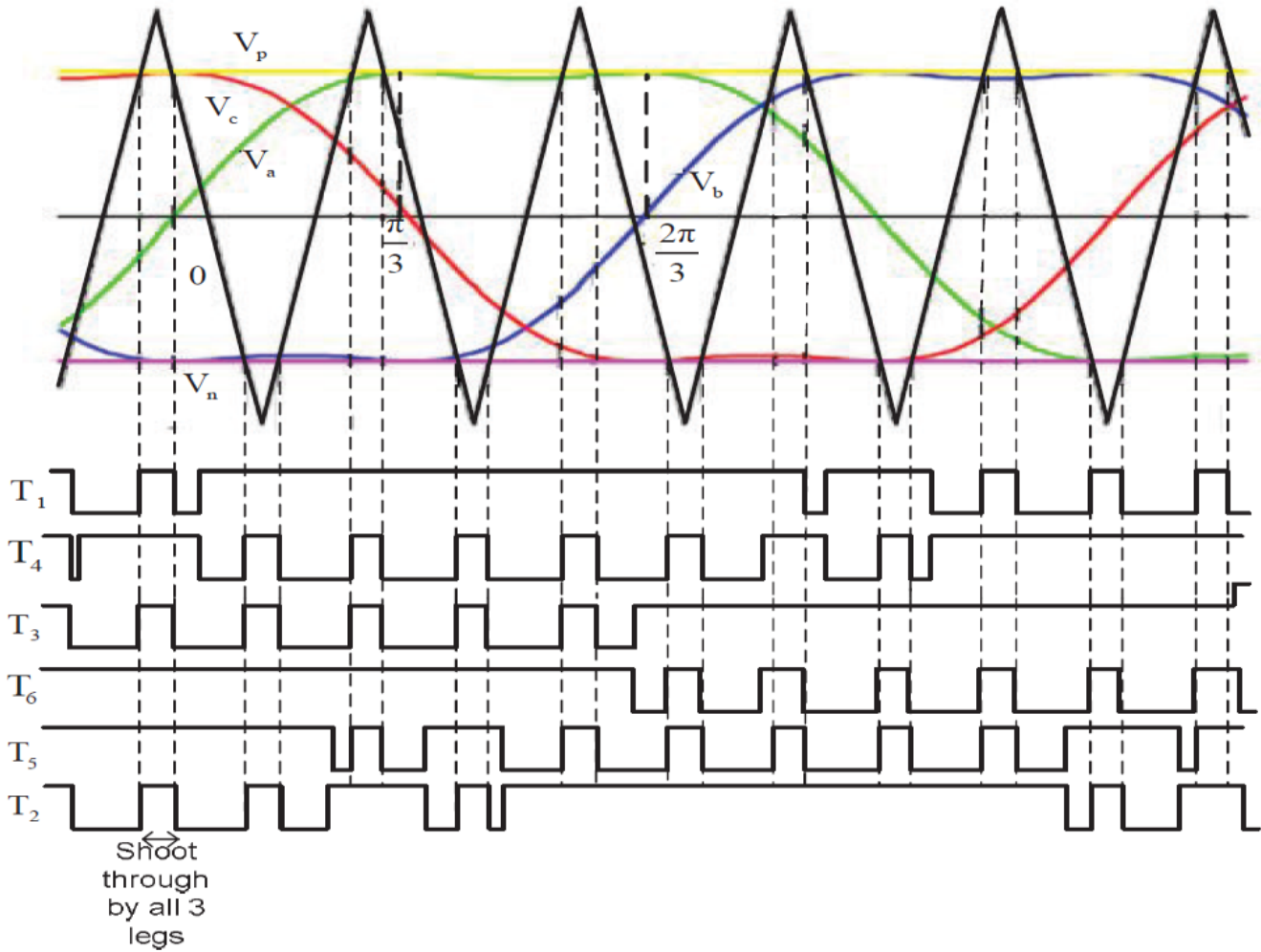Modulation Index, $\qquad M = \dfrac{\pi G}{3\sqrt{3G - \pi}}$

Fig. 7. Carrier based PWM Scheme with third harmonic injection

Boost Factor, $$B = \frac{3\sqrt{3G - \pi}}{\pi}$$

The ac output voltage of the ZSI with this scheme is given as

$$V_{ac} = \frac{9\sqrt{6}}{2\pi} * \frac{\sqrt{3M.B - \pi}}{\pi} V_{rms} M$$

Where V_{rms} is per phase PMSG generated voltage

3. Control Strategy of Proposed Topology for Mppt Implementation

To achieve better performance of AC line voltage control of ZSI and PMSG generated voltages are sensed and compared to predefined reference values. The boost factor is determined by the time duration of the shoot and the desired output voltage. The boost factor is the control variable of the ZSI voltage and the modulation index for that of load voltage. The complete controller block diagram for a DDWECS with PMSG and ZSI is shown in Fig. 8. During fluctuating voltage conditions, the ZSI DC connection voltage is modified by periodic shoot insertion through states following the PMSG generated voltage. Based on the PMSG voltage variations via the voltage feedback loop, the control

of dc connection voltage is carried out. The DC connection voltage is calculated and compared in this mode and error is processed to change the shooting period by state. The modulation index and the boost factor that relies on the shoot through time inserted in the traditional switching waveform are the two parameters to be adjusted to get the desired output AC voltage in the ZSI.

4. Results and Discussion

This section describes the MATLAB/ SIMULINK tool used to model the horizontal axis wind turbine and permanent generator equations. At a cut in wind velocity of 3m/s, the direct-drive permanent magnet generator begins to create electricity and ceases at a cutout wind velocity of 12m/s. Fig. 9 depicts the relationship between turbine speed and time for different wind speeds.

Fig. 10 shows the simulated waveforms of wind turbine speed and produced voltage for various values of wind velocity. 116 rpm @ 6m/s, the wind turbine generator generates 182 Volts from the permanent magnet generator due to the rotor's increased number of poles. At a wind speed of 10m/s, the voltage is 275V. At 3m/s and 10m/s, the produced voltage has a frequency of 7Hz and a maximum of 25Hz, respectively
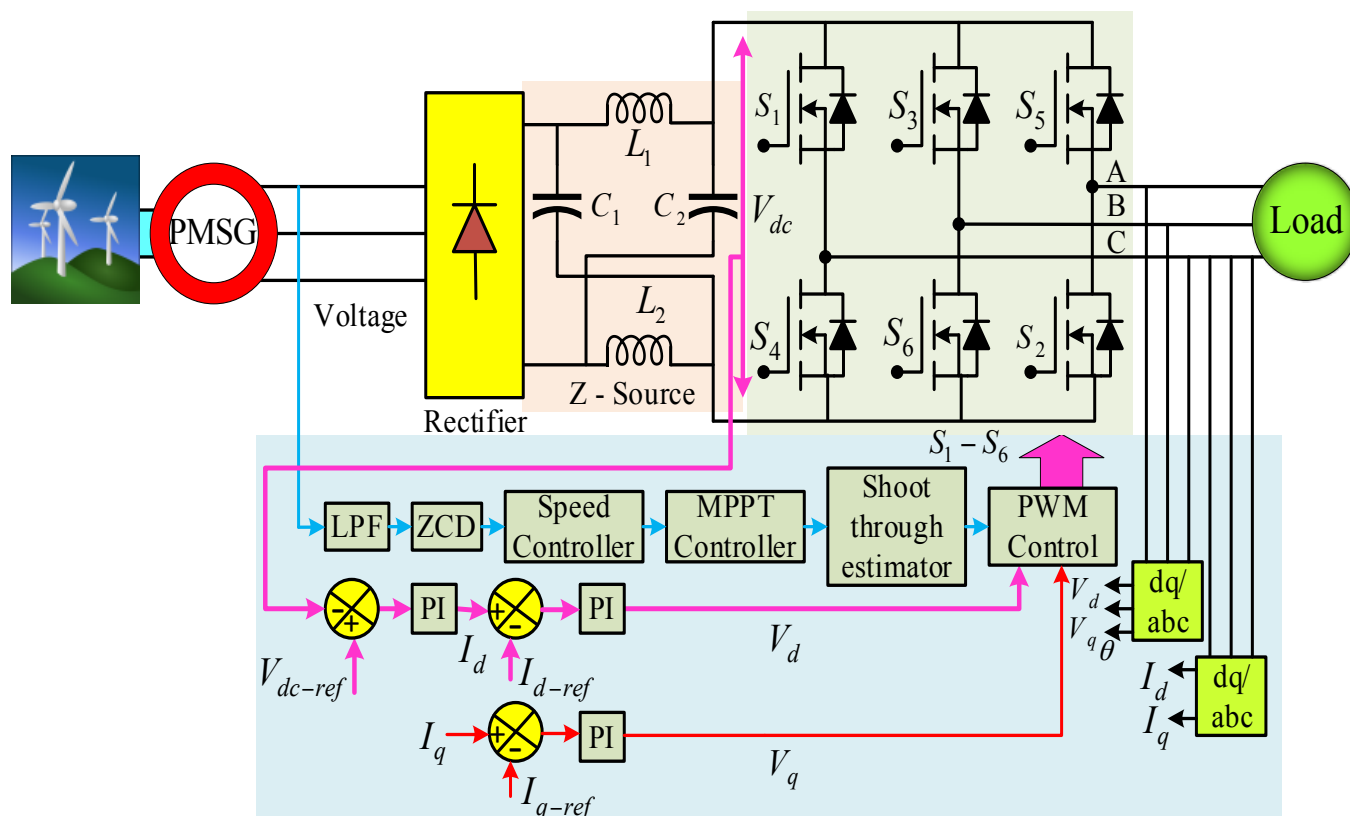
Fig. 8. Control strategy of ZSI- DDWECS for MPPT implementation

In the MATLAB/SIMULINK program, the two-stage power converter, which consists of the rectifier, the ZSI, and the MPPT sensor less controller, is modeled and simulated. When different wind speeds were used, the model was simulated and the results were examined. The results of the simulations for various wind velocity settings are shown in Table. 1, for reference. It is clear from the table that the PMSG cannot capture the whole power spectrum. The amount of energy derived from wind grows in tandem with the increase in wind velocity. The entire power of the wind turbine, on the other hand, cannot be produced without the use of the MPPT controller.
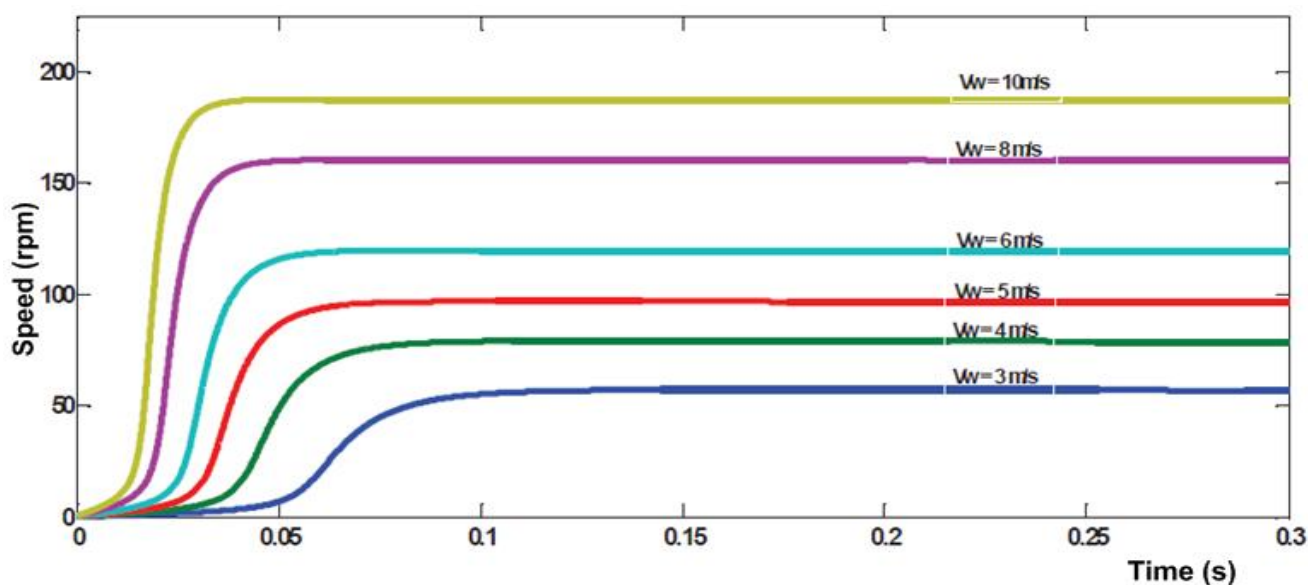
Fig. 9. Wind turbine speeds for various wind velocity conditions
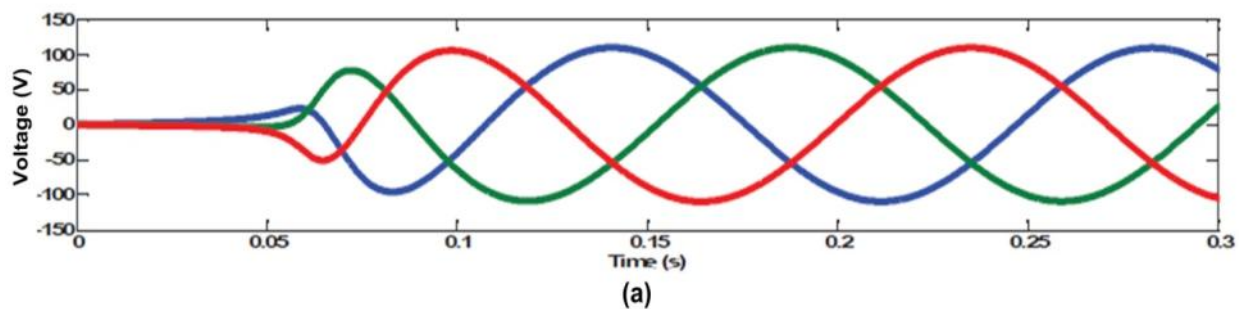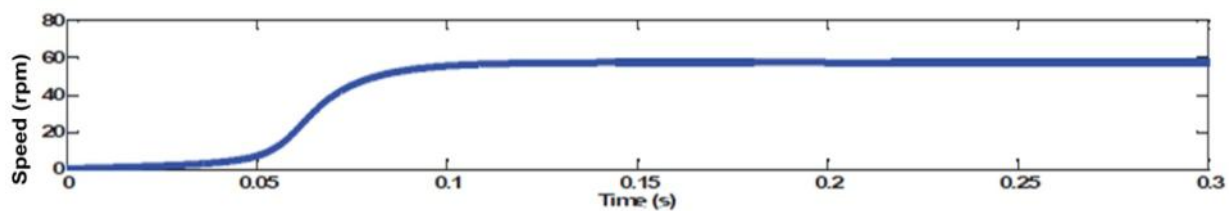
(a)
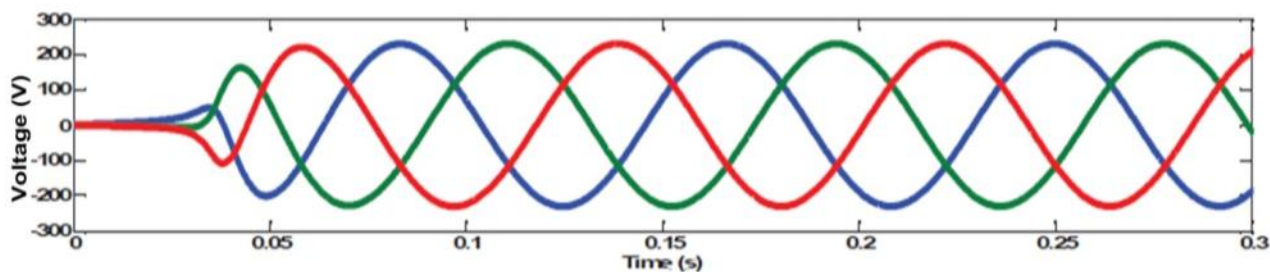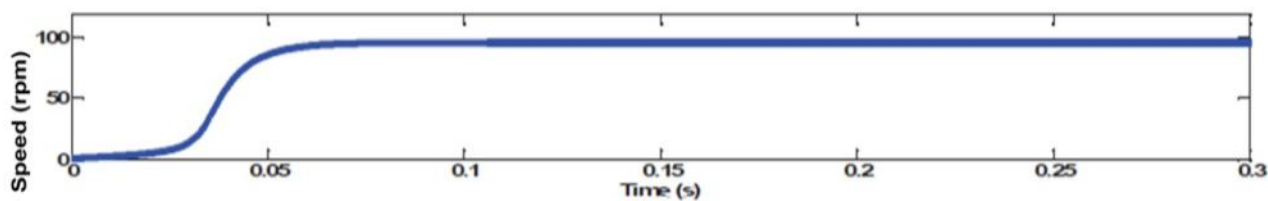
(b)
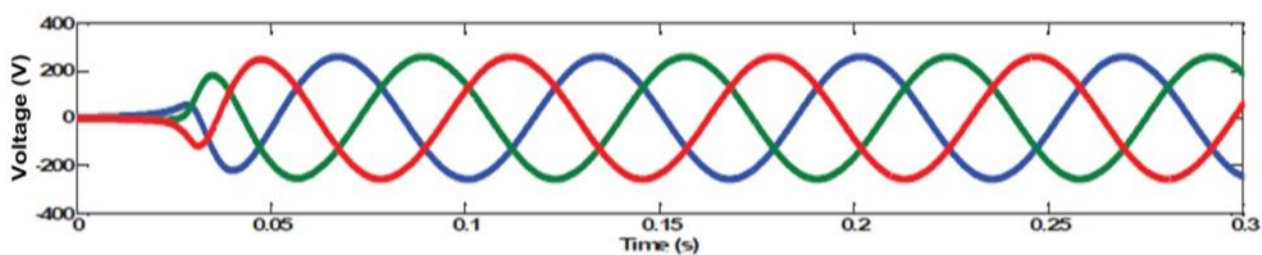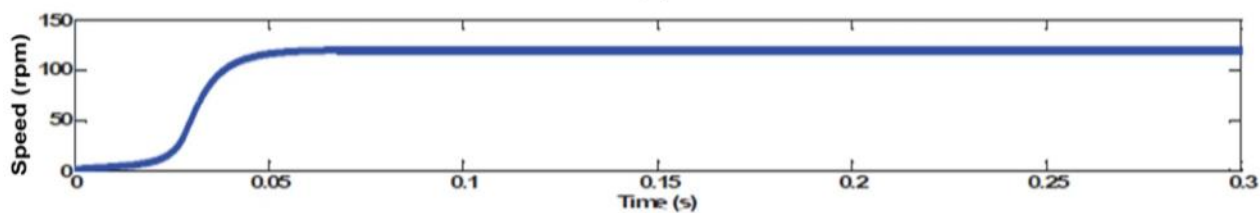
(c)
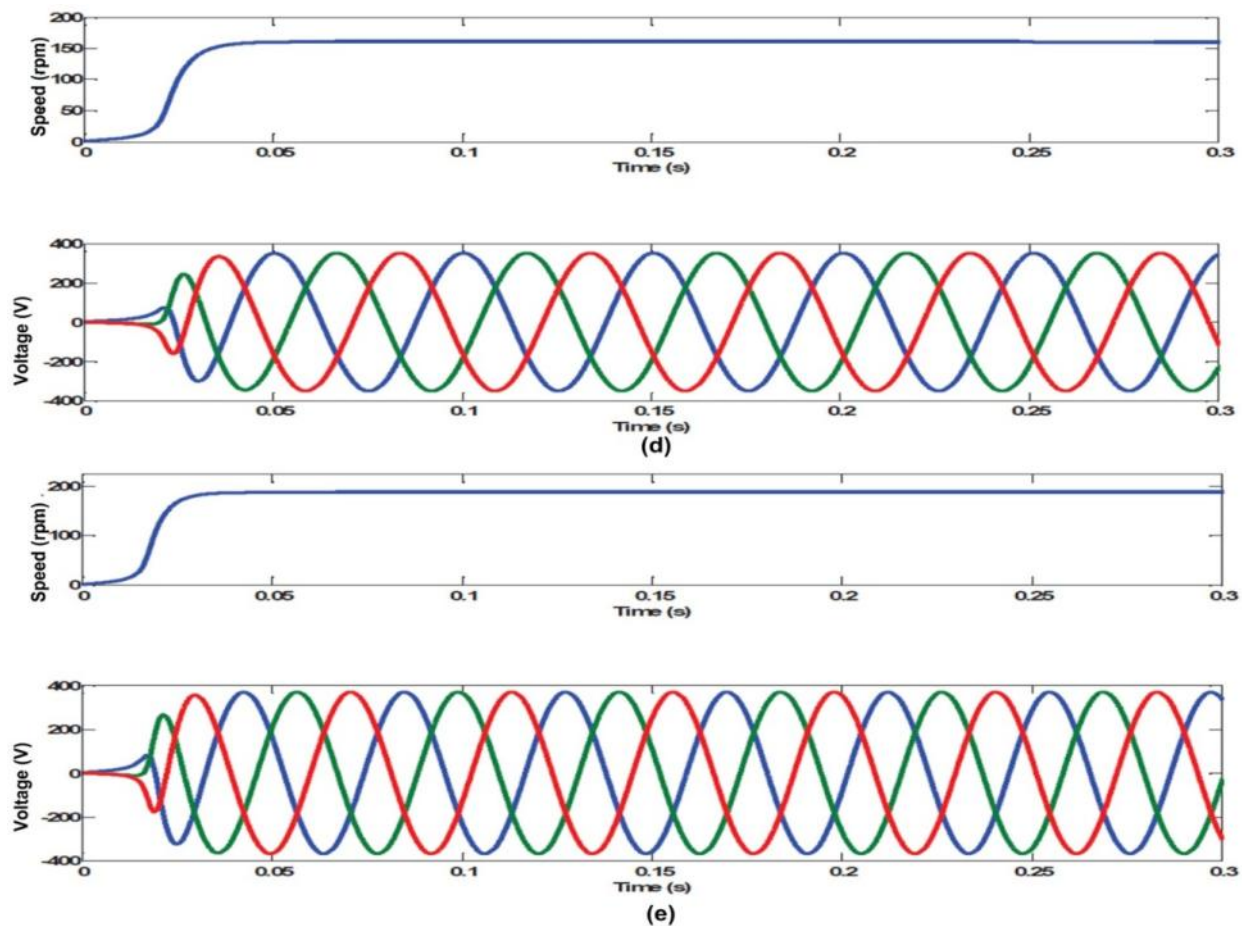
Fig. 10. Simulated waveforms of turbine speed and PMSG generated voltage for wind velocity of (a) 3m/s (b) 5m/s (c) 6m/s (d) 8m/s (d) 8m/s and (e) 10m/s
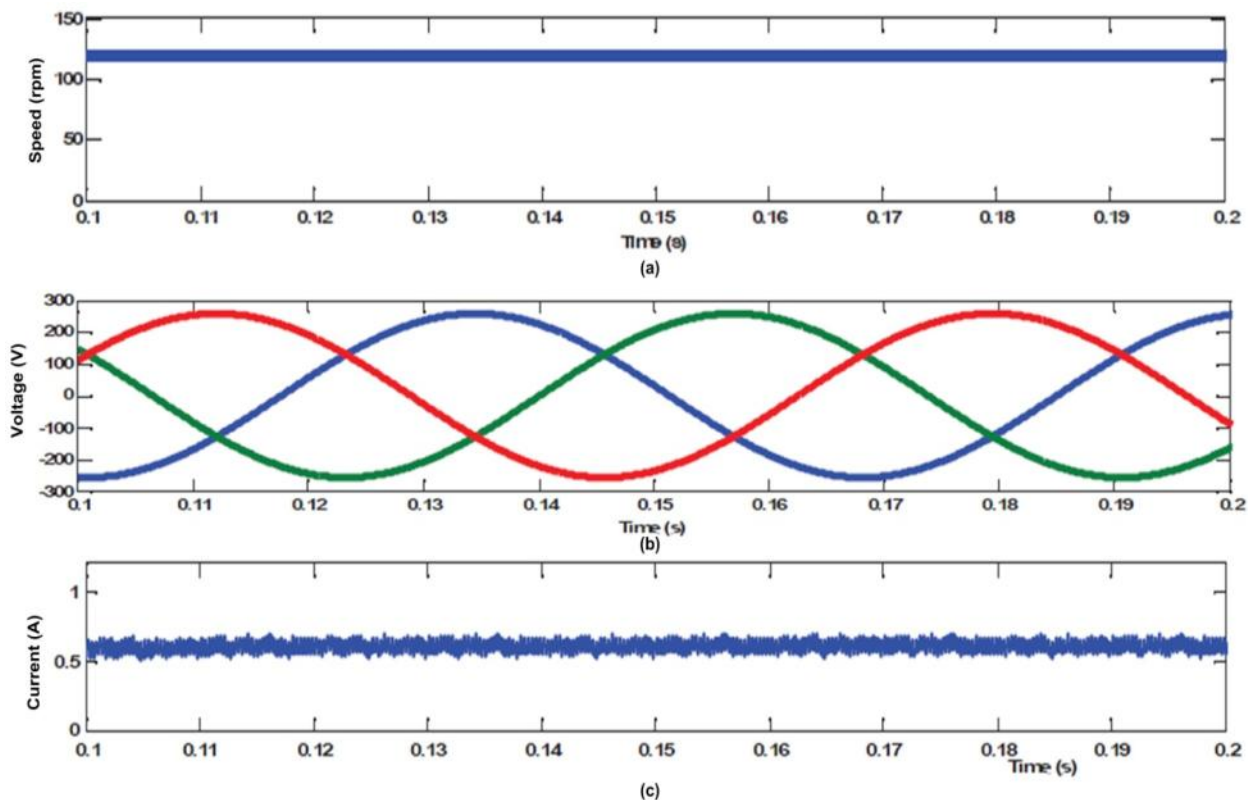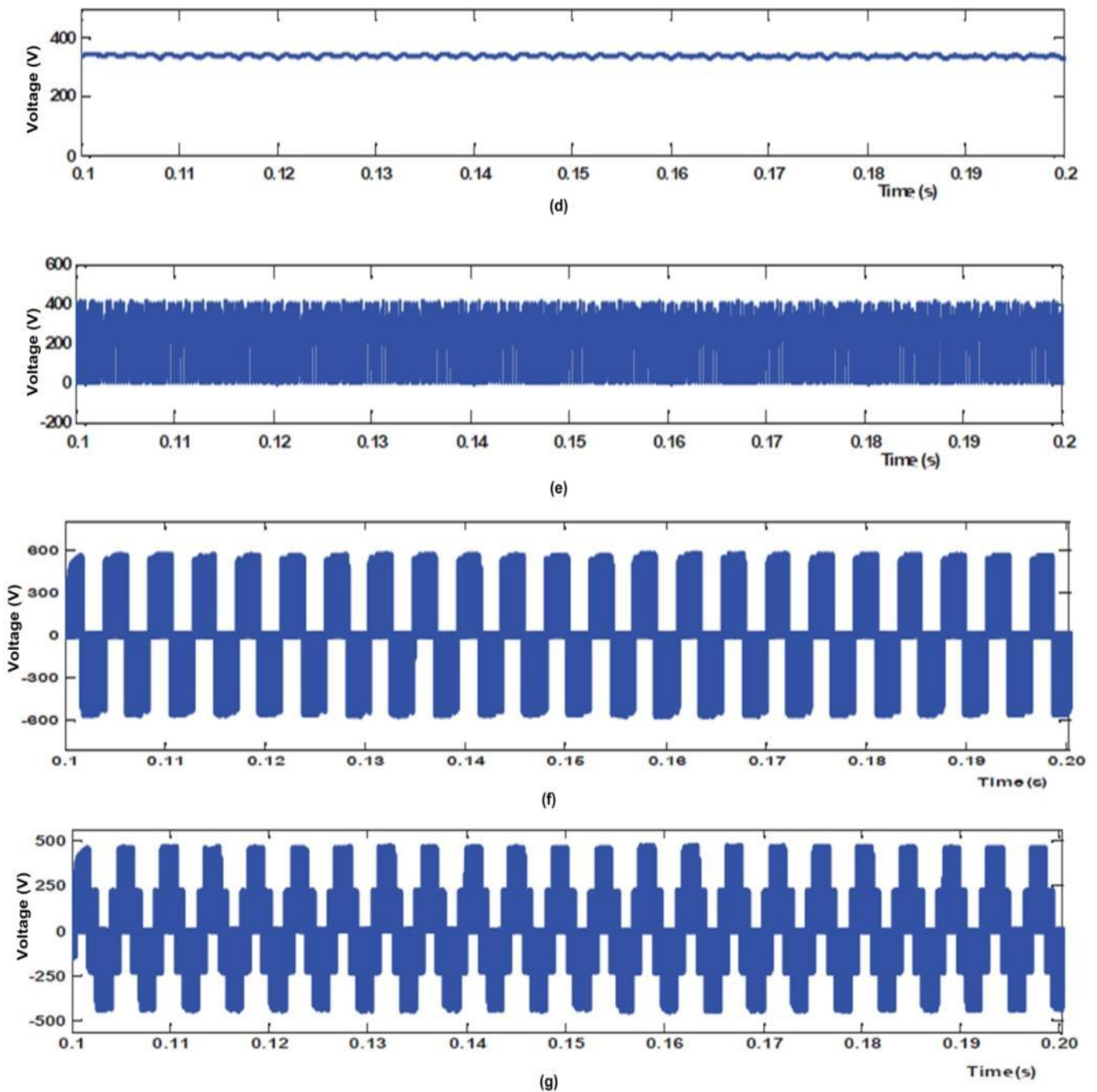
Fig. 11. Simulated results of proposed DDWECS with ZSI controlled by THIPWM Scheme (a) Wind turbine speed (b) PMSG generated voltage (c) Inductor current (d) Capacitor voltage (e) DC link voltage (f) Line voltage and (g) Phase voltage

Fig. 11 shows the simulated waveforms of the proposed DDWECS with ZSI controlled by the THIPWM scheme. The model is simulated for a wind velocity of 6m/s turbine speed of 116rpm, generated voltage of 182 Volts, the load of 0.5kW shoot through duty ratio of 0.3 and modulation index of 0.7. The DC line voltage of 400V obtained for the input voltage of 182V AC with a shoot through duty ratio of 0.3 is as shown in Fig. 11(e). ZSI is controlled by modified space vector pulse width modulation to predict its performance which is analyzed for a wind velocity of 6m/s and generator speed of 116rpm and

generated voltage of 182V. The shoot through duty ratio D_0 0.3 and modulation index M 0.7 are selected to obtain the desired value of space vector pulses for ZSI.

The shoot through placement in the zero states is varied according to PMSG generated voltage. Fig. 12 (c) to Fig. 12 (e) show the inductor current, capacitor voltage and DC link voltage waveforms respectively. When compared with the THIPWM scheme the voltage and current ripples magnitude are reduced and hence switching voltage stress is reduced significantly.
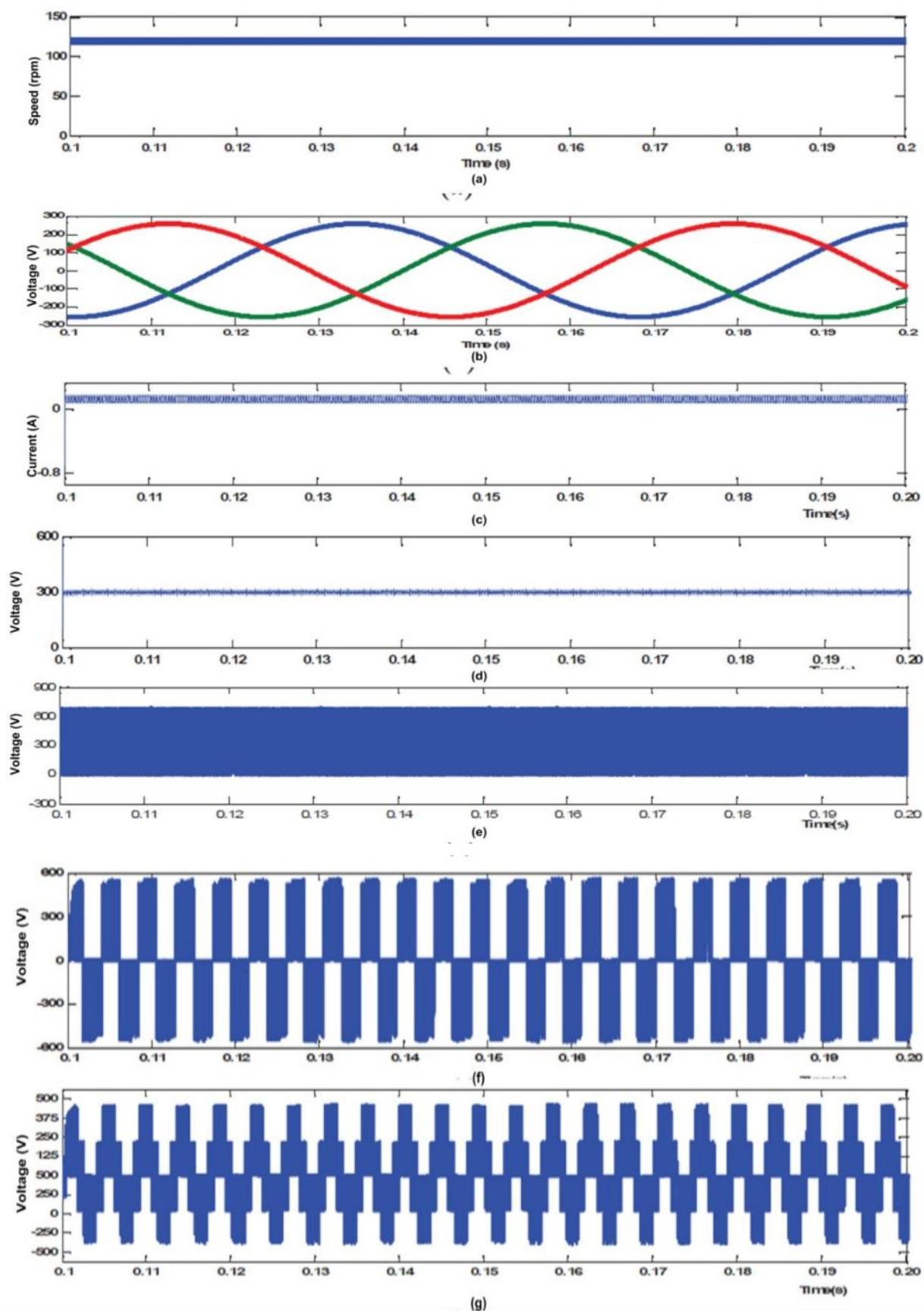
Fig. 12. Simulated results of proposed WECS with ZSI controlled by MSVPWM scheme (a) Wind turbine speed (b) PMSG generator voltage (c) Inductor current (d) Capacitor voltage (e) DC link voltage (f) Line voltage and (g) Phase voltage
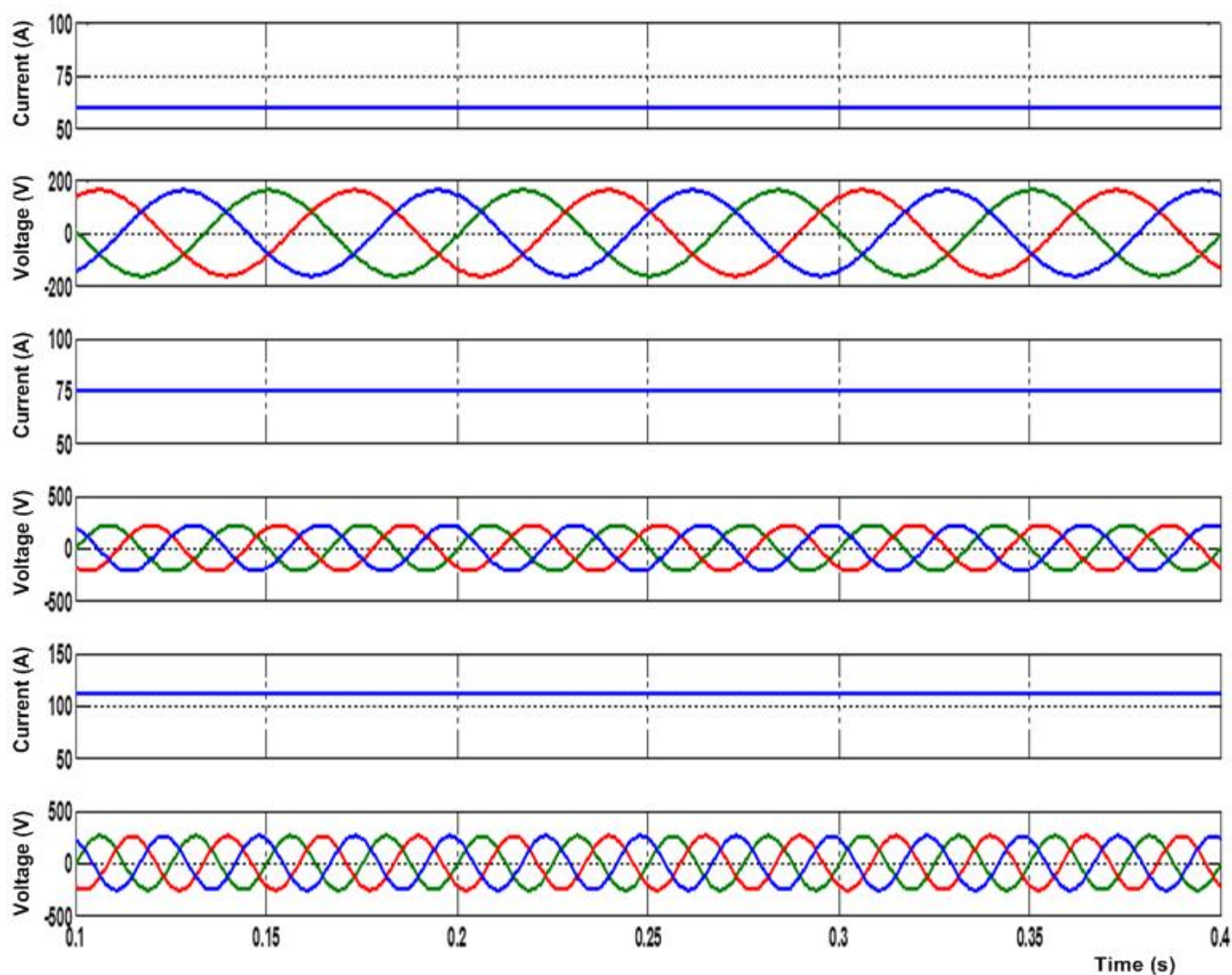
Fig. 13. Voltage and current waveforms of PMSG at different velocities (a) at 5 m/s, (b) at 10 m/s, (c) at 12 m/s

DDWECS simulations using an MPPT controller are displayed in Table 2 as simulated readings. With wind speeds of 5 meters per second and a rotational speed of 99 revolutions per minute, it is noted from the simulation results that 262 watts are the highest power collected. The wind turbine with PMSG's predicted waveforms at various wind velocities is shown in Fig. 13. Fig 14 shows the corresponding ZSI output voltages. From the waveforms, it is identified that the ZSI terminal voltage is maintained constant by timely alternating the shoot-through duty ratio of the ZSI. The proposed wind turbine generator works in the maximum power point region after implementing the MPPT controller. It is noted that the proposed control strategy shows an immediate follow-up of the maximum power point during the rise in wind speed from 6 to 8 m/s, but the traditional algorithm provides a slow response to the maximum power for the change in wind speed. Figs.15 MPPT response for rapid change in wind velocity (a)-(c) demonstrates the complex reaction to abrupt changes in wind velocity of the proposed WECS. The active and reactive powers fluctuate and eventually achieve a stable state. The sensor less MPPT controller determines the optimal rotor speed to monitor maximum power and maintain the output voltage. The analysis and simulation have shown that the proposed MPPT controller has satisfied the objective of extracting maximum power at any wind speed. The proposed MPPT algorithm is 0.05sec faster than the existing method and also the power extraction is around 25 watts greater than the existing MPPT method.

Table 1. PMSG generated voltages for different wind speeds

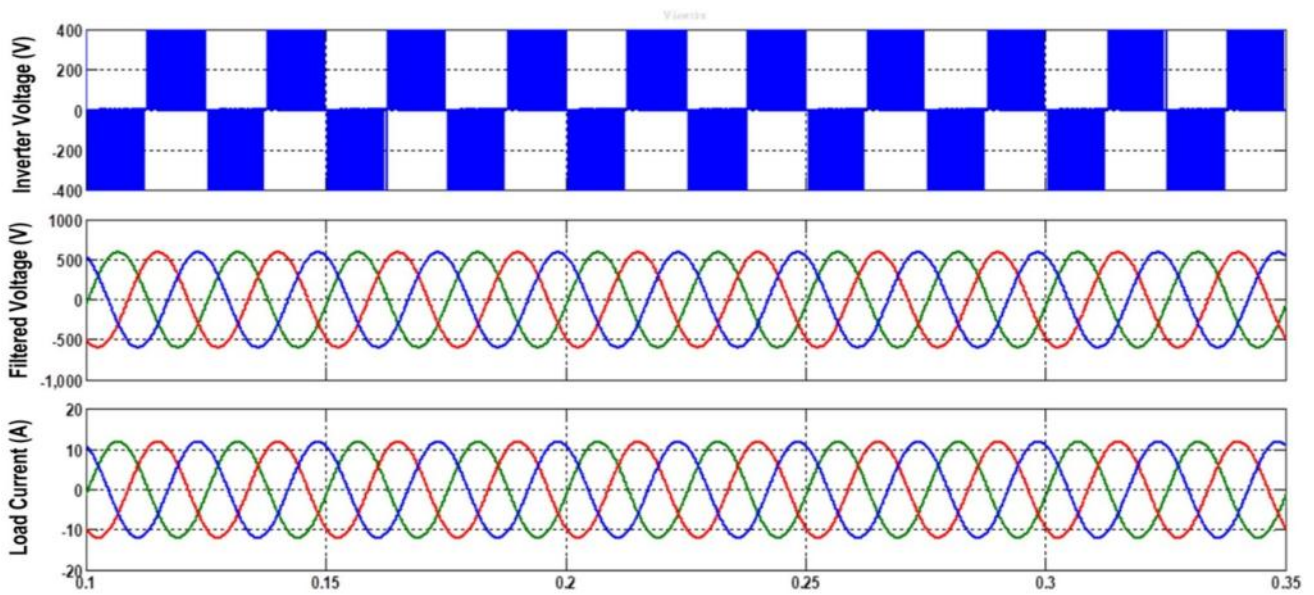| S.No	Wind Velocity (m/s)	PMSG Output voltage (V)	Generator speed (rpm)
1	3	75	68
2	4	136	75
3	5	165	99
4	7	188	120
5	8	245	147
6	10	275	165

Fig. 14. ZSI output voltage and current waveforms (a) Terminal Voltage of ZSI , (b) ZSI Voltage with filter (c) Load current
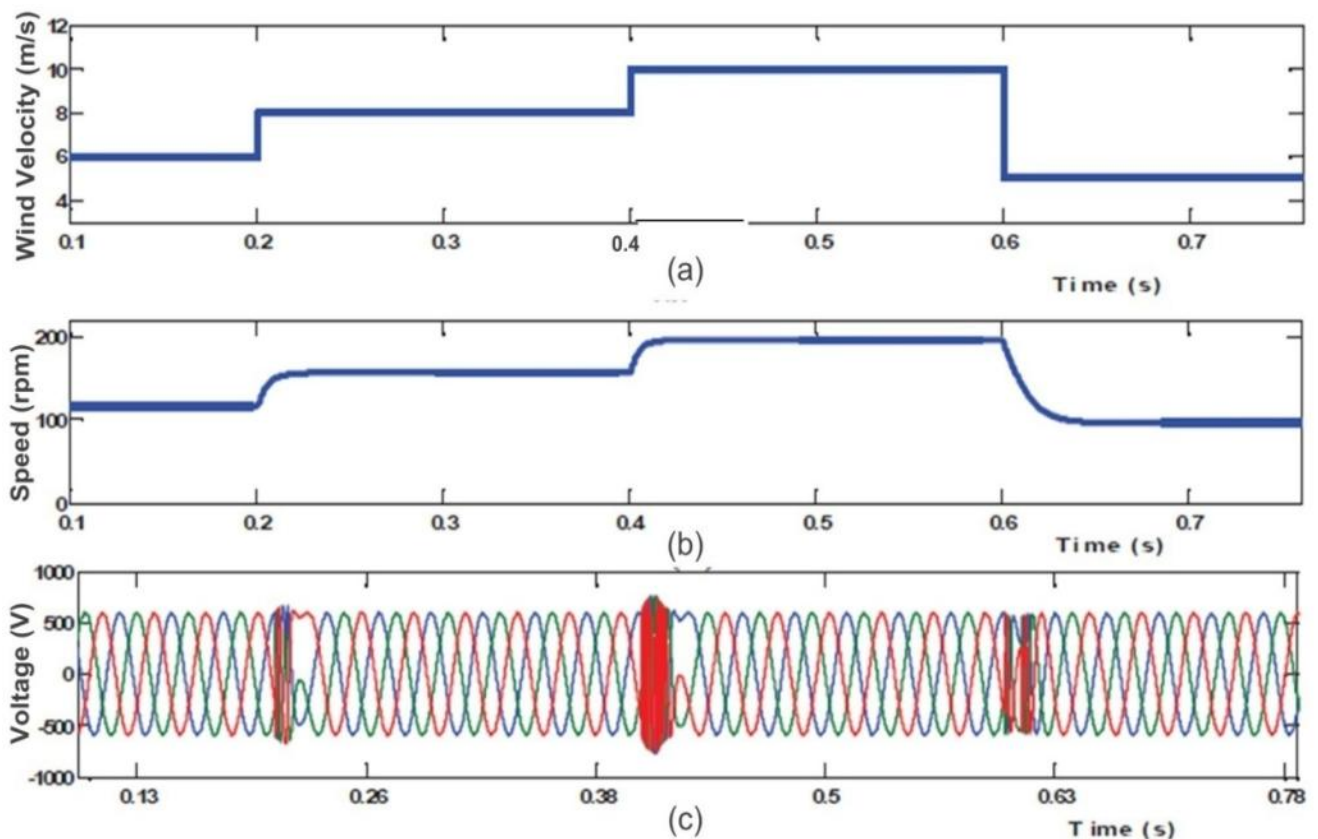

Fig. 15. MPPT response for rapid change in wind velocity (a)Wind velocity (b) Generated speed (c) Filtered ZSI voltage

5. Performance Analysis

The performance analysis of Z-Source Inverter for two types of PWM switching schemes is discussed here. The ZSI performance is analyzed for various values of PMSG generated voltage and different loading conditions. This is done to predict the suitable PWM scheme for ZSI. For comparison analysis, shoot through placement, voltage gain, switching stress and input and output THD are taken into consideration. Table 2 gives the simulation readings of ZSI boost factor and modulation index with three different PWM schemes for different values of PMSG generated voltage.

Table 2. Variation of shoot through duty ratio in three PMSG generated voltages.

S. No	Wind velocity (m/s)	PMSG output voltage (V)	Simple Boost PWM [39]		THI		SVPWM	
			Shoot through duty ratio	Boost factor	Shoot through duty ratio	Boost factor	Shoot through duty ratio	Boost factor
1	3	75	0.34	4.2	0.38	4.5	0.44	4.35
2	4	136	0.26	2.1	0.275	2.3	0.38	2.05
3	5	165	0.16	1.47	0.176	1.55	0.34	1.55
4	7	188	0.146	1.38	0.145	1.40	0.32	1.40
5	8	245	0	0.98	0	1	0	1
6	10	275	0	0.98	0	1	0	1

Table 3. Percentage THD of two different PWM schemes as a function of load power

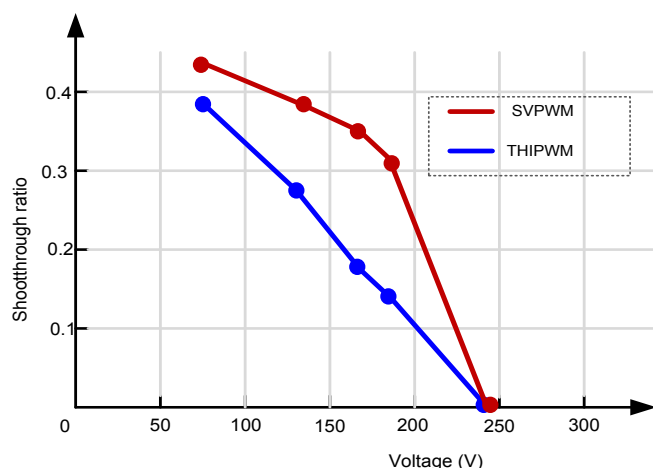| Load power (kW)	Simple Boost PWM [39]		THI		SVPWM	
	Input current THD (%)	Output voltage THD (%)	Input current THD (%)	Output voltage THD (%)	Input current THD (%)	Output voltage THD (%)
0.25	32.2	12.62	25.5	11.55	21.4	7.75
0.5	28.8	14.83	28.9	14.52	26.8	8.42
0.75	33.2	18.04	32.5	17.28	30.9	9.35
1	37.6	18.91	38.5	18.76	34.42	10.56

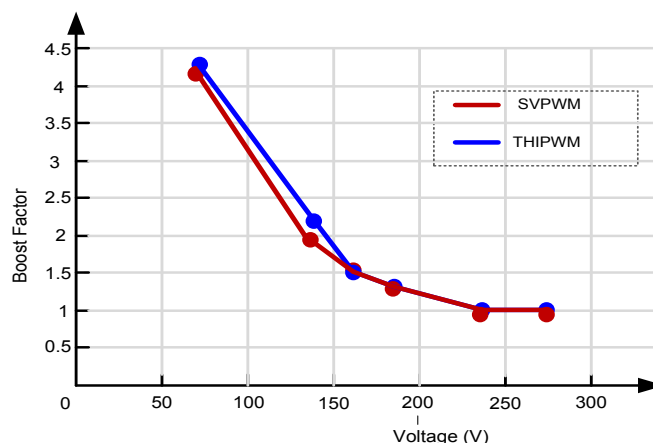**Fig. 16.** Variation of boost factor of ZSI PWM Schemes with variation in PMSG voltage

Fig. 17. Variation of ZSI boost factor with variation in PMSG voltage

The shoot through placement in each PWM scheme is adjusted according to input voltage variation. From Fig 16, it is observed that the variation of shoot through duty ratio D_0 in the THIPWM scheme is lesser than in the SVPWM scheme. Fig 17 shows the corresponding variations of boost factor of ZSI for different values of PMSG generated voltage. Table 3 gives the simulated readings for variations in input current and output voltage Total Harmonic Distortion of Z-Source inverter under different PWM schemes with variations in load power. For 1kW load, the SVPWM based ZSI has the input current harmonic distortion of 34.42% and output voltage harmonic distortion of 10.56% whereas they are 37.6 %, 38.5% and 18.91%, 18.76% in the simple boost PWM THI PWM scheme.

6. Conclusion

This study review provides the maximum power point tracking algorithm for ZSI-based DDWECSs, PMSG with more pole pairs and the basic operating modes of Z-Source inverter for direct-drive wind energy conversion system with its equivalent circuits were briefly explained. To reduce these power conversion stages and to overcome the limitations of conventional systems, the ZSI based DDWECS is introduced. In this system, the distribution of shoot through periods in two PWM control methods with ZSI, such as maximum boost with THI and MSVPWM is carried out. A comparative study is done between the MSVPWM and THIPWM. It is found that the MSVPWM places the shoot through period faster. MSVPWM reduces voltage ripples by 15V and reduces input current THD by

3.6% and output voltage THD by 7.8%. The THI-based ZSI system has decreased switching stress across the power switches for varying shoot through the duration. The MSPVWM is superior at managing THD and shoot-through period than the ZSI.

References

[1] E.P.P.S. Ramos, L.D.O. Assís, R.S. Mena, P.G. Triviño, C.A.G. Vázquez and L.M.F. Ramírez, "Averaged Dynamic Modeling and Control of a Quasi-Z-Source Inverter for Wind Power Applications," IEEE Access, Vol. 9, pp. 114348-114358, 2021.

[2] S.M. Barakati, J.D. Aplevich, and M. Kazerani, "Controller design for a wind turbine system including a matrix converter," Proceedings of IEEE Power Engineering Society, General Meeting, pp. 1-8, 2007.

[3] Z. Wu, Y. Iida and Y. Uematsu, "The flow fields generated by stationary and travelling downbursts and resultant wind load effects on transmission line structural system," Journal of Wind Engineering and Industrial Aerodynamics, DOI:10.1016/j.jweia.2021.104521, Vol. 210, pp. 1-15, 2021.

[4] Y. Zhang, S. Huang, S. Hu, "Ride-through strategy of quasi-Z-source wind power generation system under the asymmetrical grid voltage fault," IET Electric Power Applications. Vol.11, pp. 504–511, 2017.

[5] M. Kesraoui, N. Korichi, and A. Belkadi, "Maximum power point tracker of wind energy conversion system," Renewable Energy, Vol.36, No.11, pp. 2655-2662, 2011.

[6] Z.P. Fang, "Z-Source Inverter," IEEE Transactions on Industry Applications, Vol. 39, No.2, pp. 504-510, 2003.

[7] M.A.H. Navas, G.F. Lozada, J.L.A. Puma, A.J.A. Torrico and A.J.S. Filho, "Battery Energy Storage System Applied to Wind Power System Based On Z-Source Inverter Connected to Grid," IEEE Latin America Transactions, Vol. 14, No. 9, pp. 4035-4042, Sept. 2016.

[8] J. Li, J. Liu, and L. Zeng, "Comparison of Z-Source Inverter and Traditional Two Stage Boost-Buck Inverter in Grid-tied Renewable Energy Generation," IEEE 6th International Conference on Power Electronics and Motion Control, pp.1493-1497, 2009.

[9] K.V. Bhadane, M.S. Ballal, A. Nayyar, D.P. Patil, T.H. Jaware and H.P. Shukla, "A Comprehensive Study of Harmonic Pollution in Large Penetrated Grid-Connected Wind Farm," Mapan - Journal of Metrology Society of India, DOI:10.1007/s12647-020-00407-z, Vol.36, pp. 729–749, 2021.

[10] S. Rajakaruna, Y. Jayawickrama, and N. Maw, "Steady-State Analysis and Designing Impedance Network of Z-Source Inverters," IEEE Transactions on Industrial Electronics, Vol.57, No.7, pp. 2483-2491, 2010.

[11] A. Chub, O. Husev, A. Blinov and D. Vinnikov, "Novel Isolated Power Conditioning Unit for Micro

Wind Turbine Applications," IEEE Transactions on Industrial Electronics. Vol. 64, pp. 5984–5993, 2017.

[12] R. Bharanikumar, "Certain Investigations on Direct Drive Wind Energy Conversion System with Reduced Stage Power Conversion using Z-Source Inverter and Matrix Converter," Ph.D. Thesis, Anna University Chennai, India, 2012.

[13] Ch. R. Reddy, K. Naresh, P.U. Reddy and P Sujatha, "Control of DFIG Based Wind Turbine with Hybrid Controllers," International Journal of Renewable Energy Research, Vol. 10, No. 3, pp. 1488-1500, 2020.

[14] Y. Zhang, Z. Cheng, Q. Chen and Q. Li, "An Enhanced Half-Quasi- Z -Source Inverter for Wind Energy Conversion System with D-PMSG" Complexity, doi:10.1155/2021/9962115, Vol. 2021, pp. 1-15, 2021.

[15] R.I. Putri, F. Ronilaya, I.N. Syamsiana, "Maximum Power Extraction For Hybrid Solar Wind Renewable Energy System Based on Swarm Optimization," International Journal of Renewable Energy Research, DOI: 10.20508/ijrer.v11i3.12161.g8253, Vol. 11, No. 3, pp. 1215-1222, 2021.

[16] Y. Nima, S.H. Fathi, N. Farokhina and H.A. Abyaneh, "THD Minimization Applied Directly on the Line-to-Line Voltage of Multilevel Inverters," IEEE Transactions on Industrial Electronics, Vol.59, No.1, pp.373-380, 2012.

[17] E. Vani and N. Rengarajan, "Reduction of harmonics in a wind power conversion system by the optimal function of a Vienna rectifier and switched inductance Z source inverter," Research Journal of Biotechnology, Vol. 2017, No. 2, pp. 188–198, 2017.

[18] V. Agarwal, R.K. Aggarwal, P. Patidar and C. Patki, "A Novel Scheme For Rapid Tracking of Maximum Power Point in Wind Energy Generation Systems," IEEE Transactions on Energy Conversion, Vol. 25, No. 1, pp. 228-236, 2010.

[19] S.Y. Zhang, S. Huang, D. Luo, "A Novel Half Quasi-Z-source Inverter for Wind Energy Conversion Systems," Zhongguo Dianji Gongcheng Xuebao/ Proceedings of the Chinese Society of Electrical Engineering, Vol.37, pp. 5107–5117, 2017.

[20] Y. Liu, B. Ge, A. Haitham and F.Z. Peng, "A modular multilevel space vector modulation for photovoltaic quasi-z-source cascade multilevel inverter," Twenty-Eighth Annual IEEE Applied Power Electronics Conference and Exposition (APEC), California, pp. 714-718. 2013.

[21] R. Dehghanzadeh, V. Behjat, M. R. Banaei, "Dynamic modeling of wind turbine based axial flux permanent magnetic synchronous generator connected to the grid with switch reduced converter," Ain Shams Engineering Journal, Vol. 9, No. 1, pp. 125–135,2018.

[22] S. A. Saleh and R. Ahshan, "Resolution-Level-Controlled WM Inverter for PMG-Based Wind Energy Conversion System," IEEE Transactions on Industry Applications, Vol. 48, No. 2, pp. 750-763, March-April 2012.

[23] E.P.P.S. Ramos, L. de O. Assis, R. Sarrias, P. García, C.A. García and L.M. Fernández, "Large-Scale Wind Turbine With Quasi-Z-Source Inverter and Battery," 22nd IEEE International Conference on Industrial Technology (ICIT), Valencia, pp. 403-408, 10-12 March 2021.

[24] Y. Li, S. Jiang, G.J. Cintron, and F.Z. Peng, "Modeling and Control of Quasi-Z- Source Inverter for Distributed Generation Applications," IEEE Transactions on Industrial Electronics, Vol. 60, No.4. 2013.

[25] Y. Liu, B. Ge, H. Abu and F.Z. Peng, "Impedance design of 21-kW quasi-z-source H-bridge module for MW-scale medium-voltage cascaded multilevel photovoltaic inverter," 2014 IEEE 23rd International Symposium on Industrial Electronics (ISIE), Istanbul, Turkey, pp. 2490-2495, 1-4 June 2014.

[26] S. Bayhan, H. Abu-Rub and R. S. Balog, "Model Predictive Control of Quasi-Z-Source Four-Leg Inverter," IEEE Transactions on Industrial Electronics, Vol. 63, No. 7, pp. 4506-4516, July 2016.

[27] Y. Li, F. Z. Peng, J. G. Cintron-Rivera and S. Jiang, "Controller design for quasi-Z-source inverter in photovoltaic systems," 2010 IEEE Energy Conversion Congress and Exposition, Atlanta, GA, USA, pp. 3187-3194, 12-16 Sept. 2010.

[28] S. Fitzgerald, R. Kelso, P. Grimshaw, A. Warr, "Observations of the flow experienced by a track cyclist using velodrome, wind tunnel, and potential flow investigations with an instrumented bicycle," Journal of Wind Engineering and Industrial Aerodynamics, DOI:10.1016/j.jweia.2020.104374, Vol. 206, pp. 1-12, Nov 2020.

[29] Y. Liu, B. Ge, F. J. T. E. Ferreira, A. T. de Almeida and H. Abu-Rub, "Modeling and SVPWM control of quasi-Z-source inverter," 11th International Conference on Electrical Power Quality and Utilisation, Lisbon, Portugal, pp. 1-7, 17-19 Oct. 2011.

[30] N. Priyadarshi, S. Padmanaban, D. M. Ionel, L. Mihet-Popa and F. Azam, "Hybrid PV-Wind, micro-grid development using quasi-Z-source inverter modeling and control-experimental investigation," Energies, DOI:10.3390/en11092277, Vol. 11, No. 9, pp. 1-15, 2018.

[31] R. Datta and V. T. Ranganathan, "A method of tracking the peak power points for a variable speed wind energy conversion system," IEEE Transactions on Energy Conversion, vol. 18, no. 1, pp. 163-168, March 2003.

[32] H. Li, and Z. Chen, "Design optimization and site matching of direct-drive permanent magnet wind power generator systems," Renewable Energy, Elsevier, Vol. 34, No. 4, pp. 1175-1184, 2009.

[33] P. Fernandez, F.D. Reijedo, A. Vidal, A.G. Yepes, J. Malvar, O. Lopez, A. Nogueiras and J.D Gandoy "A

Signal Processing Adaptive Algorithm for Selective Current Harmonic Cancellation in Active Power Filters," IEEE International Symposium on Industrial Electronics, Vol. 56, pp. 2946- 2951, 2010.

[34] F. Wang, Y. Zhang and Y. Shen, "Comparison of different structures for variable speed constant frequency wind power generator," 2008 International Conference on Electrical Machines and Systems, Wuhan, pp. 2234-2238, 17-20 Oct. 2008.

[35] D. Ghaderi, S. Padmanaban, P. K. Maroti, B. Papari, J. and B. Holm-Nielsen, "Design and implementation of an improved sinusoidal controller for a two-phase enhanced impedance source boost inverter," Computers and Electrical Engineering, DOI: 10.1016/j.compeleceng.2020.106575, Vol. 83, ,pp. 1-18, May 2020.

[36] D.C. Meena, M. Singh, A.K. Giri, "A Modified NLMS Control Algorithm for Coordinated Operation in Three-Phase Wind-Energy Conversion System", International Journal of Renewable Energy Research, DOI: 10.20508/ijrer.v11i4.12454.g8344, Vol. 11, No. 4, pp.1621-1629, 2021.

[37] V. F. Pires, D. Foito, A. Cordeiro and A. J. Pires, "A Bidirectional DC-DC Converter to Interlink Unipolar and Bipolar DC Microgrids," 2021 9th International Conference on Smart Grid (icSmartGrid), Setubal, Portugal, pp. 37-42, 29 June-1 July 2021.

[38] A. Radwan, I. Khouri and X. Jiang, "Modeling and Control of Current-Source Converter-Based AC Microgrids," 2020 IEEE 8th International Conference on Smart Energy Grid Engineering (SEGE), Oshawa, Canada, pp. 97-101, 12-14 Aug. 2020.

[39] A. Belkaid, I. Colak, K. Kayisli and R. Bayindir, "Design and Implementation of a Cuk Converter Controlled by a Direct Duty Cycle INC-MPPT in PV Battery System," International Journal of Smart Grid, DOI: 10.20508/ijsmartgrid.v3i1.37.g42, Vol 3, No 1, pp. 1-7 , 2019.

[40] V. Mishra, R.D. Shukla, P. Gupta, "An Approach towards Application of Semiconductor Electronics Converters in Autonomous DFIM Based Wind Energy Generation System: A Review," International Journal of Smart Grid, DOI: 10.20508/ijsmartgrid. v3i3.69.g61, Vol 3, No 3, pp. 1-11 , 2019.

[41] M. Quraan, Q. Farhat and M. Bornat, "A new control scheme of back-to-back converter for wind energy technology," 2017 IEEE 6th International Conference on Renewable Energy Research and Applications (ICRERA), San Diego, USA, pp. 354-358, 5-8 Nov 2017.

[42] K. Kajiwara, R. Daimon, Y. Ohta, A. Segami, N. Matsui and F. Kurokawa, "Voltage Balance of Multiconnected Half Bridge Converter," 2021 10th International Conference on Renewable Energy Research and Application (ICRERA), Istanbul, Turkey, pp. 439-442, 26-29 Sept. 2021.

Improvement of Power Quality in Grid Integrated Smart Grid Using Fractional-Order Fuzzy Logic Controller

D Chandra Sekhar* iD , PVV Rama Rao**‡ iD , R Kiranmayi*** iD

*Department of EEE, JNTUA, Ananthapuramu, India

**Department of EEE, MVSR Engineering College, Hyderabad, India

*** Department of EEE, JNTUA, Ananthapuramu, India

(dcsekhar@mrec.ac.in, pvvmadhuram@gmail.com, kiranmayi0109@gmail.com)

‡
D Chandra Sekhar; dcsekhar@mrec.ac.in

Abstract- This paper investigates a fractional-order Fuzzy logic controller (FOFLC) for improving the performance of the Smart Grid. The proposed FOFLC improves the steady-state and transient performance of the solar-wind-grid integrated system. Fuzzy maximum power point tracking (MPPT) algorithm-based DC-DC converters are used to get the most power out of solar panels. A permanent magnet synchronous generator (PMSG) is used to extract the most power from the wind. An intelligent FOFL controller controls back-to-back voltage source converters (VSC) to optimize both power generation. This proposed methodology was implemented by optimal power converters, which improved the overa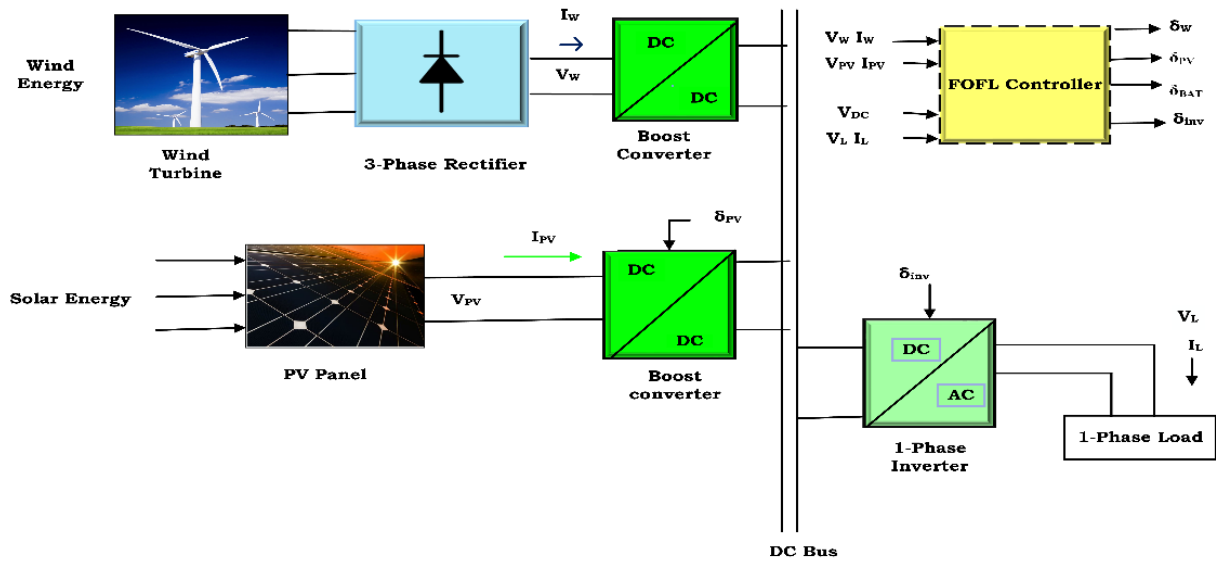ll system performance to an acceptable level. The simulation results show that the proposed control method works well for a wide range of smart grid modes and non-linear fault scenarios. From the simulations it is clear that the current's harmonic content is reduced by 1.04% to 0.67% and voltage harmonics is reduced 8.31% to 0.31% in FOFLC in contrast to ANFIS controller.

Keywords FOFLC; Maximum power point tracking, Power quality, PV-wind-grid integration, MATLAB/Simulink,

1. Introduction

In recent years the usage of renewable energy sources (RES) is popular over traditional fossil fuel-based energy sources like hydro and thermal. RES sources are free from air pollutants (eco-friendly), with more reliability and optimum cost. To extract maximum power from solar different MPPT algorithms are proposed in the literature such as perturb and observe [1], incremental conductance (IC), and fuzzy intelligent Maximum power point tracking (MPPT) [2]. In this paper to get maximum power from photovoltaic (PV), the fuzzy MPPT technique is adopted. Maximum power extracted from the wind with tip-speed ratio control, lower relationship-based, perturbation and observation (P&O), hybrid control [3] and intelligent control strategies [4], [5] based techniques like neural, fuzzy, and adaptive-neuro fuzzy interfaced system (ANFIS). Stand-alone integrated hybrid power sources [6], [7] are modeled and controlled well to satisfy the load demand [8]–[10]. It is further extended to dynamic energy management between the RES sources is proposed with conventional control techniques.

After doing a literature review, it was discovered that ANFIS is a popular controller due to its simplicity. As previously stated, it is frequently employed in power system applications. The filter parameter is the most difficult aspect of the ANFIS design. In real-time practice, this filter

parameter is tuned based on the user's requirements. We know that the advanced control state feedback control strategy is more versatile, allowing for optimal design [11]–[14].

A blend of neural and fuzzy rationale procedures offers to take care of issues and challenges in the plan fuzzy has been executed by [30]. The new methodology in the design of the neural organization is known as a recurrent neural network (RNN) which is an improvement over the current controllers and is actualized in [15] The yield of a dynamic framework is a component of a past yield or previous information or both, thusly recognizable proof and control of dynamic framework are an inborn errand contrasted with a static framework [15]–[20]. The feed-forward neural fuzzy organizations have a significant downside so their application is restricted to static planning issues [21]– [26]. In this way, to recognize dynamic frameworks, repetitive neuro-fuzzy organizations ought to be utilized. A TSK-type intermittent fuzzy organization is intended for dynamic frameworks [27-30].

In light of the audit, it is presumed that the motions in the dynamic power frameworks can be damped by the versatile fuzzy controller. The exploration work is done to check the presentation of FACTS devices for upgrading framework execution. The FOFLC is proposed for the power stabilizer. The PID, as ANFIS controller boundaries are prepared by particle swarm optimization (PSO). The FOFLC can be made as a self-learning controller utilizing an iterative learning

strategy clarified. Developmental calculations are equal and worldwide pursuit methods. Since they all the while assessing numerous focuses in the inquiry space, they are bound to unite toward the worldwide arrangement clarified.

The next sections of this article are composed of the system configuration PV wind integrated grid in section 2. The proposed FOFL control scheme is in section 3. MATLAB environmental-based simulation results are shown in section 4 and the conclusion is given in section 5.

The main objective of the methodology is to implement optimal power converters, which improved the overall system performance to an acceptable level.

A model of a grid-integrated solar-wind smart grid system is shown in Figure 1. Smart grid systems must optimize performance, dependability, and operational efficiency. This study creates a novel model of a smart grid-connected PV/WT hybrid system. A photovoltaic array, wind turbine, asynchronous (induction) generator, controller, and converters are all part of the system. The model is created using the MATLAB/Simulink software suite. Based on the construction of an MPPT, the P&O technique is employed to maximize the generated power. The recommended model's dynamic behavior is investigated in a range of operational circumstances.

2. System Configuration

Fig. 1. Model of proposed PV-wind integrated grid

2.1. Design of Photo Voltaic Cell

The design of a solar cell in general is connected by a I_{LGC} in parallel with a diode and resistors which are associated in anti-parallel which is shown in Figure 2 and control solar cell power.
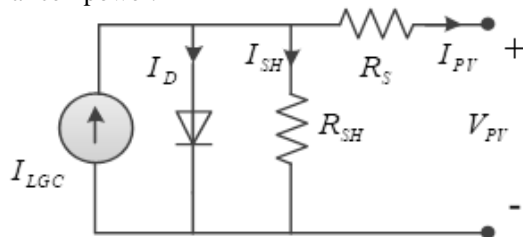
Fig.2. Representation diagram of PV cell

In the figure, PV panels are connected in an array to generate the desired output voltage and current, and the voltage, current are given mathematically;

$$\text{Vseries} = \sum_{j=1}^{n} V_j = V1 + V2 + \cdots \ldots \ldots \ldots + Vn \quad (1)$$

$$V_{seriesoc} = \sum_{j=1}^{n} V_j = V_{oc1} + V_{oc2} + \cdots \ldots \ldots + V_{ocn} \text{ for } I = 0 \quad (2)$$

$$I_{parallel} = \sum_{j=1}^{n} I_j = I_1 + I_2 + \ldots \ldots \ldots + I_n \quad (3)$$

$$V_{parallel} = V_1 = V_2 = \ldots \ldots = V_n \quad (4)$$

By default, bypass diodes are used in solar panels to reduce overvoltage in the system. However, it raises the expense of the system.

2.2. DC-DC Converters

A fuzzy MPPT algorithm is now employed to regulate the switching pattern in order to attain the PV module's maximum power output. The dynamic performance and overall efficiency of the PS network are improved by this fuzzy logic controller (FLC) based direct current (DC) converter, which sends less oscillating voltage to the series VSCs[29].
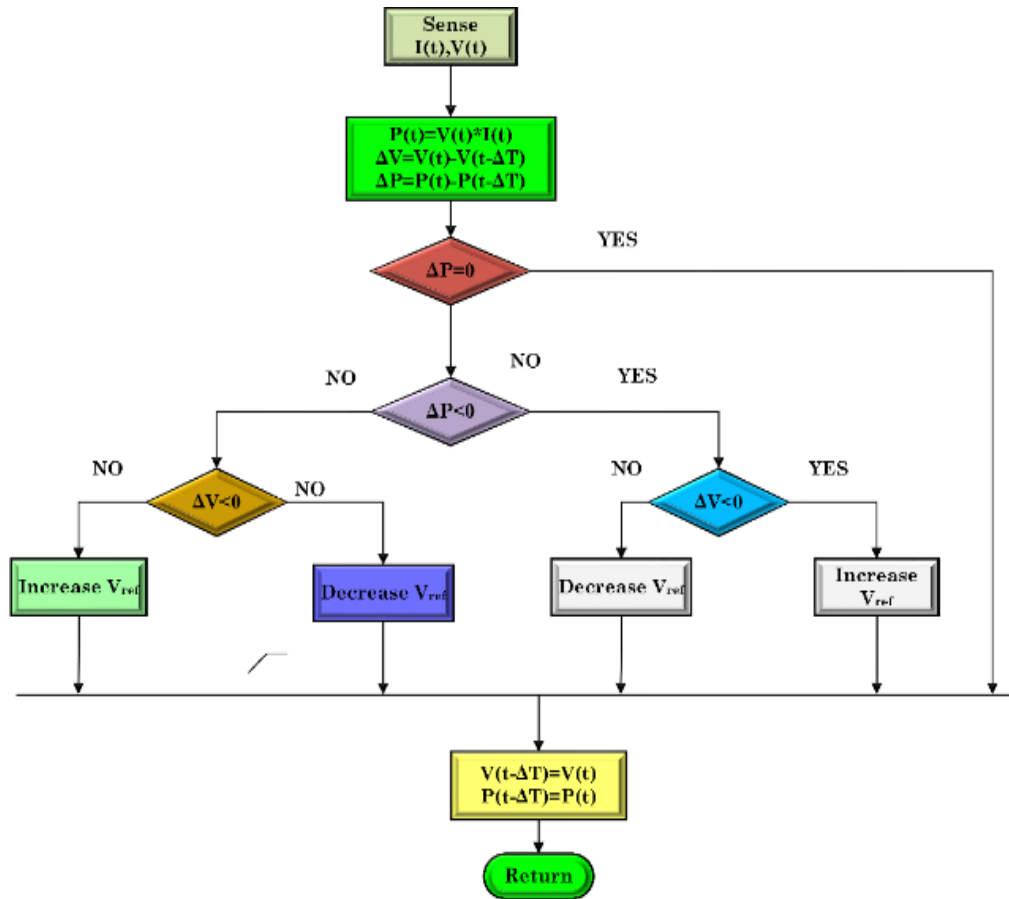
Fig.3. MPPT Algorithm

2.3. *Design of Permanent Magnetic Synchronous Based Wind Energy*

Because the permanent magnet synchronous generator (PMSG) is a brushless DC machine, it has a simple and durable design. When compared to the doubly-fed induction generator (DFIG) generator, it is less expensive. By adjusting terminal voltages of the PMSG's rotor circuit, it regulates the actual, reactive power of the wind energy conversion system (WECS) system. As a result, it regulates the power factor of the entire WECS. PMSG is used to accomplish desired speed management without the need for slip rings[28]. Mathematically PMSG represents in the dq0 axis:

$$Vgq = (Rg + p.Lq).iq + We.Ld\ id \quad (5)$$

$$Vgd = (Rg + p\ Ld).id - We\ Lqiq \quad (6)$$

where Vgd and Vgq represent the stator voltages in the direct and quadrature axis.

$$Te = \frac{3}{2}\ Pn[\varphi + iq - (Ld - Lq)id\ iq] \quad (7)$$

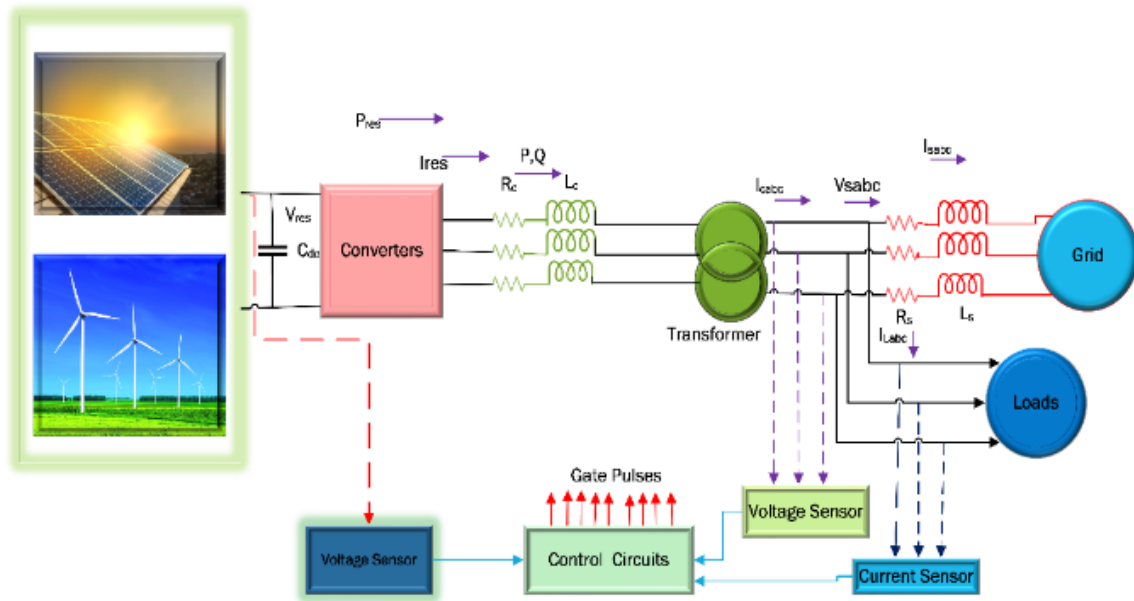If id=0, the electromagnetic torque is described as in (8).

$$Te = \frac{3}{2}\ Pn\psi fiq \quad (8)$$

The dynamic equation of wind turbine is described by (9).

$$J\frac{dwm}{dt} = Te - Tm - F\ Wm \quad (9)$$

3. Control Scheme

The FLC MPPT approach is comparable to the construction of FLC based voltage source inverters (VSI). This blunder is viewed as a set of ill-defined guidelines. Figure 3 shows how to choose rules, membership functions, and defuzzification. The PI control parameters are provided by these fuzzy sets. Table 1 and Figure 4 The set of fuzzy rules is shown in Figure 4(a) error, Figure 4(b) change in error, and Figure 4(c) output membership functions. Fuzzy logic reasoning differs from traditional frameworks such as NB, NS, Z, PB, and PS in both concept and substance. The actual voltage across the coupling's (V_{dcact}) point differs from the reference V_{dc}, resulting in an error that is fuzzified, rectified, and transmitted to the scheme later de-fuzzification.

Fig. 4. Simulation diagram for the proposed model
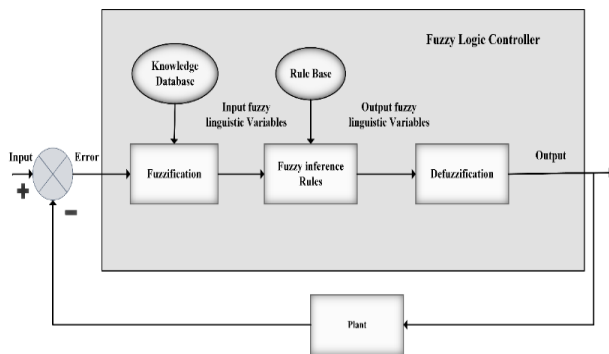
Fig. 5. Fuzzy inference system

Table 1. Rules set by Fuzzy Controller

		Error (E)						
		NB	NM	NS	Z	PS	PM	PB
Change in Error (ΔE)	NB	NB	NB	NB	NS	NS	NS	Z
	NS	NB	NM	NS	NS	Z	PS	PS
	Z	NS	NM	NS	Z	PS	PM	PM
	PS	NS	NS	Z	PS	PM	PB	PB
	PB	Z	NB	PS	PS	PB	PS	PB

3.1. VSI controller design by using FOFLC

3.1.1. Fractional Order Fuzzy Logic Controller (FOFLC)

The FOFLC is very much famous to understand the derivative operator. The numerical expression for FOPI[24] is

$$C(s) = Kp + \frac{Ki}{s^{\lambda}}$$

(1)

λ is range of (0,1).

If $\lambda \geq 2$ is high-order value that is equal to the conventional controller. The F.O is mentioned in (1) is common character of PI controller. To resolve the issues in FOFL controller effective filters can be used. The fitting range is (ω_b, ω_h). The fractional-order function [24] is

$$K(s) = (1 + bs/d\omega b)/(1 + bs/d\omega h)$$

(2)

Where 0<λ<1, s=jw, b>0, d>0, and

$$K(s) = \left(\frac{bs}{d\omega b}\right)^{\lambda}\left(1 + \frac{-ds+d}{ds^2+b\omega hS}\right)^{\lambda}$$

(3)

In frequency range between $\omega b < \omega < \omega h$ by including Taylor polynomial expansion form which occurs

$$K(s) = (bs/d\omega b)^{\lambda}\left(1 + \lambda P(S) + \frac{\lambda(\lambda-1)}{2}p^2(s)\right)$$

(4)

Here $p(s) = \frac{-ds^2+d}{ds^2+b\omega hs}$

(5)

It is initiated that

$$s^{\lambda} = \frac{(d\omega b)^{\lambda b-\lambda}}{\left[1+\lambda P(S)+\frac{\lambda(\lambda-1)}{2}p^{2(s)}\right]}\left(\frac{1+\frac{bs}{d\omega b}}{1+\frac{ds}{d\omega h}}\right)^{\lambda}$$

(6)

Estimated the Taylor polynomial leads to

$$S^{\lambda} = \frac{d\omega b}{b}\frac{ds^2+b\omega hs}{d(1-\lambda)s^2+b\omega hs+d\lambda}\left(\frac{1+\frac{bs}{d\omega b}}{1+\frac{ds}{d\omega h}}\right)^{\lambda}$$

(7)

The FO is defined as

$$S^{\lambda} = \frac{d\omega b}{b}\frac{ds^2+b\omega hs}{d(1-\lambda)s^2+b\omega hs+d\lambda}\left(\frac{1+\frac{bs}{d\omega b}}{1+\frac{ds}{d\omega h}}\right)^{\lambda}$$
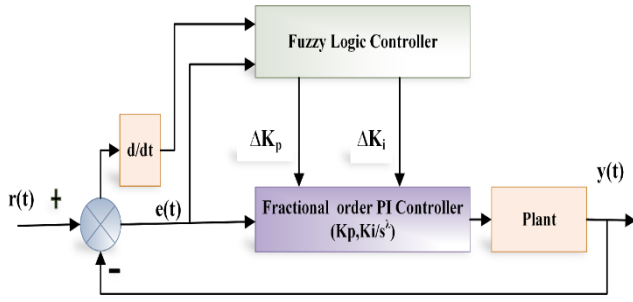
(8)

Equation (8) is balanced only when poles are located on left hand side of complex s-plane.
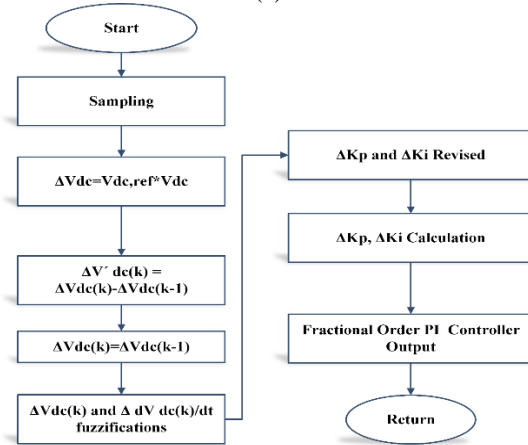
The poles of equation (8) are

$$d(1-\lambda)s^2 + b\omega hS + d\lambda$$

(9)

The negative poles in real part for 0<λ<1.The poles in equation (7) is in range of $(\omega l | \omega h)$.The (6)[th] equation is approximated by uninterrupted -time coherent simulation [24].

$$K(s) = \lim_{n\to\infty} Kn(s) = \lim_{n\to\infty} = -N\frac{1+\frac{s}{\omega k}}{1+\frac{s}{\omega k}}$$
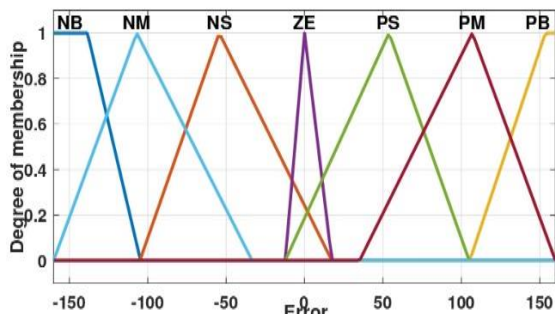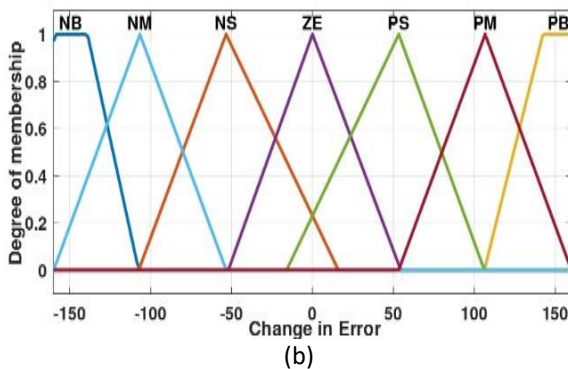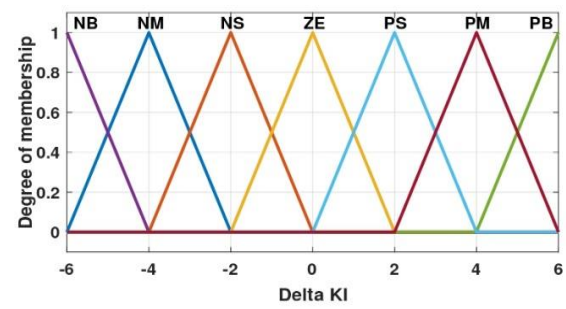
(10)

(a)

(b)

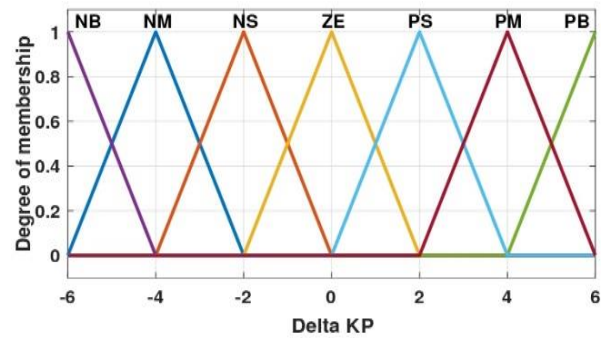**Fig. 6**. (a) Control diagram of FOFL Controller (b) Flowchart

(a)

(b)

(c)

(d)

Fig.7. Membership function for (a) error, (b) change in error, and (c) ΔK_I (d) ΔK_P

The proposed fuzzy logic controller is shown in Figure 5. The proposed FLC has two input membership function, two output membership function which is shown in Figure 7. The gain values kp, ki are computed by using following equations

kp=Kp+ΔKp   (11)

ki=Ki+ΔKi   (12)

Here, kp,ki are initial values of gain FLC and ΔKp, ΔKi are scaling factors from FLC. The proposed control structure is applicable for wind energy management systems where $V_{dc,ref}$, $I_{dc,ref}$ are inputs which are connected to Kp,Ki.The change in gain values can be derived from equations 11& 12 respectively. Zero order band which is connected to FLC is used to approximate constants. The rule table for proposed control strategy is given in Table 1.

4. Simulation Results

The variation of DC link voltage (step response) is momentarily considered at point t=1 sec as shown in Figure 7. The variation of PV-wind power production based on its availability considered as shown in Figure 8. In PV cell irradiance considered as 1 kw/ms up to t=0.3, momentarily it is changed to 0.9 $kW/m\%$, the time between 0.3 s to 0.5 s. At t=0.5 s to 0.6 s irradiance is 0.4 $kW/m\%$ decreases, and between t=0.6 s to t=0.8 s irradiance considered as 0.6 $kW/m\%$. Similar variation of wind power generation is considered as 0.82 m/s to t=2 ms. After wind is increased to 1.1 m/s in time between t=2 s to 4 sec. Further wind decreased

to 0.7 m/s time between t=4 s to t=6 s and wind increases to drastically up to 1.2 m/s from time between t=6 s to t=8 s.

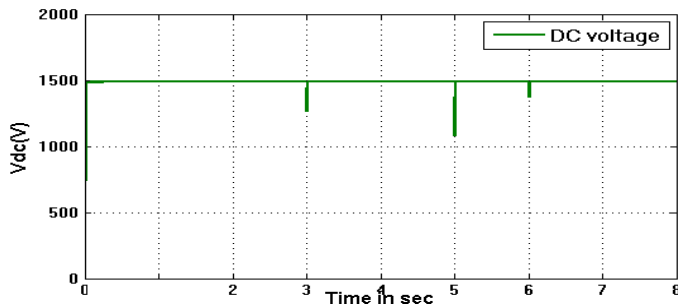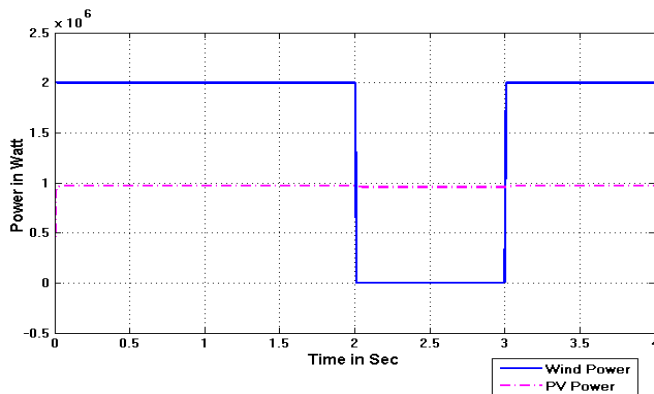Figure.7 Step variation of DC link voltage

Fig. 8. Variation of solar-wind power generation

### 4.1. FOFLC Based VSI Controller Design

The performance of the smart grid with both PV-wind power generation is shown in Figures 9(a) to 9(g) those are PMSG speed, voltage at DC link capacitor, wind power, solar power, grid current, voltage across CPI, VSR modulation respectively. From the Figures 8(b) and 8(f) it is clear that fixed voltages are produced with even variable PV-wind power generation. Effective power management done between grid-PV-wind (smart grid) with employing ANFIS operated VSC converters.
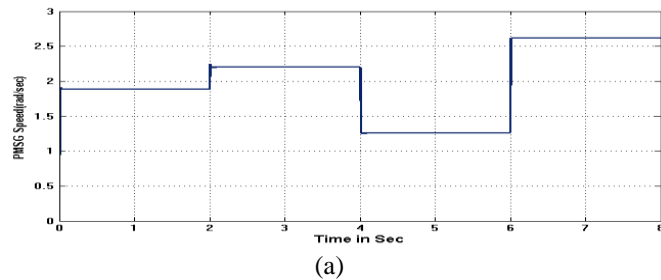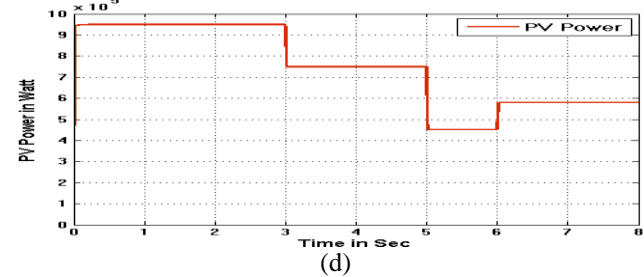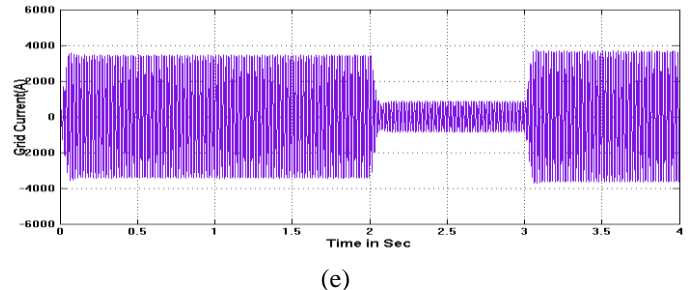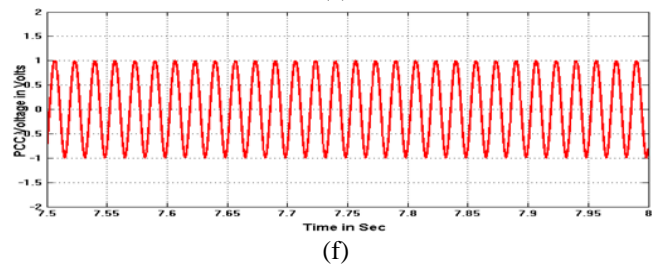

(a)
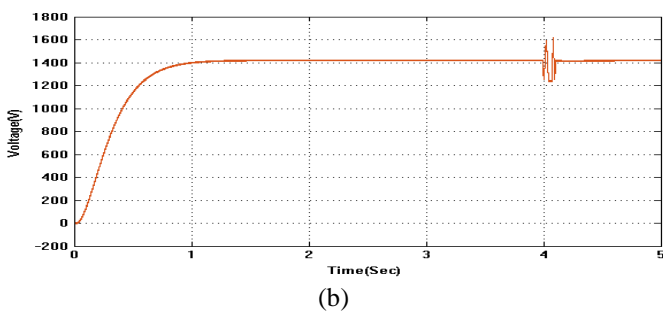
(b)
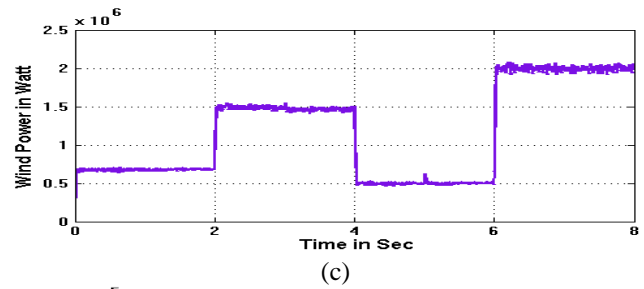
(c)

(d)

(e)

(f)
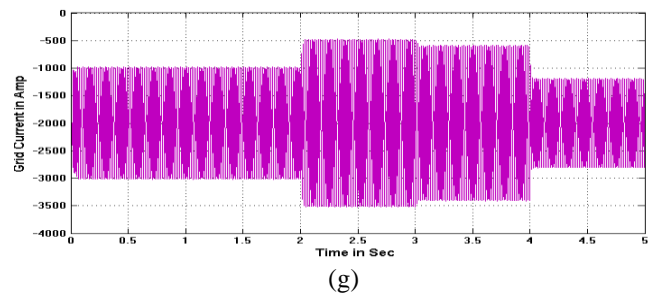
(g)

Fig. 9. Performance of the smart grid with both PV-wind power generation (a) PMSG speed (rad/sec), (b) DC link voltage, (c) wind power (W), (d) solar power (W), (e) grid current, (f) voltage at CPI, and (g) VSR modulation

4.2. Performance of the System Only with Wind Power Generation

The energy management of the smart-grid only with wind is described in this session. In this low or zero irradiance (during night) appearances power establishment done by solar is minimum. In this situation wind energy is only prime responsible to reach the load demand. The output simulation

results are illustrated in Figures 10(a) to 10(c). Those are wind speed, wind power and grid current respectively.
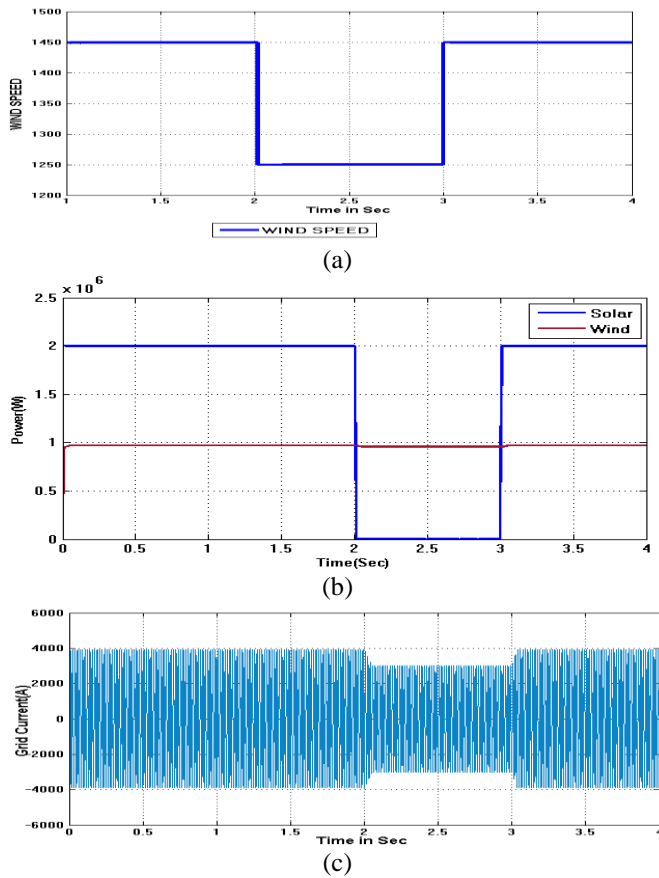

(a)

(b)

(c)

Fig.10. Simulation results of the system only with wind power generation (a) wind speed, (b) wind power, and (c) grid current

4.3. Performance of the System Only With Solar Power Generation

In this scenario, the smart grid's performance with solar electricity and low wind power generation is studied. Figure 11 depicts the output simulation results and their performance. Wind power, solar power, and grid current are depicted in Figures 11(a) to 11(c)
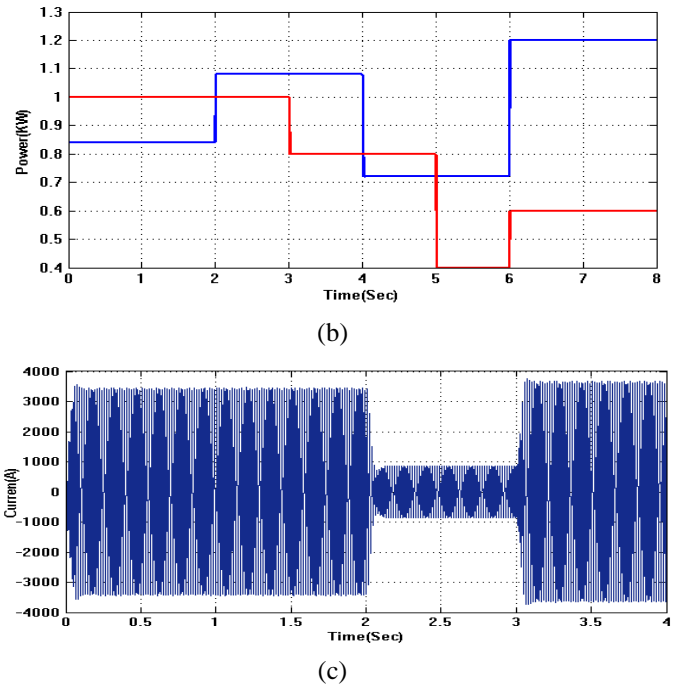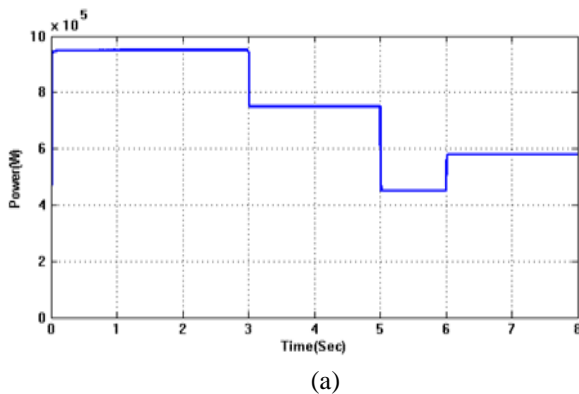

(a)

(b)

(c)

Fig. 11. Simulation result of (a) wind speed (b) solar power and (c) grid current

4.4. Performance of the system with symmetrical fault

From Figure 12 comparison of DC link voltage with protection controller and without controller it clear that with using proposed technique the oscillations occurred in grid current is less.
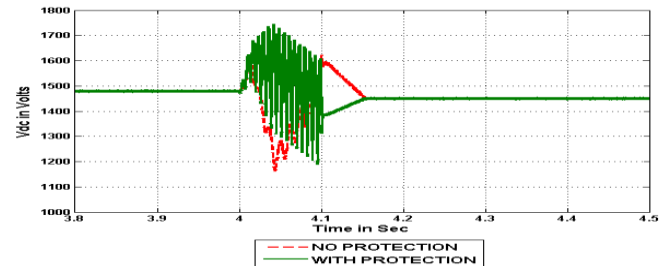
Fig. 12. DC link voltage with and without protection

It is mitigated within the first four cycles. Total harmonic distortion (THD) of grid current and grid voltage of conventional controller and proposed controller is shown in Figure 13. Comparison THD for grid current with Figure 13(a) ANFIS controller and Figure 13(b) proposed controller and shown in Figure 14. Comparison THD for grid voltage with Figure 14(a) ANFIS controller Figure 14(b) proposed controller respectively.

The results demonstrate that with the FOFL controller, grid current THD is percent and grid voltage THD is percent. This controller can also adjust for all parameters effectively. As a result, the FOFL controller is the most effective of the ANFIS controllers that have been designed. Table 2 shows a comparison of THD with ANFIS and FOFL controllers.
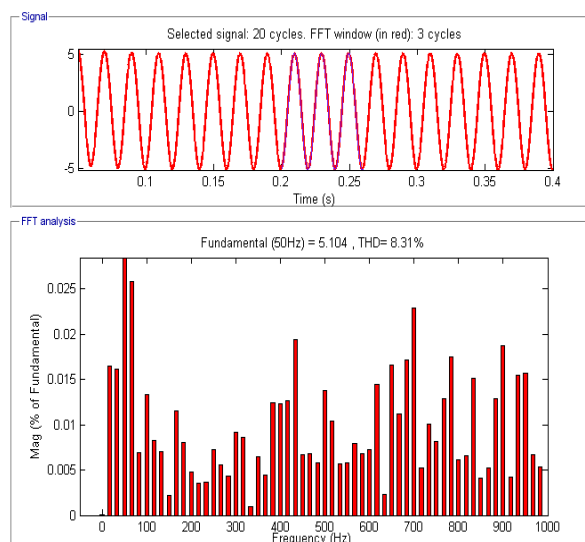
(a)
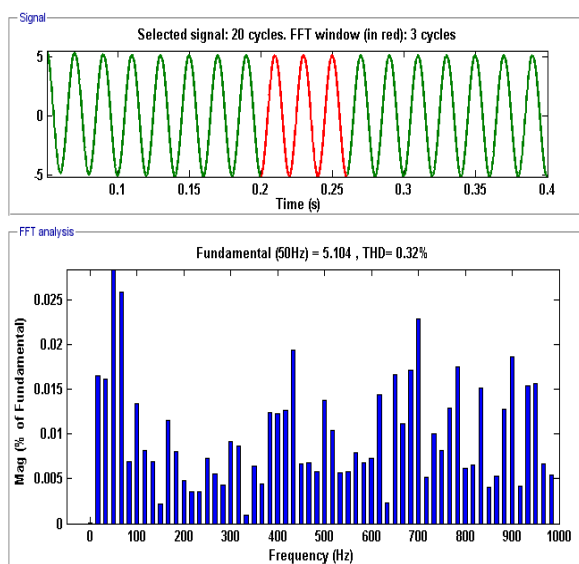
(b)

Fig. 13. THD for grid voltage comparison with (a) ANFIS controller and (b) proposed controller

Table 2. Comparison table for THD

S. No	Parameters	ANFIS Controller	Proposed Controller (FOFLC)
01	Grid Current	1.04%	0.67%
02	Grid Voltage	8.31%	0.31%
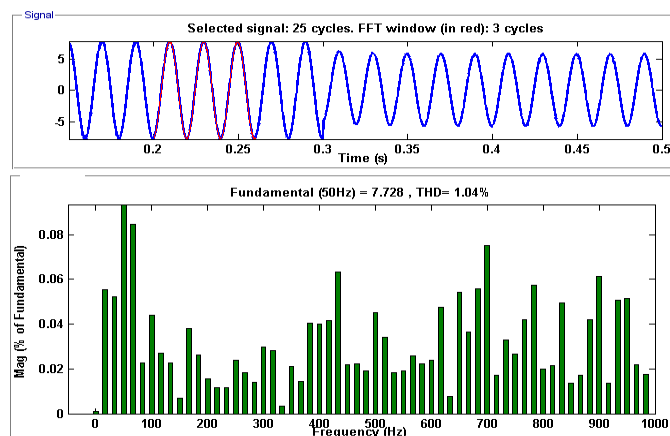
(a)
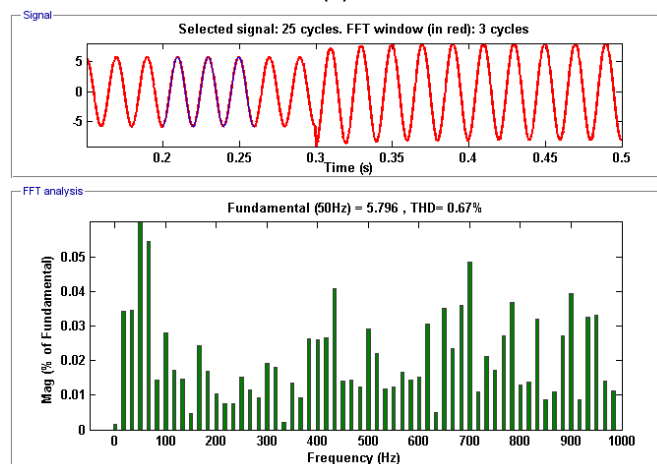
(b)

Fig. 14. THD for grid current comparison with (a) ANFIS controller and (b) proposed controller

5. Conclusion

This research investigates an efficient FOFL controller-based smart grid to improve power quality. Obtained simulation results for performance systems only with solar power and low wind energy, with wind energy and low solar power, and both solar-wind powers, are presented. From the simulations it is clear that the current's harmonic content is reduced by 1.04% to 0.67% and voltage harmonics are reduced from 8.31% to 0.31% in FOFLC in contrast to the ANFIS controller. In addition, it is observed that it has improved dynamic performance compared to the conventional control-based techniques like ANFIS controller, and individual loop control techniques. The proposed FOFL controller-based approach reduces network failure tolerance and improves the power quality. Future study could focus on how to improve the suggested method such that tracking errors are asymptotically stable, as well as how to improve control performance in the face of nonlinear inputs like load variations, and generation fluctuations and how to improve power quality in smart grids.

References

[1] S. Salman, X. AI, and Z. WU, "Design of a P&O algorithm based MPPT charge controller for a stand-alone 200W PV system," Protection and Control of Modern Power Systems, vol. 3, no. 1, Dec. 2018, doi: 10.1186/s41601-018-0099-8.

[2] D. Haji and N. Genc, "Fuzzy and P&O based MPPT controllers under different conditions," in 2018 7th International Conference on Renewable Energy Research and Applications (ICRERA), Oct. 2018, pp. 649–655, doi: 10.1109/ICRERA.2018.8566943.

[3] B. Bhandari, S. R. Poudel, K.-T. Lee, and S.-H. Ahn, "Mathematical modeling of hybrid renewable energy system: A review on small hydro-solar-wind power generation," International Journal of Precision Engineering and Manufacturing-Green Technology, vol. 1, no. 2, pp. 157–173, Apr. 2014, doi: 10.1007/s40684-014-0021-4.

[4] M. G. Simoes, B. K. Bose, and R. J. Spiegel, "Fuzzy logic based intelligent control of a variable speed cage machine wind generation system," in Proceedings of PESC '95-Power Electronics Specialist Conference, 1995, vol. 1, pp. 389–395, doi: 10.1109/PESC.1995.474840.

[5] R. Chedid, F. Mrad, and M. Basma, "Intelligent control of a class of wind energy conversion systems," IEEE Transactions on Energy Conversion, vol. 14, no. 4, pp. 1597–1604, 1999, doi: 10.1109/60.815111.

[6] T. Hirose and H. Matsuo, "Standalone hybrid wind-solar power generation system applying dump power control without dump load," IEEE Transactions on Industrial Electronics, vol. 59, no. 2, pp. 988–997, Feb. 2012, doi: 10.1109/TIE.2011.2159692.

[7] K. Kant, C. Jain, and B. Singh, "A hybrid diesel-wind -PV-based energy generation system with brushless generators," IEEE Transactions on Industrial Informatics, vol. 13, no. 4, pp. 1714–1722, Aug. 2017, doi: 10.1109/TII.2017.2677462.

[8] K. Sharma and D. K. Palwalia, "Robust controller design for DC-DC converters using fuzzy logic," in 2017 4th International Conference on Signal Processing, Computing and Control (ISPCC), Sep. 2017, pp. 477–481, doi: 10.1109/ISPCC.2017.8269726.

[9] P. K. Ray, S. R. Das, and A. Mohanty, "Fuzzy-controller-designed-PV-based custom power device for power quality enhancement," IEEE Transactions on Energy Conversion, vol. 34, no. 1, pp. 405–414, Mar. 2019, doi: 10.1109/TEC.2018.2880593.

[10] M. Bollen, J. Zhong, F. Zavoda, J. Meyer, A. McEachern, and F. Córcoles López, "Power quality aspects of smart grids," Renewable Energy and Power Quality Journal, vol. 1, no. 08, pp. 1061–1066, Apr. 2010, doi: 10.24084/repqj08.583.

[11] S. Gheorghe, G. Gheorghe, N. Golovanov, and C. Stanescu, "Results of power quality monitoring in Romanian transmission and distribution system operators," in 2016 International Conference on Applied and Theoretical Electricity (ICATE), Oct. 2016, pp. 1–6, doi: 10.1109/ICATE.2016.7754628.

[12] M. E. Ralph, "Control of the variable speed generator on the Sandia 34-m vertical axis wind turbine," presented at the Windpower '89 Conf. San Francisco, CA, 1989.

[13] T. A. Lipo, "Variable speed generator technology options for wind turbine generators," NASA Workshop, Cleveland,. 1984.

[14] C. Nayar and J. H. Bundell, "Output power controller for a wind-driven induction generator," IEEE Transactions on Aerospace and Electronic Systems, vol. AES-23, no. 3, pp. 388–401, May 1987, doi: 10.1109/TAES.1987.310837.

[15] P. G. Casielles, J. G. Aleixandre, J. Sanz, and J. Pascual, "Design, installation and performance analysis of a control system for a wind turbine driven self-excited induction generator," in Proceedings ICEM '90, 1990, pp. 988–993.

[16] D. A. Torrey, "Variable-reluctance generators in wind-energy systems," in Proceedings of IEEE Power Electronics Specialist Conference-PESC '93, 1993, pp. 561–567,doi: 10.1109/PESC.1993.471982.

[17] C. Brune, R. Spe, and A. K. Wallace, "Experimental evaluation of a variable-speed, doubly-fed wind-power generation system," in Conference Record of the 1993 IEEE Industry Applications Conference Twenty-Eighth IAS Annual Meeting, 1994, pp. 480–487, doi: 10.1109/IAS.1993.298967.

[18] D. M. F. G. Roger, "IEEE recommended practice and requirements for harmonic control in electric power systems," IEEE Std. 519-2014, vol. 2014, 2014.

[19] G. C. D. Sousa, B. K. Bose, and J. G. Cleland, "Fuzzy logic based on-line efficiency optimization control of an indirect vector-controlled induction motor drive," IEEE Transactions on Industrial Electronics, vol. 42, no. 2, pp. 192–198, Apr. 1995, doi: 10.1109/41.370386.

[20] G. C. D. Sousa and B. K. Bose, "A fuzzy set theory based control of a phase-controlled converter DC machine drive," IEEE Transactions on Industry Applications, vol. 30, no. 1, pp. 34–44, 1994, doi: 10.1109/28.273619.

[21] Krishna, D., M. Sasikala, and V. Ganesh. "Adaptive FLC-based UPQC in distribution power systems for power quality problems." *International Journal of Ambient Energy* 43, no. 1 (2022): 1719-1729.

[22] P. E. Bett and H. E. Thornton, "The climatological relationships between wind and solar energy supply in Britain," Renewable Energy, vol. 87, pp. 96–110, Mar. 2016, doi: 10.1016/j.renene.2015.10.006.

[23] D. Krishna, M. Sasikala, and V. Ganesh, "Mathematical modeling and simulation of UPQC in distributed power systems," in 2017 IEEE International Conference on Electrical, Instrumentation and Communication Engineering (ICEICE), Apr. 2017, pp. 1–5, doi: 10.1109/ICEICE.2017.8191886.

[24] Krishna, D., Sasikala, M. & Kiranmayi, R. FOPI and FOFL Controller Based UPQC for Mitigation of Power Quality Problems in Distribution Power System. *J. Electr. Eng. Technol.* **17,** 1543–1554 (2022).

[25] M. Saleh, Y. Esa, N. Onuorah and A. A. Mohamed, "Optimal microgrids placement in electric distribution systems using complex network framework," *2017 IEEE 6th International Conference on Renewable Energy Research and Applications (ICRERA)*, 2017, pp. 1036-1040, doi: 10.1109/ICRERA.2017.8191215.

[26] Mhel, Hassan Raji, and Amina Mahmoud Shakir. "Total Harmonic Distortion Reduction of 9-Level Packed E-Cell (PEC9) Inverter." International Journal of Smart Grid-ijSmartGrid 6, no. 1 (2022): 13-22.

[27] Sekhar, D. Chandra, PVV Rama Rao, and R. Kiranmayi. "Conceptual Review on Demand Side Management, Optimization Techniques for the Improvement of Power Quality in Smart Grids." In *2022 Second International Conference on Artificial Intelligence and Smart Energy (ICAIS)*, pp. 1640-1647. IEEE, 2022.

[28] Mazouz, Farida, Sebti Belkacem, and Ilhami Colak. "DPC-SVM of DFIG Using Fuzzy Second Order Sliding Mode Approach." International Journal of Smart Grid-ijSmartGrid 5, no. 4 (2021): 174-182.

[29] Y. Iwasaki, K. Yukita, T. Hosoe and K. Ikeda, "Basic study for the construction of a microgrid using small wind turbines as the main power source [PDF Not Yet Available In IEEE Xplore]," 2021 9th International Conference on Smart Grid (icSmartGrid),2021,pp.1-1,doi: 10.1109/icSmartGrid52357.2021.9551236.

[30] A. A. Ameri, M. B. Camara and B. Dakyo, "Efficient Energy Management for Wind-Battery Hybrid System Based Variable Frequency Approach," 2021 10th International Conference on Renewable Energy Research and Application (ICRERA), 2021, pp. 125-130, doi: 10.1109/ICRERA52334.2021.9598696.

Coordinated IPFC and SMES Strategy for Stability Analysis of Renewable Energy Based Contemporary Interconnected Power System with FOPID Controller

Ch. Naga Sai Kalyan*(iD), G. Swapna**(iD), S. Rajasekaran***(iD), A. N. Venkateswarlu****(iD),

B. Srikanth Goud*****‡(iD), Ch. Rami Reddy******(iD)

*Department of Electrical and Electronics Engineering, Vasireddy Venkatadri Institute of Technology, Guntur, India-522 508.

**Department of Electrical and Electronics Engineering, Koneru Lakshmaiah Education Foundation, Guntur, India- 522 302.

***Department of Electrical and Electronics Engineering, Vignana Bharathi Institute of Technology, Hyderabad, Ghatkesar, Telangana, India.

****Department of Electrical and Electronics Engineering, Vignan's Lara Institute of Technology and Science, Vadlamudi, Guntur, India-522 213.

*****Department of Electrical and Electronics Engineering, Anurag University, Venkatapur, Ghatkesar, Medchal, Telangana, India-500088.

******Department of Electrical and Electronics Engineering, Malla Reddy Engineering College, Maisammaguda, Secunderabad, Telangana, India-500 100.

(kalyanchallapalli@gmail.com, swapna@kluniversity.in, drsekar.ee@gmail.com, atyam2000@gmail.com, srikanth.b@anuraghyd.ac.in, crreddy229@gmail.com)

‡Corresponding Author; B. Srikanth Goud, Anurag University, Venkatapur, Ghatkesar, Medchal, Telangana, India-500088.

Tel: +91 903 093 7167, srikanth.b@anuraghyd.ac.in

Abstract- In this paper, an amalgamation of fractional calculus theory with integral order (IO) controller that is fractional order PID (FOPID) fine-tuned with water cycle algorithm (WCA) a natured inspired optimization technique is proposed as a secondary regulator for renewable-based contemporary interconnected power system (IPS). Investigation performed on IPS subjected to the perturbations of 10% step load on area-1 (10%SLP). System nonlinearity features of communication time delays (CTDs) are considered to conduct a more realistic analysis. Simulation results reveal the predominance of CTDs on IPS performance. The sovereignty of presented FOPID has been demonstrated with traditional IO type regulators like PI, and PID under unique perturbed conditions. Further, the device superconducting magnetic energy storage (SMES) is incorporated in each area and the interline power flow controller (IPFC) is operated in conjunction with the tie-line is operated. Responses of IPS reveal the enhancement in the dynamic performance of the system under the coordination of IPFC-SMES with the WCA tuned FOPID regulator.

Keywords FOPID regulator, Water cycle algorithm, SMES-IPFC strategy, CTDs, 10%SLP.

1. Introduction

Today's world is more focusing on reducing carbon emissions to control global warming. Moreover, the fossil fuels which constitute the carbon emissions in the environment are rapidly depleting. With the motto of handover of fossil fuels to future generations and minimizing their effect of emissions on the modern-day environment, renewable power generation units are gaining momentum in the electrical sector. With the rapid growth of industrialization, the electricity demand is continuously increasing. To meet the load demands, renewable power-generating sources (RPGS) are extensively integrated with the existing grid. The IPS network is becoming complex with RPGS integration and requires more sophisticated control techniques to ensure IPS stability and reliability.

The entire IPS is segregated into various control areas and each area is integrated with different power generation sources. The control areas are together interlinked with a transmission line called a tie-line to facilitate power exchange. Tie-line power and control area frequency deviations are power full indicators in assessing the stability, reliability and security of large scale IPS networks. The deviation in control area frequency arises with the lapse between the generation of real power and existing load demand. Thus the lapse between power generation and demand must be monitored and regulated continuously and automatically. The automatic action is filled by employing the load frequency controller (LFC) in each control area. A bulk quantity of literature is reported on LFC study and researchers are proposed numerous control technics and their efficacy is tested by considering various power system models as test systems [1].

Owing to the advantage of conventional controllers like PI and PID [2] in design simplicity, researchers are widely implemented as secondary regulators to LFC study. Moreover to make the controller performance more effective, researchers are adopted various meta-heuristic optimizations like Salp swarm technique (SST), fruit fly algorithm (FFA) [3], imperialist competitive approach (ICA), dragon search optimizer (DSO), flower pollination (FPA) algorithm [4], modified bat algorithm (MBA), multi verse optimizer (MVO), whale optimization technique (WOT), ant lion optimizer (ALO) [5], chemical reaction optimizer (CRO), genetic algorithm (GA) [6], seagull optimization algorithm (SOA) [7], simulated annealing (SA), firefly algorithm (FA) [8], marine predictive approach (MPA) [9], teaching learning based (TLBO) [10], optimizer, water cycle algorithm (WCA) [11-12], elephant heard technique (EHT) [13], artificial field algorithm (AEFA) [14], fractal search-pattern search (FSPS) [15], gravitation search technique (GST), backtracking search algorithm (BSA) [16], particle swarm optimizer (PSO) [17], squirrel search algorithm (SSA), cuckoo search technique (CST) [18], grey wolf optimizer (GWO) [19], biogeography optimizer (BGO), moth flame optimizer (MFO) [20], mine blast technique (MBT), bacterial foraging algorithm (BFA) [21], differential evolution (DE) [22], quasi-oppositional GWO, etc. are reported. But the PI and PID regulators are best suitable for only models of linearized characteristics.

In realistic practice, no power system network is linear and has deliberated with generation rate constraints (GRC), a practical non-linearity feature to regulate the generation lowering and rising. Thus, researchers are focused on implementing fuzzy logic control (FLC) techniques for LFC in association with PI and PID. Different FLC controllers such as WCA based fuzzy (F) PID [23], big bang-big crunch (BBBC) [24] tuned FPID, and SA based FPI [25], ICA [26] tuned FOFPI-FOPD is available in past studies. The design of FLC is more complex and requires skilled technicians. Moreover, the framing of fuzzy rules and selection of membership functions greatly influences FLC performance.

Further, researchers are focused on the design of sliding mode controllers (SMC) and robust control techniques. However, the robust control technique involves more mathematical modelling and its application to complex IPS are time taking. Thus, FO controllers are gaining momentum and are more efficacious compared to traditional regulators. FOPI, FOPI-FOPD and FOPID are based on optimization algorithms like the sine cosine approach (SCA) [27], CRO, Falcon optimizer (FO) [28], Volleyball algorithm (VBA) [29], lion algorithmic approach (LAA) [30], lightning search algorithm (LSA), crow search technique (CST) etc. are reported.

A literature survey discloses that FOPID based on SOA is not available in the literature. SOA is the latest technique and is widely grabbing the attention of researchers as a solution to engineering problems. Apart from the secondary control techniques, territorial strategy is necessitated for the contemporary IPS with RPGS as the power generation from renewable units is very intermittent. Implementation of high voltage DC transmission line with AC tie-line is rigorously implemented by the researchers [31]. Contrary to AC-DC lines, coordinated flexible AC transmission system devices and energy storage devices (ESDs) are newly implemented by researchers [32].

Considering the above literature this paper contributes the following.

a) Contemporary renewable-based IPS is designed in MATLAB/SIMULINK.

b) WCA based FOPID is implemented as a secondary regulator in each control area.

c) Efficacy of FOPID is deliberated with PI, and PID performances.

d) Contemporary IPS are investigated with and without CTDs considerations.

e) The impact of CTDs on contemporary IPS performance is visualized and justified.

f) SMES-IPFC coordinated control is implemented for performance enhancement.

g) The sensitivity test is conducted to demonstrate secondary and territorial strategy robustness.

2. Introduction

Contemporary IPS considered for investigation in this paper comprises two areas having a 5:3 generation ratio. Area-1 consists of traditional power generations of thermal, hydro and gas with a total capacity of 1250MW.
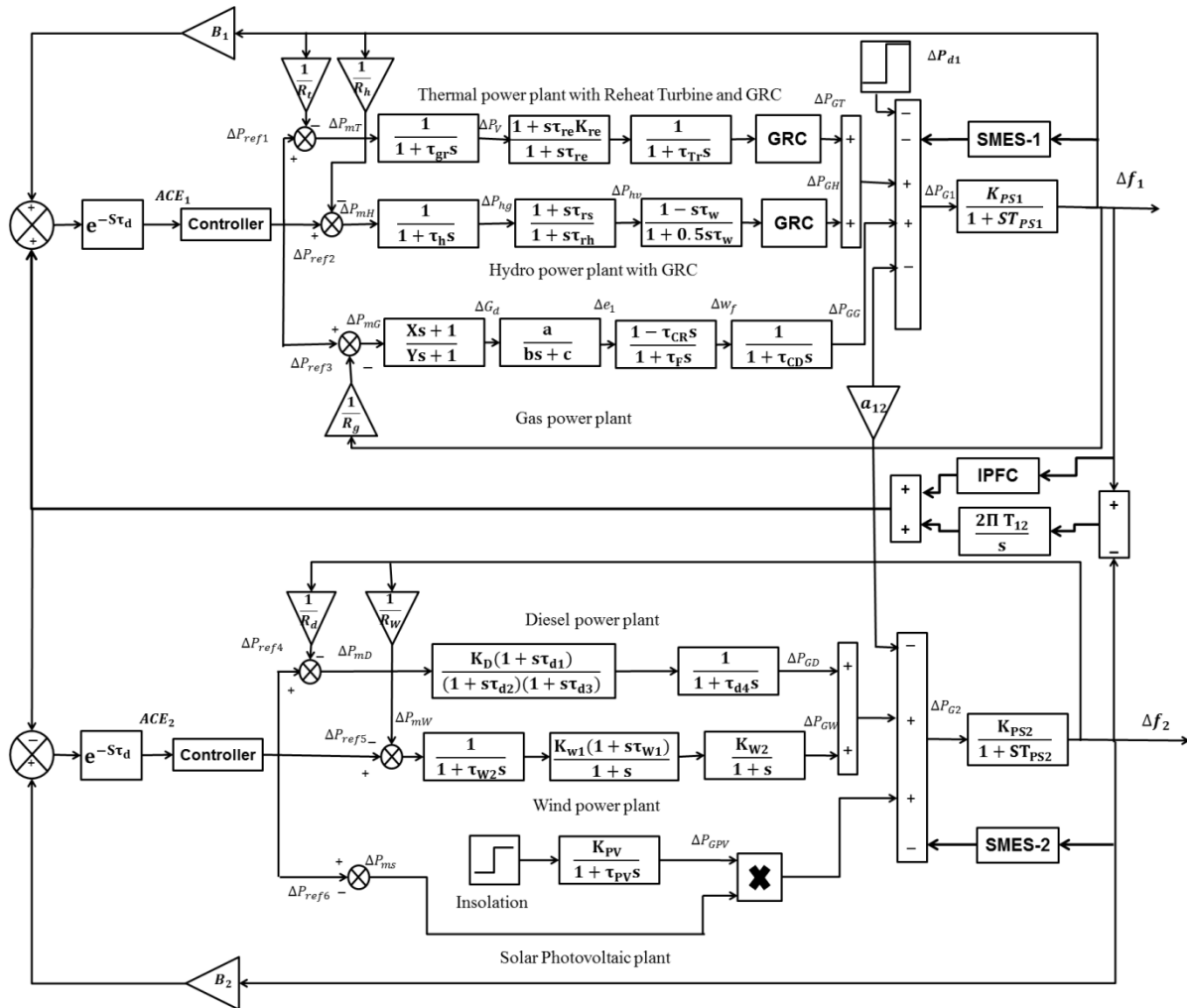

Fig. 1. Model of contemporary IPS considered for investigation.

In contrast to area-1, area-2 with 750MW total capacity incorporates renewable sources like solar photovoltaic penetration and wind unit along with a diesel plant. The contemporary IPS model comprised of RPGS is shown in Fig.1, and is developed in the domain of MATLAB/SIMULINK and the required parameters are chosen from [31-32]. The realistic constraint of limiting the real power generation raising and lowering that is GRC is perceived in this paper for both hydro and thermal units. Apart from that, the CTDs are perceived with the IPS model to establish the investigation nearer to realistic practice. The practical contemporary IPS is resided to a wide extent and employs many measuring devices located at remote points. The data from the device at a remote point is transmitted to the control centre to generate an error signal. The generated signal is received by the regulator in the plant location. The transmitting and signal receiving among various devices at different points will only take place with communication peripherals. Thus, communication peripherals inherit the time delay nature and these delays are playing their part in the performance of IPS. Due to the delay in signal

transmitting and receiving there exists a delay in varying the generation. The operating point of the power system is altered regularly to keep the difference between real power demand and generation minimum. The real power mismatch is a direct analogy to the control area frequency and hence the stability. Thus, CTDs are needed to be confiscated at the time of regulator design. Transport type of CTDs are perceived in this paper and is modelled as [33]

$$e^{-s\tau_d} = \frac{1 - \frac{\tau_d}{2}s}{1 + \frac{\tau_d}{2}s} \tag{1}$$

3. Controller and Objective Function

The formulated problem in this paper is related to the control literature, thus the design of the FOPID regulator should follow the Caputo definition. Normally, the FO integral and derivative parameters are derived from FO

differential equations subjected to initial conditions at zero. The FO integral-differential parameters for FOPID [34] regulator in this work are obtained from the derivative α^{th} of function f(t) is provided in (2).

$$D_t^\alpha f(t) = \frac{1}{\Gamma(m-\alpha)} \int_o^t \frac{D^m f(T)}{(t-T)^{\alpha+1-m}} dT, m-1 \prec \alpha \prec m \quad (2)$$

The modelling of FOPID is given in (3)

$$U_i(s) = K_P + \left(\frac{K_I}{s^\lambda}\right) + \left(K_D s^\mu\right) \quad (3)$$

The parameters are to be located optimally for better performance subjected to the index of integral square error (ISE) function in this work. ISE is more efficacious when it comes to the aspect of balancing peak minimization and settling time among other time-domain indices.

$$J_{ISE} = \int_0^{t_{sim}} \left(\Delta f_1^2 + \Delta P_{tie12}^2 + \Delta f_2^2\right) dt \quad (4)$$

4. Superconducting magnetic energy storage

For the stability of realistic contemporary renewable-based IPS models, there will always be scope for the utilization of ESDs as territorial regulators. SMES is chosen to be incorporated with the investigative power system in this work on account of its efficacy and bulk storage capability when compared to other ESDs. The key components in the SMES device are power conditioning set up and coil wounded to the magnetic core. To attain superconductivity the wounded coil is maintained at cryogenic temperature, with this the conductor attains lossless nature. Usually, energy is stored in SMES at off-peak durations and delivered energy to the grid instantly whenever it has been required. The operation of SMES for storage purposes is noiseless, zero carbon emission and eco-friendly. The power conditional set-up in SMES regulates the energy storage and dissipation process concerning the deviation in control area frequency. Frequency deviation is correlated to real power mismatch, as the Δf in any control region falls behind the limits then instantly SMES injects energy to the grid to minimize the mismatch before the variation in power system operating point came into action. Modelling of SMES deliberated in this study is given in (5) and the time and gain parameters perceived are $T_{SMES}=0.9972$, and $K_{SMES}=0.9080$ respectively.

$$G_{SMES} = \frac{K_{SMES}}{1+sT_{SMES}} \quad (5)$$

5. Interline Power Flow Controller

IPFC is one of the most dominant devices among all the available FACTs controllers. It employs several voltage source control units and is coupled to a common dc link. It can compensate for the flow of power in multiple transmission lines. Thus, to damp out the oscillations in tie-line power flow and to compensate for the line flow IPFC is

integrated into conjunction with the line in this paper for LFC of the contemporary renewable-based IPS model. The architecture of IPFC deliberated in this paper is shown in Fig.2 [35].

Upon laying IPFC in conjunction with the line, the variation in tie-line flow is modelled as

$$\Delta P_{tie12}(s) = \Delta P_{IPFC}(s) + \Delta P_{tie12}^0(s) \quad (6)$$

The effect of IPFC on power flow in tie-line is given by

$$\Delta P_{IPFC}(s) = \left(K_1 \Delta f_1(s) + K_2 \Delta P_{tie12}^0(s)\right) * \left(\frac{1}{1+sT_{IPFC}}\right) \quad (7)$$
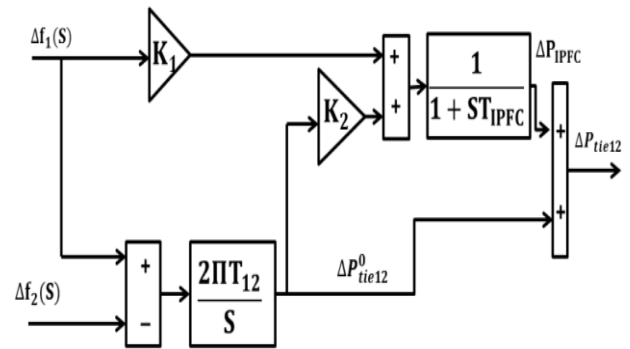

Fig. 2. IPFC architecture.

6. Water cycle algorithm

WCA is the modern optimization approach inspired by the process of the water cycle in nature and how streams and rivers finally fly into the sea in the practical world. The optimization process in this approach initiates with raindrops or snowdrops as initial particles. The emergence of snowdrops and raindrops in the mountain regions will flow downhill and forms streams or rivers. The formed stream or rivers flow downwards continuously and at last, merged with the sea. Here, the raindrops act as populations and the sea is the best solution. Here, in this paper, the WCA mechanism is implemented to find the gains of the FOPID regulator optimally. Hence, the raindrops are nothing but the parameters of the FOPID controller that are to be initiated randomly in an array as follows [36]:

$$RD_i = Y_i = [K_P, K_I, K_D, \lambda, \mu] \quad (8)$$

$$RD \quad Population = \begin{bmatrix} RD_1 \\ - \quad - \quad - \\ RD_i \\ - \quad - \quad - \\ RD_{N_{POP}} \end{bmatrix} \quad (9)$$

Later, the ISE index for every RD has to be evaluated using the equation provided in (10-11) and the positions of streams/rivers are initiated and subjected to the consideration of merging with the sea finally.

$$Position_{New}^{Stream} = Position^{Stream} + rand() * C * \quad (Position^{River} - Position^{Stream}) \quad (10)$$

$$\text{Position}_{\text{New}}^{\text{River}} = \text{Position}^{\text{River}} + \text{rand}()\ast C \ast \tag{11}$$
$$(\text{Position}^{\text{Sea}} - \text{Position}^{\text{River}})$$

The parameter 'C' value is assigned randomly from the range [0-2]. The process of evaporation and rain in WCA is modelled in equations (12-14).

$$\left| P_{\text{sea}} - P_{\text{river}} \right| < d_{\text{max}} \tag{12}$$

$$d_{\text{max}}^{\text{new}} = d_{\text{max}} - (d_{\text{max}}/\text{max.iteration}) \tag{13}$$

$$P_{\text{stream}}^{\text{new}} = P_{\text{sea}} + \sqrt{U} \, \text{X} \, \text{rand}(1, N_{\text{var}}) \tag{14}$$

The WCA algorithm procedural flow is rendered in Fig.3 and is developed in (.m format) in MATLAB to locate the optimal parameters of FOPID in this work for the LFC study of contemporary IPS.
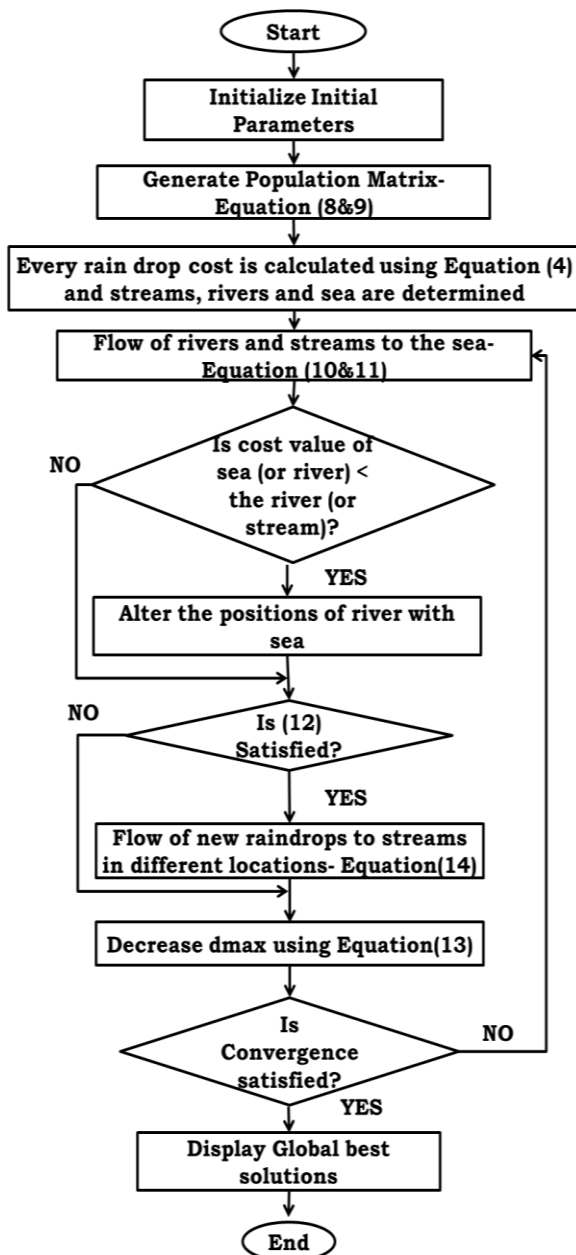
Fig. 3. WCA flowchart

7. Results and Discussion

7.1. Case-1: Analysis of contemporary IPS without considering CTDs.

Considered renewable energy sources based on contemporary IPS are investigated for 10%SLP disturbance on area-1 and the constraint of CTDs is not taken into account. Regulators of FOPID, PID and PI are placed in each control area one by one and are rendered optimally using the nature-inspired optimization technique of WCA. Dynamic responses of contemporary IPS under various regulators are compared in Fig.4, and the responses with FOPID are shown to be more enhanced in the aspects of both settling time and peaks overshoot/undershoot diminishing. Moreover, the ISE is improved and is greatly minimized with FOPID compared to others and is enhanced by 71.875%with PID and 88.30%with PI. Responses settling time in seconds are noted in Table 1 and the corresponding controller optimum gains are noted in Table 2.

(a)

(b)

(c)

Fig. 4. Case-1 Responses. (a).Δf_1, (b).ΔP_{tie12}, (c).Δf_2.

Table 1. Responses settling time under various cases.

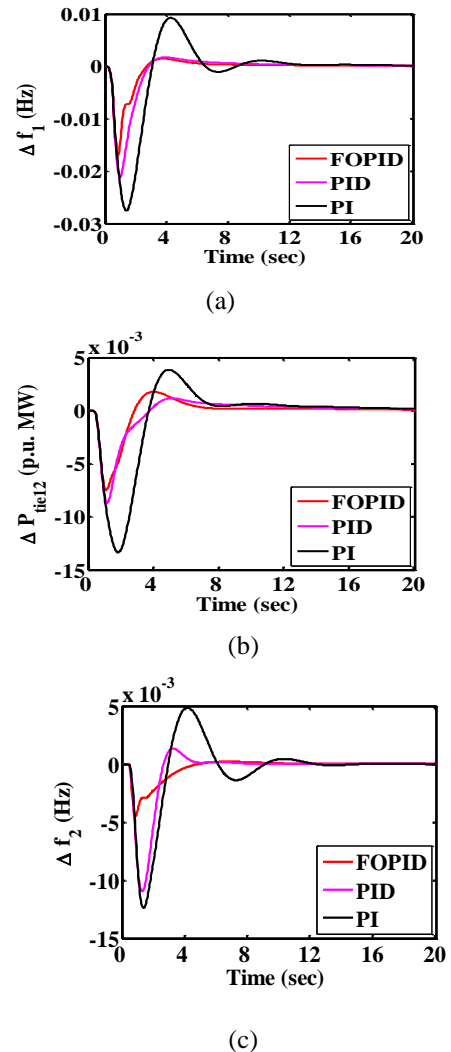| Controller	Case-1				Case-2			
	Δf_1	ΔP_{tie12}	Δf_2	ISE $*10^{-3}$	Δf_1	ΔP_{tie12}	Δf_2	ISE $*10^{-3}$
PI	12.27	15.13	11.90	22.32	21.77	22.39	14.96	72.83
PID	10.09	12.24	8.64	9.28	13.57	14.35	13.02	29.36
FOPID	7.98	8.25	7.67	2.61	11.261	11.22	9.388	13.68

Table 2. Controller optimal gains.

Parameters	Case-1			Case-2		
	PI	PID	FOPID	PI	PID	FOPID
Case-1	$K_P=0.996$ $K_I=0.042$	$K_P=0.835$ $K_I=0.125$ $K_D=0.448$	$K_P=0.308$ $K_I=0.198$ $K_D=0.188$ $\mu=0.558$ $\lambda=0.450$	$K_P=0.896$ $K_I=0.102$	$K_P=0.678$ $K_I=0.251$ $K_D=0.484$	$K_P=0.411$ $K_I=0.201$ $K_D=0.199$ $\mu=0.672$ $\lambda=0.542$
Case-2	$K_P=0.975$ $K_I=0.073$	$K_P=0.868$ $K_I=0.220$ $K_D=0.268$	$K_P=0.291$ $K_I=0.098$ $K_D=0.367$ $\mu=0.431$ $\lambda=0.406$	$K_P=0.798$ $K_I=0.094$	$K_P=0.796$ $K_I=0.218$ $K_D=0.309$	$K_P=0.398$ $K_I=0.316$ $K_D=0.298$ $\mu=0.562$ $\lambda=0.497$
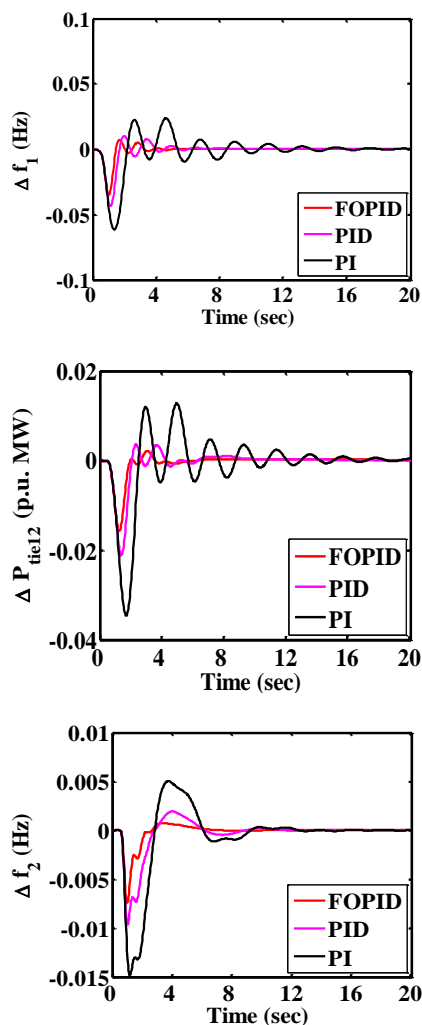
7.2. Case-2: Analysis of contemporary IPS with considering CTDs.

The practical constraint of CTDs is considered with renewable-based contemporary IPS in this case for the identical disturbance in a load of 10%SLP. Responses of considered IPS under various regulators are compared in Fig.5 and is concluded primarily that FOPID dominates the performances of PID and PI. Even though the contemporary IPS is conceived with CTDs, FOPID showcases its supremacy in handling the deviations to reach a steady condition in a quick time. Thus, WCA based FOPID is declared the best compared to other IO type classical controllers. The additional parameters in FOPID provide better regulation in damping out the oscillations and further the ISE for FOPID is strengthened by 81.216%with PI and 53.405% with PID.
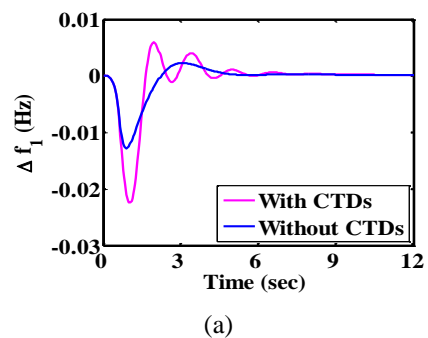
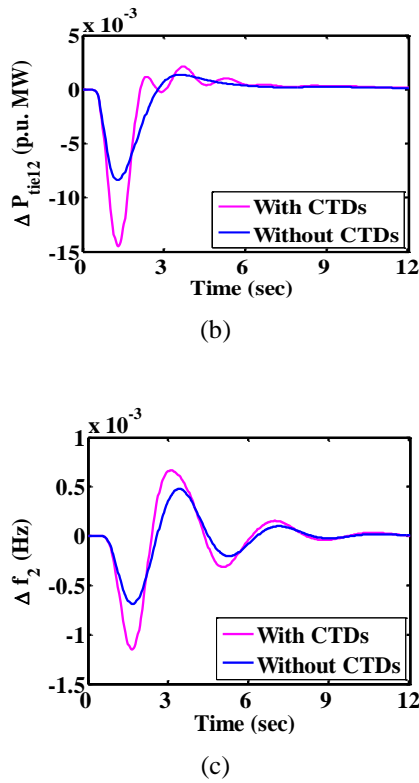

(a)

Fig. 5. Case-2 Responses. (a).Δf_1, (b).ΔP_{tie12}, (c).Δf_2

(b)

(a)

(c)

Fig. 6. Case-3 Responses. (a).Δf_1, (b).ΔP_{tie12}, (c).Δf_2.

7.3. Case-3: Demonstrating CTDs impact on performance of contemporary IPS.

From the above analysis, it has been concluded that the WCA based FOPID is more efficacious. Hence responses of contemporary renewable-based IPS with and without CTDs under FOPID are compared in Fig.6 to show the impact of CTDs. Noticing from Fig.6, that responses of contemporary IPS including CTDs are exhibiting more deviations in the frequency of control area-1 (Δf_1), control area-2 (Δf_2) and tie-line power (ΔP_{tie12}) compared to the situation of not including CTDs with the system. This means there will be a definite time lag in signal transmitting and receiving within different devices located at faraway points via communication channels. With these delays, there will be a lag in the command signal from the control centre to the controller at the plant site. Thus, the necessary action performed by the regulator in changing the power system operating point is performed with some delays. The mismatch in real power may even get worsened due to these CTDs thereby affecting the IPS performance. Despite more deviations in responses of IPS considering the CTDs, the designed regulator drags the deviations to steady conditions. Thus, this paper recommends CTDs consideration with IPS models in the study of LFC while developing the secondary regulator. The delay in the time of 0.12 seconds is considered in this work which is a realistic one. It is noteworthy that performing the LFC analysis on IPS models without addressing the CTDs effect of the designed regulator may not yield beneficial results in case of unpredictable delays emerging within the system.

(a)

(b)

(c)
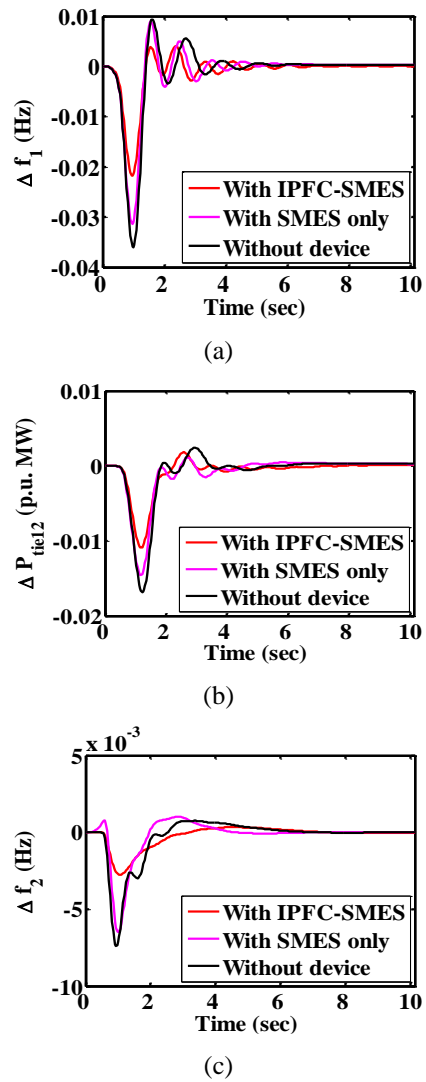
Fig. 7. Case-4 Responses. (a).Δf_1, (b).ΔP_{tie12}, (c).Δf_2.
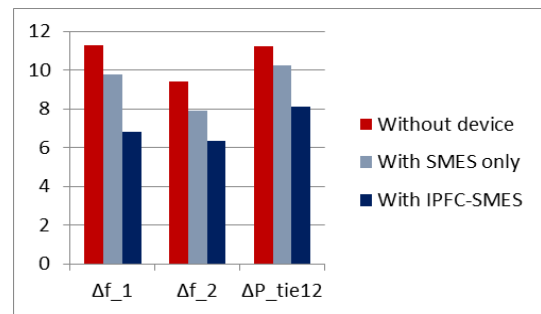
Fig. 8. The bar-chart represents settling time in seconds (on the Y-axis) for Case-4.

7.4. Case-4: Analysis of contemporary IPS with considering CTDs under coordinated IPFC-SMES strategy.

To overcome the subsidiary deviations that had occurred in the system performance while considering CTDs, it is adequate to implement the territorial strategy. In this work, initially, the renewable-based considered contemporary IPS is incorporated with SMES in each area and the behaviour of the system under load disturbances is analysed. Later, IPFC is incorporated in conjunction with AC tie-line along with

SMES in both the areas and the responses are compared in Fig.7. Observing Fig.7 concluded that on implementing the strategy of SMES-IPFC there exists a considerable enhancement in IPS performance. IPFC works more efficacious in damping out inter-area oscillations and SMES facilitates a considerable shrink in deviations of respective control area frequency. The settling time of IPS responses is indicated in the form of a bar chart in Fig.8, for easy interpretation.

7.5. Case-5: Sensitivity test.

The suggested WCA optimized FOPID regulator in coordination with the territorial strategy of SMES-IPFC in renewable sources based contemporary IPS is targeted with loadings in both the areas and also with random loading in area-1. The IPS responses for loading in both the areas are rendered in Fig.9, and random loadings it has been depicted in Fig.10. From sensitivity analysis, it has been observed that the deviations in IPS responses are not seen much even though the system is loaded in both areas. Moreover, with the effective strategy of SMES-IPFC, the performance of the IPS looks more stable even if it is subjected to random loadings. Thus, FOPID based on WCA with SMES-IPFC territorial strategy presented in this paper is robust.
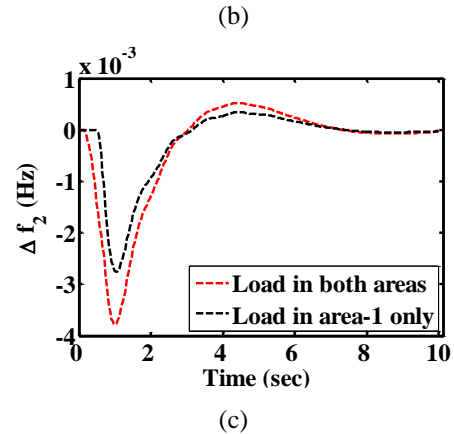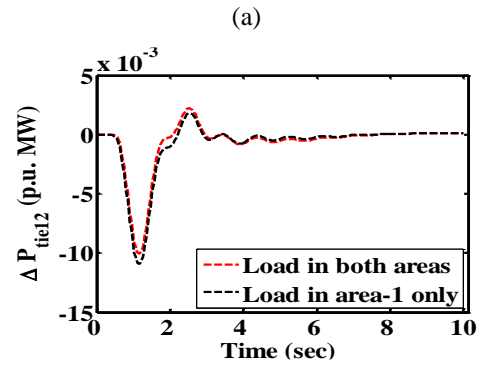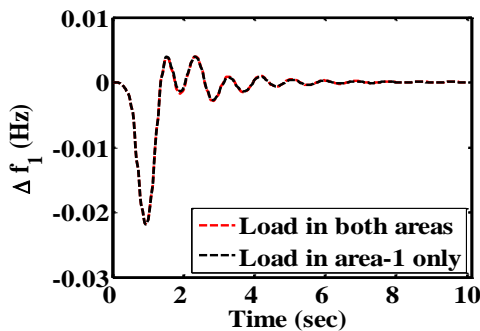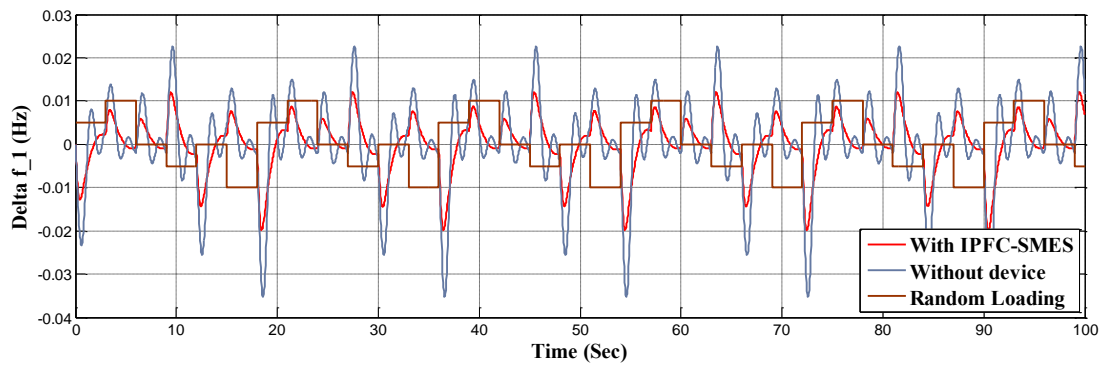
(a)

(b)

(c)

Fig. 9. Case-5 responses with load in both the areas. (a).Δf_1, (b).ΔP_{tie12}, (c).Δf_2.

(a)
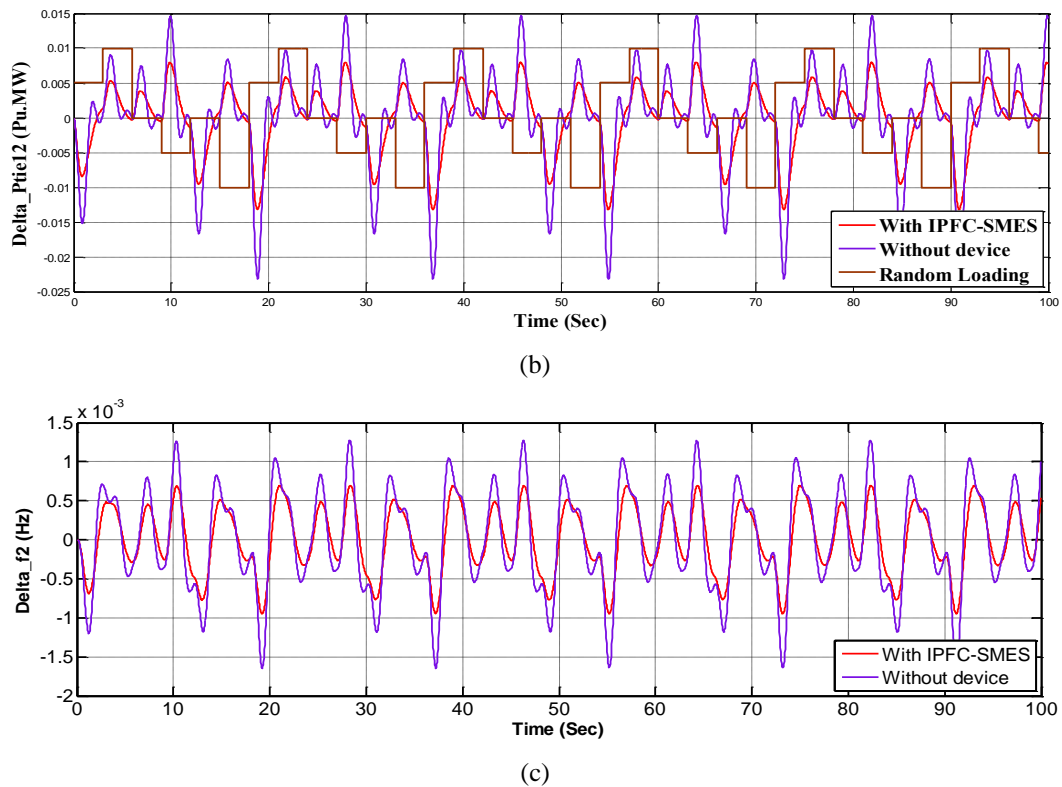
Fig. 10. Case-5 responses with random laoding.(a).Δf_1, (b).ΔP_{tie12}, (c).Δf_2.

8. Conclusion

WCA tuned FOPID is implemented successfully for renewable sources based on contemporary IPS in the LFC study. Efficacy of FOPID is showcased with PI, PID conventional regulators. The test system is perceived with CTDs in the vision of performing analysis in more practical aspects. The dynamic behaviour of the investigative system has been analysed with and without considering CTDs to showcase its impact. Simulation results reveal the significance of CTDs on power system performance. With CTDs the system responses are slightly deviated more and also concede more time to settle down because of the delay in delivering the control signal to the generators to alter the operating point. This paper suggests considering test system models with CTDs to avoid the chances of instability due to unexpected time delays. Later, SMES-IPFC coordinated strategy is implemented in the contemporary IPS under WCA based FOPID regulator. Test system responses reveal the enhancement in dynamic behaviour with SMES-IPFC devices under the same perturbed conditions. Robustness of FOPID along with SMES-IPFC coordinated regulation is revealed with random loadings of sensitivity analysis.

References

[1] D. H. Tungadio, and Y. Sun, "Load frequency controllers considering renewable energy integration in power system", Energy Reports, Vol. 05, pp.436-454, (2019).

[2] C. N. S. Kalyan, and G. S. Rao, "Coordinated SMES and TCSC damping controller for load frequency control of multi area power system with diverse sources", International Journal on Electrical Engineering and Informatics, Vol.12, No.04, pp.747-769, (2020).

[3] B. Mohanty, and P. K. Hota, "Comparative performance analysis of fruit fly optimisation algorithm for multi-area multisource automatic generation control under deregulated environment", IET Gener Transm Distrib, Vol.09, No.14, pp.1845–1855, (2015).

[4] I. Hussain, S. Ranjan, D. C. Das, and N. Sinha, "Performance analysis of flower pollination algorithm optimized PID controller for Wind-PV-SMES-BESS-diesel autonomous hybrid power system", Int J Renew Energy Res, Vol.07, No.02, pp.643-651, (2017).

[5] A. Fathy, and A. M. Kassem, "Antlion optimizer-ANFIS load frequency control for multi-interconnected plants comprising photovoltaic and wind turbine", ISA Transactions, Vol.87, pp.282-296, (2019).

[6] E. Cam, G. Gorel, and H. Mamur, "Use of the genetic algorithm-based fuzzy logic controller for load-frequency control in a two area interconnected power system", Appl Sci, Vol.07, No.03, 308, (2017).

[7] C. N. S. Kalyan and C. V. Suresh, "Higher order degree of freedom controller for load frequency control of multi area interconnected power system with time delays", Global Transitions Proceedings, https://doi.org/10.1016/j.gltp.2022.03.020, 2022

[8] K. Jagatheesan, B. Anand, S. Samanta, N. Dey, A. S. Ashour, and V. E. Balas, "Design of a proportional-integral-derivative controller for an automatic generation control of multi-area power thermal systems using firefly algorithm", IEEE/CAA J Autom Sin, Vol.06, No.02, pp.503-515, (2019).

[9] A. H. Yakout, M. A. Attia, and H. Kotb, "Marine predator algorithm based cascaded PIDA load frequency controller for electric power systems with wave energy conversion systems", Alexandria Engineering Journal, Vol.60, pp.4213-4222, (2021).

[10] B. K. Sahu, T. K. Pati, J. R. Nayak, S. Panda, and S. K. Kar, "A novel hybrid LUS–TLBO optimized fuzzy-PID controller for load frequency control of multi-source power system", Int J Electr Power Energy Syst, Vol.74, pp.58-69, (2016).

[11] C. N. S. Kalyan, "Determination of appropriate GRC modelling for optimal LFC of multi area thermal system", 2021 IEEE International Power and Renewable Energy Conference (IPRECON), 2021, pp.1-6, 10.1109/IPRECON52453.2021.9640892

[12] C. N. S. Kalyan, B. S. Goud, C. R. Reddy, M. Bajaj, and G. S. Rao, "SMES and TCSC coordinated strategy for multi-area multi-source system with water cycle algorithm based 3DOF-PID controller", Smart Science, 2022, https://doi.org/10.1080/23080477.2022.2054199

[13] S. Dewangan, T. Prakash, and V. P. Singh, "Design and performance analysis of elephant herding optimization based controller for load frequency control in thermal interconnected power system", Optimal Control Applications and Methods, Vol.42, pp.144-159, (2021).

[14] C. N. S. Kalyan, B. S. Goud, C. R. Reddy, M. Bajaj, N. K. Sharma, H. H. Alhelou, P.Siano and S. Kamel, "Comparative performance assessment of different energy storage devices in combined LFC and AVR analysis of multi-area power system", Energies, Vol.15, No.2, 629, (2022).

[15] D. Saha, and L. C. Saikia, "Automatic generation control of an interconnected CCGT thermal system using stochastic fractal search optimized classical controllers", Int Trans Electr Energy Syst, Vol.28, No.05, pp.1-25, (2018).

[16] D. Guha, P. K. Roy and S. Banerjee, "Application of backtracking search algorithm in load frequency control of multi-area interconnected power system", Ain Shams Engineering Journal, Vol.9, No.2, pp.257-276, (2018).

[17] Naga sai kalyan, C., Sambasiva rao, G. (2021) Performance index based coordinated control strategy for simultaneous frequency and voltage stabilization of multi-area interconnected system. In: Singh A.K., Tripathy M. (eds) Control Applications in Modern Power System. Lecture Notes in Electrical Engineering, Vol 710. Springer, Singapore. https://doi.org/10.1007/978-981-15-8815-0_4

[18] A. Y. Abdelaziz, and E. S. Ali, "Cuckoo Search algorithm based load frequency controller design for nonlinear interconnected power system", Int J Electr Power Energy Syst, Vol.73, pp.632-643, (2015).

[19] C. N. S. Kalyan, "UPFC and SMES based coordinated control strategy for simultaneous frequency and voltage stability of an interconnected power system", 2021 1st International Conference on Power Electronics and Energy (ICPEE), 2021, pp.1-6, 10.1109/ICPEE50452.2021.9358576

[20] B. Mohanty, B. V. S. Acharyulu, and P. K. Hota, "Moth-flame optimization algorithm optimized dual-mode controller for multiarea hybrid sources AGC system", Optimal control applications and methods, Vol.39, No.02, pp.720-734, (2018).

[21] A. Panwar, G. Sharma, I. Nasiruddin, and R. C. Bansal, "Frequency stabilization of hydro– hydropower system using hybrid bacteria foraging PSO with UPFC and HAE", Electr Power Syst Res, Vol.161, pp.74-85, (2018).

[22] C. N. S. Kalyan, and C. V. Suresh, "Differential Evolution based Intelligent Control approach for LFC of Multiarea Power System with Communication Time Delays", 2021 International Conference on Computing, Communication, and Intelligent Systems, 2021, PP.868-873, doi: 10.1109/ICCCIS51004.2021.9397112.

[23] C. N. S. Kalyan, B. S. Goud, C. R. Reddy, H.S.Ramadan, M. Bajaj, and Z.M.Ali, "Water cycle algorithm optimized type II fuzzy controller for load frequency control of a multi-area multi-fuel system with communication time delays", Energies, Vol.14, No.17, 5387, (2021).

[24] S. Jain, and Y. V. Hote, "Design of fractional PID for load frequency control via internal model control and big bang big crunch optimization", IFAC Papers Online, Vol.51, pp.610-615, (2018).

[25] K. R. M. V. Chandrakala and S. Balamurugan, "Simulated annealing based optimal frequency and terminal voltage control of multi source multi area system", International Journal of Electrical Power and Energy Systems, Vol.78, pp.823-829, (2016).

[26] Y. Arya, "A new optimized fuzzy FOPI-FOPD controller for automatic generation control of electric power systems", Journal of Franklin Institute, Vol.36, pp.5611-5629, (2019).

[27] W. Tasnin, and L. C. Saikia, "Comparative performance of different energy storage devices in AGC of multi-source system including geothermal power plant", Journal of Renewable and Sustainable Energy, Vol.10, 024101, (2018).

[28] C. N. S. Kalyan, B. S. Goud, C. R. Reddy, B. N. Reddy, M. Bajaj, and A.V.Sudhakar, "Falcon optimizer based PIDD controller for AGC of dual area realistic system with AC-DC links", 2021 International Conference on Technology and Policy in Energy and Electric Power (ICT-PEP), 2021, pp.6-10, 10.1109/ICT-PEP53949.2021.9600946

[29] A. Prakash, S. Murali, R. Shankar, and R. Bhushan, "HVDC tie-link modelling for restructured AGC using a novel fractional order cascade controller", Electric Power Systems Research, Vol.170, pp.244-258, (2019).

[30] D. Sharma, and N. K. Yadav, "Lion Algorithm with Levy Update: Load frequency controlling scheme for two-area interconnected multi-source power system", Trans Inst Meas Control, Vol.41, No.14, pp.4084-4099, (2019).

[31] C. N. S. Kalyan and G. S. Rao, "Frequency and voltage stabilization in combined load frequency control and automatic voltage regulation of multi area system with hybrid generation utilities by AC/DC links", International Journal of sustainable energy, Vol.39, No.10, pp.1009-1029, (2020).

[32] C. N. S. Kalyan and G. S. Rao, "Combined frequency and voltage stabilization of multi-area multisource system by DE-AEFA optimized PID controller with coordinated performance of IPFC and RFBs", International Journal of Ambient Energy, https://doi.org/10.1080/01430750.2020.1860130, (2020).

[33] C. N. S. Kalyan and G. S. Rao, "Demonstrating the effect of excitation cross coupling and communication time delays on automatic generation control", 2021 4th Biennial International Conference on Nascent Technologies in Engineering (ICNTE), 2021, pp.1-6, 10.1109/ICNTE51185.2021.9487779

[34] S. Sondhi, and Y. V. Hote, "Fractional order PID controller for load frequency control", Energy Conversion and Management, Vol.85, pp.343-353, (2014).

[35] C. N. S. Kalyan and G. S. Rao, "Impact of communication time delays on combined LFC and AVR of a multi-area hybrid system with IPFC-RFBs coordinated control strategy", Prot Control Mod Power Syst, Vol.6, No.7, (2021), https://doi.org/10.1186/s41601-021-00185-z

[36] H. Eskandar, A. Sadollah, A. Bahreininejad, and M. Hamdi, "Water cycle algorithm-A novel meta-heuristic optimization method for solving constrained engineering optimization problems", Computers & Structures, Vol.110, pp.151-166, (2012).

RESEARCH ARTICLE

COVID-19 Prevention: an IoT - Based Solution for Effective Social Distancing and Contact Tracing

Pradeep M[1]*, P.Kamalakar[2], V.Ganesh kumar[2] and Rekharani Maddula[3]

[1]Associate Professor, Department of ECE, Shri Vishnu Engineering College for Women, Bhimavaram, Andhrapradesh, India-534202.
[2]Associate Professor, Department of EEE, Malla Reddy Engineering College, Maisammaguda, Secunderabad, Telangana, India-500100.
[3]Assistant Professor, Department of Physics, Gokaraju Lailavathi Womens Engineering College, Hyderabad, Telangana, India-500090.

*Address for Correspondence
Pradeep M
Associate Professor, Department of ECE,
Shri Vishnu Engineering College for Women,
Bhimavaram, Andhrapradesh, India-534202.
Email: pradeep_ece@svecw.edu.in

ABSTRACT

Corona virus has infected millions of individuals throughout the world, and the number of sick persons continues to rise. Humans get the virus through direct, indirect, or close contact with infected individuals. This proposed work introduces a new feature, an intelligent community distance system, that allows people to maintain community distances among others in both indoor and outdoor locations, therefore avoiding COVID-19 exposure and delaying its spread both locally and internationally. The proposed research aims to monitor an IoT-based portable monitoring device that is designed to measure COVID-19 signals. Furthermore, by monitoring real-time GPS data, the device immediately alerts medical authorities concerned about any confinement violations of patients who may be infected. Also, find out what new tool will be beneficial for tracking and predicting COVID-19 collections. To aid in the analysis of COVID-19, the solution incorporates a mobile system coupled with a portable device that is equipped with clever IoT capabilities (complex data analysis and intelligent data detection) incorporated inside the system. A comparison of several machine learning classifier algorithms such as SVM, Random Forest, KNN, and Decision Tree is presented as the best model for making predictions and determining accuracy. We observed that KNN performs better, with a 95 percent accuracy rate. COVID-19 will be utilized to avoid the transmission of illness in future global health concerns using an automatic social distance monitoring and contact tracking system.
Keywords: Corona virus, COVID-19, community distance system, social distance

INTRODUCTION

COVID-19 is an extremely severe infectious virus that causes a highly contagious respiratory disease (SARS-CoV-2). SARS-CoV-2 is a virus that targets the respiratory system and causes symptoms including poisoning, fever, nausea, and shortness of breath. Many nations have used Lockdown to avoid the pandemic, in which the government forces inhabitants to stay at home during this vital period. Community health services, such as the Centers for Disease Control and Prevention (CDC), have to make it clear that avoiding close contact with other individuals is the most efficient strategy to prevent the transmission of Covid-19. To keep the turns to the Covid-19 outbreak flat, the earth's population are used to rigorous activity. During incarceration, community activities, team activities, and congregational activities such as travel, meetings, gatherings, workshops, and prayers were prohibited. People are encouraged to coordinate and conduct events as much as possible via phone and email to avoid personal interaction. In order to keep the virus from spreading, individuals are being advised to practice good hygiene, such as hand washing regularly, wearing a mask, and avoiding close contact with ill persons. There is, however, a distinction between knowing what to do to decrease viral spread and actually doing it [1].Using public broadcasts among persons at least one metre away is one well-known method of preventing the spread of Covid-19. The corona virus is spread from person to person by minute droplets from the nose and mouth, according to WHO. To put it another way, social dispersal is the greatest strategy for minimizing physical contact with probable corona virus carriers by keeping at least a metre between individuals.Covid-19 antiretroviral measures are supported by the planned work. It offers a way to locate individuals in public locations such as retail malls, banks, markets, temples, mosques, public transportation, and government offices [2]. In order to reduce the danger of disease transmission inside congested indoor environments, monitoring and support of social isolation has become more necessary [3].

In public locations, social measures such as contrasting signs on the chairs deter individuals from sitting close to one other (Fig.1). In modern times, the greatest form of prevention is social isolation and wearing a face mask. The World Health Organization (WHO) standards give a full examination of external activities that must be rigorously adhered to: WHO guidelines for follow-up: (1) Prior to exposure, the face mask or cover must be worn. (2) When leaving a private location, a person must maintain a public distance throughout his or her time in public settings. As a result, there is no lasting treatment in the absence of medical assistance. Few initiatives are being done throughout the world to employ IOT data as a preventive or predictive strategy against Covid-19, or as models in epidemiology. With the use of a food security camera that can analyze live or offline to detect social divisions and face mask covering in the official, public, or public area, a vision tool for controlling social distance and face mask at work has been developed. will aid in the monitoring of health policy The Practicing Health regimen helps people live longer and reduce rashes [5].

The COVID-19 outbreak has wreaked havoc on human mobility patterns as well as social behavior connected to everyday mobility. In order to conduct corrective actions at this time, it is necessary to understand illness dissemination patterns and mechanisms among neighbors. Countries throughout the globe are pursuing developments in mobile technology and the Internet of Things (IoT) to help maintain track of common connections to track persons close to identified COVID-19 patients to improve the efficacy of social media tracking. Even once vaccine therapy becomes available in 2021, the COVID-19 management plan will continue to look to the future in terms of digital communication, which is an important aspect of the response, and the adoption of preventative measures like social isolation and masks. In-depth information of the applicability of the various technologies, as well as the usability, privacy, and trade-offs of ethical principles involved, after several months of usage of digital contact monitoring technology. Due to recent developing data on worldwide information for the distribution of digital contact tracking technology, we give a full study of digital communication tracking solutions in terms of their processes and technologies in this proposal. Data collecting and interpretation should be established in contact tracking apps. Figure 2 shows contact tracing zones in public spaces.

Related work

Sengupta *et al* [6] argue that a plan to respond to environmental outbreaks should be developed to aid in the tracking and tracking of safety-related problems in industrial and community settings. Controlling infectious diseases and their spread necessitates comprehensive communication. To track human activity, the framework will incorporate video feeds from surveillance cameras and IoT edge devices located in industrial or public spaces. The architecture suggested here is a hybrid method to integrating feeds from current cameras and IoT devices with cloud-based computer-based edges. S. Srinivasan et al provide a comprehensive and successful solution based on the binary category for detecting a person, detecting a breach of social distance, and detecting a face-to-face mask separation utilising object identification, integration, and Convolution Neural Network (CNN). In this scenario, video databases were monitored using YOLOv3, a local collection based on congestion audio applications (DBSCAN), Dual Shot Face Detector (DSFD), and MobileNetV2 based Binary classifier. They did this through comparative study on various facial expressions and face mask classification methods. Finally, a strategy for labelling video databases is proposed. Video data is utilised for system testing and to compensate for public data shortages. System performance is accurately assessed, Fl score as and predictive timing, which should be low enough to be applied in a practical way [7].

A Khanfor et al. [8] provide a functional framework for improving pedestrian safety while roaming the real-world map of the smart city using the notion of Social IoT (SIoT). The goal is to limit the danger of infection in highly populated places where social distance may be an issue. While analysing the movement of other devices, the proposed walkway proposes a pedestrian path in real time. First, IoT devices were divided into communities based on two SIoT connections that took into consideration device locations as well as friendship norms among their owners. As a result, the weights on the city map roadways represented their safety requirements. After that, they employ the Dijkstra algorithm, which is a navigation algorithm, to propose the safest path to go. The potential to achieve a trade between the two most secure and quicker routes depending on pedestrian preferences was demonstrated using imitation effects in a real-world IoT data collection. This research [9] proposes a signal processing architecture that enables for combined topic movement analysis and automated temperature testing. The system includes infrared sensors that use temperature data to track subject mobility and health. Existing IoT wireless devices placed according to different structures link the sensors to the network. The goal of the programme is to link the local action of the headers by tracking their equal distance and route of arrival, as well as the remarkable finding of body temperature in individuals near the IR sensors. This article examines acceptable practises as well as proper application implementation employing field standards, with a focus on Bayesian approaches. For privacy neutrality, the suggested framework may be used to both public and private health-care services, as well as intelligent living and shared space circumstances.

W. Lv and colleagues propose chain, an expanded and illegal blockchain protocol. 1) By integrating the anonymous evidence-based protocol with the key security mechanism, the SRC protocol's SRC secrecy and the accompanying block structure are enhanced. As a result, there is no longer any link between personal identify and on-chain location data. The on-chain property owner may still claim ownership at that moment without releasing the secret key to anybody else. 2) Proposed a field-based practise of incentives to encourage IoT witnesses to promote the monitoring industry's oversight. The suggested communication tracking and location verification technique works effectively in the actual world, according to several results. To assure the availability of monitoring of digital communications in the actual world, the suggested contract tracking protocol's power consumption, time delay for each procedure, and BLE performance have been studied [10].

S. Arun Kumar et al. present a preventative method in this study, proposing the notion of a smart wrist band with a heat sensor and IoT technology. Blood pressure measures are also taken from time to time with the use of a blood pressure sensor. As a result, once the temperature or blood pressure are determined to be abnormal, this gadget helps to generate an alarm. With the use of IoT technology, faster information is transmitted on to the basic level user and second level relatives. As a result, by monitoring and notifying victims, this joint and active wrist band plays a critical role in saving lives.Because bacterial diseases are linked to a rise in body temperature, our device will be extremely useful in detecting them early. Traditional measurement methods frequently need human participation

and are not of combined size. These issues are addressed in this architecture, which involves minimum management and sensor configuration for temperature and blood pressure monitoring, data processing, and storage [11]. The goal of this article, by D. Chloros et al [12], is to investigate the developmental obstacles and potential for apps that track transmission, as well as how IoT systems might be used to record symptoms. The benefits and necessity for these apps' development will be highlighted by evaluating their potential. The Fluspot application was created specifically for this investigation. By raising public awareness and providing timely information, Fluspot hopes to help reduce the spread of infections this season. Fluspot uses a wearable IoT device to closely monitor flu flows and collect user inputs for viral propagation to the site. This anonymised and aggregated data is shown on a map to provide a more accurate picture of the situation in each location. Another major element is that the artefact's ability to monitor wearable indications is critical for users in their daily lives. The work by A. Waheed et al. [13] examines a range of technologies utilised in a variety of situations, including social isolation and prevention, isolation and isolation, COVID detection and assessment, therapy and patient care, and hospital administration. This study discusses transparent planning, technical techniques, and digital procedures, as well as the most up-to-date intelligent technologies in a range of disciplines that can aid in overcoming coronavirus intensity. IoT, AI, and machine learning play a significant role in the fight against COVID-19. AI has made a substantial contribution to the resource management pandemic, public awareness, security management, and supporting professionals in implementing stringent standards.

In the COVID-19 era, V. Shubina et al tracking of wearable contact is garnering increasing focus in order to successfully prevent sickness. As a result, identifying viable technologies for tracking wireless communication and their wearability is critical. Existing contact monitoring app trading necessitates a detailed examination of technical skills such as accuracy, power consumption, availability, error sources when dealing with wireless channels, privacy concerns, and hurdles to larger apparel market access. We find, based on considerable literature study, that demarcated buildings, when compared to intermediate techniques, provide a superior location to trade in terms of accuracy and user willingness to utilise them, taking privacy issues into account. This study gives a brief summary of the technological options available for human monitoring services, describes fundamental concepts that influence the efficiency of digital communication tracking, and discusses the effects of wear on coping with viral infection transmission [14]. T. Luo et al. [15] provide a model for infectious, contagious, infectious, asymptomatic disease, Diagnosis, and Death (SEINRHD). The model was created using epidemiological data from COVID-19 in China and the estimation of social network heterogeneity. The original Wuhan public epidemic was recreated and updated with accurate data. We utilised this model to look into strategies to manage the outbreak in instances when three-dimensional signals were not apparent. On the basis of effective replication rates, the occurrence of exceptionally high infections, and the kind and structure of transmission, the impact of undetected cases on the propagation of the epidemic was estimated. Asymptomatic patients can be managed to assist the infection curve shorten. When compared to asymptomatic and non-symptomatic tracking, tracking 75% of non-symptomatic patients results in a total reduction of 32.5 percent in new cases. During the outbreak, emphasis should be placed on illness control and prevention in families.

Proposed Method

System Overviem
The following sub-systems make up the proposed system: 1) An Arduino Uno-based temperature measuring device 2) IoT system that measures the Arduino board via social distancing 3) on the server 4) A security guard smartphone application. To begin, everyone attempting to enter the residence must pass an unmodified temperature check. We're utilising an Arduino Uno with an infrared thermometer (e.g., MLX906148) or a hot camera sensor for this (AMG88339 for example). It also employs the ESP8266 Wi-Fi module for MQTT protocol connection with Edge servers. If that person's body temperature is anomalous, the door is locked, and a MQTT message is delivered to the server, providing both the temperature and the location where it was recorded. This message is received by the server, which then transmits it and carries on. with a security guard's smartphone app, so they can arrive and make

sure the individual isn't attempting to enter a work zone. In specific regions, Arduino board devices verify whether public distances are being utilised properly or not. Similarly, when public distances do not operate well in particular rooms, a MQTT message will be sent to alert security personnel. Message processing, event logging, reflection, and message transmission are accomplished on the server side using the MQTT broker and the triple semantic store. Edge servers receive communications, do semantic annotations, and make assumptions to choose the appropriate security guard to notify. Security guards utilise a basic Android mobile app that receives MQTT messages from the server and visualises data about the position. Figure 3 depicts social distancing with a smart device for Covid-19, with the goal of ensuring that COVID-19 safety rules are followed appropriately indoors. The proposed calculation will provide a satisfactory result for physical separation using an ultrasonic sensor. The following is the pseudo-code for the suggested calculation:

IR Sensor

There are two sorts of temperature measurement tools: touch and non-touch. Thermocouples, heat-resistant heat exchangers (RTDs), thermistors, and semiconductor temperature sensors are examples of infrared temperature sensors used in communication equipment. Because contact lenses monitor temperature, they require physical contact with the item being measured to bring the sensor body up to temperature. When a relatively big sensor meets a tiny object and functions as a heat sink, the temperature of the object may be altered. Figure 5: Infrared sensor

Ultrasonic Sensor

Ultrasonic sensors use ultrasonic waves to measure distance. The sensor head sends out an ultrasonic wave that is reflected back to it from the direction. Ultrasonic sensors use the time between output and reception to calculate the distance to the target. The ultrasonic sensor can identify items that are far away from the robot. The ultrasonic sensor, unlike the touch sensor, is not affected by physical contact. The range gives you plenty of room to react.For distances of 10 inches or more, an ultrasonic sensor is often utilised, whereas for shorter distances, a light sensor is typically employed. Ultrasonic sensors detect moving things and measure each object's relative location and movement. The vertical movement of each ultrasonic sensor is measured using a measurement of the measurement range, and the movement in the measuring area is measured using a modified distance data conversion. Figure 6 depicts an ultrasonic sensor.

Social Distancing Algorithm

This is the second step of our framework proposal. The suggested social distance monitoring algorithm serves two purposes. Function 1 aids in the identification of things in the picture. It employs a detection approach to offer human positions as aggregate values like XA (left), YA (top), XB (right), and YB (bottom) (bottom).

$$X = (X_A + X_B) / 2 \quad (1)$$

$$Y = (Y_A + Y_B) / 2 \quad (2)$$

where XA, YA, XB, and YB are the left, top, right, and bottom compound numbers of an object. Coin or centroid values are X and Y. These parameters are also passed on to the next function, which calculates social distance. The distance between the two items is calculated using the Euclidean distance, which indicates their closeness, as indicated in Eq. 3. When comparing this distance vector to the previously indicated threshold value, the choice was taken. If the Euclidean range is less than a specific threshold, it is thought that the two elements did not adhere to the conditions of social reduction or did not generate enough space between them.

$$D = \sqrt{(X2 - X1)2} + (Y2 - Y1)2 \quad (3)$$

Where (X1, X2) and (Y1, Y2) are Centroid values of two objects.

Pseudocode

To distinguish between human and object in the context of physical removal.

1. Human or item in the range of ultrasonic sensors.
2. output: Notifying the client with a sound signal.
3. Uses the ULTRASONIC sensor module to detect the presence of individuals.
4. If a person or moving object is detected, measure the distance between them.
5. If the distance is less than 2 metres, activate the sound directive for that distance alone.
6. Prepare a message and caution for safe separation and disinfection if the distance is similar to 1.5 m.
7. The message will be repeated till the person does not clean. Individuals must push the reset button after disinfection.

Algorithm: Social Distancing Measurement

Input: I_N: Image I containing N Number of frames of size 225x225x3
Output :D: Distance between two objects
Initialize Parameter:
Threshold = 90.0,
Human_Count= 0;
Cvo = [],
Lcvo = [],
Cen = [],
Center = [],

Function Object_Coordinates(V)
Picks = Human_Detection_Framework (VN)
For (X_A, Y_A, X_B, Y_B) in Pick :
Cvo = $[X_A, Y_A, X_B, Y_B]$
C1 = $((X_A + X_B) * 0.5)$
C2 = $((Y_A + Y_B)*0.5)$
Cen = [C1,C2]
Center.append(Cen)
Lcvo.append(Cvo)
Human_Count +=1

End For
Return Human_Count, Lcvo,center,Image
End *Function*

Temperature Checking

Using a wireless IR sensor, the temperature checking system based on Adriano Uno detects the passenger's temperature. One by one, the passengers pass. If the temperature of the passenger is higher than the average human body temperature (37 °C), the Adriano Uno generates a signal to lock the door to prevent the person from entering the building and sends a MQTT message indicating that a person with a high body temperature has been detected at a specific location. Otherwise, the door to let the individual in is opened.

RESULT AND ANALYSIS

The IoT-based portable monitoring device is meant to measure the signals associated with COVID-19 and uses a machine learning model to anticipate the different machine learning techniques. Machine Learning techniques to increase the model's accuracy and impact, as well as to avoid disease transmission in future global health issues.

Pradeep *et al.,*

Figure 7 shows the various machine learning algorithms. KNN delivers the best set of performance values with a 95 percent accuracy. The performance of two persons was examined in the distant sensing test, and it is projected to decline as the number of people inside the distance view rises. The distance monitor's performance fluctuates with object distance from the camera, as it does with the measurement initially derived between pixels and meters. Figure 8 shows how K-Means algorithms are used to calculate social distance. It is utilized to execute two points on the folks who have been detected. Because social distancing is tested between a minimum of two individuals, the cluster's minimum necessary points are set to two, and the two-person distance parameter is set to two meters. If the space between two people is very small, it is considered risky; if the distance is greater, it is considered safe. The performance of all of the models was evaluated using criteria such as accuracy, specificity, precision, recall/sensitivity, and F1 score, as shown in Table 1. KNN is trustworthy for monitoring IoT-based portable monitoring device is developed to measure the signals connected with COVID-19, according to the accuracy values of four models. With the highest F1 score of the four models, KNN emerges as the best. Although the SVM model is relatively similar to the decision tree, it cannot be regarded a robust model because to its poor recall of 0.83.

CONCLUSION

The proposed technology is based on real-time sensors such as infrared (IR) and ultrasonic sensors for effective social distancing and contact tracing for COVID-19 prevention. Temperature, heart rate, SpO2, and cough rate are all measured using the wearable sensor layer. It also sends real-time patient GPS position data to medical administrators and notifies family members to alleviate stress. During the epidemic, the app's peripheral interface is in charge of storing, collecting, and analysing data in order to monitor and govern public life and administration. The Android mobile app is quite helpful in informing family responders on patient status and lowering transmission rates. The wearable gadget is totally functional in terms of receiving patient health symptoms both during and after an illness. In order to control, monitor, and control patients who may be infected with COVID-19 in the spread of the disease, this system was tested and verified in real time at the hospital. A wearable gadget might be used as a model, allowing airport travellers to sit alone as they arrive and depart. This work has undergone significant investigation in order to deliver the greatest device performance by comparing current domains. The project's new features are used for a variety of purposes, including measuring health symptoms, tracking and monitoring a patient while detained, storing data to predict the situation, and notifying authorities in a timely manner so that they can be properly monitored and use the Android platform to stay informed. Respondents' family members' patient status. Our suggested technique might potentially be utilised to avoid disease spread in the future in the case of global health issues. Also, take use of this proposed technology, which can assist in diagnosing and treating early symptoms.

REFERENCES

1. Y. C. Hou, M. Z. Baharuddin, S. Yussof and S. Dzulkifly, "Social Distancing Detection with Deep Learning Model," *2020 8th International Conference on Information Technology and Multimedia (ICIMU)*, 2020, pp. 334-338, doi: 10.1109/ICIMU49871.2020.9243478.
2. A. H. Ahamad, N. Zaini and M. F. A. Latip, "Person Detection for Social Distancing and Safety Violation Alert based on Segmented ROI," *2020 10th IEEE International Conference on Control System, Computing and Engineering (ICCSCE)*, 2020, pp. 113-118, doi: 10.1109/ICCSCE50387.2020.9204934.
3. N. H. Motlagh *et al.*, "Monitoring Social Distancing in Smart Spaces using Infrastructure-Based Sensors," *2021 IEEE 7th World Forum on Internet of Things (WF-IoT)*, 2021, pp. 124-129, doi: 10.1109/WF-IoT51360.2021.9595897.
4. https://binged.it/3rD1btm
5. B.Sathyabama, A. Devpura, M. Maroti and R. S. Rajput, "Monitoring Pandemic Precautionary Protocols using Real-time Surveillance and Artificial Intelligence," *2020 3rd International Conference on Intelligent Sustainable Systems (ICISS)*, 2020, pp. 1036-1041, doi: 10.1109/ICISS49785.2020.9315934.
6. Sengupta, K., Srivastava, P.R. HRNET: AI-on-Edge for Mask Detection and Social Distancing Calculation. *SN COMPUT. SCI.* **3,** 157 (2022). https://doi.org/10.1007/s42979-022-01023-1

7. S. Srinivasan, R. Rujula Singh, R. R. Biradar and S. Revathi, "COVID-19 Monitoring System using Social Distancing and Face Mask Detection on Surveillance video datasets," *2021 International Conference on Emerging Smart Computing and Informatics (ESCI)*, 2021, pp. 449-455, doi: 10.1109/ESCI50559.2021.9396783.

8. A. Khanfor, H. Friji, H. Ghazzai and Y. Massoud, "A Social IoT-Driven Pedestrian Routing Approach During Epidemic Time," *2020 IEEE Global Conference on Artificial Intelligence and Internet of Things (GCAIoT)*, 2020, pp. 1-6, doi: 10.1109/GCAIoT51063.2020.9345900.

9. S. Savazzi, V. Rampa, L. Costa, S. Kianoush and D. Tolochenko, "Processing of Body-Induced Thermal Signatures for Physical Distancing and Temperature Screening," in *IEEE Sensors Journal*, vol. 21, no. 13, pp. 14168-14179, 1 July1, 2021, doi: 10.1109/JSEN.2020.3047143.

10. W.Lv, S. Wu, C. Jiang, Y. Cui, X. Qiu and Y. Zhang, "Towards Large-Scale and Privacy-Preserving Contact Tracing in COVID-19 Pandemic: A Blockchain Perspective," in *IEEE Transactions on Network Science and Engineering*, vol. 9, no. 1, pp. 282-298, 1 Jan.-Feb. 2022, doi: 10.1109/TNSE.2020.3030925.

11. S. Arunkumar, N. Mohana Sundaram and D. Ishvarya, "Temperature Sensing Wrist Band for Covid-19 Crisis," *2021 International Conference on Advancements in Electrical, Electronics, Communication, Computing and Automation (ICAECA)*, 2021, pp. 1-5, doi: 10.1109/ICAECA52838.2021.9675689.

12. D. Chloros and D. Ringas, "Fluspot: Seasonal flu tracking app exploiting wearable IoT device for symptoms monitoring," *2020 5th South-East Europe Design Automation, Computer Engineering, Computer Networks and Social Media Conference (SEEDA-CECNSM)*, 2020, pp. 1-7, doi: 10.1109/SEEDA-CECNSM49515.2020.9221843.

13. A. Waheed and J. Shafi, "Successful Role of Smart Technology to Combat COVID-19," *2020 Fourth International Conference on I-SMAC (IoT in Social, Mobile, Analytics and Cloud) (I-SMAC)*, 2020, pp. 772-777, doi: 10.1109/I-SMAC49090.2020.9243444.

14. V. Shubina, A. Ometov and E. Simona Lohan, "Technical Perspectives of Contact-Tracing Applications on Wearables for COVID-19 Control," *2020 12th International Congress on Ultra Modern Telecommunications and Control Systems and Workshops (ICUMT)*, 2020, pp. 229-235, doi: 10.1109/ICUMT51630.2020.9222246.

15. T. Luo, Z. Cao, Y. Wang, D. Zeng and Q. Zhang, "Role of Asymptomatic COVID-19 Cases in Viral Transmission: Findings From a Hierarchical Community Contact Network Model," in *IEEE Transactions on Automation Science and Engineering*, doi: 10.1109/TASE.2021.3106782.

Table 1. Classification result for four models

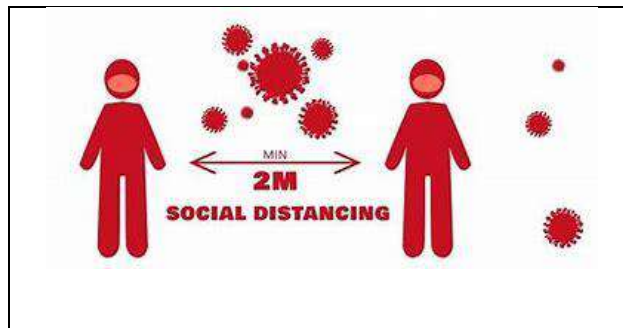| Models	Evaluation Metrices								
	TP	TN	FP	FN	Accuracy	Specificity	Precision	Recall	F1Score
SVM	28	6	2	3	0.60	0.70	0.63	0.90	0.75
Random Forest	29	6	2	2	0.88	0.75	0.73	0.75	0.90
KNN	29	5	3	2	0.95	0.89	0.90	0.93	0.92
Decision tree	26	6	2	5	0.65	0.75	0.69	0.73	0.72

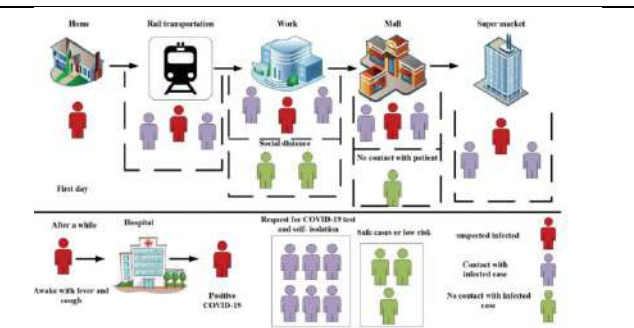**Fig.1.Social distancing [4]**

Fig.2. Contact tracing areas in public places
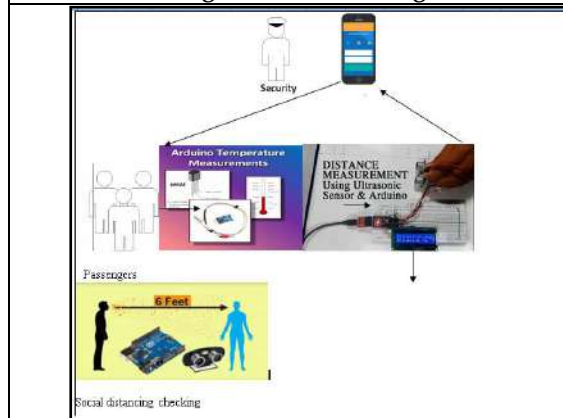

Fig. 3. Overall Architecture of Social Distancing
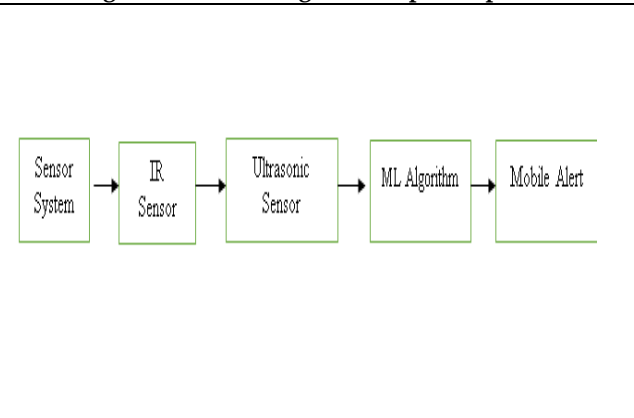

Fig.4.Social Distancing using Smart Device For COVID-19
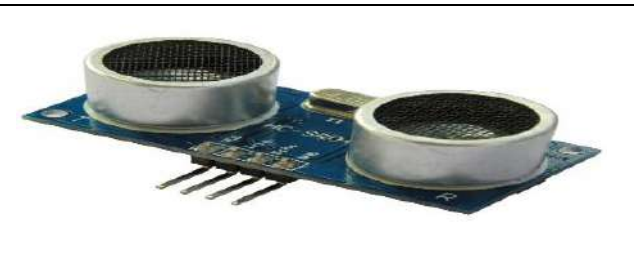

Fig. 5. IR Sensor

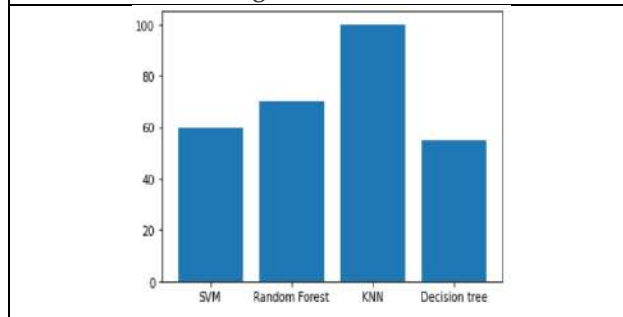

Fig . 6. Ultrasonic Sensor

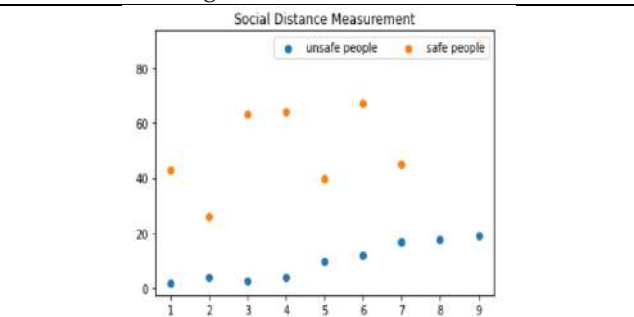**Fig.7. Machine learning's algorithms**

Fig.8. Social Distance Measurement

Smart Agricultural Management System using Big Data Analysis and Internet of Things

Dhruva R. Rinku[1]*, Y.Sudha[2], S.Bharathi[2] and G.Ravikishore[3]

[1]Associate Professor, Department of ECE, CVR College of Engineering, Hyderabad, India.
[2]Department of EEE, Malla Reddy Engineering College (Autonomous), Maisammaguda, Secunderabad, Telangana State, India-500100.
[3]Department of ECE, Vidya Jothi Institute of Technology, Chilkur Road, Hyderabad, Telangana State, India - 500075.

*Address for Correspondence
Dhruva R. Rinku
Associate Professor, Department of ECE,
CVR College of Engineering,
Hyderabad, India.
Email: rinkudhruva.ravi@gmail.com

ABSTRACT

The information provided by a smart agriculture management system varies depending on the crop. It automatically regulates numerous agricultural gadgets while also reducing agricultural manpower. Temperature sensor, humidity sensor, leaf sensor, GPS module, and image sensor are used in this study to collect various data on a specific crop in the agricultural area. These details are transferred to the CC3200 launch pad and subsequently saved in the cloud. The information is obtained from the cloud via an Android application and provided to the customer or farmers. The decision-making and prediction in this android framework are based on cloud data, which is analyzed utilizing ANN, fuzzy logic, and neuro fuzzy systems. Farmers will benefit greatly from the suggested method. The proposed method performance measured by the following parameters accuracy 89%, precision 87%, recall 85% and execution time 120 ms.

Keywords: sensor, CC3200 launch pad, ANN, fuzzy logic and neuro fuzzy system.

INTRODUCTION

Crop growth development, corporate farms, agricultural engineering, crop development section, harvesting and transportation, smart weighbridge, agricultural financials, agronomy, vehicle management, and farmer assistance portal are all examples of agriculture management systems (AMS). AMS provides detailed information on the crop as well as control measuring procedures for that crop [1]. It includes everything and even maintains track of the

48848

numerous agricultural processes performed on the crop. It also contains advice on calculating amounts for various inputs like as pesticides, seed, harvesting schedule, support organization, fertilizer, and labor planning [2]. Agricultural inventory management systems are used to give agricultural statistics such as crop damage, production detection, seasonal monitoring, data mining services, and online up-to-date data warehouse [3]. Information and communication technology, big data analysis, internet of things, cloud computing, robots, artificial intelligence, and other technologies are all used in smart farming [4]. The communication between the processor and the sensor, as well as the processor and the client, is established using information and communication technology [5]. Big data analysis is utilized to give diverse crop information such as seed, variety, fertilizer, insecticides, and so on. We must forecast the future utilizing numerous big data analysis approaches based on this diverse data. IoT is a new technology that connects various kinds of devices to the cloud and processor, including temperature sensors, leaf sensors, image sensors, moisture sensors, humidity sensors, and so on [6]. Each device communicates with the cloud or processor via a wired or wireless link. Artificial intelligence is used to construct a hardware or software system model to maintain an agricultural management system in an effective manner employing robotic techniques such as automated irrigation, automatic fertilizer, and automatic diseases prevention and control systems, among others. For decision-making and prediction, artificial neural networks, fuzzy logic, and neuro fuzzy systems are commonly utilized [7].

METHODOLOGY

This research provides farmers with useful information as well as recommendations for numerous agricultural issues. This system gathers data from temperature sensors, humidity sensors, leaf sensors, a GPS module, an image sensor, wind flow sensors, and soil sensors, among other sensors. This data is stored in the CC3200 processor and then transferred to the cloud. The Android application pulls data from the cloud and sends it to agriculture producers or clients. The block diagram of proposed method is shown figure (1).

TEMPERATURE SENSORS
The LM 35 temperature sensor is linked to the CC3200 CPU. It's a temperature sensor with a precision integrated circuit. The output voltage is proportional to the temperature in Celsius [8]. The ambient air temperature and surface temperature are measured by this sensor. It can detect temperatures ranging from -55 to +150 degrees Celsius. Figure 2 shows the pin arrangement of the LM 35.

HUMIDITY SENSORS
The humidity sensor is a three-pin device, as shown in Figure (3). It is used to determine the moisture content and temperature of the air. The ratio of moisture in the air at a given temperature to the highest value of moisture at the same temperature is known as relative humidity [9]. Two electrodes are placed in the agricultural area to monitor humidity.

LEAF SENSORS
The water loss or water shortage stress in agricultural plant leaves is measured using a leaf sensor [10]. The automatic irrigation management system makes extensive use of this data. The automated watering system is turned on if the information value exceeds the threshold value; otherwise, it is turned off. Figure 4 shows the pin arrangement of a leaf sensor [11].

GPS MODULE
The GPS module is utilised to determine the current geographical position. The latitude and longitude data are used to denote the location. It is a gadget that can read information from a satellite [12]. When the GPS module is turned on, the latitude and longitude of the current geographical position are shown automatically. Figure 5 shows the GPS module pin arrangement .

Dhruva R. Rinku *et al.*,

IMAGE SENSOR

The image of the agricultural area was captured using an image sensor. It detects and transmits data and is used to create an image matrix [13]. In general, pictures are represented as matrices, with each member in the matrix being referred to as a pixel. Every pixel has a value, which spans from 0 to 255. It's a type of electronic imaging device that can store both analogue and digital data [14]. Figure 6 shows the image sensor pin layout with the CC3200. We are employing the image sensor MT9D111 camera module with the CC3200 launch pad in this research. The newest SDK Firmware Package software is required. This image sensor is capable of capturing QVGA images in JPEG format [15].

CC3200 LAUNCH PAD

The CC3200 Launch pad was created with internet of things applications in mind. It is a descendant of arm cortextm-m4. Wi-Fi capability and internet on a chip are two of the CC3200 launch pad's main features. The open source software Energia is used to programme the CC3200 launch pad and gear [16]. It offers the user with some basic default example programmes for various hardware applications; we may edit the current example programmes to meet our needs or create new ones. Figure 7 shows the text editor in the Energia software development environment. The hardware view of CC3200 shown in figure(8).

CLOUD

In this research work we are using IBM cloud [17]. The following steps are used to store the sensor's data or information to cloud as shown in figure 10.
1. Create a software to save sensor data in the cloud.
2. Join the IBM Watson Internet of Things platform. Service that begins immediately
3. Data visualization
4. Add your gadget to the Watson IoT platform.
5. Connecting to a registered device on the IBM Watson IoT platform

Android Application

To make an android application, you'll need the Android SDK tool. Home, Sensors, Prediction, Management System, and Other Information are the five key sections of the Android application. For decision-making and autonomous control of diverse devices, artificial neural networks (AN), fuzzy logic, and neuro fuzzy systems are employed. Figure 11 depicts the Android application framework . The java software is used to transfer data from the cloud to the android application, while the XML programme is used to construct the android frame layout [18]. The artificial neural network (ANN) is a supervised learning approach for classification and recognition. If-then rules are used in fuzzy logic to make decisions [19]. Neuro fuzzy method is a hybrid system. It is a combination of ANN and Fuzzy logic used for both classification and decision-making applications.

RESULT ANALYSIS

Three methodologies are used in the implementation of this suggested system: ANN, Fuzzy logic, and Neuro fuzzy system. The accuracy value is used to guide the evolution of the proposed system. Figure 12 to 15 and Table 1to 4 shows the compression graph for the suggested system. In this graph, the ANN technique outperforms the Fuzzy logic method in terms of accuracy [20]. When compared to ANN and fuzzy logic, the neuro fuzzy system produces better results.

CONCLUSION

Smart agriculture management system offers farmers with a wealth of helpful information and beneficial recommendations, and it can control and automate all other equipment connected to it. Each sensor is connected to the processor, and the sensor readings are saved in the cloud so that farmers can readily access all of the metrics

using an Android app. Farmers can minimise crop loss and possibly boost agricultural product yields if they discover the illness in the plant at an early stage. In this proposed method using the android application model makes everyone to access the information and is easier and faster. In future we are planning to implement the app in various local languages like Tamil, Hindi, Malayalam, Bengali.etc .This method provide above 85% of accuracy.

REFERENCES

1. S. Qazi, B. A. Khawaja and Q. U. Farooq, "IoT-Equipped and AI-Enabled Next Generation Smart Agriculture: A Critical Review, Current Challenges and Future Trends," in IEEE Access, vol. 10, pp. 21219-21235, 2022, doi: 10.1109/ACCESS.2022.3152544.
2. U. Shafi et al., "A Multi-Modal Approach for Crop Health Mapping Using Low Altitude Remote Sensing, Internet of Things (IoT) and Machine Learning," in IEEE Access, vol. 8, pp. 112708-112724, 2020, doi: 10.1109/ACCESS.2020.3002948.
3. H. A. Alharbi and M. Aldossary, "Energy-Efficient Edge-Fog-Cloud Architecture for IoT-Based Smart Agriculture Environment," in IEEE Access, vol. 9, pp. 110480-110492, 2021, doi: 10.1109/ACCESS.2021.3101397.
4. O. Friha, M. A. Ferrag, L. Shu, L. Maglaras and X. Wang, "Internet of Things for the Future of Smart Agriculture: A Comprehensive Survey of Emerging Technologies," in IEEE/CAA Journal of AutomaticaSinica, vol. 8, no. 4, pp. 718-752, April 2021, doi: 10.1109/JAS.2021.1003925.
5. A. D. Boursianis et al., "Smart Irrigation System for Precision Agriculture—The AREThOU5A IoT Platform," in IEEE Sensors Journal, vol. 21, no. 16, pp. 17539-17547, 15 Aug.15, 2021, doi: 10.1109/JSEN.2020.3033526.
6. W. Zhao, X. Wang, B. Qi and T. Runge, "Ground-Level Mapping and Navigating for Agriculture Based on IoT and Computer Vision," in IEEE Access, vol. 8, pp. 221975-221985, 2020, doi: 10.1109/ACCESS.2020.3043662.
7. N. N. Misra, Y. Dixit, A. Al-Mallahi, M. S. Bhullar, R. Upadhyay and A. Martynenko, "IoT, Big Data, and Artificial Intelligence in Agriculture and Food Industry," in IEEE Internet of Things Journal, vol. 9, no. 9, pp. 6305-6324, 1 May1, 2022, doi: 10.1109/JIOT.2020.2998584.
8. A. Vangala, A. K. Das, N. Kumar and M. Alazab, "Smart Secure Sensing for IoT-Based Agriculture: Blockchain Perspective," in IEEE Sensors Journal, vol. 21, no. 16, pp. 17591-17607, 15 Aug.15, 2021, doi: 10.1109/JSEN.2020.3012294.
9. M. S. Farooq, O. O. Sohail, A. Abid and S. Rasheed, "A Survey on the Role of IoT in Agriculture for the Implementation of Smart Livestock Environment," in IEEE Access, vol. 10, pp. 9483-9505, 2022, doi: 10.1109/ACCESS.2022.3142848.
10. M. A. Ferrag, L. Shu, X. Yang, A. Derhab and L. Maglaras, "Security and Privacy for Green IoT-Based Agriculture: Review, Blockchain Solutions, and Challenges," in IEEE Access, vol. 8, pp. 32031-32053, 2020, doi: 10.1109/ACCESS.2020.2973178.
11. E. -T. Bouali, M. R. Abid, E. -M. Boufounas, T. A. Hamed and D. Benhaddou, "Renewable Energy Integration Into Cloud & IoT-Based Smart Agriculture," in IEEE Access, vol. 10, pp. 1175-1191, 2022, doi: 10.1109/ACCESS.2021.3138160.
12. D. Xue and W. Huang, "Smart Agriculture Wireless Sensor Routing Protocol and Node Location Algorithm Based on Internet of Things Technology," in IEEE Sensors Journal, vol. 21, no. 22, pp. 24967-24973, 15 Nov.15, 2021, doi: 10.1109/JSEN.2020.3035651.
13. R. Alfred, J. H. Obit, C. P. -Y. Chin, H. Haviluddin and Y. Lim, "Towards Paddy Rice Smart Farming: A Review on Big Data, Machine Learning, and Rice Production Tasks," in IEEE Access, vol. 9, pp. 50358-50380, 2021, doi: 10.1109/ACCESS.2021.3069449.
14. T. Anand, S. Sinha, M. Mandal, V. Chamola and F. R. Yu, "AgriSegNet: Deep Aerial Semantic Segmentation Framework for IoT-Assisted Precision Agriculture," in IEEE Sensors Journal, vol. 21, no. 16, pp. 17581-17590, 15 Aug.15, 2021, doi: 10.1109/JSEN.2021.3071290.
15. R. K. Singh, R. Berkvens and M. Weyn, "AgriFusion: An Architecture for IoT and Emerging Technologies Based on a Precision Agriculture Survey," in IEEE Access, vol. 9, pp. 136253-136283, 2021, doi: 10.1109/ACCESS.2021.3116814.

16. V. P. Kour and S. Arora, "Recent Developments of the Internet of Things in Agriculture: A Survey," in IEEE Access, vol. 8, pp. 129924-129957, 2020, doi: 10.1109/ACCESS.2020.3009298.

17. G. Castellanos, M. Deruyck, L. Martens and W. Joseph, "System Assessment of WUSN Using NB-IoT UAV-Aided Networks in Potato Crops," in IEEE Access, vol. 8, pp. 56823-56836, 2020, doi: 10.1109/ACCESS.2020.2982086.

18. S. I. Hassan, M. M. Alam, U. Illahi, M. A. Al Ghamdi, S. H. Almotiri and M. M. Su'ud, "A Systematic Review on Monitoring and Advanced Control Strategies in Smart Agriculture," in IEEE Access, vol. 9, pp. 32517-32548, 2021, doi: 10.1109/ACCESS.2021.3057865.

19. G. Nagasubramanian, R. K. Sakthivel, R. Patan, M. Sankayya, M. Daneshmand and A. H. Gandomi, "Ensemble Classification and IoT-Based Pattern Recognition for Crop Disease Monitoring System," in IEEE Internet of Things Journal, vol. 8, no. 16, pp. 12847-12854, 15 Aug.15, 2021, doi: 10.1109/JIOT.2021.3072908.

20. G. Manogaran, C. -H. Hsu, B. S. Rawal, B. Muthu, C. X. Mavromoustakis and G. Mastorakis, "ISOF: Information Scheduling and Optimization Framework for Improving the Performance of Agriculture Systems Aided by Industry 4.0," in IEEE Internet of Things Journal, vol. 8, no. 5, pp. 3120-3129, 1 March1, 2021, doi: 10.1109/JIOT.2020.3045479.

21. P. K. Kashyap, S. Kumar, A. Jaiswal, M. Prasad and A. H. Gandomi, "Towards Precision Agriculture: IoT-Enabled Intelligent Irrigation Systems Using Deep Learning Neural Network," in IEEE Sensors Journal, vol. 21, no. 16, pp. 17479-17491, 15 Aug.15, 2021, doi: 10.1109/JSEN.2021.3069266.

22. G. Delnevo, R. Girau, C. Ceccarini and C. Prandi, "A Deep Learning and Social IoT Approach for Plants Disease Prediction Toward a Sustainable Agriculture," in IEEE Internet of Things Journal, vol. 9, no. 10, pp. 7243-7250, 15 May15, 2022, doi: 10.1109/JIOT.2021.3097379.

Table 1: Performance Analysis based on accuracy

Sensors	Accuracy			
	MDC	**ANN**	**Fuzzy**	**Neuro-Fuzzy**
Temperature	65	71	78	89
Humidity	68	75	75	85
Leaf	65	76	76	86
Image	67	75	74	87

Table 2: Performance Analysis based on Recall

Sensors	Recall (%)			
	MDC	**ANN**	**Fuzzy**	**Neuro-Fuzzy**
Temperature	64	75	78	87
Humidity	65	71	76	89
Leaf	64	72	77	87
Image	64	71	78	82

Table 3: Performance Analysis based on Precision

Sensors	Precision (%)			
	MDC	**ANN**	**Fuzzy**	**Neuro-Fuzzy**
Temperature	61	74	77	84
Humidity	63	75	76	85
Leaf	64	75	77	86
Image	62	76	78	84

Dhruva R. Rinku *et al.,*

Table 4: Performance Analysis based on accuracy

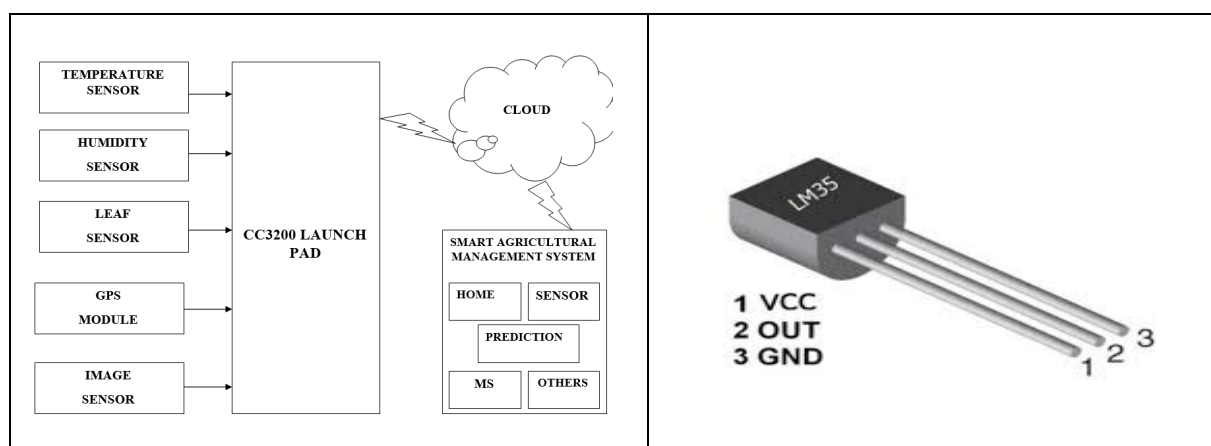| Sensors	Execution time (ms)			
	MDC	**ANN**	**Fuzzy**	**Neuro-Fuzzy**
Temperature	321	256	190	120
Humidity	325	245	180	115
Leaf	362	235	178	123
Image	385	286	175	145

Figure 1: Block Diagram for proposed System
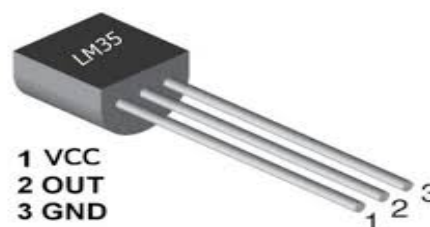
Figure 2: Temperature Sensor

Figure3: Humidity Sensor

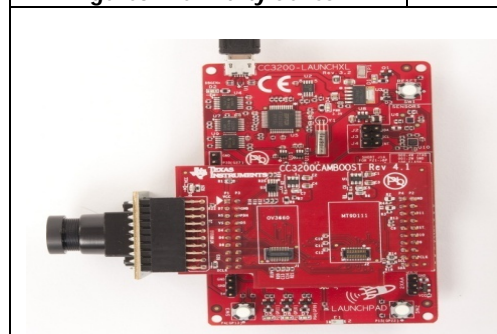**Figure 4:Leaf Sensor**
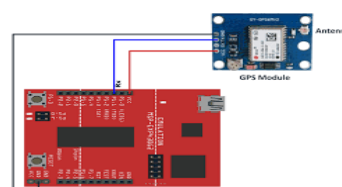
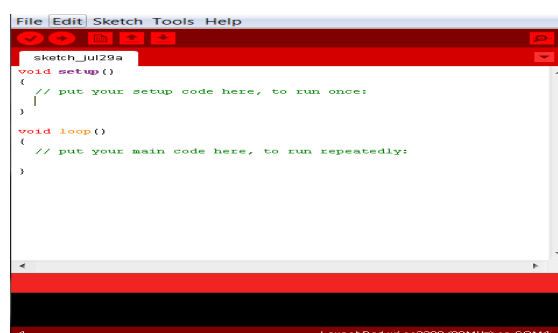**Figure 5 :GPS module**

Figure 6: Image sensor

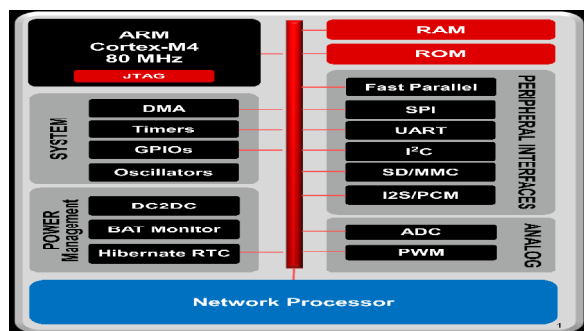**Figure 7: CC3200 Launch Pad**

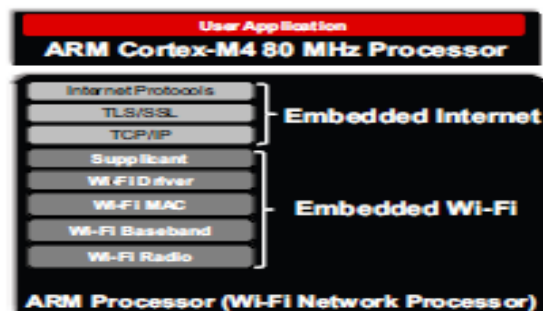**Figure 8: Hardware View of CC3200**

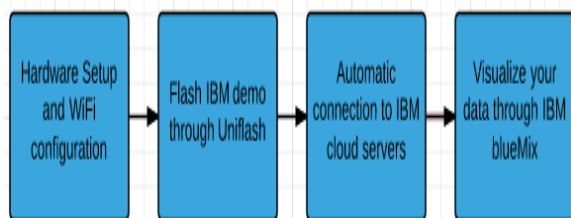**Fig 9:　CC3200: the Software view of CC3200**
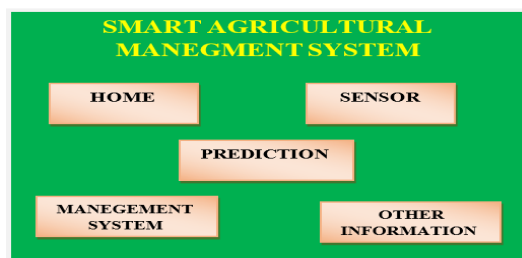

Figure 10. Cloud data storage

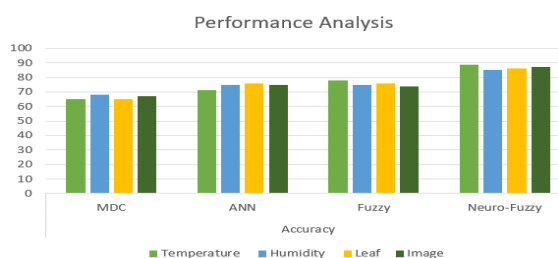**Figure11: Android Application Frame work**

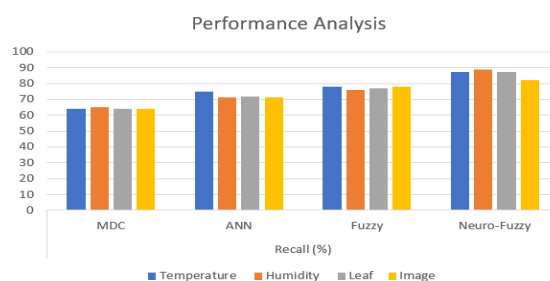**Figure 12: Performance Analysis based on accuracy**

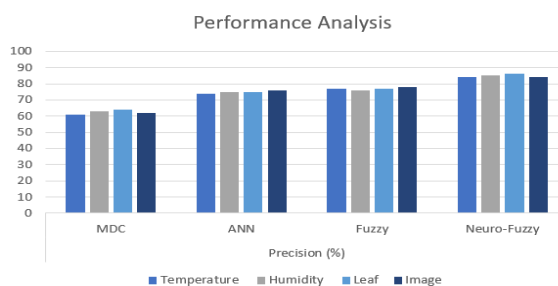**Figure 13: Performance Analysis based on Recall**

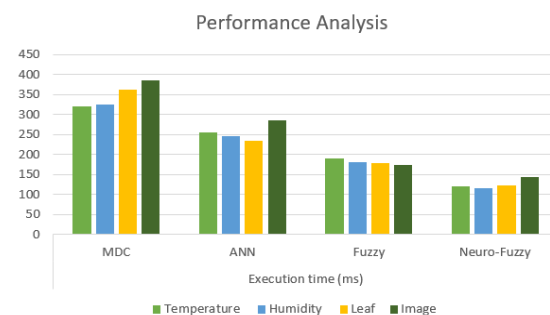**Figure 14: Performance Analysis based on precision**

Figure 15: Performance Analysis based on Execution time

Neural Network System based on Real time Object Detection and Recognition for Video Surveillance Systems

Raja Reddy Duvvuru[1]*, K. Anitha Reddy[2], P. Chandana Priya[3], K.Vimala Kumar[4] and   B. Sudharshan Reddy[5]

[1]Associate Professor, EEE Department, Malla Reddy Engineering College, Secundrabad, Telangana, India.
[2]Assistant Professor, EEE Department, Malla Reddy Engineering College, Secundrabad, Telangana, India.
[3]Assistant Professor, Department of CSE, Malla Reddy University, Secundrabad, Telangana, India.
[4]Assistant Professor, Department of EEE, JNTUKUCEN, Narasaraopet, Guntur, India.
[5]Professor, CIVIL Department, Malla Reddy Engineering College, Secundrabad, Telangana, India.

*Address for Correspondence
Raja Reddy Duvvuru,
Associate Professor,
EEE Department,
Malla Reddy Engineering College,
Secundrabad, Telangana, India
Email: rajajntuacep@gmail.com

ABSTRACT

In this work, one of the crucial issues that many of the previous works are concentrating on is the recognition and tracking of the item. Due to the increasing demand for video surveillance system applications including traffic control, medical image processing, and satellite image processing, object recognition and tracking are particularly well-liked. This method is also among the most potent ones used in applications based on artificial intelligence, machine learning, and computer vision. Understanding the type of images, attributes, locations of each image in space, and tracking the movements of each object while it is moving are the main goals of these fundamental object recognition based systems. Since human identification has received so much attention in the research that has already been done, many object detection apps focus primarily on it. This section outlines a novel method for object recognition that uses the CNN methodology to recognise both live and non-living objects. The major goal of this section is to provide a framework for classifying items into living and non-living categories. Once they have been discovered, they can then be categorised using the support vector machine technique, which is useful for identifying theft utilising surveillance systems.

Keywords: CNN, Image processing, SVM.

Raja Reddy Duvvuru *et al.,*

INTRODUCTION

In modern Object recognition is one of the main challenges facing most computer vision work. Increasing demands on surveillance, security, traffic management and medical imaging are particularly popular in object detection and tracking [1]. It is also a product of strong algorithms in machine learning, computer vision and hardware advances that enable a couple of minutes of highly data-intensive calculations. The ultimate aim of the vision-based detection is to understand the type of objects in the picture, their characteristics, and their location in the space and to move or track the object. In the area of image processing, numerous research projects have been undertaken and successfully carried out. Automatic surveillance systems based on real-time videos of public spaces are becoming necessary due to growing concerns about public safety and security. These surveillance systems must be installed in busy and critical locations such as markets, malls, renowned eateries, train stations, etc [2-4]. They are also most in demand for traffic control and examination, activity recognition and tracking, fault detection in industrial applications, and semantic video indexing, without restricting their application to security beneath public places. The approach utilised is to initially detect the target of interest in individual frames in order to do the high level objectives of categorization or tracking a target from video stream [5-7].

Background subtraction is a surveillance technique that is employed in various works. By separating the background and foreground pixels in the frame being processed, this approach extracts the foreground object, or the target that is moving. Many researchers have taken full use of this method's advantages, particularly its performance when a stationary video camera is present and its lighting invariance. A crucial factor to take into account is creating a background model of the video frame that was collected. For feature extraction for detection of objects, textures such as Local Pattern Binary (LBP) [8-10] of the image have been considered. Pixel neighbourhood operations are used to compute LBP characteristics. Histogram of oriented gradients is a common feature descriptor for object detection. HOG features are shape descriptors that represent an object in specific directions in terms of intensity gradients. In [11], the researchers took advantage of HOG [12] functions, citing their invariance properties in regard to transformations such as rotation, deformities and conditions of illumination.

System Design for the proposed method
The system design phase gives the proposed research project an abstract representation that outlines the entire workflow of the study and how each module must be executed and integrated by the effective application development.

Design diagram- High level
This design diagram describes the representation of all the modules in the proposed technique and provides solution for the services offered by the system to produce the high quality design for the research work. In a multi-project model, such an outline is important to ensure that each supporting element design is consistent with the neighboring designs and the large picture. All the services of the proposed system, the platform used and the process of implementation should be described in the brief manner and any important change needed to be done and integrated to be specified in this stage. Furthermore, all major commercial, legal, environmental, safety and safety matters should be considered briefly [13-15].

Design Diagram-High level
The bubble graphs used in this diagram can be classified as dfds. One of the simplest graphical representations, as seen in figures 1 and 2, is the data flow diagram [16].

Case Diagram
Case diagram is shown in the figure below. The functionality for the communication will be documented and carried out in accordance with how 3 explains the interaction between the application framework and the end user.

Raja Reddy Duvvuru *et al.*,

Characters who participate in the process are referred to as on-screen characters, while those who perform outside the parameters are referred to as performing artists. The primary goal of this design diagram is to explain how each module communicates with the others in a way that aids in the execution of the work [17-19].

Design Diagram-Activity

The activity diagram describes in the figure .4, presents the important activities carried out in the research work. In this diagram the circles represents the start of the activity and the end of an activity and the rectangle boxes defines the modules of each proposed research work [20-21].The purpose of activity diagram in the proposed framework is to make sure the workflow of the application development is implemented according to the desired requirements provided by the end users. The developer will refer these design diagrams for the implementation of the work.

Process of identification of objects and the classification technique

Step 1: Input the video that contains both human and non-living moving objects.

Step 2: Pre-processing the input video: The input video to be pre-processed is two different steps:

❖ Divide the input video into frames and store individually.

❖ Once frames are generated apply the morphological operations over the input video.

Image Pre-Processing and Annotation

Image Pre-Processing involves processing or cleaning of images. This step focuses on removal of noise and distortion, sharpening, intensity normalization, etc. The VOC dataset is refined with only person images and annotated according to the format of YOLO model. A text file is created for each image in the same directory with the same name that contains object number and object coordinates on this image, for each object in new line. The object numbers an integer number of object from zero to total number of classes – 1, and object coordinates are float values relative to width and height of image, it can be equal from (0.0 to 1.0). The ID card images are only pre-processed [22-25].

Training the YOLO model and testing

After pre-processing and annotation, the person dataset is divided into training and testing datasets. We train the YOLO model using training dataset until we get a better mean Average Precision (map). After the training, it is tested with testing dataset. YOLO is a full convolution network consisting built using darknet-53. It detects objects at three different strides (8, 16 and 32) which help to detect smaller objects. The provided input image will be divided into S*S grid and each of the cell will be made of the coordinated of (x, y, w, h) and the confidence of the object. The representation of the coordinates x, y defines the position of the boundary box which is relatively grid in nature. The coordinates with w, h is represented as the width and height of the detected boundary box. The probability of each grid is predicted for C categories. The confidence is determined by the probability model that includes the target and the prediction detection box [26]. The object is defined as Pr which stands for the target object that falling under the cell. If the confidence is presents then it is defined using:

C (Object) = Pr (Object)*IOU (Prod, Truth)   (1)

The cell doesn't contain any kind of the object and the confidence values is defined as C (object)] =0. The IOU is defined as the overlapping rate for which the bound of candidate and the truth value of the ground can be defined as the ration of union and the intersection of the grounds [11-13].Then the classification of the objects is achieved by classifying them into their respective categories. Here, multi class SVM classification is used by supervised learning for the output of the object class. The quality of CNN classification is determined over video data set checking: The category output is the class to which an object is identified. In a single frame, a vector containing all classes detected is generated as an output for multiple objects of different lasses.

Raja Reddy Duvvuru *et al.,*

Extraction of features for the identification of Non-Living objects

This section presents the detailed study of how the extraction of features has been implemented and the mathematical model related to the techniques used for feature extraction technique used will be described [27].

Corner Detector using Shi-Tomasi Technique

The Harris Corner Detector is an experimental model that detects the corner features from the video frames that provides higher texture features with minimal propositional changes. The harries technique is mainly used to detect the corners of the frames and it is carried out as follows:

The intensity of the pixel proposition is defined in I(x, y) for the position (x, y) of each window frame of the input video, and if the window moves by small margin the shift (e, v), will be marked with I(x+u, y+v). Since the main objective is to locate regions or windows with small displacements in the image, the intensity is expressed mathematically.

$$E(u,v) = \sum_{x,y} w(x,y)[I(x+u, y+v) - I(x,y)]^2 \qquad \text{....... (1)}$$

The weight function is defined with 'W' and the high intensity variation in the window frames may lead to the result of E (u, v).

The Taylor's series and simplification technique of Equation 1, provides the results in,

$$M = \sum w(x,y) \begin{bmatrix} I_x^2 & I_x I_y \\ I_x I_y & I_y^2 \end{bmatrix} \qquad \text{.... (2)}$$

The Eigen values of matrix is defined as M is used to find out suitable corners sing the score value,

$$S = |M| - k(trace(M))^2 \qquad \text{..... (3)}$$

If λ_1, λ_2 Are Eigen values of M, then $|M| = \lambda_1 \lambda_2$ andtrace (M) = $\lambda_1 + \lambda_2$ Each corners of the frame is represented using S, to predict the high score value. The smaller change in the calculation is calculated using the Shi-Tomasi technique, that leads to the determining the most suitable corner defined in 'n', rather than identifying the each and every corner of the feature [28].

Shi-Tomasi score for corner detection follows-

$$S = min(\lambda_1, \lambda_2). \qquad \text{............. (4)}$$

If the score, S exceeds a threshold it is considered as a corner.

Determining the optimal flow using Lucas-Kanade technique

The optical flow of the detected fame has to be determined, that track the movement of the objects in frame when the object is moving or during the rotation of the camera. The optical flow of any kind of entity from one frame to another frame in a video is to be determined. The proposed algorithm Lucas-Kanade [29-31] is mainly based on the type of optical flow theory, where all the video frames remain in the similar kind of intensity and the pixels in the frames have similar kind of movements and the pixels rate between successive each frames smaller in nature. A pixel rate [32] with the intensity rate defined as I(x,y,t) in a frame at time interval defined as t after the movement with a small displacement defined as (d_x, d_y) in the consecutive frames with a difference of time d_t Is expresses as:

$$I(x,y,t) = I(x + d_x, y + d_y, t + d_t) \qquad \text{..(5)}$$

The flow of an optimal equation for the movement of objects in an image is given as-

$$\frac{\partial_f}{\partial_x}\frac{d_x}{d_t} + \frac{\partial_f}{\partial_y}\frac{d_y}{d_t} + f_t = 0 \qquad \text{.............. (6)}$$

50302

Raja Reddy Duvvuru *et al.*,

The optical flow motion of the vectors using Lucas-Kanade method is defined by solving Equation (6):

$$\begin{bmatrix} u \\ v \end{bmatrix} = \Sigma_i \begin{bmatrix} f_{x_i}^2 & f_{x_i}f_{y_i} \\ f_{x_i} & f_{y_i}^2 \end{bmatrix}^{-1} \Sigma_i \begin{bmatrix} -f_{x_i}f_{t_i} \\ -f_{y_i}f_{t_i} \end{bmatrix} \qquad ..... (7)$$

The representation of the displacement defined I (u, v) represents the of the object between consecutive frames.

RESULTS AND DISCUSSIONS

The framework can be integrated within the Mat lab tool kit that makes it possible to use its toolboxes for the computer vision and machine learning to easily integrate mathematical computations for the identification and classification of artifacts. After extraction, the video processing is carried out smoothly on each frame. The toolbox for image processing includes several filtering and refining functions required to process an identified image before processing. A maximum of 15 videos containing standard products of various classes are collected. The dataset has been divided into three groups–5 video training datasets and 8 video test data sets required for vector support machine technique. Figure 6 below shows the histogram of frames extracted from video 1 in which different objects are recognized in the same way after extracting characteristics, as in Figure 7 and Figure 8 various objects detected from video 6 and video 7 respectively. The final results are drawn using the proposed CNN framework where the input is given to the framework that contains both human and non-living objects in the video dataset. The input video will be processed and detects the background and fore-ground of the objects. Initially pre-processing is applied to remove noise in the video and then morphological operations are applied to analyze the color pixel of the detected frames.

CONCLUSION

This work presented a new approach for object recognition using Vector Machine based classification in Video Surveillance Systems and Lucas-Kanade technique. In this article, the artifacts are correctly identified and their position from an unknown location is calculated. First, object recognition using Shi-Tomasi and Lucas-Kanade techniques will be stored, and the context subtraction will be applied when an object from extracted frames of the input video is recognized. Then the classification of the objects in their individual categories is accomplished by supervised learning with the help vector machine classification. The precision of the technique being proposed is analyzed by the total number of frames detected by object compared to the total number of frames. In this chart four input videos from different sources of various sizes and backgrounds were taken, and for each video we should achieve 92 percent accuracy. Where frames vary from 500 to 1500 for each video, the exactness of the identification of the objects is 80 to 95% for each video.

REFERENCES

1. C S Pillai, AnandaBabu J, "Object Recognition using Lucas-Kanade Technique and Support Vector Machine Based Classification in Video Surveillance Systems", International Journal of Engineering and Advanced Technology(IJEAT), Vol. 9 Issue -1,October-2019, ISSN:2249-8958.
2. Elliott, D.: Intelligent video solution: A definition, Security, pp. 46–48, 2010.
3. Avidan, S.: Ensemble tracking, IEEE Trans. Pattern Anal. Mach. Intell., vol. 29, no. 2, pp. 261– 271, Feb. 2007.
4. Kushwaha, A., Sharma, C., Khare, M., Srivastava, R., Khare, A.: Automatic multiple human detection and tracking for visual surveillance system. 2012 International Conference on Informatics, Electronics Vision (ICIEV), pp. 326-331.
5. B. D. Lucas, T. Kanade, "An iterative image registration technique with an application to stereo vision," in IJCAI, 1981.

6. M. Everingham, L. Van Gool, C. K. Williams, J. Winn, A. Zisserman, "The Pascal Visual Object Classes (VOC) Challenge", IJCV, 2010, pp. 30.

7. Avidan, S.: Ensemble tracking, IEEE Trans. Pattern Anal. Mach. Intell., vol. 29, no. 2, pp. 261– 271, Feb. 2007.

8. Khan, Z., Gu, I.: Joint feature correspondences and appearance similarity for robust visual object tracking, IEEE Trans. Inf. Forensics Security, vol. 5, no. 3, pp. 591–606, Sep. 2010.

9. Dalal, N., Triggs, B.: Histograms of oriented gradients for human detection, in Proc. CVPR, 2005, pp. 886–893.

10. Wang, L.: Abnormal walking gait analysis using silhouette-masked flow histograms, in Proc. ICPR, 2006, vol. 3, pp. 473–476.

11. Wang, S., Lee, H.: A cascade framework for a real-time statistical plate recognition system, IEEE Trans. Inf. Forensics Security, vol. 2, no. 2, pp. 267–282, Jun. 2007.

12. Yu, X., Chinomi, K., Koshimizu, T., Nitta, N., Ito, Y., Babaguchi, N.: Privacy protecting visual processing for secure video surveillance, in Proc. ICIP, 2008, pp. 1672–1675.

13. Park, U., Jain, A.: Face matching and retrieval using soft biometrics, IEEE Trans. Inf. Forensics Security, vol. 5, no. 3, pp. 406–415, Sep. 2010.

14. Cong, Y., Yuan, J., Luo, J.: Towards scalable summarization of consumer videos via sparse dictionary selection, IEEE Trans.Multimedia, vol. 14, no. 1, pp. 66–75, Feb. 2012.

15. Cong, Y., Gong, H., Zhu, S., Tang, Y.: Flow mosaicking: Real-time pedestrian counting without scene-specific learning, in Proc. CVPR, 2009, pp. 1093–1100.

16. k. Cheng, Q. Liu, R. Tahir, L. K. Eric and L. He, "Multi-Camera Logical Topology Inference via Conditional Probability Graph Convolution Network," *2021 IEEE International Conference on Multimedia and Expo (ICME)*, 2021, pp. 1-6, doi: 10.1109/ICME51207.2021.9428335.

17. L. H. Jadhav and B. F. Momin, "Detection and identification of unattended/removed objects in video surveillance," *2016 IEEE International Conference on Recent Trends in Electronics, Information & Communication Technology (RTEICT)*, 2016, pp. 1770-1773, doi: 10.1109/RTEICT.2016.7808138.

18. R. Alimuin, A. Guiron and E. Dadios, "Surveillance systems integration for real time object identification using weighted bounding single neural network," *2017IEEE 9th International Conference on Humanoid, Nanotechnology, Information Technology, Communication and Control, Environment and Management (HNICEM)*, 2017, pp. 1-6, doi: 10.1109/HNICEM.2017.8269461.

19. G. Pavithra, J. J. Jose and T. A. Chandrappa, "Real-time color classification of objects from video streams," *2017 2nd IEEE International Conference on Recent Trends in Electronics, Information & Communication Technology (RTEICT)*, 2017, pp. 1683-1686, doi: 10.1109/RTEICT.2017.8256886.

20. K. S. Kumar, S. Prasad, P. K. Saroj and R. C. Tripathi, "Multiple Cameras Using Real Time Object Tracking for Surveillance and Security System," *2010 3rd International Conference on Emerging Trends in Engineering and Technology*, 2010, pp. 213-218, doi: 10.1109/ICETET.2010.30.

21. B. Hdioud, A. Ezzahout, Y. Hadi and R. O. Haj Thami, "A real-time people tracking system based on trajectory estimation using single field of camera view," *2013 International Conference on Computer Applications Technology (ICCAT)*, 2013, pp. 1-4, doi: 10.1109/ICCAT.2013.6522038.

22. S. Sen, A. K. Das and S. P. Chowdhury, "Saving Electrical Power in a Surveillance Environment," *2009 Seventh International Conference on Advances in Pattern Recognition*, 2009, pp. 274-277, doi: 10.1109/ICAPR.2009.38.

23. V. Mathew, T. Toby, A. Chacko and A. Udhayakumar, "Person re-identification through face detection from videos using Deep Learning," *2019 IEEE International Conference on Advanced Networks and Telecommunications Systems (ANTS)*, 2019, pp. 1-5, doi: 10.1109/ANTS47819.2019.9117938.

24. J. Tang, R. Ding and X. Tian, "Real-Time Target Detection Algorithm Based on Background Modeling," *2013 Fourth International Conference on Digital Manufacturing & Automation*, 2013, pp. 970-974, doi: 10.1109/ICDMA.2013.227.

25. S. Alfasly, B. Liu, Y. Hu, Y. Wang and C. -T. Li, "Auto-Zooming CNN-Based Framework for Real-Time Pedestrian Detection in Outdoor Surveillance Videos," in *IEEE Access*, vol. 7, pp. 105816-105826, 2019, doi: 10.1109/ACCESS.2019.2931915.

Raja Reddy Duvvuru *et al.,*

26. L. Qu, J. Wang, S. Xin, M. Qin and J. Dong, "A System for Detecting Sea Oil Leak Based on Video Surveillance," *2011 Third Pacific-Asia Conference on Circuits, Communications and System (PACCS)*, 2011, pp. 1-3, doi: 10.1109/PACCS.2011.5990183.

27. A. Singh, T. Anand, S. Sharma and P. Singh, "IoT Based Weapons Detection System for Surveillance and Security Using YOLOV4," *2021 6th International Conference on Communication and Electronics Systems (ICCES)*, 2021, pp. 488-493, doi: 10.1109/ICCES51350.2021.9489224.

28. X. Song, L. Wang, H. Wang and Y. Zhang, "Detection and identification in the intelligent traffic video monitoring system for pedestrians and vehicles," *The 7th International Conference on Networked Computing and Advanced Information Management*, 2011, pp. 181-185.

29. B. Ashwini, B. Deepashree, B. N. Yuvaraju and P. S. Venugopala, "Identification of vehicles in traffic video," *2016 International Conference on Signal Processing, Communication, Power and Embedded System (SCOPES)*, 2016, pp. 588-593, doi: 10.1109/SCOPES.2016.7955507.

30. C. -Y. Wang, P. -Y. Chen, M. -C. Chen, J. -W. Hsieh and H. -Y. M. Liao, "Real-Time Video-Based Person Re-Identification Surveillance with Light-Weight Deep Convolutional Networks," *2019 16th IEEE International Conference on Advanced Video and Signal Based Surveillance (AVSS)*, 2019, pp. 1-8, doi: 10.1109/AVSS.2019.8909855.

31. Z. Zhen-Jie and W. Qi, "Research on Detection and Tracking of Moving Vehicles in Complex Environment Based on Real-Time Surveillance Video," *2020 3rd International Conference on Intelligent Robotic and Control Engineering (IRCE)*, 2020, pp. 42-46, doi: 10.1109/IRCE50905.2020.9199246.

32. Y. Chen, B. Wu, H. Huang and C. Fan, "A Real-Time Vision System for Nighttime Vehicle Detection and Traffic Surveillance," in *IEEE Transactions on Industrial Electronics*, vol. 58, no. 5, pp. 2030-2044, May 2011, doi: 10.1109/TIE.2010.2055771.
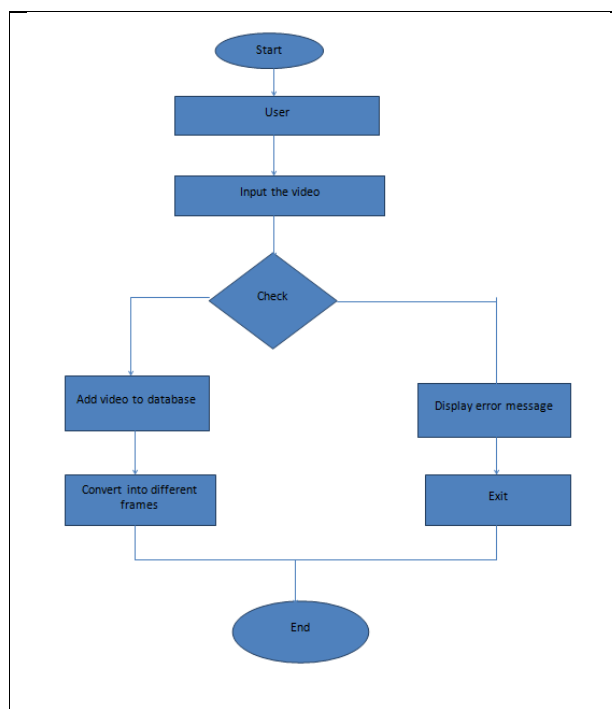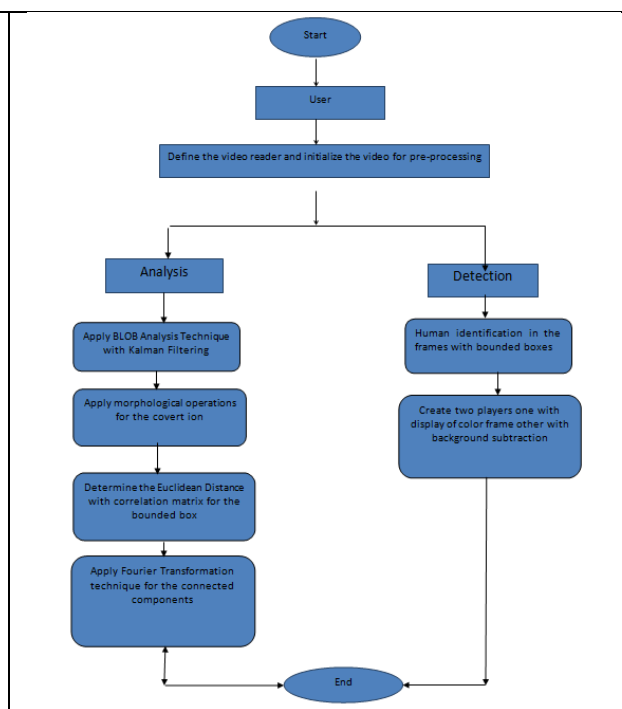
Fig. 1: Data Flow Diagram for Add Database

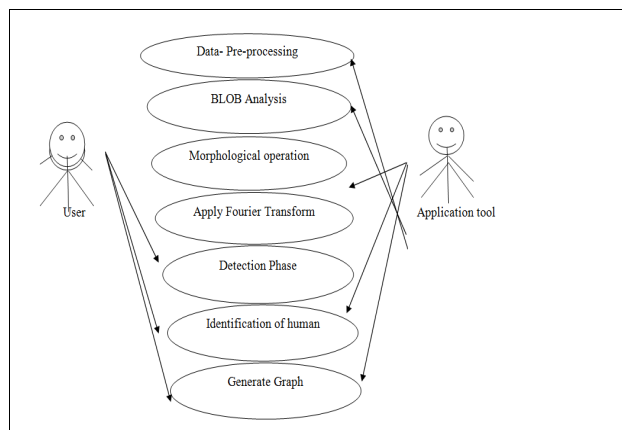**Fig. 2: Data Flow Diagram for Proposed Technique**

Raja Reddy Duvvuru *et al.,*

Figure 3: The Use case diagram for Proposed Technique
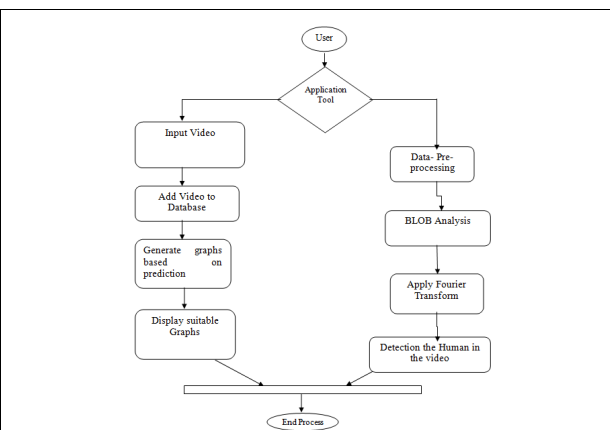

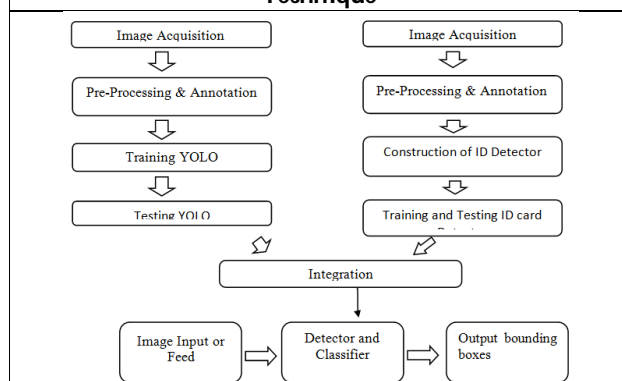**Figure 4: The activity diagram for Proposed Technique**

Figure 5: System Architecture of proposed Framework

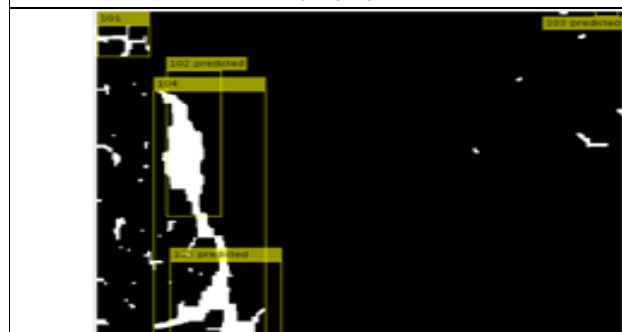**Figure 6: Frame extraction for the detected objects in the input video 1**

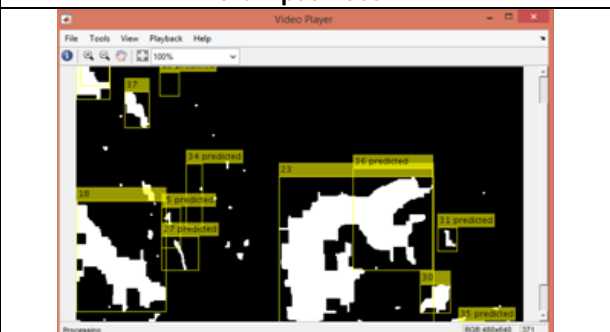**Figure 7: Frame extraction for the detected objects in the input video2**

Figure 8: Frame extraction for the detected objects in the input video3

Venu Yarlagadda[1,*]
A. Giri Prasad[1]
Ch. Rami Reddy[2,4],
T. Nireekshana[1]
B. V. Seshu Kumari[3]
P.V.V Satyanarayana[4]

Suppression of Ferranti Effect of Transmission System Using Closed Loop Control of FACTS Devices

JES

Journal of
Electrical
Systems

Modern power systems need the expansion of EHV and UHV power Transmission networks due to the exponential rise in power demand. The Ferranti effect needs the attention of researchers on the dynamic variation of loads in interconnected power systems. This article focuses on the development of closed-loop control circuitry for both Static Synchronous Compensator (STATCOM) and Static Var Compensator (SVC). The developed transmission system Simulink model has been simulated and Ferranti Effect is observed for both no-load and lightly loaded conditions. The closed-loop control circuits along with power circuits of STATCOM and SVC have been developed and simulated and the results show the significant suppression of the Ferranti effect by both of the shunt devices.

Keywords: Ferranti effect; closed-loop control of SVC; TSC-TCR; Suppression of Ferranti effect; Closed loop control of SVC, STATCOM.

1. Introduction

The transmission system is used to enhance the power transmission capability of the interconnected power system network in which the Ferranti effect significantly influences the system behavior all over the network due to dynamic load disturbances [1-2]. The severity of the effect adversely affects due to the increase of line lengths of both medium and long transmission lines [3]. This effect is addressed with the application of Flexible A.C Transmission Systems(FACTS) devices especially shunt-connected devices viz [4]. STATCOM and SVC. The main author contributions are as follows

- Transmission systems models with medium and long transmission lines have been developed for the simulation study of the Ferranti effect and its suppression.
- Designed and developed the models of shunt FACTS devices such as STATCOM and SVC.
- Developed the closed-loop control system for both of the said devices for mitigation of the Ferranti effect.
- Analysis has been performed for suppression of the Ferranti effect using both devices and results have proved the significance of closed-loop control in omitting the Ferranti effect.

The remaining article is structured as follows
Section II is describing the various components of the test systems, STATCOM power and closed-loop control circuits, SVC power and closed-loop control circuits and Section III used to describe the simulation results without any controller, with closed-loop control of

* Corresponding author: Venu Yarlagadda, Electrical and Electronics Engineering, VNR Vignana Jyothi Institute of Engineering and Technology, Hyderabad, India 500090 E-mail: venu_y@vnrvjiet.in
[1]Department of Electrical and Electronics Engineering, VNR Vignana Jyothi Institute of Engineering and Technology, Hyderabad
[2]Department of Electrical and Electronics Engineering, Joginapally B. R. Engineering College, Hyderabad, India 500034
[3]Department of Information Technology, VNR Vignana Jyothi Institute of Engineering and Technology, Hyderabad 500090
[4] Department of Electrical and Electronics Engineering, Malla Reddy Engineering College, Secunderabad, India 500100

STATCOM and with closed-loop control of SVC and lastly conclusions of this work followed by the references.

2. Materials and Methods

2.1 The Transmission system

The medium and long transmission lines are the main constituent part of the transmission system which is the root cause of the Ferranti effect and it is observed in both medium and long transmission lines [5]. A long transmission line equivalent circuit is depicted in Fig.1model and it is clearly illustrated in Fig.2,the receiving end voltage magnitude (V_R) is higher than that of sending end voltage (V_S) and it adversely increases with line length [6-8].
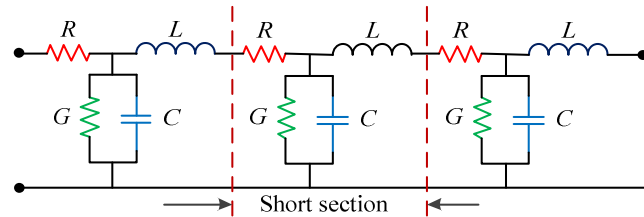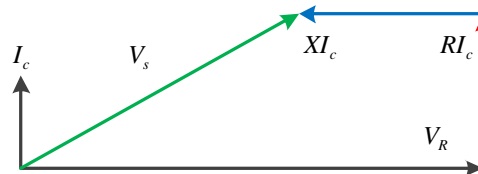

Fig.1. Long Transmission line model

Fig.2. Ferranti effect phasor illustration

2.2. Static Var Compensator (SVC)

The developed system for the simulation study as illustrated inFig.3comprises the generating station, transmission system feeding the load, SVC is connected at the receiving end load bus including a closed-loop controller [9,15]. The susceptance of the device can be controlled with the control of the firing angle of the TCR and Fig.4. Shows the schematic diagram of SVC and the equations from (1) to (7) describes the mathematical modeling of SVC [10,15].
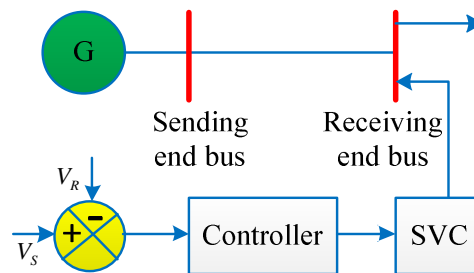

Fig.3. Test system single line diagram with closed loop controlled SVC
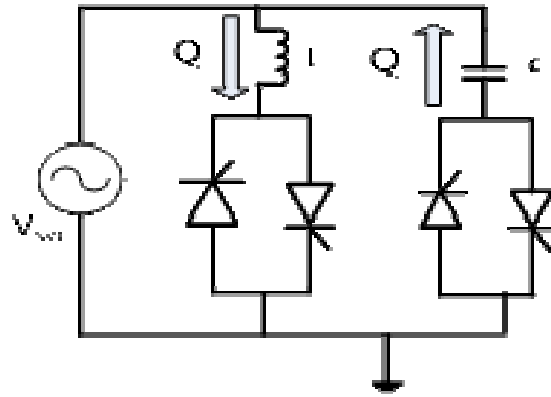
475

Fig.4 :SVC Schematic circuit of SVC

$$B_{SVC} = B_{TSC} - B_{TCR} \qquad (1)$$

$$= X_L - X_C /\pi[2(\pi-\alpha)+sin2\alpha] \div [X_C X_L] \qquad (2)$$

$$B_{TCR} = B_L ((\pi-2\alpha-sin\alpha)/\pi) + Bc \qquad (3)$$

$$Q_{SVC} = V_{BUS}^2 \frac{(Xc\,[2\pi-\alpha+sin2\alpha]-\pi XL)}{} \qquad (4)$$

$$Q_{SVC} = V_t(V_t - V_{ref}) X_{SL} \qquad (5)$$

$$Q_{SVC} = B_{SVC} \times V_{ref}^2 \qquad (6)$$

$$Q_{SVC}^{min} \leq Q_{SVC} \leq Q_{SVC}^{max} \qquad (7)$$

2.3. STATCOM

STATCOM is a shunt-connected device and the mathematical modelling of STATCOM has been described in equations (8) to (10) andFig.5 depicts the STATCOM Schematic Diagram [11,16]

$$L\frac{di_{ac}}{dt} = R + V_{ac} - V_{at} \qquad (8)$$

$$L\frac{di_{bc}}{dt} = R + V_{bc} - V_{bt} \qquad (9)$$

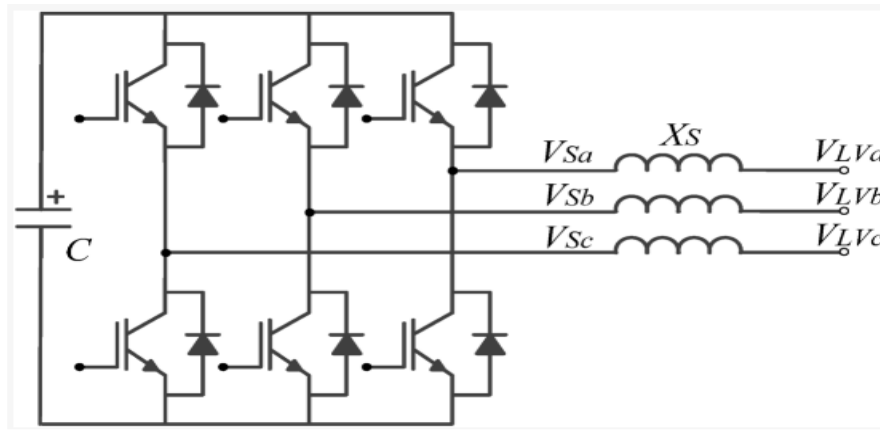$$L\frac{di_{cc}}{dt} = R + V_{cc} - V_{ct} \qquad (10)$$

Fig.5 :STATCOM Schematic Diagram

The test system is developed with closed-loop control of the STATCOM, it is composed of a power plant feeding the load through a transmission network [12-16]. Fig.6. shows the single line diagram system of with STATCOM and Fig.7. STATCOM closed-loop control circuit

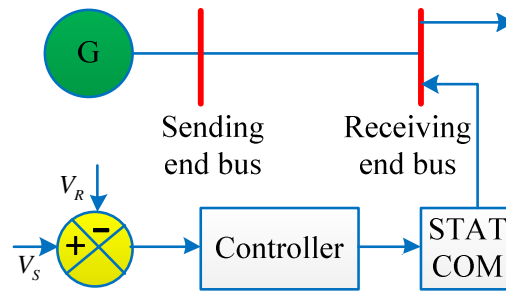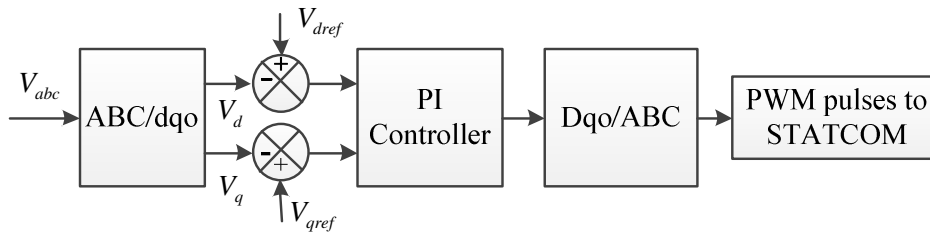

Fig.6. Single line diagram system of with STATCOM

Fig.7. STATCOM closed-loop control circuit

3. Result analysis and discussion

3.1. STATCOM Results

The Simulink model of the test system for presenting the case study is developed with all described blocks said earlier and is being simulated and results have been presented int his section below and it is illustrated in Fig.8 below.
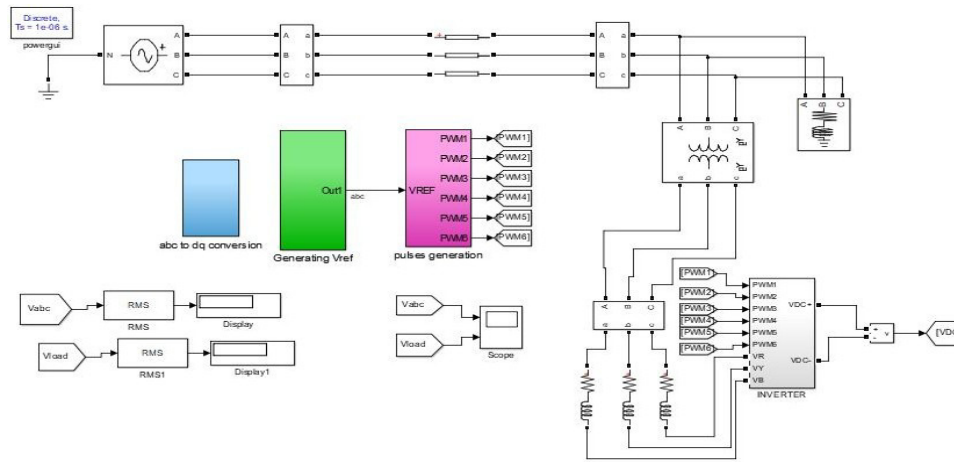
Fig.8.MATLABSimulinkmodelwith closed-loop control of STATCOM

Table.1 shows the line parameters, Table. 2depicts the simulation results of the transmission system without STATCOM, and Table.3 encapsulate the Ferranti effect results with STATCOM**.**

Table1. Transmission line parameters

S.No	Specifications	Value
1	R in Ohm/kM	0.1322
2	L in H/kM	2.1625e-3
3	C in F/kM	7.70628e-9
4	Length in kM	400,500,600
5	Sending endvoltageinkV	230 kV

Table2: The Ferranti effect results without STATCOM.

S.No	Line Length(kM)	V_S in kV	V_R in kV at NL	V_R in kV at Lightly loaded conditions
1	400	230	263	260.4
2	500	230	286.8	281.3
3	600	230	319.5	310.8

Table. 3: The Ferranti effect results with STATCOM.

S.No	Line Length(kM)	V_S in kV	V_R in kV at NL	V_R in kV at Lightly loaded conditions
1	400	230	230	230
2	500	230	230	230
3	600	230	230	230

3.1. SVC Results

This part shows the simulation results of SVC, Table3 illustrates the simulation results for no load and lightly loaded conditions without SVC and Table4:Simulation results for no load and lightly loaded conditions with SVC, which proves that the closed-loop control of SVC is quite effective in suppressing the Ferranti effect. Fig.9. shows the Simulink power circuit and closed-loop control circuits with SVC, Fig.10. depicts the Closed loop control circuit of SVC Fig.11. shows the Closed loop firing circuit of SVC. Fig.12 to 21 illustrate the waveforms of receiving and sending voltages without and with SVC, these results prove that the closed-loop control of SVC is quite effective in suppressing the Ferranti effect for both no load and lightly loaded conditions.

Table3:Simulation results for no load and lightly loaded conditions without SVC

S. No	Line Length in kM	Vs in kV	Vr in KV Under no load	Vr in KV under lightly loaded condition
1.	400	230	263	260.4
2.	500	230	286.8	281.3
3.	600	230	319.5	310.8

Table4:Simulation results for no load and lightly loaded conditions with SVC

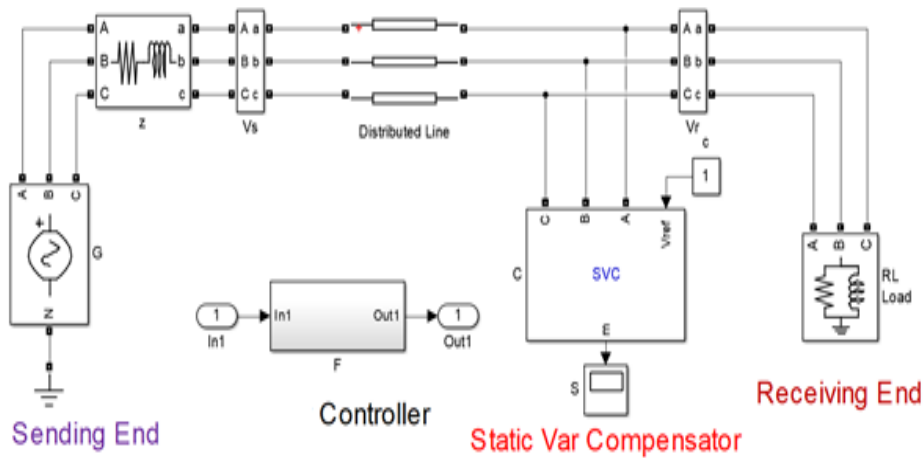| S. No	Line Length in kM	Vs in kV	Vr in kV Under no load	Vr in kV under lightly loaded condition
1.	400	230	230	230
2.	500	230	230	230
3.	600	230	230	230

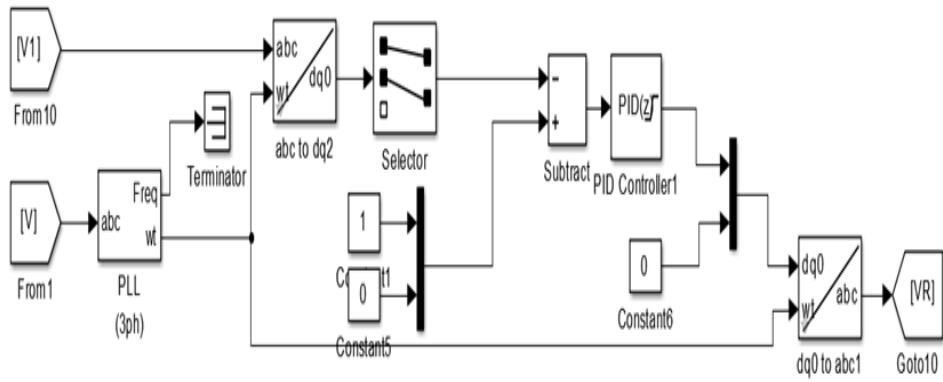Fig.9. Simulink Power Circuit and closed loop control circuits with SVC
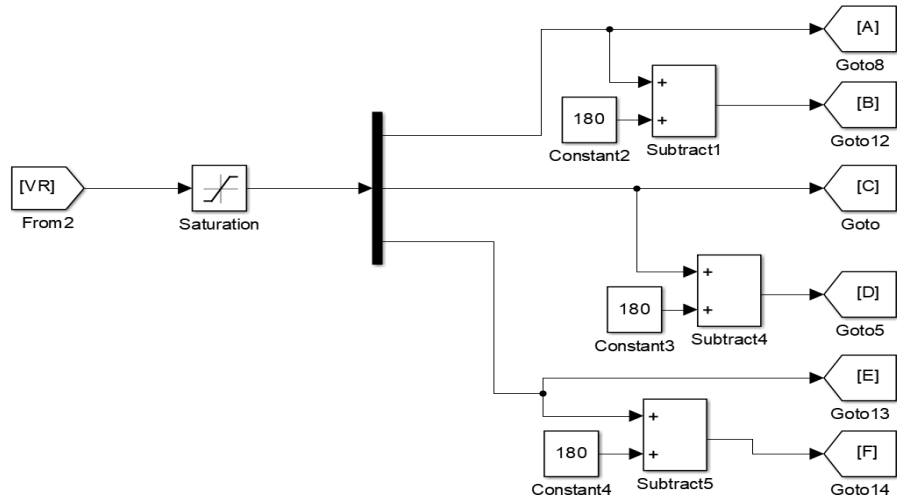
Fig.10. Closed loop control circuit of SVC

Fig.11. Closed loop firing circuit of SVC
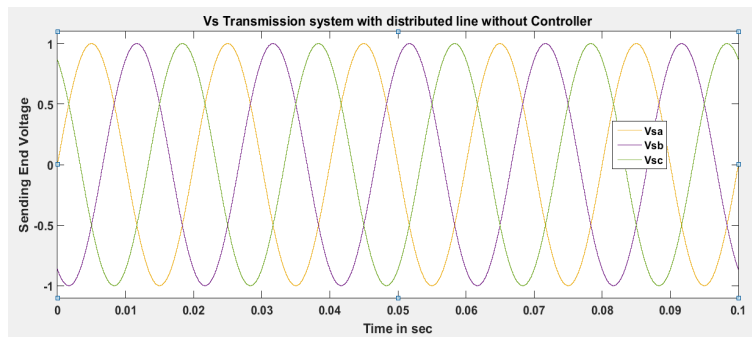
Fig.12. Vs without controller with distributed line
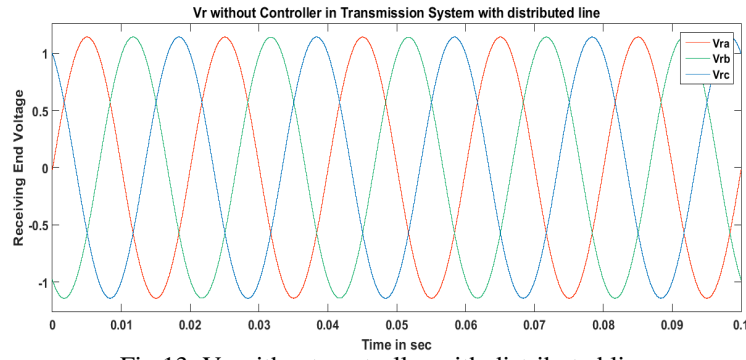
Fig.13. Vr without controller with distributed line
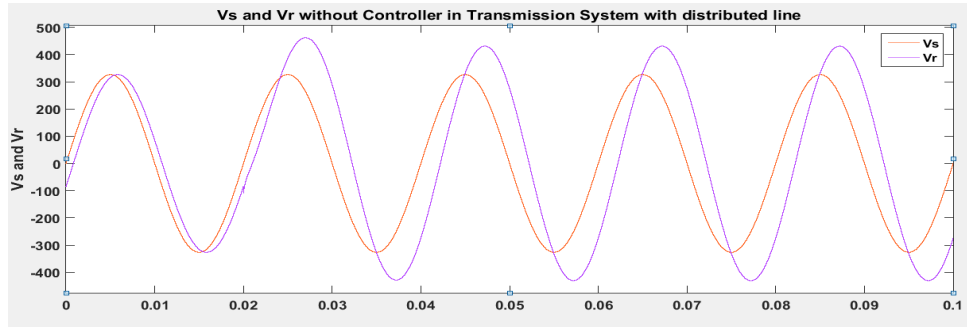
Fig.14. Vs and Vr in distributed line without controller

Fig.15. Vs and Vrin distributed line without controller

Fig.16. Vr with pi-line without controller

Fig.17. Actual values of Vs and Vr with pi-line and without controller

Fig.18. Vs and Vr in with fuzzy controlled SVC for nominal pi-line

Fig.19. Vs and Vr in without SVC for didtributed line
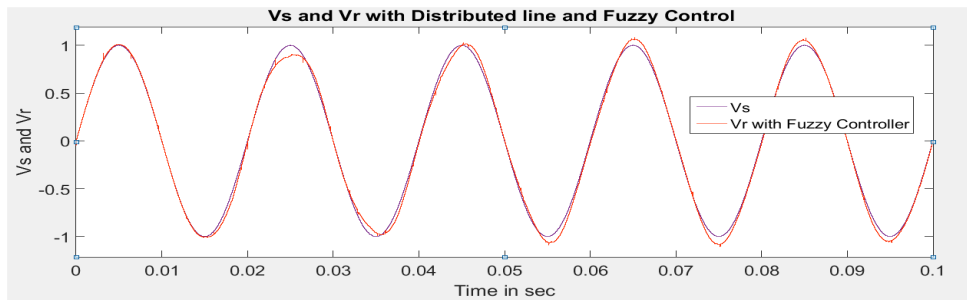
Fig.20. Sending end and receiving end voltages with SVC for didtributed line

482
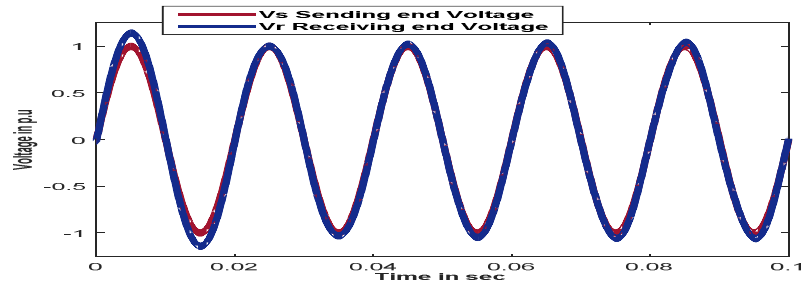
Fig.21. Sending end and receiving end voltages at NL
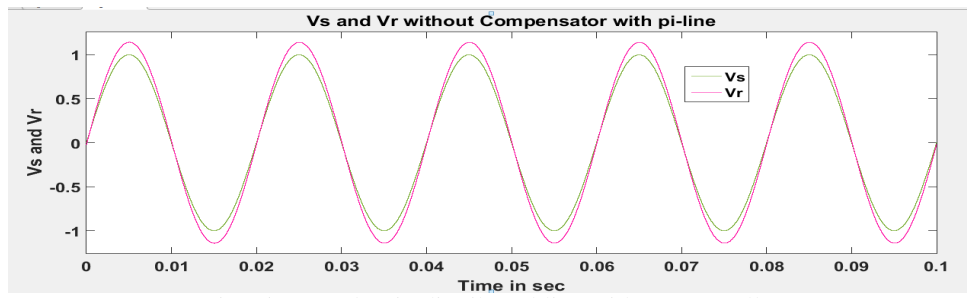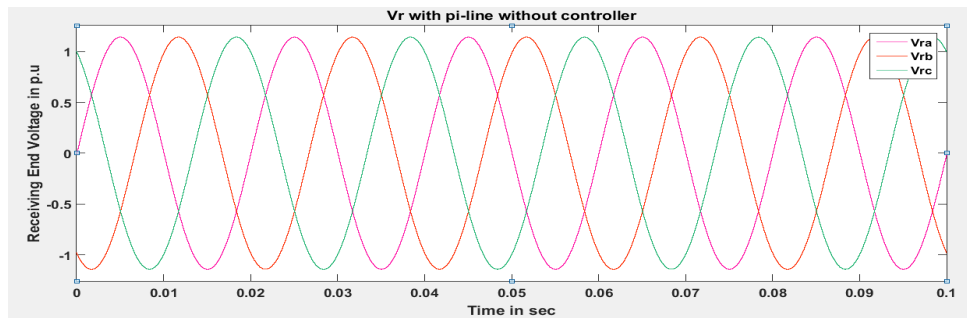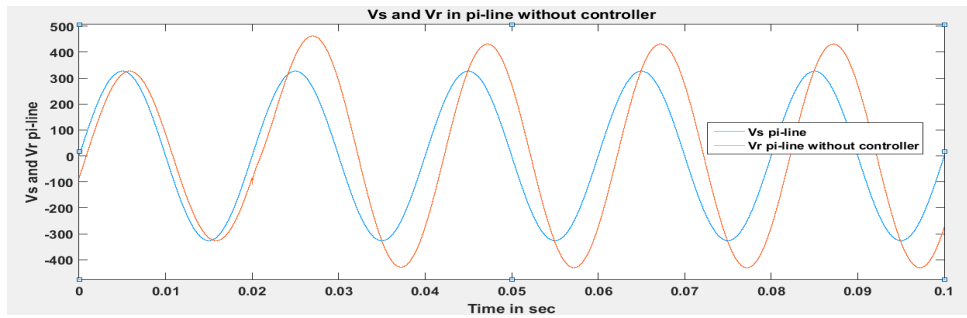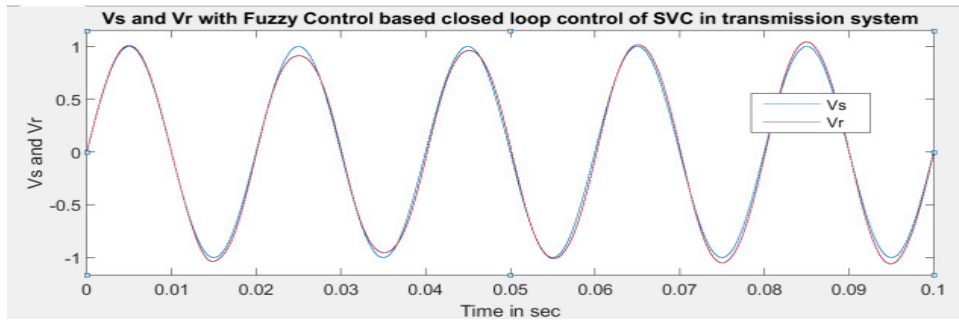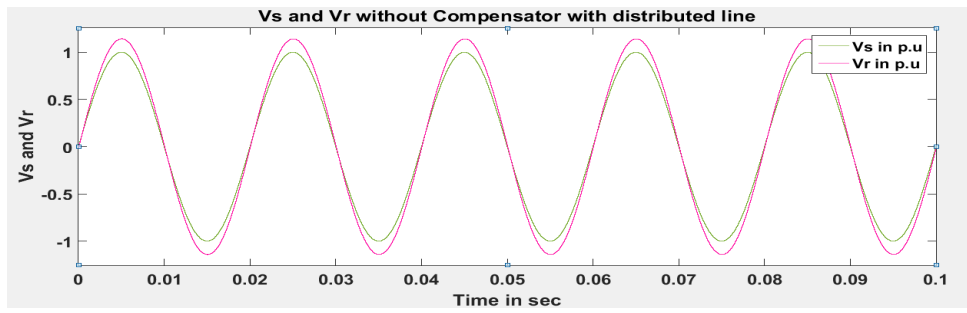
The Transmission test systems have been developed and simulated for both no load and lightly loaded conditions and the Ferranti effect has been adversely increasing as Fig.22 depictstheFerranti effect with the variation of line length on noload and Fig.23 Illustrates the Ferranti effect with a variation of line length on lightly loading conditions. The closed-loop control systems were developed for both STATCOM and SVC separately and simulated the test system with these controllers and suppressed the Ferranti effect as illustrated by the following figures. Fig. 24 shows the no-load voltages at 400 km line length which illustrates no-load receiving voltages without any controller, with closed-loop control of STATCOM and with closed-loop control of SVC, similarly,Fig. 25 encapsulates the no-load voltages at 500 km line length and Fig. 26 depicts no load voltages at 600 km line length. The subsequent figures illustrate as Fig. 27 shows lightly loaded condition voltages at 400 km line length, Fig. 26 illustrates the lightly loaded condition voltages at 500 km line length and Fig. 28 depicts the lightly loaded condition voltages at 600 km line length respectively and Fig. 29 shows Lightly loaded condition voltages at 600 km line length. All these results prove that both of the shunt-connected FACTS devices such as STATCOM and SVC are quite effective in suppressing the Ferranti effect with closed-loop control mode.
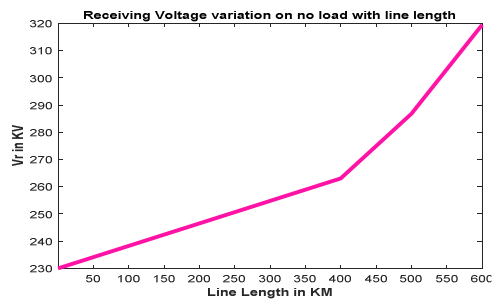
Fig.22 Illustration of ferranti effect with variation of line length on no laod
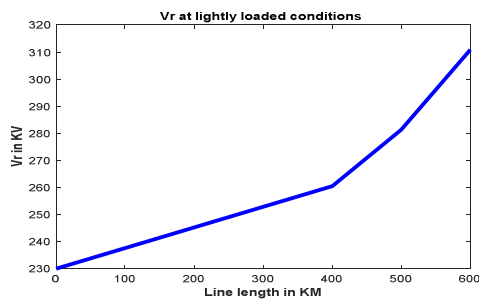
Fig.23 Illustration of ferranti effect with variation of line length on lightly loading conditions

483
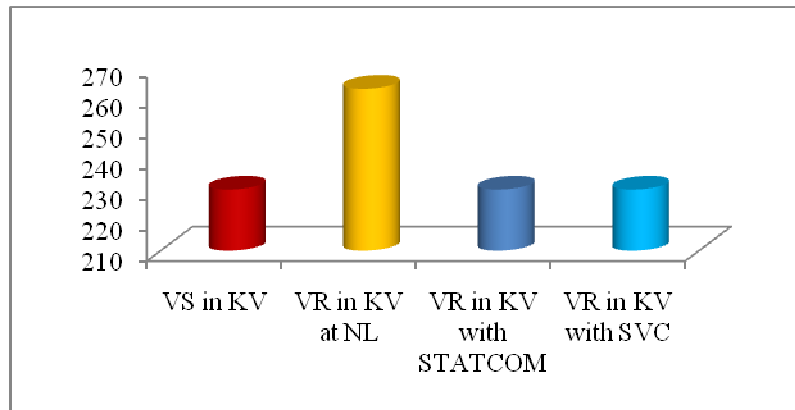
Fig. 24: No load voltages at 400 km line length
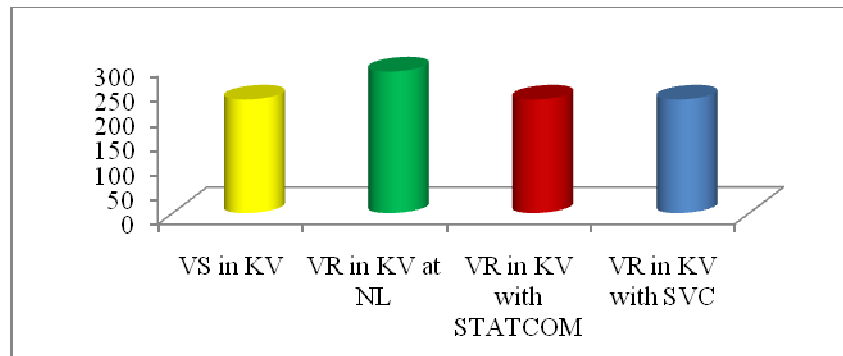
Fig. 25: No load voltages at 500 km line length
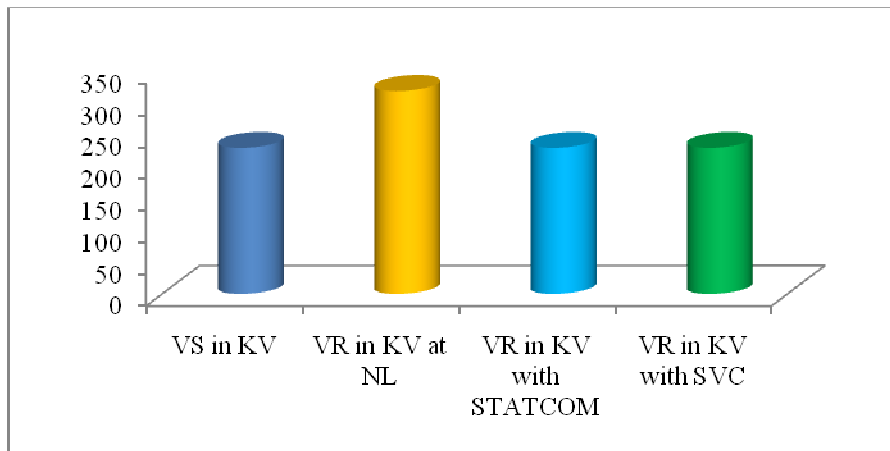
Fig. 26: No load voltages at 600 km line length
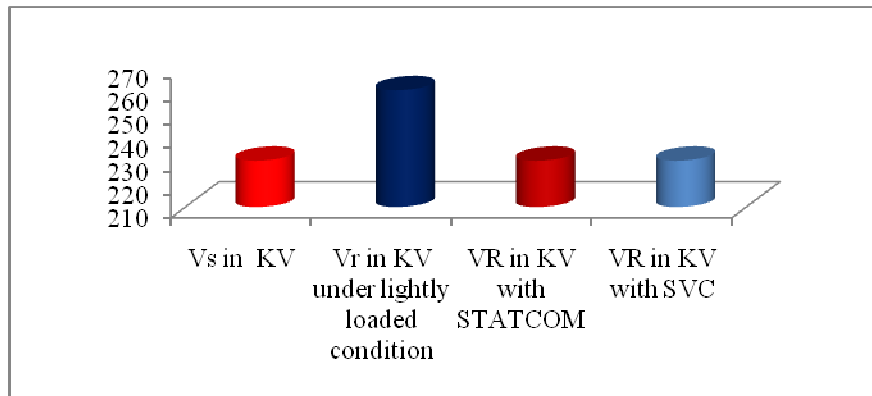
Fig. 27: Lightly loaded condition voltages at 400 km line length
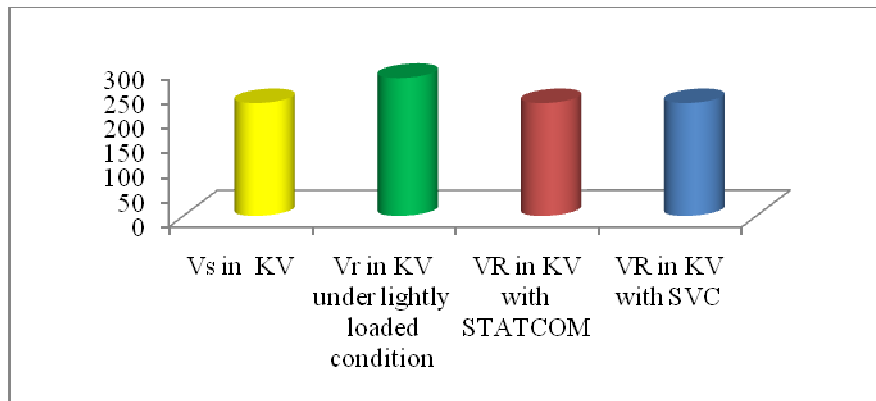
Fig. 28: Lightly loaded condition voltages at 500 km line length
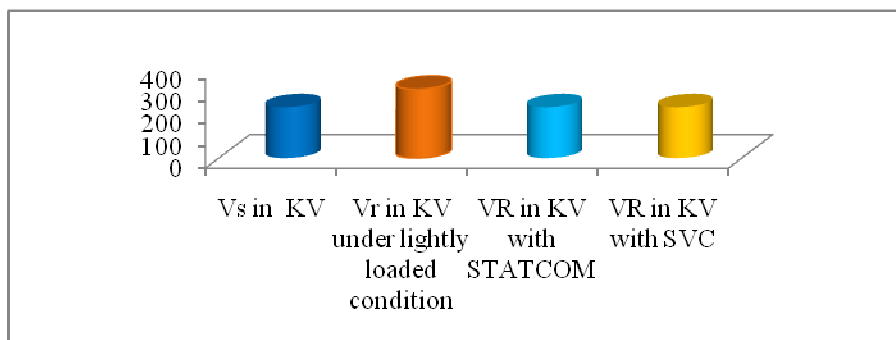
Fig. 29: Lightly loaded condition voltages at 600 km line length
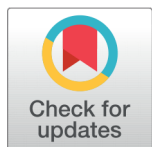
4. Conclusions

The test systems for the case study have been built with medium and long lines. Both models for case1 and case2 have been simulated without and with closed-loop controls of both Static Synchronous Compensator(STATCOM) and Static Var Compensator (SVC) under no-load and lightly loaded conditions. Simulation results without any controller show the adverse effect of the Ferranti effect and closed loop controls of both STATCOM and SVC results prove that these two shunt-type FACTS Controllers are quite effective in controlling receiving end voltage for both no load as well as lightly loaded conditions.

References

[1] Venu Yarlagadda, G. Lakshminarayana, G. Ambati, T. Nireekshana and G. A. Karthika, "Mitigation of Ferranti Effect and Voltage Control in Transmission Systems Using Fuzzy Logic Controlled SVC," *2022 International Conference on Smart Technologies and Systems for Next Generation Computing (ICSTSN)*, 2022, pp. 1-6, doi: 10.1109/ICSTSN53084.2022.9761300.

[2] Venu Yarlagadda, Giri Prasad Ambati, E.Shiva prasad, KuntlaVeeresham, G.Radhika, "Synchronous and Voltage Stability Improvement using SVC and TCSC and its Coordination Control" Design Engineering, ISSN: 0011-9342, vol-2021, issue No: 6, pp: 3624-3635.

[3] G. Chavan, S. Acharya, S. Bhattacharya, D. Das and H. Inam, "Application of static synchronous series compensators in mitigating Ferranti effect," *2016 IEEE Power and Energy Society General Meeting (PESGM)*, 2016, pp. 1-5, doi: 10.1109/PESGM.2016.7741380.

[4] Venu Yarlagadda, D.Ravi Kumar, E.Shiva prasad , Giri Prasad Ambati , Lakshminarayana Gadupudi , "Prototype models of FACTS Controllers and its Optimal Sizing and Placements in Large Scale Power Systems using Voltage Stability Indices" Design Engineering , ISSN: 0011-9342, vol-2021,issue No:6,pp: 3636-3659.

[5] Y. Venu, Nireekshana, T., Phanisaikrishna, B. (2021). Mitigation of Ferranti Effect Using Thyristor Controlled Reactor. In: Komanapalli, V.L.N., Sivakumaran, N., Hampannavar, S. (eds) Advances in Automation, Signal Processing, Instrumentation, and Control. i-CASIC 2020. Lecture Notes in Electrical Engineering, vol 700. Springer, Singapore. https://doi.org/10.1007/978-981-15-8221-9_236

[6] Venu Yarlagadda, NireekshanaTuraka, Giri Prasad Ambati, S Poornima "Optimization of Voltage Stability based Shunt and Series Compensation using PSO" Design Engineering Vol2021, Issues 7, Pages 8679–8694.

[7] Tingyi He, Shengnan Li, Shuijun Wu, Ke Li, "Small-Signal Stability Analysis for Power System Frequency Regulation with Renewable Energy Participation", Mathematical Problems in Engineering, vol. 2021, Article ID 5556062, 13 pages, 2021. https://doi.org/10.1155/2021/5556062

[8] J. Liu, W. Yao, J. Wen et al., "Impact of power grid strength and PLL parameters on stability of grid-connected DFIG wind farm," IEEE Transactions on Sustainable Energy, vol. 11, no. 1, pp. 545–557, 2020.

[9] X. Yan, "A review of cyber security risks of power systems: from static to dynamic false data attacks," Protection and Control of Modern Power Systems, vol. 5, no. 3, pp. 8–19, 2020.

[10] G. Tu, Y. Li and J. Xiang, "Analysis and Control of Energy Storage Systems for Power System Stability Enhancement," 2019 Chinese Control Conference (CCC), 2019, pp. 560-565, doi: 10.23919/ChiCC.2019.8865814.

[11] S. R. Paital, P. K. Ray and A. Mohanty, "A review on stability enhancement in SMIB system using artificial intelligence based techniques," 2018 IEEMA Engineer Infinite Conference (eTechNxT), 2018, pp. 1-6, doi: 10.1109/ETECHNXT.2018.8385324.

[12] B. Baadji, H. Bentarzi and A. Bouaoud, "SMIB power system model with PSS for transient stability studies," 2017 5th International Conference on Electrical Engineering - Boumerdes (ICEE-B), 2017, pp. 1-5, doi: 10.1109/ICEE-B.2017.8191996.

[13] S.Kalyani, M.Prakash and g. A.Ezhilarasi, "Transient stability studies in SMIB system with detailed machine models," 2011 international conference on recent advancements in electrical, electronics and control engineering, 2011, pp. 459-464, doi:10.1109/iconraeece.2011.6129781.

[14] Cherkaoui, N.; Haidi, T.; Belfqih, A.; El Mariami, F.; Boukherouaa, J.A Comparison Study of Reactive Power Control Strategies inWind Farms with SVC and STATCOM. Int. J. Electr. Comput.Eng. 2018, 8, 4836.

[15] V. Yarlagadda, J. V. Rao, G. Ambati, S. N. V. Karthik Kumar and K. Rajesh, "Integrated Voltage and Generator Stability Analysis of a Three Bus System Combining SMIB and SMLB Systems," 2021 Second International Conference on Smart Technologies in Computing, Electrical and Electronics (ICSTCEE), 2021, pp. 1-7, doi: 10.1109/ICSTCEE54422.2021.9708590.

[16] Yarlagadda, V., Karthika, G.A., Ambati, G., Kumar, C.S. (2022). Wind Energy System Using Self Excited Induction Generator with Hybrid FACTS Device for Load Voltage Control. In: Mekhilef, S., Shaw, R.N., Siano, P. (eds) Innovations in Electrical and Electronic Engineering. ICEEE 2022. Lecture Notes in Electrical Engineering, vol 893. Springer, Singapore. https://doi.org/10.1007/978-981-19-1742-4_6

*Corresponding author.

jskumar457@gmail.com

Competing Interests: None

An Efficient Transform based Low Rank Tensor Completion to Extreme Visual Recovery

Sunil Kumar Jyothula[1,2]*, **Jaya Chandra Prasad Talari**[3]

1 Research scholar, Department of Electronics and Communication Engineering, JNTUA, Anantapur, Andhra Pradesh, India
2 Assistant Professor, Department of Electronics and Communication Engineering, Malla Reddy Engineering College, Secunderabad, Telangana, India
3 Professor, Department of Electronics and Communication Engineering, Rajeev Gandhi Memorial College of Engineering and Technology, Affiliated to JNTUA, Nandyal, Andhra Pradesh, India

Abstract

Objective: To propose an optimization approach in recovering of the corrupted tensors in the high dimensional real time data. **Methods:** The recovering of corrupted tensors is performed by low-rank tensor completion methods. The tensor decomposition methods are used in tensor completion methods. These Tensor decomposition methods; candecomp / parafac (CP), tucker and higher-order Singular Value Decomposition (HoSVD) are used to minimize the rank of a tensor data. The limitations are in finding the rank of a tensor. **Findings:** The recovered data using the lifting transform induced tensor-Singular Value Decomposition (t-SVD) technique were assessed utilizing the Peak Signal to Noise Ratio (PSNR), Structural Similarity (SSIM), Naturalness Image Quality Evaluator (NIQE), and Perceptual Image Quality Evaluator (PIQE). When compared to state-of-the-art approaches, the low rank assumption condition with the lifting transform consideration gave good data recovery for every missing ratio. **Novelty:** The missing data is calculated by lifting polyphase structures by utilizing the available data. The polyphase structures are splitting the value into equivalent multiple triangular matrices, these are processed with the t-SVD to have the better approximation tensor rank.

Keywords: Tensor Completion; Transformbased Optimization; 5/3 Lifting Wavelet Transform; Lowrank tensor completion; tSVD

1 Introduction

Estimating the missing tensor observations from the limited uncorrupted tensor observations is very difficult[1]. To recover missing observations, repeated patterns present in the image may be used[2]. It is providing the solutions to wide range of problems in machine learning, computer vision, appearance acquisition, video coding, scan completion, subspace clustering, and compressed sensing applications[3–6]. The two-dimensional data completion difficulties are addressed with the nuclear norm approach; it replaces the rank function[7] and it is termed as Low Rank Minimization.

Singular value thresholding technique used to provide solutions to numerous Low-Rank optimization problems. It had poor recovery in the two-dimensional data because the all-singular values are minimized, it led to the loss of major structure information. The truncated nuclear norm regularization[8] minimizes singular values based on rank by performing the two-step process. The singular value shrinkage process is performed along with the optimization process. Identification of a rank for the two-dimensional is simple and computation costs are also low. If the missing ratio is increasing the recovering of the image becomes more difficult and less accurate. An introduction of a sparse regularizer can provide a better approximation. The sparse regularizer is framed with a two-step process[9]; firstly, a transform operator induced with singular value decomposition is used to find the missing data and update the data; and secondly, solves the constrained optimization function. This constrained optimization function is addressed by Alternating Direction Method of Multipliers (ADMM) framework. In the case of multidimensional data, finding the optimal rank (tensor rank) is a difficult task, because of the multidimensional algebraic properties.

Kilmer et al.[10] introduced the t-SVD approach; it is well performing in capturing the spatial-shifting correlation of high dimensional data. Let the three-dimensional data tensor be decomposed as two orthogonal tensors and one diagonal tensor as similar to two-dimensional SVD. The tensor completion algorithms High Accuracy Low Rank Tensor Completion (HaLRTC), Fast Low Rank Tensor Completion (FaLRTC) and Simple Low Rank Tensor Completion (SiLRTC) are introduced[6]. Further, to improve the recovery of high dimensional data, the truncated nuclear norm is extended to tensors and introduced with the Discrete Cosine Transformation (DCT)[11]. Here the inclusion of DCT provides piecewise similarity among the recovered tensors in the image. The unitary transform-based t-SVD approach was introduced to improve PSNR in hyperspectral images[12]. Here another transform-based t-SVD approach is presented to improve the visual quality of the highly corrupted high-dimensional data. The second-generation wavelet transform[13] features: the original data may be changed with its inverse transform without affecting the basic structural information; auxiliary memory is not needed to implement. It is also a reversible integer wavelet transform, easy to implement and understand.

A linked transform-based low-rank tensor representation that fully uses the redundancy in spatial and spectral / temporal dimensions and multi-scale spatial nature, resulting in an efficient multi low tensor rank approximation. They have used two spatial dimensions with the two-dimensional framelets, and for temporal /spectral dimension one / two-dimension Fourier transform is used, and a Karhunen - Loéve transform (by singular value decomposition) to the changed tensors[14]. Tensor Train rank reduction is conducted on a created higher-order tensor called group by stacking comparable cubes, which naturally and completely exploits Tensor Train rank's ability to create high-order tensors. To every group of Tensor Train, low-rankness is produced by perturbation analysis[15].

The residual texture information in a spectrum variation image is considered by spatial domain spectral residual total variation (SSRTV). SSRTV calculating a 2DTV for the residual image after evaluating the difference between the pixel values of neighboring bands. Low-rank Tucker decomposition takes advantage of hue, saturation, and intensity (HSI) worldwide, low-rankness and spatial–spectral correlation (LRTD). Furthermore, the $l_{2,1}$ norm was shown to be more effective in dealing the sparse noise, particularly sample-specific noise like stripes[16]. In the Tensor Ring (TR) decomposition methodology, the block Hankelization method is used to convert the corrupted tensor data into a 7-D higher order tensor. With rank, incremental and multistage methods, the higher order tensor is recovered by employing TR decomposition. Here the rank incremental approach is used to determine TR rankings[17].

The existing and proposed approaches were evaluated using the Full Reference Assessment metrics named PSNR and SSIM, and No-Reference Assessment metrics named NIQE[18], and PIQE[19]. The values obtained are superior to the existing approaches.

The main contributions of the work are

● The 5/3 wavelet filter-based lifting scheme induced t-SVD is proposed to recover the high dimensional data, when the data consists of more than 80 percent of corrupted observations.

● The visual quality of highly corrupted high-dimensional data under low tensor rank assumptions is improved.

● The PSNR and SSIM are calculated for the reported high when compared with the existing approaches. The NIQE and PIQE are very small, which indicates extreme visual recovery with local and global information.

1.1 Notations and Preliminaries

The notations used are: Lowercase characters, such as $'\mathscr{X}'$ are used to represent the scalars. Lowercase boldface characters, such as $'\mathscr{X}'$ are used to represent vectors. Matrices are symbolized by capital characters, such as $'\mathscr{X}'$. The boldface uppercase scripting characters, such as $'\mathscr{X}'$ indicate the tensors. The ith frontal, lateral and horizontal slices are represented as $\mathscr{X}(:,:$

$,i)$, $\mathscr{X}(:,i,:)$ and $\mathscr{X}(i,:,:)$respectively. Eqn. (1) and (2) are the block circulant tensor and unfolded tensor [3~6].

$$bcirc(\overline{X}) \triangleq \begin{bmatrix} X^{(1)} & X^{(n3)} & \ldots & X^{(2)} \\ X^{(2)} & X^{(1)} & \ldots & X^{(3)} \\ . & . & \ldots & . \\ . & . & \ldots & . \\ . & . & \ldots & . \\ X^{(n3)} & X^{(n3-1)} & \ldots & X^{(1)} \end{bmatrix} \tag{1}$$

$$unfold(X) \triangleq \begin{bmatrix} X^{(1)} \\ X^{(2)} \\ . \\ . \\ . \\ X^{(n3)} \end{bmatrix} \tag{2}$$

The following properties and notations are used in the solving of the objective function.

Tensor Product [3~6] Let $\mathscr{X} \in \mathbb{R}^{n1 \times n2 \times n3}$ and $\mathscr{Y} \in \mathbb{R}^{n2 \times n4 \times n3}$ and . The tensor product between x and y can be written as

$$x * y = \text{fold}(\text{bcirc}(x).\ \text{unfold}(y)) \tag{3}$$

Tensor Transpose [3~6] The transpose of a tensor $X \in R^{n1 \times n2 \times n3}$ becomes as X^T with order n2´n1´n3. The frontal slice needs to be transposed and then the order of the frontal slices from 2 to n3 are may be reversed.

$$\left(X^T\right)^{(1)} = \left(X^1\right)^{(T)}$$

$$\left(X^T\right)^{(i)} = \left(X^{n3-i+2}\right)^{(T)}, i = 2,3,\ldots,n3 \tag{4}$$

Identity Tensor [3~6] The identity tensor $X \in R^{n1 \times n2 \times n3}$ contains the first frontal slice $n \times n$ identity matrix, remaining frontal slices contains all zeros.

Orthogonal Tensor [3~6] A tensor $x \in \mathbb{R}^{n1 \times n2 \times n3}$ orthogonal if it satisfies

$$\mathscr{X}^T * \mathscr{X} = \mathscr{X} * \mathscr{X}^T = \mathfrak{I} \tag{5}$$

The Table 1 describes the notations with descriptions that are used.

2 5/3 Lifting induced t-SVD

The high-dimensional data processing requires huge storage, high data speeds for transmission, and accessing is difficult; to simplify the usage of storage and transmission data rates; the data will be compressed or encoded, during these processes, the tensor gets damaged. The corrupted tensors are less; the tensor can be recovered with conventional algorithms easily. If more tensors are corrupted the existing approaches are unable to recover. Here a transform-based optimization model is discussed to recover the tensors.

2.1 5/3 Lifting Wavelet Transform

The lifting wavelet transforms (LWT) play a vital role in image denoising, image compression, and image inpainting. The LWT features are: less computational complexity, fast, allows the one to custom design the filters, polyphase representation and allows in-place implementation. To build sparse approximations of most real time data, the LWT generated correlation structure may be used. The lifting structure begins with the well-known filters (h,g) and the filters are split into even and odd parts forming a polyphase matrix as

$$P(z) = \begin{bmatrix} h_e & g_e \\ h_o & g_o \end{bmatrix}$$

Table 1. Notation and Description

Notation	Description
$\lVert . \rVert_F$	Frobinous Norm
$\lVert . \rVert_2$	l_2-norm or m-norm
I	Corrupted high dimensional image
U, V	Unitary tensors obtained from tensor SVD
s_i	Prediction coefficients
t_i	Updation coefficients
$\widehat{X}$	Reconstructed matrix
$\widehat{I}$	Recovered tensor
h, g	Low pass and high pass filters
h_e, h_o	Even and Odd tensors obtained with low pass filter
g_e, g_o	Even and Odd tensors obtained with high pass filter
candecomp	Canonical Decomposition
parafac	Parallel Factorization

The polyphase matrix is factorized using the successive division method, which involves utilizing the Euclidean algorithm of the greatest common divisor (GCD) and selecting the proper Laurent polynomials. The factorization process aims to express the polyphase matrix as a series set of lower and upper triangular matrices. The first column of the polyphase matrix is factorized which results in the following matrix decomposition

$$\begin{bmatrix} h_e \\ h_o \end{bmatrix} = \prod_{i=1}^{n} \begin{bmatrix} q_i(z) & 1 \\ 1 & 0 \end{bmatrix} \begin{bmatrix} k \\ 0 \end{bmatrix}$$

k is the greatest common divisors and $q_i(z)$ is the quotient in the ith step of the successive division approach of finding the greatest common-divisors.

Complementary polyphase filter g^0can be found where another polyphase matrix \widehat $\widehat{P}(z)$

$$\widehat{P}(z) = \begin{bmatrix} h_e(z) & \widehat{g_e}(z) \\ h_o(z) & \widehat{g_o}(z) \end{bmatrix} = \prod_{i=1}^{n} \begin{bmatrix} q_i(z) & 1 \\ 1 & 0 \end{bmatrix} \begin{bmatrix} k & 0 \\ 0 & 1/k \end{bmatrix}$$

The final polyphase factorization may be written as

$$\widehat{P}(z) = = \prod_{i=1}^{n} \begin{bmatrix} 1 & s_i(z) \\ 0 & 1 \end{bmatrix} \begin{bmatrix} 1 & 0 \\ t_i(z) & 1 \end{bmatrix} \begin{bmatrix} k & 1 \\ 1 & 1/k \end{bmatrix}$$

k is the non-zero constant and $s_i(z)$ and $t_i(z)$ represents the dual lifting and primal lifting stages, respectively.

The analysis polyphase matrix gives the direct implementation of the forward transform of the lifting scheme. When compared to the standard wavelet approach, this reduces computing complexity. The better performance of the lifting scheme is dependent on the choice of the wavelet filter. Wavelet family has wide range of wavelet filters are available. The wavelet filter '$spl\ 53'$ is the most familiar and lossless conversion filter. The 5/3 wavelet is a biorthogonal wavelet with simple analysis and synthesis stages. It is able to calculate coefficients effectively with a smaller number of computations. The 5/3 filter-pair is made up of the 5 coefficients analysis low pass filter $'h'$, and the 3 coefficients analysis high-pass filter $'g'$. Figure 1 shows the lifting wavelet forward and reverse steps.
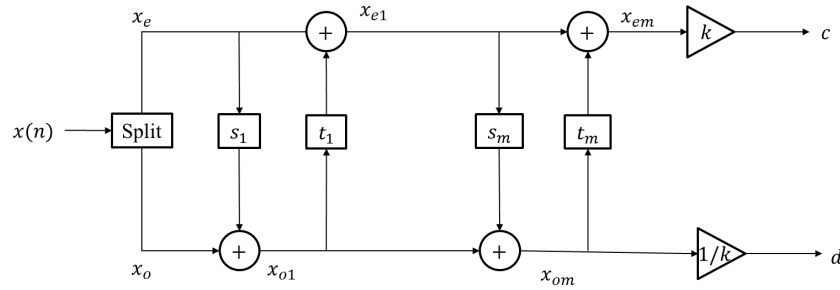
Fig 1. Lifting wavelet forward and reverse process

The tensor-SVD is performed to the lifting coefficients to obtain the sparse data in the corrupted data. Figure 2 shows the tensor-SVD process. Suppose $I \in C^{n_1 \times n_2 \times n_3}$ it can be factorized as $U \in C^{n_1 \times n_1 \times n_3}, V \in C^{n_2 \times n_2 \times n_3}$ and $S \in C^{n_1 \times n_2 \times n_3}$. Where the U, V, are the unitary tensors and S is the diagonal tensor consists of singular values of the high-dimensional data.
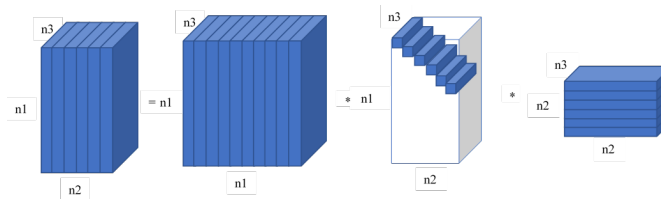
Fig 2. Tensor SVD of 3-dimensional data

The diagonal tensor will be reduced by using the truncation of uncorrelated singular values, it may be used the convex optimization, by utilizing W objective function can be reduced. The augmented Lagrange function becomes as eqn. (6)

$$\mathscr{J}_{k+1} = \arg \min_{\mathscr{J}} \| \mathscr{J} \|_* + \lambda \| \mathscr{W} \|_F$$

$$\mathscr{L}(\mathscr{J}, \mathscr{W}, \mathscr{Y}, \mu) = \| \mathscr{J} \|_* - \operatorname{tr}\left(A_k * W * \mathscr{B}_k^T\right) + \langle y, \mathscr{J} - \mathscr{W} \rangle + \frac{\mu}{2} \| \mathscr{J} - W \|_F^2 \tag{6}$$

Keep $\mathscr{W}_k$ and $\mathscr{Y}_k$ invariant $\mathscr{J}_{k+1}$ will be updated

$$J_{k+1} = \| \mathscr{J} \|_* + \langle \mathscr{Y}, \mathscr{J} - W \rangle + \frac{\mu}{2} \| \mathscr{J} - \mathscr{O} \|_F^2 \tag{7}$$

$$\mathscr{J}_{k+1} = \| \mathscr{J} \|_* + \frac{\mu}{2} \left\| J - \left(\mathscr{W}_k - \frac{1}{\mu} \mathscr{Y}_k \right) \right\|_F^2 \tag{8}$$

Based on the singular value thresholding shrinkage operation eqn. 9. can be solved easily.
By fixing the $\mathscr{J}_{k+1}$ and $\mathscr{Y}_k$ we solve $\mathscr{W}$

$$\mathscr{W}_{k+1} = \arg \min_{\mathfrak{W}} \mathscr{L} \left(J_{k+1}, W_k, y_k \right)$$

$$= \arg \min_{\mathfrak{W}} \frac{\mu}{2} \| J_{k+1} - W_k \|_F^2 - \operatorname{tr} \left(\left(\mathscr{A}_k * W * \mathscr{B}_k^T \right) + \langle y_k, J_{k+1} - \mathscr{W}_k \rangle \right) \tag{9}$$

$$W_{k+1} = I_{k+1} + \frac{1}{\mu} \left(A_l^T * B_l + Y_k \right) \tag{10}$$

The update of $\mathscr{Y}_{k+1}$ is as eqn. 11

$$y_{k+1} = y_k + \mu \left(J_{k+1} - \mathscr{W}_{k+1} \right) \tag{11}$$

The proposed steps are framed as below

Algorithm: Lifting based t-SVD for Tensor Completion
Observation:
$\mathscr{I}$ is original incomplete data set, Ω represents the known elements, $\blacksquare_c$ indicates the unknown elements.
Initialization: $t = 1, \mathscr{Y} = \mathscr{J}, W = \mathscr{J}, k = 1, \varepsilon, \mu = 5 \times 10^{-4}, l = 50$
given $\mathscr{J} \in \mathbb{R}^{m \times n \times p}$
Calculate the lifting coefficnets to tensor $\mathscr{J}_k$
Approximations $'c'$ and details $'d'$ will be calculated using the 5/3 lifting wavelet filter
$[\mathscr{U}, \mathscr{S}, \mathscr{V}] = t - SVD(\mathscr{T}(\mathscr{J}_k))$ where $\mathscr{U}_k \varepsilon \mathbb{C}^{m \times m \times p}, \mathscr{V}_k \varepsilon \mathbb{C}^{n \times n \times p}, \mathscr{T}(\mathscr{J}_k)$ indicates the transform of data.
Compute $\mathscr{A}_l$ and $\mathscr{B}_l$ as follows $(r \leq \min\{m, n\})$
$\mathscr{A}_l = \mathscr{U}(:, 1 : r; :)^T; \mathscr{B}_l = \mathscr{V}(:, 1 : r; :)^T$
update $\mathscr{J}_{k+1}, \mathscr{W}_{k+1}, \mathscr{Y}_{k+1}, \mu$
Keep $\mathscr{W}_k$ and y_k invariant and update $\mathscr{J}_{k+1}$ from $L(\mathscr{J}, \mathscr{W}_k, y_k, \mu)$
By fixing $\mathscr{J}_{k+1}$ and $y_k W$ may be calculated as
$\mathscr{W}_{k+1} = \arg\min_{\mathscr{W}} \mathscr{L}(\mathscr{J}, \mathscr{W}_k, \mathscr{Y}_k, \mu)$
Update $\mathscr{Y}_{k+1}$ directly through
$\mathscr{Y}_{k+1} = y_k + \mu(\mathscr{J}_{k+1} - \mathscr{W}_{k+1})$:
$k = k + 1$
Until $\|\mathscr{J}_{k+1} - \mathscr{J}_k\| \leq \varepsilon$ or $k > l$
Output: The Recovered Image $\hat{J} = \mathscr{J}_{k+1}$

The 5/3 lifting wavelet inclusion in t-SVD, which is improving the effective calculation of missing tensors. The analysis filter coefficients are predicted by the odd location tensors by using the even location tensors. The even locations tensors are the approximation information it will have and the odd location tensors will have the details information of tensors. The odd location tensors may not be used in the prediction and updation of the odd location tensors. The missing or corrupted tensors will be updated with this process. The tensor SVD is applied to the retrieved tensors to minimize the rank of a tensor in the augmented lagrangian approach.

3 Results and Discussion

The proposed approach is tested with the various classes of images like natural images, and scenes, etc. The system configuration used for the work is Intel i5 8th generation processor with 8GB RAM, MATLAB 2019a. The images used for experimentation are of size 256⊠256 and they are listed in Figure 3.
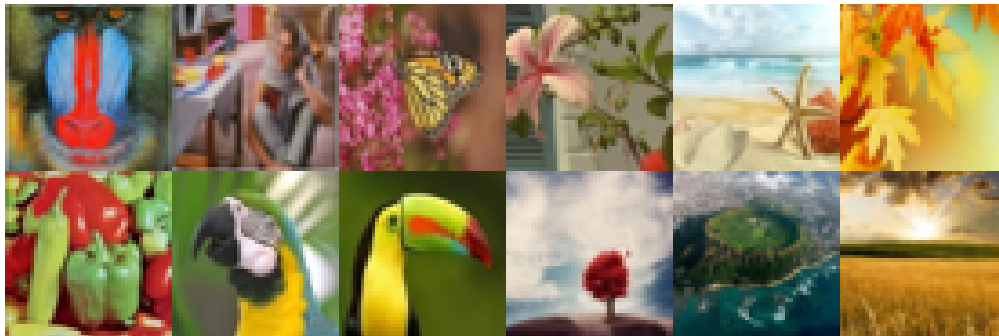
Fig 3. Sample High-dimensionaldata set

The color images are degraded by 10% to 90% random pepper noise to make the intensity values to zero. The 5/3 wavelet with decomposition and reconstruction level is 2. The tensor rank 'r' is considered to be from 1 to 10. The optimal values are achieved at rank 3. The $\varepsilon = 10^{-3}, \rho = 1.05, l = 50$, and $\mu = 5 \times 10^{-4}$ to balance the efficiency and the accuracy of our approach. The FRIQA metrics PSNR and SSIM are used to evaluate the approaches. The PSNR is evaluated as

$$psnr = 10log_{10} \frac{(maximum \ value \ in \ the \ tensor \ elements)^2}{MSE^2} \qquad (12)$$

(12)

where −

The SSIM is evaluated with the luminance distortion, contrast distortion and loss of correlation.

$$ssim = l(I,R)\,c(I,R)\,s(I,R)$$

Where $\quad l(I,R) = \frac{2\mu_I\mu_R + C_1}{\mu_I^2 + \mu_R^2 + C_1}$, $c(I,R) = \frac{2\sigma_I\sigma_R + C_2}{\sigma_I^2 + \sigma_R^2 + C_2}$ and $s(I,R) = \frac{2\sigma_{IR} + C_3}{\sigma_I\sigma_R + C_3}$

Here μ_I and μ_R are indicates the mean values of the reference and recovered data. σ_I and σ_R are indicates the standard deviation of the reference and recovered data. C_1, C_2 and C_3 are the positive constants to avoid null denominator.

Table 2. Comparison of PSNR (in dB) of recovered images by the proposed and existing methods

Image	TNNR[8]	LRTF[5]	Lifting based t-SVD (Proposed)
	24.29	26.91	32.53
	17.93	20.57	29.54
	19.96	22.39	31.38

Table 2 represents the comparison of PSNR values in existing and the proposed methods recovered images from 85% missing observations.Here PSNR alone is not considered concluding which gives better performance. The SSIM, NIQE, and PIQE also considered they provided remarkably good results.

Fig 4. Recovered image results at 70% missing ratio with existing and proposed images. (a) Reference Image, (b) 70% of data randomly corrupted, (c) FaLRTC (Existing), (d) HaLRTC (Existing), (e) T-TNN with APGL(Existing), (f) T-TNN with APGL(Existing) (g) LRTM with APGL(Proposed), and (h) LRTM with ADMM (Proposed)

In Figure 4, Figure 5, and Figure 6 show the recovered images with the existing and proposed approaches, from the 70%, 80%, and 90% corrupted images, respectively. Fig 4 (i), and (ii) shows the reference image and 70% of the corrupted data in the image. In Figure 4 c-h show the existing and proposed approaches recovered images. The proposed approach recovered images have high visual clarity, when compared to existing approaches recovered images. Similarly, and Figure 5 and Figure 6 show that, the corrupted ratio is increased further by 80% and 90% the proposed approach is able to recover with good visual quality.

Fig 5. Recovered image results at 80% missing ratio with existing and prposed images. (a) Reference Image, (b) 80% of data randomly corrupted, (c) FaLRTC (Existing), (d) HaLRTC (Existing), (e) T-TNN with APGL (Existing), (f) T-TNN with APGL (Existing) (g) LRTM with APGL (Proposed), and (h) LRTM with ADMM (Proposed)

The performance evaluation parameters are stated in Figure 7 and Figure 8. The missing ratio to 10% to 90% the PSNR, SSIM, NIQE and PIQE are plotted for various images. Two image results are presented.

Figure 7 shows the PSNR, SSIM, NIQE, and PIQE measures of recovered pepper color image from 10 percent to 90 percent corrupted observations. The existing and proposed approaches have almost similar PSNR values, but the SSIM values are different. The proposed approach has superior values than existing approaches. The NRIQA metrics NIQE and PIQE results are very minimal values are obtained, which is conveying that the proposed approach is better than existing approaches. The PIQE values of recovered data are fluctuating when the missing ratio is small, to those recovered data also given high values, but image quality is good. These differences are identified with existing algorithms also.

Figure 8 presents the FRIQA and NRIQA evaluation metrics for recovered results of high-dimensional data (color image). The missing ratio vs PSNR of the recovered scene image at different missing ratios. To these images set of high-dimensional data achieved small improvement in the PSNR values, with proposed approach and the SSIM values are high at the high missing ratios with the proposed approach. The NIQE and PIQE to different missing ratios of recovered scene image. Figure 9 shows FRIQA and NRIQA metrics with different missing ratios, with different ranks. At small ranks, the PSNR values are good at high missing ratios and the SSIM with different ranks and different missing ratios, at low ranks; thee SSIM values are high at high missing ratios. With the smaller rank, the recovered pepper image at 80% missing ratio is attained as 0.8918 with tensor rank 5.

Similarly, the PSNR achieved as 31.62dB to the same missing ratio and rank. The NIQE is describes the naturalness in the recovered image, while calculating the NIQE score, reference image is not considered. The value is attained as 9.4 to the recovered image at 80% missing ratio with rank 5. Minimum values always indicate the good recovery of the image. Another NRIQA metric is used to evaluate the recovered data i.e., PIQE. The PIQE is also not required to have any reference to evaluate and the value is 27.33. The proposed approach has got the minimum values compared with existing approaches.
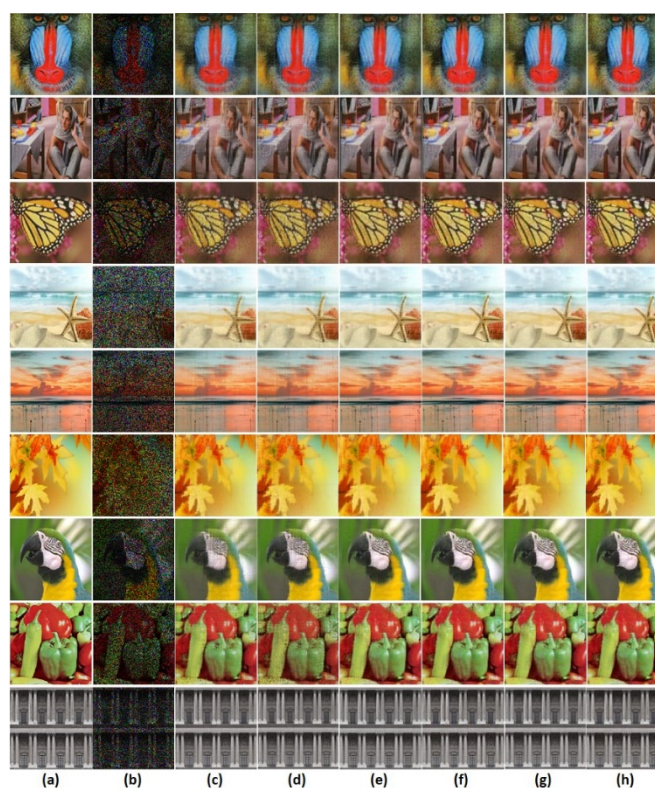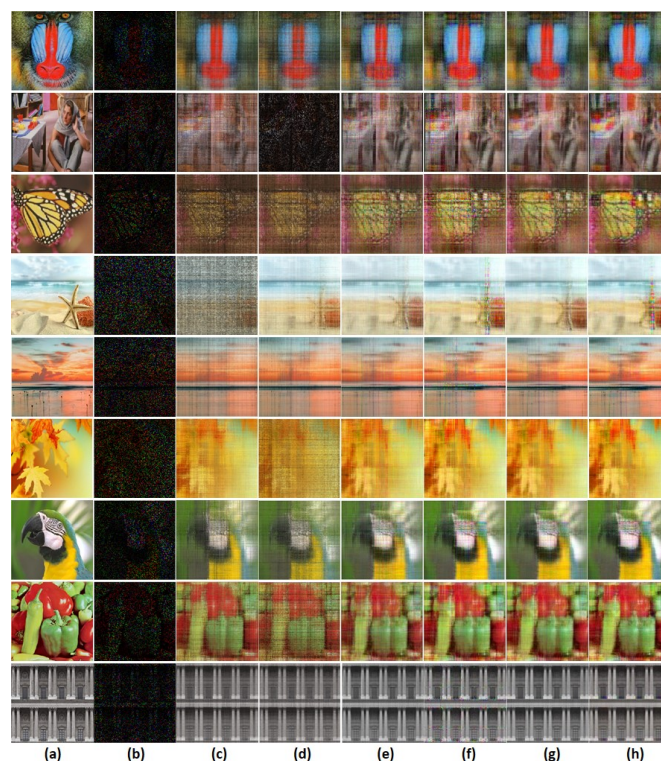
Fig 6. Recovered image results at 90% missing ratio with existing and proposed images. (a) Reference Image, (b) 90% of data randomly corrupted, (c) FaLRTC (Existing), (d) HaLRTC (Existing), (e) T-TNN with APGL (Existing), (f) T-TNN with APGL (Existing), (g) LRTM with APGL (Proposed), and (h) LRTM with ADMM (Proposed)
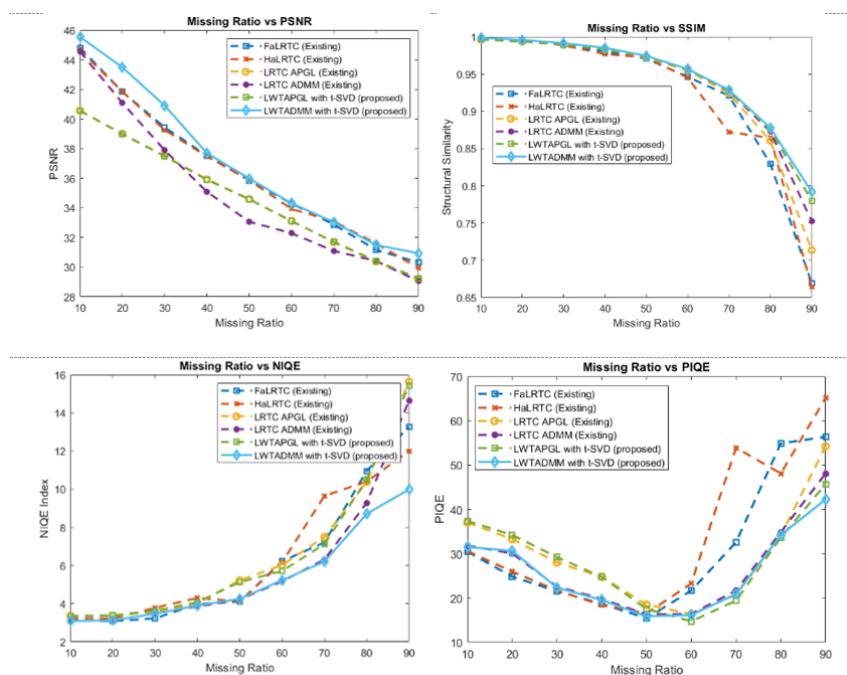
Fig 7. Performance evaluationmetrics for the recovered pepper image at various missing ratios
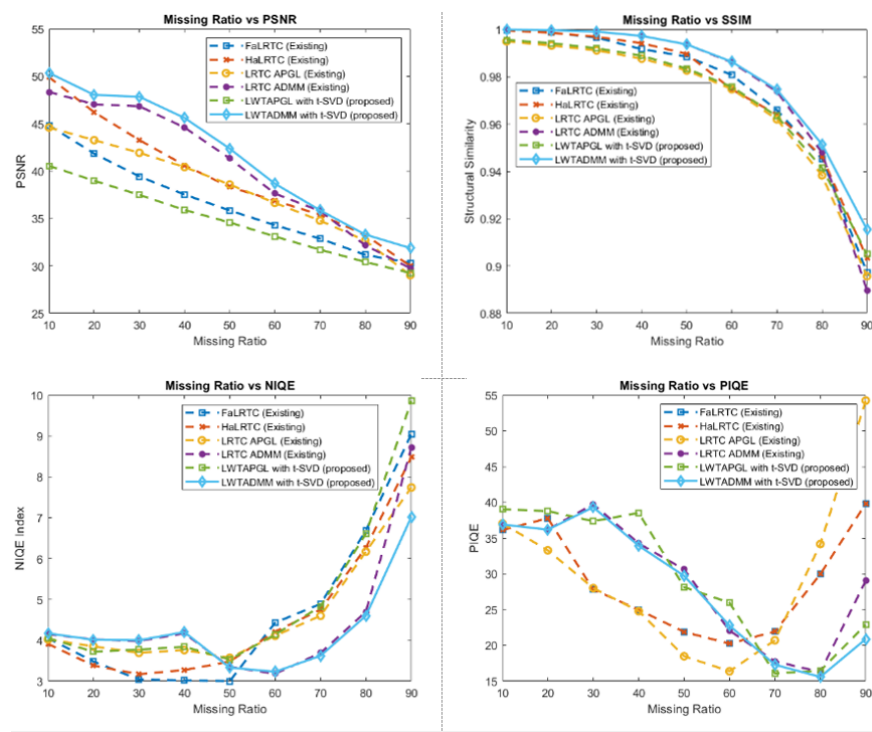
Fig 8. Performance evaluationmetrics for the recovered scene image at various missing ratios
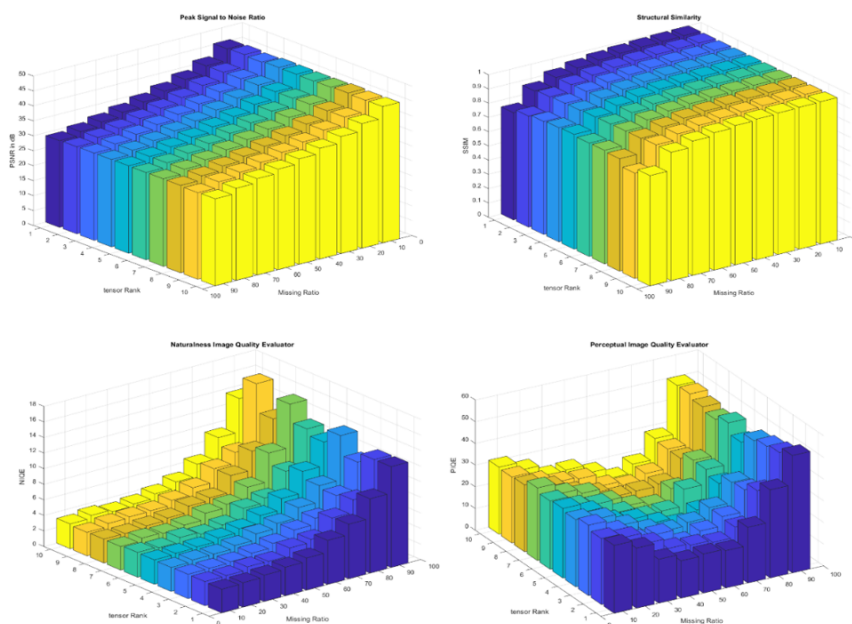
Fig 9. Performance metrics withvarious ranks and with different missing ratios

4 Conclusions

The proposed approach is able to recover the high dimensional data from very less observations efficiently. The lifting wavelets features in-place and custom design of filters are made the design simple, fast and accurate with tensor low rank assumptions. The t-SVD helps in finding the minimum tensor rank. The proposed approach is evaluated with the FRIQA and NRIQA measures along existing methods. The PSNR and SSIM recorded as high values 31.62dB and 0.8918 respectively to recovered image at 80% corrupted observations. The NRIQA measures NIQE and PIQE values are reported as minimum values (9.4 and 27.33 respectively) at highly corrupted ratios. The missing ratio is increasing, the recovery is consistent in proposed approach compared with the state-of-the-art methods.

References

1) Xue S, Qiu W, Liu F, Jin X. Low-Rank Tensor Completion by Truncated Nuclear Norm Regularization. *2018 24th International Conference on Pattern Recognition (ICPR)*. 2018;p. 2600–2605. doi:10.1109/ICPR.2018.8546008.
2) Su Y, Wu X, Liu W. Low-Rank Tensor Completion by Sum of Tensor Nuclear Norm Minimization. *IEEE Access*. 2019;7:134943–134953. Available from: https://dx.doi.org/10.1109/access.2019.2940664.
3) Zhang L, Song L, Du B, Zhang Y. Nonlocal Low-Rank Tensor Completion for Visual Data. *IEEE Transactions on Cybernetics*. 2021;51(2):673–685. Available from: https://dx.doi.org/10.1109/tcyb.2019.2910151.
4) Huang H, Liu Y, Liu J, Zhu C. Provable tensor ring completion. *Signal Processing*. 2020;171:107486–107486. Available from: https://dx.doi.org/10.1016/j.sigpro.2020.107486.
5) Chen L, Jiang X, Liu X, Zhou Z. Logarithmic Norm Regularized Low-Rank Factorization for Matrix and Tensor Completion. *IEEE Transactions on Image Processing*. 2021;30:3434–3449. Available from: https://dx.doi.org/10.1109/tip.2021.3061908.
6) Liu J, Musialski P, Wonka P, Ye J. Tensor Completion for Estimating Missing Values in Visual Data. *IEEE Transactions on Pattern Analysis and Machine Intelligence*. 2013;35(1):208–220. Available from: https://dx.doi.org/10.1109/tpami.2012.39.
7) Recht B, Fazel M, Parrilo PA. Guaranteed Minimum-Rank Solutions of Linear Matrix Equations via Nuclear Norm Minimization. *SIAM Review*. 2010;52(3):471–501. Available from: https://dx.doi.org/10.1137/070697835.
8) Hu Y, Zhang D, Ye J, Li X, He X. Fast and Accurate Matrix Completion via Truncated Nuclear Norm Regularization. *IEEE Transactions on Pattern Analysis and Machine Intelligence*. 2013;35(9):2117–2130. Available from: https://dx.doi.org/10.1109/tpami.2012.271.
9) Dong J, Xue Z, Guan J, Han ZF, Wang W. Low rank matrix completion using truncated nuclear norm and sparse regularizer. *Signal Processing: Image Communication*. 2018;68:76–87. Available from: https://dx.doi.org/10.1016/j.image.2018.06.007.
10) Kilmer ME, Martin CD. Factorization strategies for third-order tensors. *Linear Algebra and its Applications*. 2011;435(3):641–658. Available from: https://dx.doi.org/10.1016/j.laa.2010.09.020.
11) Han ZF, Leung CS, Huang LT, So HC. Sparse and Truncated Nuclear Norm Based Tensor Completion. *Neural Processing Letters*. 2017;45(3):729–743. Available from: https://dx.doi.org/10.1007/s11063-016-9503-4.
12) Song G, Ng MK, Zhang X. Robust tensor completion using transformed tensor singular value decomposition. *Numerical Linear Algebra with Applications*. 2020;27(3). Available from: https://dx.doi.org/10.1002/nla.2299.
13) Ganesan T, Rajarajeswari P, Nayak SR, Bhatia AS. A novel genetic algorithm with CDF5/3 filter-based lifting scheme for optimal sensor placement. *International Journal of Innovative Computing and Applications*. 2021;12(2/3):67–67. doi:10.1504/IJICA.2021.113746.
14) Wang JL, Huang TZ, Zhao XL, Jiang TX, Ng MK. Multi-Dimensional Visual Data Completion via Low-Rank Tensor Representation Under Coupled Transform. *IEEE Transactions on Image Processing*. 2021;30:3581–3596. Available from: https://dx.doi.org/10.1109/tip.2021.3062995.
15) Ding M, Huang TZ, Zhao XL, Ng MK, Ma TH. Tensor train rank minimization with nonlocal self-similarity for tensor completion. *Inverse Problems & Imaging*. 2021;15(3):475–475. Available from: https://dx.doi.org/10.3934/ipi.2021001.
16) Kong X, Zhao Y, Chan JCW, Xue J. Hyperspectral Image Restoration via Spatial-Spectral Residual Total Variation Regularized Low-Rank Tensor Decomposition. *Remote Sensing*. 2022;14(3):511–511. Available from: https://dx.doi.org/10.3390/rs14030511.
17) Farnaz S, Andrzej C. Image Completion in Embedded Space Using Multistage Tensor Ring Decomposition. 2021;4. Available from: https://doi.org/10.3389/frai.2021.687176.
18) Mittal A, Soundararajan R, Bovik AC. Making a "Completely Blind" Image Quality Analyzer. *IEEE Signal Processing Letters*. 2013;20(3):209–212. Available from: https://dx.doi.org/10.1109/lsp.2012.2227726.
19) Venkatanath N, Praneeth D, Chandrasekhar BM, Channappayya SS, Medasani SS. Blind image quality evaluation using perception based features. *2015 Twenty First National Conference on Communications (NCC)*. 2015;p. 1–6. doi:10.1109/NCC.2015.7084843.

INDIAN JOURNAL OF SCIENCE AND TECHNOLOGY

Check for updates

*** Corresponding author**.

jalalkashmire@gmail.com

Competing Interests: None

Optimization of Environmental Data to Improve Safety in Coal Mine using Wireless Sensor Networks

Syed Jalal Ahmad[1]*, **Mohammed Moyed Ahmed**[2], **Ishrath Unissa**[3]

1 Malla Reddy Engineering College Autonomous Main Campus, Hyderabad, India
2 MLR Institute of Technology, Hyderabad, India
3 CMR Technical Campus, Hyderabad, India

Abstract

Objective: Design and implementation of an intelligent system to exploit the safety of Coal mine employees using wireless sensor Network. **Methods:** In this work, we collect environmental data such as harmful gases, temperature/humidity data, earth pressure, vibration, and groundwater level in the mine, by using Wireless Sensor Networks (WSN). A real time environmental data is continuously being monitored and analyzed to handle the current situation of the mine. Moreover, safety alert system can be activated in time to minimize the risk of the mine workers. Here we make use of location-based energy efficient routing protocol to minimize the delay, optimizes the energy between end nodes and a mat lab as simulation tool to compare the results. **Findings:** The presented system finds an extensive use in coal mine industry to provide the safety of employees. However, the designed system can also be employed in railway and road tunnels to check the continuous real time environment conditions of the tunnel and accordingly desired actions have to be taken place. Moreover, the designed system can provide the new base to the research community to precede the research in this field. **Novelty:** The presented approach is simple to operate, cost effective, energy efficient when compared to the existing approaches i.e., B. Vinodh kumar, Banda Srikanth and Kishore V (Please refer figure 6, 7 & 8 for comparisons with different parameters) and has a dynamic control mechanism based on current situation.

Keywords: WSN; Zigbee; environmental data; sensors; WPAN

1 Introduction

Ensuring safety and a healthy environment at the workplace in underground coal mines is very important as it is directly related to the life and health of the workers. There have been unfortunate accidents in which casualties occurred due to explosions and burial mine accidents in the human race. In particular, major risk factors related to mine ventilation include harmful gas, explosive gas, dust, temperature, humidity, and radiation. Many theories and models have been designed and implemented to minimize the coal mine accidents [1–3], however minimum attention is given towards finding the

data like location, number of workers, equipment, and real time environmental data such as gas, wind speed in the mine, temperature, and humidity in the mine. So effective and efficient system need to be addressed that can provide the safety against serious accidents in the Coal Mine. Nowadays wireless sensor networks (WSN) are being widely used to secure health and safety in mine operations since it is autonomous and can be deployed quickly and easily anywhere irrespective of place, position and time. Also, it is a technology that processes and measured the data by establishing wireless connection between end nodes using sensors and also consumes less power[4]. Thus, by using this technology in underground mine one can detect or predict accidents. Li et al[5] presented a review paper in which the authors discuss the safety issues of coal mine employees and the importance of information technology in the coal mine. B. Vinodh Kumar et al., & Komuro N and Suzumaru R[6,7] presented IoT based Underground Coalmine Safety System, in which the authors use different types of sensors and a microcontroller to explore the situation inside the coal mine, however, this approach may not be the optimum in real-time application as no real-time data has been taken to investigate the current scenario and accordingly formulate the decision, also the circuit is complex and improves the delay. The authors of[8,9] proposed different models to improve the safety measurements of coal mine. But the requirement of huge data storage makes the system model the least effective and cannot be used effectively in coal mines to tone down the issues of risk assessment. Y. Zhu and G. You[10] developed a model to provide safety to the coal mine employees using WSN. In this paper, the authors set a constant threshold limit for various sensors which is not based on the mine statistical data, so as a result of which, it may pass wrong information and may not be optimum for real-time application in the coal mine, furthermore the circuitry is complex and introduces more delay which reduces its importance in real-time application. Umashankar et al[11] presented a model to optimize energy using WSN. In this steady, the authors try to improve the energy of the node so that lifetime of the node can be improved. This method has enormous importance in the coal mine to minimize the energy problems and enhance the life span of the node to large extent. Banda et al.,[12] presented a routing protocol to improve the security of coal mines using fuzzy logic, however, the generation of fuzzy rules increases the delay and reduces the throughput and may not be the optimum solution for real-time applications in the coal mine.

In domestic underground coal mines, many mines are deeply deteriorated due to over-mine. As a result of which safety-related issues may not be provided in the mine and collapses which cause accidents. In addition, pollutants such as exhaust gas generated by the movement of diesel vehicles, equipment during working hours, and post-blast gas generated after blasting work are continuously emitted in underground mines. Also, harmful gas is above the standard value due to the poor ventilation system inside the mine[13]. So, there is a risk of serious damage to human life, therefore it is essential to manage air quality in underground coal mines. Due to these problems, the development of a mine safety monitoring and alert system is essential. Underground tunnel communication is the main issue in coal mines, as it has a serious problem such as data transmission failure due to radio link failure. In a temporary mine environment, it is difficult to establish successful wireless communication due to various factors. Such as dust, humidity, temperature, the moving location of the workplace, the difficulty of positioning vehicle equipment, placing transmission, reception antennas, and various tunnel structures due to the mine methods. The Wireless Sensor Networks seems to be the solution of Coal mine safety in which the sensor node detects and processes the data from environmental sensors and communicates to relay nodes. The wireless technology that has been commonly used for major applications of wireless sensor networks is Zigbee, because it is a low-speed, low-power, low-cost wireless personal area network WPAN. Here the Coordinator node receives the data from the relay nodes and transmits it to the central control room. Several theories and methods have been proposed[14–16] to investigate coal mine safety using wireless sensor networks. Thayumanavan et al and N Sathishkumar et al.,[17,18] proposed IOT based security to the coal mine, however the designed algorithms are complex and increases delay, therefore may not be the optimum solution for real time coal mine. N. The Zigbee Alliance developed the PHY layer and MAC layer standard technology of IEEE 802.15.4 for Wireless personnel area networks (WPANs) and standardized higher protocol layers (i.e. Network layer, application layer), which are being used according to the application environment of the Zigbee standards. The other technologies of WPANs that can be used to develop a wireless sensor network are IEEE 802.15.2-based Ultra-Wide Band (UWB) and IEEE 802.15.1-based Bluetooth technology. IEEE 802.11-based Wi-Fi technology of wireless local area network (WLAN) is also widely used in wireless sensor networks.

Table 1 represents the comparative summary of each of the above-mentioned technologies. From Table 1 it has been observed that among all the technologies of WPAN, Zigbee has a relatively slow data transmission rate (i.e.0.25 Mbps). However, it has a wide network capacity that supports long-distance communication and is comparatively simple to build a network. The Wi-Fi method consumes considerably more power than the personal wireless communication methods, so the battery replacement is frequent; therefore, it is unfeasible for applications requiring a low-speed connection.

Establishing an environmental monitoring system using a wireless sensor network in an underground mine, with a relatively small amount of data transmission, requires long-distance communication and an extensive network in a long-extended mine shaft. Considering these aspects, Zigbee has been chosen as a communication technology scheme to investigate the coal mine steady. In this steady, a real-time model for underground coal mine has been developed to monitor the Coal

Table 1. Comparative summary

Parameters	WPAN			WLAN
	UWB	Bluetooth	Zigbee	Wi-Fi
Communication distance (m)	<10	10	50-500	50-100
Frequency range (GHz)	3.1-10.6	2.4	2.4	2.4 or 5
Data rate (Mbps)	100-500	1	0.25	11
Network capacity (nodes)	10-500	7	65,536	32
Power consumption (mW)	30	1-100	20-40	500-1000
Complexity	Mid-High	High	Low	High
Usage in Domestic Mine	O	X	X	O

Mine situation continuously using wireless Sensors and Zigbee technology. Moreover real time data from wireless sensors has been continuously analyzed to get current threshold limit of data, accordingly safety alert system can be activated to improve the safe working conditions In all the above presented approaches very less or no attention was given towards real time environmental data, No doubt few models[6,12,14] considered sensor data, however they fixed a threshold limit of data to predict accidents, which may not always true because the parameters which are responsible for mine accidents are varied with respect to environmental conditions occurred in the mine. Therefore, an information and communication system needs to be addressed which can continuously monitor the real time data in the mine and accordingly desired action has to be taken. The deep mines

The rest of the paper is organized as follows, in section 2 we describe the methodology of the proposed approach, in section 3 we present results and discussion, furthermore we conclude our paper in section 4.

2 Methodology

In the presented approach we follow Zigbee devices with a star topology to build a wireless sensor network. As each node has the advantage of being able to configure in a mesh topology that can be a router, end device, and a full-function device setting as a coordinator. The hardware used in this study consists of a coordinator, a router, and an end device. First of all, the coordinator is a network manager that has only one in each Zigbee network. It is located at the center point of the entire network and becomes the backbone for data transmitted from lower routers and the end devices; it stores the network information and delivers commands to the desired sensor node. So to select the appropriate sensor and process the date between end nodes, three different sections have been chosen to achieve the goal of coal mine safety i.e. i) Selection of Sensors ii) Hardware Configuration and iii) Software Configuration

2.1 Selection of sensors

The sensors used in the Zigbee end device module were selected by referring to the Mine Safety Technical Data Standards and the sensor performance. Various Sensor characteristics that play a critical role in coal mine safety are summarized in Table 2.

Here the selection of sensors is based on the requirement for the safety of working people in the mine. So keeping various safety issues in mind the sensors used to measure activity are noxious gas types such as carbon monoxide (CO), carbon dioxide (CO_2), Hydrogen sulphide (H2S), and oxygen (O_2) sensors. In addition, temperature, humidity, earth pressure, and water level sensors are also installed in the module.

As a sensor selection criterion, it is chosen to measure more than the allowable concentration of harmful gases. Currently, only TLV-TWA is selected as the standard in domestic safe technology standards, which is the allowable concentration for 8 hours. Table 3 represents the maximum permissible concentration of various gases present in the mine, The standards considered here were referred to as Short-term exposure concentration (TLV-STEL) and maximum permissible concentration (TLV-C)[19]. In accumulation, humidity and temperature sensors are also chosen, since the mine has a high humidity condition due to the inflow of groundwater.

2.2 Hardware configuration

In the presented approach we use a coordinator node, a router node, and an end device. Here the coordinator node acts as a network manager in each Zigbee network[20] and is located at the center of the network to cover the entire range efficiently, furthermore acts as the backbone for data transmission between end devices and routers. Also, it plays the role of storing

Table 2. Datasheet of sensors connected to end-device Module

Parameters	CP-11		BW Max XT II		
	CO2	Temp & Hum	CO	O2	H2S
Working voltage (V)	3.4~6.4	4.5~5.5	3.5~5.5	3.5~5.5	3.5~5.5
Working Temperature (°C)	-30~40	-30~50	-30-50	-30-50	-30-50
Working Humidity (RH%)	15-85	15-90	15-90	15-90	15-90
output method	analog voltage signal	digital signal	analog voltage signal	analog voltage signal	analog voltage signal
Measuring range	0-50 PPM	Temp: -40~80°C Hum: 0~99.9 RH%	0-100 PPM	0-80%	0-100 PPM
Resolution	part per billion (ppb) Scale	1ppm	part per billion (ppb) Scale	0.1% Level	part per billion (ppb) Scale

Table 3. Exposure limit of mine gases

Gases	TLV-TWA	TLV-STEL	TLV-C
Carbon dioxide (CO2)	0.5%	3.0%	1.5%
Carbon monoxide (CO)	0.005%	0.04%	0.02%
Hydrogen sulfide (H2S)	10 ppm	15 ppm	15 ppm
Oxygen (O_2)	>19.5%	-	-

network information, delivering commands to the desired sensor nodes. Figure 1 represents the Zigbee coordinator module along with a network interface and is integrated with 3G Modem & Antenna (HSDPA, EDGE, and GPRS), quad-band Ethernet. USB 2.0 transmits and receives data through serial communication with the monitoring program in the PC via the USB port.
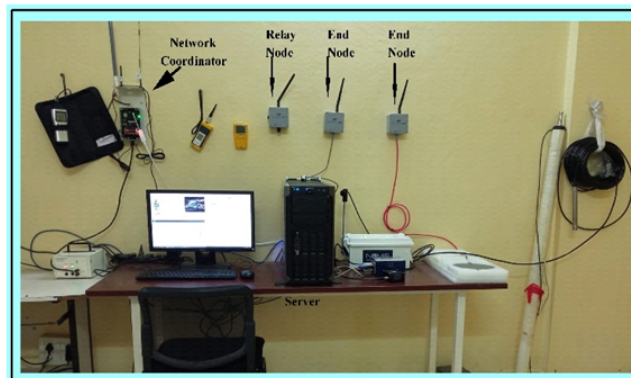
Fig 1. The hardware setup of WSN nodes & a coordinator node

Here 3G Modem fulfills our need in all respects as per our requirement, however, one can use 4G and higher modem also by choosing compatible Trans receivers and interface devices.

The role of a router in a Zigbee network is to extend the communication range of the network by relaying data transmission or reception between Zigbee nodes. It also serves as an application that can transmit data to the coordinator node. The router node composes a module with a microcontroller (MCU) and measurement sensor. The Zigbee router module used in this study is shown in Figure 3, the end device located at the end of the entire network configuration, communicates with the coordinator or router, which is the upper node. It serves to collect actual environmental data and transfers it to the coordinator node. The sensors used in the Zigbee end device module are selected by referring to the Mine Safety Technical Standards and the performance of the sensor. The measurement sensors used here are carbon monoxide (CO), carbon dioxide (CO2), Hydrogen sulfide (H2S), and Oxygen (O2). Furthermore, temperature, humidity, and earth pressure sensors are also installed to make the

system innovative and efficient.

2.3 Software Configuration

The software employed to operate the above category of hardware devices in the WSN environment is Encardio-rite software and the URL used http://162.168.0.10, in any of the browsers.

Initially, we configure different types of WSN nodes and add necessary sensors into the network to perform simulation results. Information to the added nodes can be checked under the nodes list section of the project window. Figure 3 represents the WSN with coordinate node and Zigbee technology to investigate the current scenario in the coal mine. A monitoring program that receives and processes the real-time data from the Zigbee sensor network is also represented in Figure 2. This monitoring program is a Visual Interface program that continuously receives data that is transmitted from each end device through the COM port connected to the coordinator. The transmitted data is stored in a List array and displayed in real-time through the table and graph at the top of the program (see fig. 2).

In addition, the total data stored in the program can be downloaded as a CSV file whenever required. It can be later utilized for data analysis. Collected data will be interfaced with the Lab View software, a function is developed in which the data is updated to the latest value in the string array corresponding to each sensor and automatically updated in CSV file format.
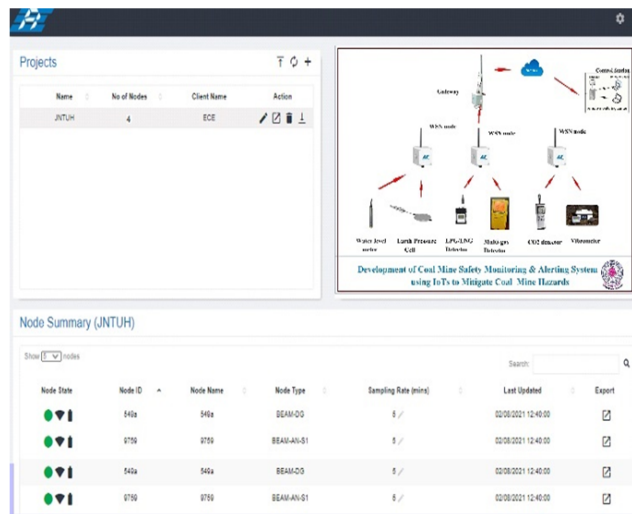
Fig 2. Software setup of WSN nodes & coordinator node

3 Results and Discussion

The data values from the environmental sensor are connected to the end nodes and are received with the monitoring interface program built into the Zigbee gateway. Here we are using LAEERP[21] protocol to find the optimum route between end nodes. In our simulated environment 21 real-time samples of data were received during measurement time (refer to Table 4), the data transmitted from the end device passes through the router node located in the middle section and is forwarded to the coordinator node, where the data is stored and taken for further analysis. The analyzed data is monitored and accordingly the threshold limit of all the sensors is set to activate the alarm system ON, if the sensor data limit exceeds the threshold limit and accordingly the safety measures have to be taken in advance. In this way threshold limit is continuously being monitored and set with respect to the real time data and dynamic operation has to be taken using lab view software.

Figure 3 represents the variation of data with respect to time. It is observed from the figure that data is varying, so a fixed threshold limit cannot maintain a real-time application.

This demonstrates the necessity of the proposed approach as the real-time data-based decision has to be taken and accordingly safety measures can be implemented in advance.

The network parameters considered for simulation are area of the network is 1500x1500 m^2, nodes taken 100, sinks 1, range 100m, packet size 1kbyte, power transmitted 18mw, power received 16mw and buffer size is 256kB.

Table 4. Measurement of Sensors data over a while

| Date/time	CO Level (ppm)	CO2 Level (ppm)	H2S Level (ppm)	O2 Level (%)	Temp (°F)	RH (%)	Earth Pressure Cell (mV/V)
7/23/2021 10:16	0.57	558	3.12	20.10	73.2	70.8	0.072
7/23/2021 11:17	0.54	558	3.14	20.20	73	70.9	0.068
7/23/2021 12:18	0.58	558	3.24	20.80	73	70.6	0.067
7/23/2021 13:19	0.56	558	3.45	21.00	73	70.6	0.071
7/23/2021 14:20	0.57	556	3.11	20.40	73	70.6	0.072
7/23/2021 15:21	0.57	555	3.29	20.92	73	70.8	0.070
7/23/2021 16:22	0.57	558	3.22	21.06	73	70.8	0.069
7/23/2021 17:23	0.57	558	3.24	21.20	73.2	70.9	0.068
7/23/2021 18:24	0.57	558	3.56	21.34	73.2	71	0.072
7/23/2021 19:25	0.57	558	3.52	21.48	73.2	70.9	0.072
7/23/2021 20:26	0.57	556	3.45	21.62	73	70.6	0.067
7/23/2021 21:27	0.57	555	3.42	21.76	73	71	0.071
7/23/2021 22:28	0.57	558	3.41	21.90	73.2	70.7	0.072
7/23/2021 23:29	0.57	558	3.26	22.04	73	70.7	0.072
7/24/2021 0:30	0.58	558	3.62	22.18	73.2	71.1	0.071
7/24/2021 1:31	0.58	558	3.12	22.32	73	71	0.072
7/24/2021 2:32	0.58	556	3.14	22.46	73	70.8	0.073
7/24/2021 3:33	0.58	555	3.24	22.60	73	70.9	0.069
7/24/2021 4:34	0.58	558	3.45	22.74	72.9	71	0.071
7/24/2021 5:35	0.58	558	3.11	20.10	72.9	71.4	0.068
7/24/2021 6:36	0.58	558	3.29	20.20	73	71.3	0.068
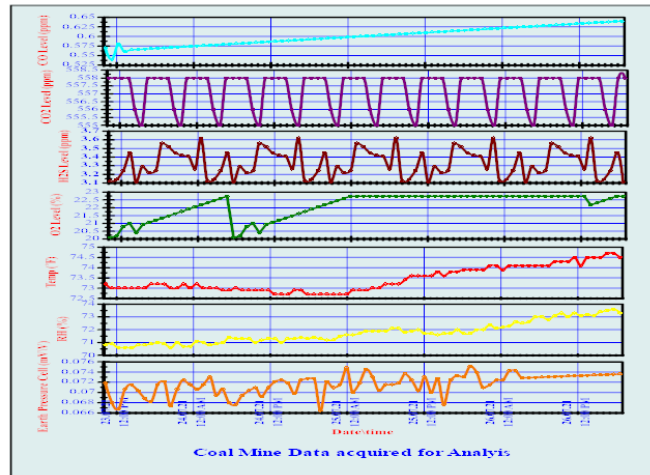
Fig 3. Graphical representation of Coal Mine data acquired over a period of time.

Figure 4 shows the localization error performance, in which we observe that the presented method shows better performance when compared with the art of work. However at some particular points, the Kishore approach is nearby to our approach, it is because at some nodes the link capacity is more and improves the performance. But if the link capacity between any two nodes within the route is marginally low it degrades the performance of the system and reduces the overall response of the method.
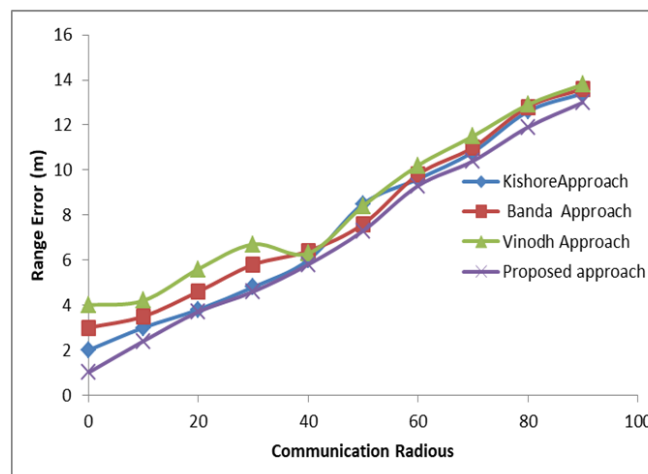
Fig 4. Localization Error Performance

Figure 5 represents the network lifetime response of the proposed approach and the art of work, from the comparative analysis it has been observed that the presented approach shows enhanced outcome when compared with the existing approaches since every node is monitored continuously for all network parameters (I.e. B.W, Energy, nodal delay and distance)

Figure 6 shows the variation of residual energy to the number of nodes, it is clear from the figure that the residual of the proposed approach is less in comparison with the existing approaches. So from the overall comparative analysis, we conclude that the presented approach has better performance when compared with the existing approaches.

The overall comparative analysis reveals that the presented approach reduces the error, optimizes the lifetime and energy of the sensor nodes, Furthermore error reduction improves the overall throughput between the end nodes and enhances the performance of the designed system

Fig 5. Response of Network lifetime

Fig 6. Variation of numberof nodes versus Average residual Energy

4 Conclusion

In this study, a real-time environmental monitoring system using the Zigbee technology model has been developed and implemented for underground coal mines, in which real time sensor data has been collected and analyzed simultaneously to get the current threshold limit of the sensed data and 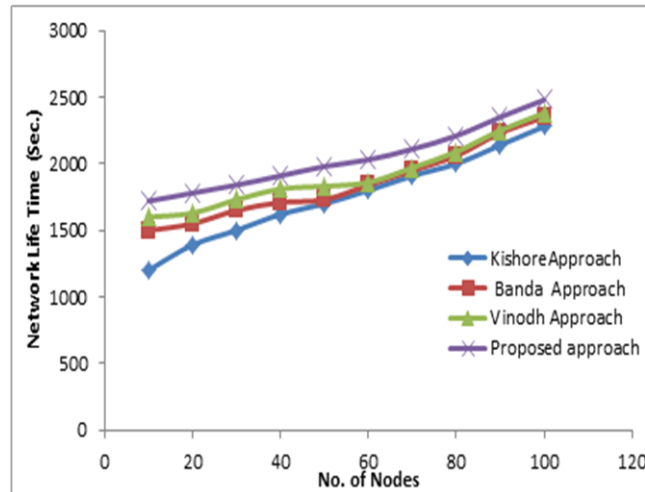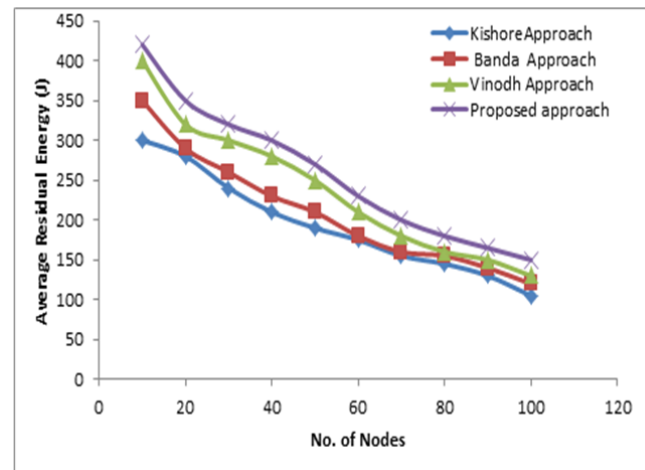accordingly safety measures have to be taken in advance to reduce coal mine accidents. To run the system smoothly and efficiently a software program has been developed using Lab View software that generates an alert alarm for the working employees in underground coal mines to take desired action of safety in advance. The presented system can be used as a basic building block of the coal mine safety for the research community. The presented model has been validated using Lab View and mat lab.

References

1) Fu W, Xu Y, Liu L, Zhang L. Design and Research of Intelligent Safety Monitoring Robot for Coal Mine Shaft Construction. *Advances in Civil Engineering*. 2021;2021:1–16. Available from: https://dx.doi.org/10.1155/2021/6897767.
2) Molaei F, Rahimi E, Siavoshi H, Afrouz SG, Tenorio V. A Comprehensive Review on Internet of Things (IoT) and its Implications in the Mining Industry. *American Journal of Engineering and Applied Sciences*. 2020;13(3):499–515. Available from: https://dx.doi.org/10.3844/ajeassp.2020.499.515.
3) Jo BW, Khan RMA, Javaid O. Arduino-based intelligent gases monitoring and information sharing Internet-of-Things system for underground coal mines. *Journal of Ambient Intelligence and Smart Environments*. 2019;11(2):183–194. Available from: https://dx.doi.org/10.3233/ais-190518.

4) Duarte J, Rodrigues F, Branco JC. Sensing Technology Applications in the Mining Industry—A Systematic Review. *International Journal of Environmental Research and Public Health*. 2022;19(4):2334–2334. Available from: https://dx.doi.org/10.3390/ijerph19042334.

5) Yang L, Birhane GE, Zhu J, Geng J. My Employees Safety and the Application of Information Technology in Coal Mine: Review. *Frontiers in Public Health*. 2021;9:1–12.

6) kumar MBV, Jayasree MB, Kiruthika MD. Iot based Underground Coalmine Safety System. *Journal of Physics: Conference Series*. 2021;1717(1):012030–012030. Available from: https://dx.doi.org/10.1088/1742-6596/1717/1/012030.

7) Komuro N, Suzumaru R. Impact on Compressed Sensing for IoT Used Indoor Environment Monitoring System. In: Lecture Notes in Electrical Engineering. Springer Singapore. 2021;p. 89–96. doi:10.1088/1742-6596/1717/1/012030.

8) Matloob S, Li Y, Khan KZ. Safety Measurements and Risk Assessment of Coal Mining Industry Using Artificial Intelligence and Machine Learning. *Open Journal of Business and Management*. 2021;09(03):1198–1209. Available from: https://dx.doi.org/10.4236/ojbm.2021.93064.

9) Kianfar AE, Sherikar M, Gilerson A, Skora M, Stankiewicz K, Mitra R, et al. Designing a Monitoring System to Observe the Innovative Single-Wire and Wireless Energy Transmitting Systems in Explosive Areas of Underground Mines. *Energies*. 2022;15(2):576–576. Available from: https://dx.doi.org/10.3390/en15020576.

10) Zhu Y, You G. Monitoring System for Coal Mine Safety Based on Wireless Sensor Network. *2019 Cross Strait Quad-Regional Radio Science and Wireless Technology Conference (CSQRWC)*. 2019;p. 1–2. doi:10.1109/CSQRWC.2019.8799111.

11) Umashankar ML. An efficient hybrid model for cluster head selection to optimize wireless sensor network using simulated annealing algorithm. *Indian Journal of Science and Technology*. 2021;14(3):270–288. Available from: https://doi.org/10.17485/IJST/v14i3.2318.

12) Srikanth B, Kumar H, Rao KUM. Secure and QOS Aware Fuzzy Logic Based Routing for Underground Coal Mine Monitoring. *International Journal of Grid and Distributed Computing*. 2019;12(1):11–30. Available from: https://dx.doi.org/10.33832/ijgdc.2019.12.1.02.

13) Yarkan S, Guzelgoz S, Arslan H, Murphy R. Underground Mine Communications: A Survey. *IEEE Communications Surveys & Tutorials*. 2009;11(3):125–142. Available from: https://dx.doi.org/10.1109/surv.2009.090309.

14) Krishnan KV, Khara S, Bagubali A, Chawla V, Ashok K. Spectrum Management using Cognitive Radio for Safety and Security of Coal Mine Workers. *Indian Journal of Science and Technology*. 2016;9(44). Available from: https://dx.doi.org/10.17485/ijst/2016/v9i44/105292.

15) Rawat SKSK, Singh DA, Bharti K. The Underground Mine Area WSN Localization Algorithm. *International journal of engineering research & technology (IJERT)*. 2021;10(08):10–080021.

16) Srikanth B, Kumar H, Rao K. A robust approach for WSN localization for underground coal mine monitoring using improved RSSI technique. *Mathematical Modelling of Engineering Problems*. 2018;5(3):225–231. Available from: https://dx.doi.org/10.18280/mmep.050314.

17) Thayumanavan CP, Ganesh CS, Janaki B, Priyadarshini K. IoT Based Coal Mine Safety and Health Monitoring System using LoRaWAN. *3rd International Conference on Signal Processing and Communication*. 2021;p. 49–53. doi:10.1109/ICSPC51351.2021.9451673.

18) Sathishkumar N, Manoj K, Muniraj M, Naveenkumar C, Praveen. Safety Monitoring System in Coal Mine Using IoT. *Journal of Physics: Conference Series*. 1916. doi:10.1088/1742-6596/1916/1/012433.

19) Shahabi R. *Optimization of Air distribution in mine ventilation networks based on Genetic Algorithm (case study: Kalariz Coal Mine*. 2019. doi:10.22044/TUSE.2019.7344.1346.

20) Ansari AH, Shaikh K, Kadu P, Rishikesh N. IOT Based Coal Mine Safety Monitoring and Alerting System. *International Journal of Scientific Research in Science, Engineering and Technology*. 2021;p. 404–410. Available from: https://dx.doi.org/10.32628/ijsrset2183188.

21) Ahmad SJ, Reddy VSK, Damodaram A, Krishna PR. Location aware and energy efficient routing protocol for long distance MANETs. *International Journal of Networking and Virtual Organisations*. 2013;13(4):327–327. Available from: https://dx.doi.org/10.1504/ijnvo.2013.064461.

RESEARCH ARTICLE

MEMS Based Automatic Fall Detection for Aged People

M.Jagadeesh Chandra Prasad[1] and Telugu Maddileti[2]*

[1]Professor, Department of ECE, Malla Reddy Engineering College [A], Hyderabad, Telangana, India.
[2]Associate Professor, Department of ECE, Malla Reddy Engineering College [A], Hyderabad, India.

*Address for Correspondence
Telugu Maddileti
Associate Professor,
Department of ECE,
Malla Reddy Engineering College [A],
Hyderabad, India.
Email: madhu14283@gmail.com

ABSTRACT

Body Falls in older adults are the significant cause of injury. Falls incorporate dropping from a standing position or from uncovered positions, for example, those on stepping stools or stepladders. The seriousness of damage is commonly identified with the height of fall often leading to disability or death. In this research generally we uses wearable sensor and vision based technique that is automatically detect body fall as early as possible. Accelerometer is used for measuring or maintaining orientation and angular velocity. In vision based procedure first we procure casings or video arrangements from the camera. The division module separates the body outline from the foundation. For Feature Extraction GLCM method is used. SVM method is used for classification. By using those methods we can surely detect the human body fall and can take the preventive measures.

Keywords: Accelerometer, SENSOR, SVM method, GLCM etc.

INTRODUCTION

The primary worry in the recent decades is with the senior or the old age population of the nation [1]. These older population experience variety of a illnesses and diseases condition at very uncertain time. Most of the time injuries are due to the falling on the ground, unconscious and hurting themselves. It will cause serious injury or sometimes death [2]. Therefore, they should be urgently transported to the emergency clinic, where they will be watched and gave medicinal assistance if wellbeing condition is indanger. Simultaneously, the measure of old peoples keeping up their independent life is developing quickly. Be that as it may, remote checking can help to prevent depicted situation, essentially diminish healthcare costs and simultaneously keep up patient's independent way of life [3]. Consequently, there is a reasonable interest in solid multi-useful remote observing frameworks for old individuals,

which gather and join various sources of medical information relating to ordinary daily routine of the monitored patient. As a response to the maturity masses, present day social medicinal services market gives a wide extent of restorative therapeutic gadgets for remote evaluating of basic wellbeing parameters. Most of the supplies is adjusted and maltreatment for spot checking and can't give a constant review of the patient's prosperity conditions. In addition, various parameters are estimated independently and checking procedure isn't synchronized. Simultaneously fall incident are viewed as one of the most widely recognized and most dangers among older populace, with about portion of nursing home occupants and 30% of freely living individuals falling every year. Along these lines, present day social healthcare will in general incorporate solid fall identification usefulness into generalobserving system. As a response to the maturity masses, present day social medicinal services market gives a wide extent of restorative therapeutic gadgets for remote evaluating of basic wellbeing parameters. Most of the supplies is adjusted and maltreatment for spot checking and can't give a constant review of the patient's prosperity conditions. In addition, various parameters are estimated independently and checking procedure isn't synchronized. Simultaneously fall incident are viewed as one of the most widely recognized and most dangers among older populace, with about portion of nursing home occupants and 30% of freely living individuals falling every year. The system consists of following parts.

i)   Image Acquisition
ii)   Segmentation
iii)   Feature Extraction
iv)   Classification.

As a rule, various parts involving the frameworks are crumbled and working independently from one another. Be that as it may, if we combine monitoring component (for example sensors, video camera, Smartphone's) into smart situations, we will almost certainly do overlook for elder individuals with different endless situation at home. With the ongoing advancement on ICT showcase wearable sensors and image processing are regularly conveyed related to environmental devices to improve fall discovery rates and limit false cautions.

LITERATURE SURVREY
Shery Oliver et.al [1] proposed to identify falls by handling with a few component extraction and grouping method for typical just as debilitated individuals. The feature extraction algorithm picked is equipped for detecting, preparing and imparting the fall event under genuine conditions. The blend of numerical information is utilized so as to identify fall with high exactness and dependability. Fouzi Harrou et.al [2] proposed Acknowledgment of human developments is exceptionally helpful for a few applications, for example, brilliant rooms, intelligent augmented experience frameworks, human detection and condition displaying. The goal of this work centers around the identification and order of falls dependent on varieties fit as a fiddle, a key test in PC vision .the recognition is accomplished with multivariate exponentially weighted moving normal (MEWMA) checking plan, which is viable in identifying falls since it is touchy to little changes. Shockingly, a MEWMA measurement neglects to separate genuine tumbles from some like-fall motions. To cure this restriction, an arrangement stage dependent on help vector machine is connected on distinguished successions. To approve this approach, two fall recognition datasets have been tried: the University of Rzeszow fall identification dataset (URFD) and the fall discovery dataset (FDD).Yoosuf Nizamet.al [3] proposed fall location for older is a noteworthy subject the extent that assistive advancements are concerned. This paper gives a survey of past chips away at human fall identification gadgets and a primer outcomes from a creating profundity sensor based gadget. The three primary methodologies utilized in fall identification gadgets, for example, wearable based gadgets, encompassing based gadgets and vision based gadgets are distinguished alongside the sensors utilized. The structures and calculations connected in every one of the methodologies and their uniqueness is additionally represented. Pooja Shukla et.al [4] proposed that the population of old people are living alone at home is more. Fall is one of the real hazards for old individuals. In some cases more seasoned individuals may quit fooling around damage to their spine (spinal rope) and that may prompt passing. Once in a while fallen harmed older might lie on the ground surface for a fewtimes after a fall episode has happened. This makes it imperative to have a fall location framework. In this paper, she proposes a novel and powerful fall location framework. Their methodology depends on movement history. Their calculation gives promising outcomes

on video successions of everyday exercises and mimicked falls. Wang, J.et.al [5] proposed, an upgraded fall recognition framework is proposed for old individual checking that depends on savvy sensors worn on the body which recognized the unplanned falls in the home medicinal services condition. By using data assembled from an accelerometer, cardio tachometer and savvy sensors, the effects of falls can be minimized andrecognized from typical every day exercises. The proposed framework has been sent in a model framework as point by point in this research.

RESULTS

Finally it is concluded that by using this method lifetime of a person can be saved and this is useful for the elderly people so they can live their life independently, Automatic falls can be easily detected through this technology. Block diagram used for the implementation of the proposed method is shown in fig.1.Prototype is constructed and tested for results and is shown in fig.2

CONCLUSION

We have reviewed different techniques for the detection of a fall event using wearable sensors. Gyroscope sensor is mandatory to detect fall. From study of computerized image processing technique we come up with a following conclusion. The GLCM functions characterize the texture of an image by calculating how often pairs of pixel with specific values and in a specified spatial relationship occur in an image, creating a GLCM, and then extracting statistical measures from this matrix. The SVM method is used for classification
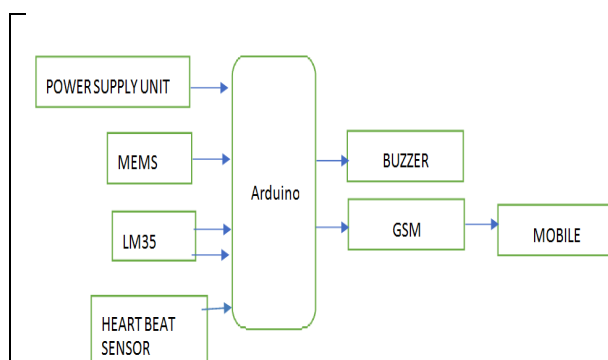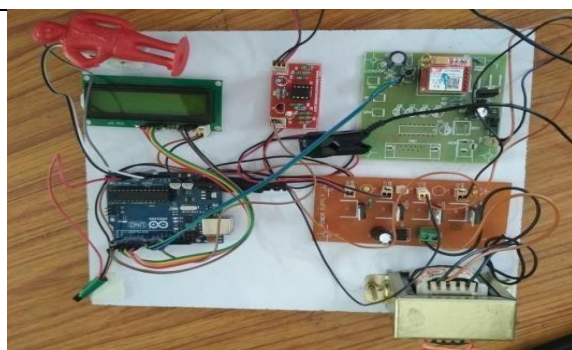
REFERENCES

1. Sheryl Oliver A, Anuradha M, Jean Justus J, Maheshwari N, "Optimized low computational algorithm for elderly fall detection based on machine learning techniques", Biomedical Research, Volume 29, Issue 20, 2018, pp. 3715- 3722.
2. Harrou F, Zerrouki N, Sun Y, Houacine A, "Vision-based fall detection system for improving safety of elderly people". IEEE Instrumentation & Measurement Magazine20, 2017, pp. 49– 55.
3. Yoosuf Nizam, Mohd Norzali Haji Mohd, M. Mahadi Abdul Jamil, " A Study on HumanFall Detection Systems: Daily Activity Classification and Sensing Techniques", International Journal of Integrated Engineering, Vol.8 No. 1 ,2016, pp. 35-43.
4. Integrated Engineering, Vol. 8 No. 1 ,2016, pp. 35-43.
5. Pooja Shukla, Arti Tiwari, "Vision based approach to human fall detection",International Journal of Engineering Research and General Science Volume 3, Issue 6, November- December, 2015, pp. 944-949.
6. Wang, J., Zhang, Z., Bin, L., Lee, S. and Sherratt, S., "An Enhanced Fall Detection Sy stem for Elderly Person Monitoring using Consumer Home Networks", IEEE Transactions on Consumer Electronics Volume 60, 2014, pp. 23-29
7. Quoc T. Huynh et al."Optimization of an Accelerometer
8. Gregory Koshmak, Maria Linden, Amy Loutfi. "Evaluation of the Android-Based Fall Detection System with Physiological Data Monitoring". 35th Annual International Conference of the IEEE EMBS Osaka, Japan, 3 - 7 July, 2013.
9. Diana Yacchiremaa,b, JaraSuárez de Pugaa, Carlos Palaua, Manuel Esteve .Fall detection system for elderly people using IoT and Big Data "Procedia Computer Science 130, 2018,pp.603–610.
10. Liang, Shengyun, et al. "Pre-impact alarm system for fall detection using MEMS sensors and HMM- based SVM classifier." 2018 40th Annual International Conference of the IEEE Engineeringin Medicine and Biology Society (EMBC). IEEE, 2018.
11. Nyan, M. N., et al. "Garment-based detection of falls and activities of daily living using 3-axis MEMS accelerometer." Journal of Physics: Conference Series. Vol. 34. No. 1. IOP Publishing, 2006.

Jagadeesh Chandra Prasad and Telugu Maddileti

12. Yu, Xinguo. "Approaches and principles of fall detection for elderly and patient." Health Com 2008- 10th International Conference on e-health Networking, Applications and Services. IEEE, 2008.
13. Gupta, Piyush, et al. "MEMS-based sensing and algorithm development for fall detection and gaitanalysis." Microfluidics, BioMEMS, and Medical Microsystems VIII. Vol. 7593. SPIE, 2010.
14. Hu, Xinyao, and Xingda Qu. "Pre-impact fall detection." Biomedical engineering online 15.1 (2016): 1-16.
15. Gong, Shulan, et al. "Design of remote elderly health monitoring system based on MEMS sensors." 2017 IEEE International Conference on Information and Automation (ICIA). IEEE, 2017.

Fig 1: Block Diagram	**Fig 2. Prototype**

Design of a Compact ISM-band Microstrip Slot Antenna for Wireless Sensor Nodes

G S K Gayatri Devi[1], S Krishna Veni[2], T Vidyavathi[3], Syed Jalal Ahmad[1]*

1 Malla Reddy Engineering College (A) Main Campus, Secunderabad, ECE
2 Gayatri Vidya Parishad College for degree & PG Courses (A) Rushikonda
3 Anil Neerukonda Institute of Technology& Sciences Sangivalasa, ECE

Abstract

Objective: To enhance the design and implementation of microstrip antenna for wireless Sensor Networks (WSN) in real-time applications **Methods:** This study uses radio communication to connect end nodes and forms a multi-hop self-organizing network with a dynamic topology. Also, the antenna is fabricated from low-cost FR-4 printed circuit board (PCB) material. The designed rectangular patch antenna operates in the industrial, scientific, and medical (ISM) frequency band of 2.45 GHz, and HFSS software analyzer is used to authenticate the proposed work. **Findings:** The designed antenna finds an extensive use in short-range wireless sensor networks, the proposed antenna reduces the return loss from 10% - 13 % and almost 15% improvement in radiation compared with K. D. Xu (2018) and E. Zhang (2020). **Novelty:** A novel short range, low power, and well directional microstrip patch antenna are designed to improve the wireless Sensor communication applications operating at 2.4 GHz and 5.3 GHz frequencies. The presented approach is simple to operate, cost-effective, energy-efficient, and has optimum return loss performance (please refer Table 2) when compared to the existing approaches.

Keywords: Microstrip antenna; Compact; HFSS; Wireless Sensor Network; dual frequency

1 Introduction

Wireless sensor networks (WSNs) have been widely used by deploying several sensor nodes to monitor the preferred structure. However, in wireless sensor nodes, the antenna design (i.e. Patch) still has gaps such as Antenna radiation design needs further enhancement, Return loss must be within tolerable limits, and utilization of power should be minimized.

Many designsand techniques[1–3] have been projected in the literature to enhance the quality of a patch antenna with different geometries in wireless sensor network applications. The designed antennas have an overall size reduction of 77% compared to the conventional rectangular patch antenna achieved by employing Hilbert geometry. However, the cast, return loss, and utilization of energy need further look up to meet the requirement of WSNs. A novel wearable antenna radiating at 5 GHz for

body-centric wireless sensor networks has been presented[4]. But the antenna consists of a conventional microstrip patch mounted on a gold base and could be worn on a finger like a ring, therefore decreasing the performance and increasing the cast of the designed system. Also, computer simulation technology (CST) Microwave Studio is used for modeling, simulation, and optimization of the antenna, as a result, the time complexity increases and reduces the overall gain.

Design of Compact E-Shaped Microstrip Patch Antenna for Wireless Body Area Network, coplanar waveguide-fed super-wideband antenna for wireless sensor networks, and Omni directional patch antenna is presented[5–7] to improve the efficiency of an antenna system. However, all the approaches studied only low-profile designs and are comprised of a modified bow-tie-shaped vertical patch, with two asymmetrical ground planes, and have been prototyped on a single-sided FR4 microwave substrate, so improves the cast and design complexity. E. Zhang et al[8] proposed a dual circularly polarized (CP) stacked patch antenna for Multiple-Input Multiple-Output (MIMO) WLAN applications (2.4-2.485 GHz). This exploits a square ring slot feeding technique and improves the performance of the system concerning the isolation and amplitude of cross-polar components. In[9] the authors designed a double L slotted microstrip patch antenna for WSN applications, in which the authors use the Sea Lion optimization algorithm to enhance the performance of an antenna in sensor nodes. In[10], a rectangular ring and a microstrip feed frequency reconfigurable antenna operating at three frequencies 2.8 GHz, 2.7 GHz, and 3.6 GHz are presented. A dual-band CPW-fed miniature planar antenna and the design analysis of a Dual Rectangular Ring Microstrip antenna with Defected Ground Structure (DGS) is presented for wireless applications[11,12]. Here the main focus was given to the design on the wideband frequency and Omni directional radiation pattern. Also in the design, the authors use substrate type FR-4 with a dielectric constant of 4.7 and tangent loss of 0.019 respectively. However, the design of the antenna is too complex and may not be the optimum solution to receive multimedia data in wireless sensor networks for live communication.

Biddut et al[13] proposed a Wide Band Microstrip Patch antenna in which the authors used multiple slots at the V band moreover the design is more composite and increases the overall return loss which reduces the performance of the system. In[14] authors proposed a Compact E-Shaped Microstrip Patch Antenna for Wireless Communication systems, however, the antenna is having narrow bandwidth and may not be suitable for wireless sensor networks. A model was proposed for wideband applications called wideband patch antenna with shorting Vias[15,16], but the designed antenna is proposed for TE02 mode propagation only and cannot be used for WSN

The authors of[17,18] presented two different approaches to improve the bandwidth of the patch antenna By using the loading parasitic patch concept, however in both approaches several parasitic patches were used to achieve the end task and increase the delay, therefore cannot be used in wireless sensor networks to communicate real-time applications. In[19] design and Numerical Analysis of a Compact Microstrip Antenna was reported, and A Spurious Free Dual Band Microstrip Patch Antenna[20] was proposed for Radio Frequency Energy Harvesting. Ahmad et al[21] presented an approach to enhance the throughput of WSN in coal mine using by observing the statistical data, however, the authors did not put any attention to monitoring the performance of the antenna used within the sensor node.

It has been observed from the above literature that energy management, radiation, and return loss still need more attention to meet the real-time application of WSN

In this paper, we present a novel compact dual-frequency microstrip fed patch antenna to execute the transmission and reception requirement of a wireless sensor network to fulfil the conditions of real-time applications. Also, the proposed designed antenna improves the radiation as well as minimizes the return loss, consequently enhancing the utilization of energy. Moreover, the designed antenna uses low cast material and optimum dimension parameters hence can be used in medical applications such as endoscopic capsules to improve the image quality & cardiac monitoring systems to observe the activity of the heart. The designed antenna is simulated using HFSS to validate the proposed approach.

2 Proposed Approach

The antenna design comprises a rectangular ring patch embedded with a circular patch inside and adopts the reactance loading method i.e., the dual-band operating characteristics are realized by loading the micro-strip, to improve the working bandwidth of the antenna while ensuring performance. Here we choose the actual geometry of the antenna as represented in Figure 1. Furthermore, the various parameters of the antenna used are i) FR4 substrate ii) relative permittivity 4. and iii) tangent loss 0.02 and thickness 0.7mm.

The transmission line model is used to design and check the performance of the proposed system. Moreover, two different frequencies (i.e. 2.4GHz and 5.3GHz) are used to operate the designed antenna to enhance the performance of the presented system. A microstrip line of 50Ω is etched on the economical substrate to provide the feed. The width of the feed line is 3mm. The antenna design consists of an outer rectangular ring-shaped patch with dimensions 30mm X 25mm to which a circular shaped stub of radius 5mm is connected. Table 1 represents the dimensions of the presented antenna.

Table 1. Dimensions of antenna Parameters

Parameter	Value (mm)
L_S	35
W_S	40
L_1	25
W_1	30
W_2	5
R	5

The width and the length of the patch can be determined by equations 1 and 2 respectively

$$W_1 = \frac{v}{2f_d\sqrt{\frac{\varepsilon_r+1}{2}}} \tag{1}$$

$$L_1 = L_{\text{effect}} - 2\Delta L \tag{2}$$
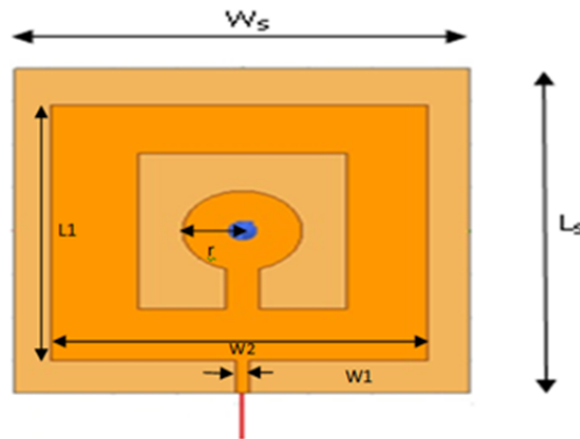
Fig 1. Antenna Geometry

Where 'f_d' = Operating Design Frequency
'$\in_r$' = Dielectric Constant or permittivity of the substrate
'v' = velocity

$$L_{effect} = \frac{v}{2f_d\sqrt{\varepsilon_{\text{effect}}}} \tag{3}$$

$$\Delta L = 0.412t\frac{\left(\varepsilon_{r_{effect}}+0.3\right)\left(\frac{w_1}{t}+0.264\right)}{\left(\varepsilon_{r_{effect}}-0.258\right)\left(\frac{w_1}{t}+0.8\right)} \tag{4}$$

$$\in_{r_{\text{effect}}} = \frac{\varepsilon_r+1}{2}+\frac{\varepsilon_r-1}{2}\left[1+12\frac{t}{w_1}\right]^{-1/2} \tag{5}$$

and 't' is the height of the designed patch antenna.

The orientation of the proposed patch antenna is represented in Figure 2. Moreover, a rectangular ring patch antenna of the dimensions specified in Table 1 is first etched on the substrate and then the dual frequency behavior is obtained by connecting a circular-shaped stub to one of the radiating edges of the patch.

The feeding line of the designed antenna is terminated with a standard Sub Miniature Version a Connector (SMA) to connect directly with other desired instruments.

Fig 2. Antenna orientation

3 Results and discussion
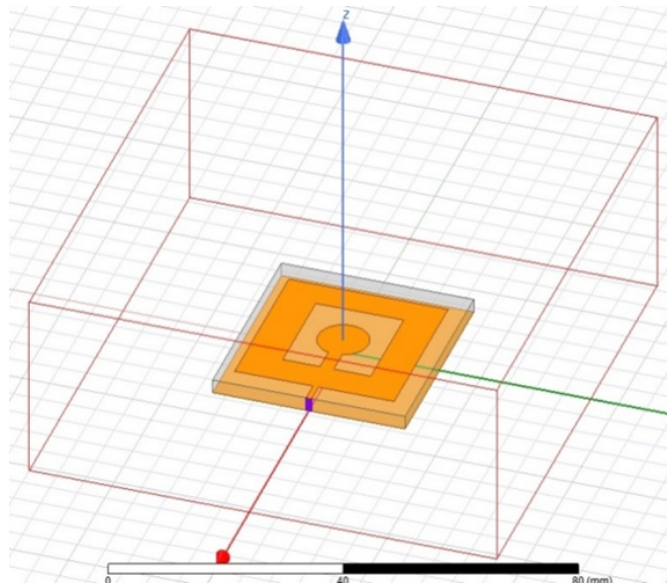
The proposed antenna is simulated using high-frequency structure simulator (HFSS) software. Figure 3 represents the return loss characteristics at 2.4GHz and 5.3GHz, moreover, it has been observed from the simulated results that the center resonance points of the antenna are f_1 =2.4GHz and f_2. 5.3GHz, respectively.
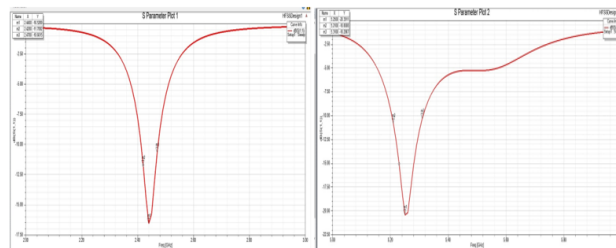
Fig 3. Return loss characteristics at 2.4GHZ & 5.3GHZ

Also, we have seen that when the return loss S_{11} <-10dB, the operating frequency range of the antenna lies in the low-frequency band (i.e. 2.420 to 2.470 GHz) and we achieved 50MHz bandwidth. However, when the frequency range of the antenna lies in the high-frequency band (i.e. 5.210 to 5.310 GHz) the bandwidth achieved is approximately equal to 100 MHz. In addition, the return loss of the antenna at the resonance point is -16.52dB and -20.39dB respectively, indicating that the antenna is well matched.

The directivity and gain plots (i.e. Polar plots) of the proposed antenna at 2.4GHz and 5.3GHz frequencies are presented in Figures 4, 5, 6 and 7 respectively.

Here we scrutinize that the antenna is highly directional and gain is improved, no doubt the gain of the designed antenna is not enhanced up to the desired requirement of wireless communication since the presented antenna has larger half power beam width to maximize the radiation.

Therefore further improvement in the gain minimizes the directivity and will reduce the overall efficiency of the proposed system. However, in the proposed system the antenna is designed for a wireless sensor network in which the distance between the sensors is limited. Since the desired range between the sensor nodes in the network is limited and does not necessitate more gain to meet the desired goal of communication through the wireless sensor network.
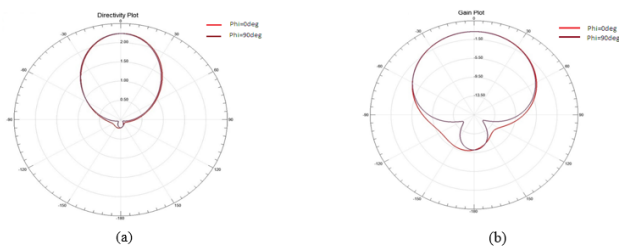
Fig 4. (a) Directivity plot at phi=0deg, phi=90deg.(f = 2.4 (b) Gain plot at phi=0deg,phi=90deg (f = 2.4 GHz)

Fig 5. (a) Directivity polar plot of the antenna at 2.4 GHz. (b) Gain polar plot at 2.4 GHz
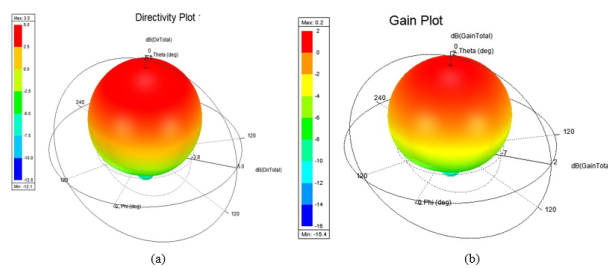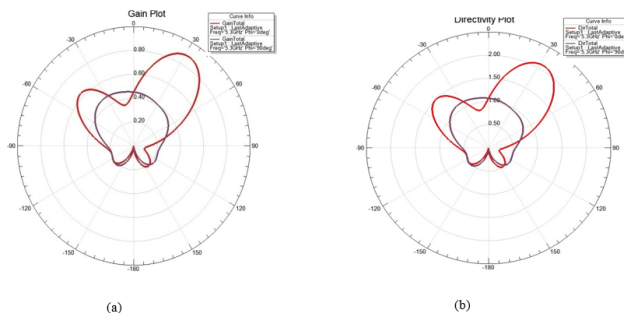

Fig 6. (a) Directivity plot at phi=0deg, phi=90deg.(f = 5.3 GHz)(b) Gain plot at phi=0deg, phi=90deg (f = 5.3GHz)
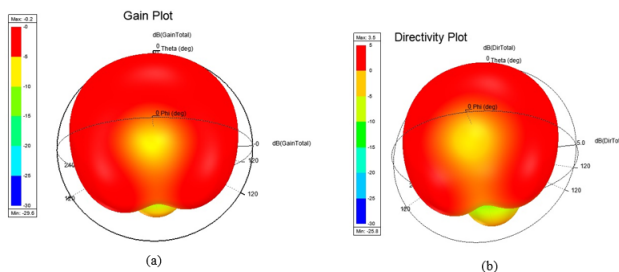

Fig 7. (a) Directivitypolar plot (f= 5.3 GHz) (b) Gain polar pattern (f=5.3 GHz)

Table 2 represents the comparative analysis of the current art of work with the proposed approach. It has been observed from Table 2 that the performance of the proposed approach is healthier when compared with the current art of the work.

The overall response of the anticipated design confirms that it can be used in a wireless sensor network to enhance faithful radiation. Furthermore, the proposed patch antenna improves the transmission and reception capability to get the desired output between the end nodes in the designed geographical wireless sensor network. Also, the presented design will give the fundamental idea to the research community to improve the performance of the patch antenna to the next step of wireless sensor network communication applications.

Table 2. Comparative Analysis

	Center frequency (GHz)	Relative Bandwidth (%)	Efficiency (n) in %	Return Loss S_{11}
16	5.85	27.4	89.11	-18.23
3	2.42	11.2	81.33	-14.25
7	4.5	8.9	85.85	-16.41
14	2.4	5.8	79.3	-13.9
19	2.5	5.1	80.2	-10
15	5.8	32	86.3	-10
Proposed Approach	2-45 & 5.3	11 & 34	89 & 92	-16.52 & - 20.39

4 Conclusion

A novel microstrip patch antenna operating at 2.4 GHz and 5.3 GHz frequencies is presented. The proposed system illustrates (refer Table 2) enhanced response of return loss, bandwidth, efficiency, directivity, and gain to get the desired output in a wireless sensor network. It has been seen that the proposed antenna is a suitable candidate for close-range wireless sensor network communication applications. In the future, it is planned to carry out studies to increase the gain of the antenna presented in this study and to expand the operating frequency bands. The radio frequency energy receiving antenna can adapt to the two frequency bands of ISM and has small in size, has low production cost, has strong practicability, and has good application prospects.

References

1) Elkorany AS, Mousa AN, Ahmad S, Saleeb DA, Ghaffar A, Soruri M, et al. Implementation of a Miniaturized Planar Tri-Band Microstrip Patch Antenna for Wireless Sensors in Mobile Applications. *Sensors*. 2022;22(2):667–667. Available from: https://doi.org/10.3390/s22020667.

2) Salih AA, Sharawi MS. A Dual-Band Highly Miniaturized Patch Antenna. *IEEE Antennas and Wireless Propagation Letters*. 2016;15:1783–1786. Available from: https://doi.org/10.1109/LAWP.2016.2536678.

3) Liang Z, Liu J, Li Y, Long Y. A Dual-Frequency Broadband Design of Coupled-Fed Stacked Microstrip Monopolar Patch Antenna for WLAN Applications. *IEEE Antennas and Wireless Propagation Letters*. 2016;15:1289–1292. Available from: https://doi.org/10.1109/LAWP.2015.2505091.

4) Farooq W, Ur-Rehman M, Abbassi QH, Yang X, Qaraqe K. Design of a finger ring antenna for wireless sensor networks. *2016 10th European Conference on Antennas and Propagation (EuCAP)*. 2016;p. 1–4. Available from: https://doi.org/10.1109/EuCAP.2016.7481827.

5) Afruz U, Kabir MA. Design of Compact E-Shaped Microstrip Patch Antenna for Wireless Body Area Network. *2022 International Conference on Innovations in Science, Engineering and Technology (ICISET)*. 2022;p. 157–162. Available from: https://doi.org/10.1109/ICISET54810.2022.9775820.

6) Azim R, Islam MT, Arshad H, Alam MM, Sobahi N, Khan AI. CPW-Fed Super-Wideband Antenna With Modified Vertical Bow-Tie-Shaped Patch for Wireless Sensor Networks. *IEEE Access*. 2021;9:5343–5353. Available from: https://doi.org/10.1109/ACCESS.2020.3048052.

7) Wu TL, Pan YM, Hu PF, Zheng SY. Design of a Low Profile and Compact Omnidirectional Filtering Patch Antenna. *IEEE Access*. 2017;5:1083–1089. Available from: https://doi.org/10.1109/ACCESS.2017.2651143.

8) Zhang E, Michel A, Pino MR, Nepa P, Qiu J. A Dual Circularly Polarized Patch Antenna With High Isolation for MIMO WLAN Applications. *IEEE Access*. 2020;8:117833–117840. Available from: https://doi.org/10.1109/ACCESS.2020.3004895.

9) George R, Mary TAJ. Design of Directional Two L shaped Microstrip Patch Antenna for WSN Applications Using Sea Lion Optimization Algorithm. *2021 International Conference on Advances in Electrical, Computing, Communication and Sustainable Technologies (ICAECT)*. 2021;p. 1–6. Available from: https://doi.org/10.1109/ICAECT49130.2021.9392454.

10) Sarangi SS, Sharma AK. Rectangular ring reconfigurable antenna for wireless communication. *2017 International Conference on Wireless Communications, Signal Processing and Networking (WiSPNET)*. 2017;p. 1701–1704. Available from: https://doi.org/10.1109/WiSPNET.2017.8300052.

11) Alam MM, Azim R, Sobahi NM. A dual-band CPW-fed miniature planar antenna for S-, C-, WiMAX, WLAN, UWB, and X-band applications. *Sci Rep*. 2022;12:7584–7584. Available from: https://doi.org/10.1038/s41598-022-11679-7.

12) Amin MKM, Ali MT, Saripuden S, Aziz AAA. Design of dual rectangular ring antenna with DGS technique for wireless application. *2012 IEEE Symposium on Wireless Technology and Applications (ISWTA)*. 2012;p. 248–253. Available from: https://doi.org/10.1109/ISWTA.2012.6373854.

13) Biddut NH, Haque ME, Jahan N. A Wide Band Microstrip Patch Antenna Design Using Multiple Slots at V-Band. *2022 International Mobile and Embedded Technology Conference (MECON)*. 2022;p. 113–116. Available from: https://doi.org/10.1109/MECON53876.2022.9751951.

14) Rana MS, Rahman MM. Study of Microstrip Patch Antenna for Wireless Communication System. *2022 International Conference for Advancement in Technology (ICONAT)*. 2022;p. 1–4. Available from: https://doi.org/10.1109/ICONAT53423.2022.9726110.

15) Chen X, Dou H. Wideband Patch Antenna with Shorting Vias. *International Journal of Antennas and Propagation*. 2022;2022:1–11. Available from: https://doi.org/10.1155/2022/2578409.

16) Liu J, Zheng S, Li Y, Long Y. Broadband monopolar microstrip patch antenna with shorting vias and coupled ring. *IEEE Antennas and Wireless Propagation Letters*. 2014;13:39–42. Available from: https://doi.org/10.1109/LAWP.2013.2295686.

17) Xu KD, Xu H, Liu Y, Li J, Liu QH. Microstrip Patch Antennas With Multiple Parasitic Patches and Shorting Vias for Bandwidth Enhancement. *IEEE Access*. 2018;6:11624–11633. Available from: https://doi.org/10.1109/ACCESS.2018.2794962.

18) Wu J, Yin Y, Wang Z, Lian R. Broadband Circularly Polarized Patch Antenna With Parasitic Strips. *IEEE Antennas and Wireless Propagation Letters*. 2015;14:559–562. Available from: https://doi.org/10.1109/LAWP.2014.2373823.

19) S, Sankar SP. Design and Numerical Analysis of a Compact Microstrip Antenna Sensor for Wireless Body Area Networks. *IEEE International Conference on Signal Processing, Informatics, Communication, and Energy Systems (SPICES) 2022*. 2022;p. 212–216. Available from: https://doi.org/10.1109/SPICES52834.2022.9774224.

20) Chindhi P, Rajani HP, Kalkhambkar G. A Spurious Free Dual Band Microstrip Patch Antenna for Radio Frequency Energy Harvesting. *Indian Journal of Science and Technology*. 2021;15(7):266–275. Available from: https://doi.org/10.17485/IJST/v15i7.2025.

21) Ahmad SJ, Ahmed MM, Unissa I. Optimization of Environmental Data to Improve Safety in Coal Mine using Wireless Sensor Networks. *Indian Journal of Science and Technology*. 2022;15(19):956–964. Available from: https://doi.org/10.17485/IJST/v15i19.686.

RESEARCH ARTICLE

Driver Drowsiness Alerting System

Telugu Maddileti[1]* and M. Jagadeesh Chandra Prasad[2]

[1]Associate Professor, Department of Electronics and Communication Engineering, Malla Reddy Engineering College, Hyderabad, Telangana, India.
[2]Professor, Department of Electronics and Communication Engineering, Malla Reddy Engineering College, Hyderabad, Telangana, India.

*Address for Correspondence
Telugu Maddileti
Associate Professor,
Department of Electronics and Communication Engineering,
Malla Reddy Engineering College, Hyderabad, Telangana, India.
Email: madhu14283@gmail.com

ABSTRACT

The growth of research and inventions in preventing road accidents has led to the development of many driver inattention monitoring systems. Some of the companies have adopted and implemented several techniques but lack the efficiency in providing the expected results. As a part of driver drowsiness detection, this paper deals with the efficient method of preventing accidents. The prevention and the control of the road accidents are possible with the help of the Smart sensing spectacles which can sense the frequency of the eye blinking and predict the drowsiness by comparing with the threshold value fed before. If the number of blinks crosses the threshold value, it gives the notification to the vibrator, which is arranged on the spectacles and alerts the driver. This notification is also sent to the mobile by Bluetooth protocol, so the mobile produces odd loud sounds to gain the attention of the driver. If the driver is unable to take control after the vibrator gives the response, this alarming sound system can be useful to alert the driver and prevent the cause of any sort of destruction. This smart sensing spectacle material is of with slim and sleek design that adds comfort and ensure driver to have a safe and proper journey.

Keywords: Smart Sensing Spectacles, Drowsiness, Vibrator, Bluetooth protocol.

INTRODUCTION

Imagine a situation that a person is going on a car for a longer distance. Suppose if the person is driving for a long-time, then the person may feel sleepy and start closing his eyes. Drowsiness may lead to an accident that causes the loss of property, loss of life, loss of money, etc. [1]. An article addressed by DC newspaper in the middle of 2018. They quoted that 2/3rd of the accidents in motorcycles and four-wheelers are due to lack of attention or due to drowsiness or sleep of the driver [2]. Moreover, the drivers in the car fall asleep due to various factors and lead to the

48496

cause of many accidents. Many surveys show that major accidents are caused due to the sleep of the driver [3]. The technological advancements must often provide some solution to overcome the problem and ensure safe and secure driving [4]. Around 1.3 billion people dead and 20 to 30 million people are bedridden due to road accidents based on the data in [5]. Out of these accidents around one-fourth are due to the drowsiness[7]. The survey reports give us a real picture of the accidents due to the drowsiness of the driver. Many survey reports on accidents caused due to drowsiness of driver are due to the factors like the observation of the driver behaviour that include yawning, [8] the closing of the eye, head movement and vehicle movement based include deviation in the lane position, overpressure on the acceleration pedal, etc. The rate of death due to the accidents caused on the highways is very much high as mentioned by the road safety statistics. Many solutions based on the sensors have been published in the market related to driver sleep, causing incidents [9]. Maintenance of the system relative to the frequency of the eye blinking on the threshold value is an essential factor for detecting driver drowsiness. Many algorithms of the existing type have evaluated based on collected data from any of these three measures-Vehicle Based, Behavioural Based, and Physiological measures as researched by the ArunSahayadhas [10]. The present system was built by using the Raspberry Pi 3 is embedded in the car in such a way that image detection is shown using the screen that displays the drowsy state of the driver and alert is done by ringing the alarms in the vehicle. But the exposure of drowsiness by the usage of the camera by image processing does not give excellent accuracy and costly as identified by Alexis Arcaya-Jordan et al. [11].In the present system, eye movement is continuously observed by using image processing for continuous detection of the eyes of the driver. The decrease in efficiency of detection is low if continuous detection is not done as identified by Ratna Kaavya M et al. [12]. So, the developed system will overcome the disadvantages of the existed system and with multiple different features. This proposed method has not been implemented due to less efficiency, and the inaccurate results during the trails with this proposed system [13]. The cost of the system, ability of the lens to identify and entire unit to process the images continuously cause the delay in the output and cannot be used in the real-time progress to solve the issue of drowsiness detection [14] [15].

Proposed Algorithm
Better Design of Spectacles
The design of the spectacles used for this drowsiness detection is very slim and compact, where drivers can easily adapt to use these, [16] and the lens of these spectacles can be changed if any sight error related problems to the driver. Moreover, the spectacles contain the control options within the edges, where the driver can control it accordingly [17].

Infrared Proximity Sensor
This sensor emits, Infrared rays and the light reflected is recorded by an IR photodiode. This blinking sensor is based on IR; there will be variations across the eye as per the blinking. The exact function depends on the position and aiming of the detector and emitter concerning the eye [18]. If the eye of the driver is closed, we get an output of digital logic 1. If the eye seems to be opened, then it gives the output as low(Digital logic 0). At last, the output of the proximity sensor is given to digital pins of the development board.

Compact Microcontroller with Bluetooth Enabled
The development board used here STM32 is very fast, and its compact size adds a benefit It is used for calculating the eye blink rate based on the input of the Ir sensor and the alarm based on comparison with the threshold value fed by the user or the manufacturer. This microcontroller is connected to the external sound alarm system using the Bluetooth communication within the vehicle and to the mobile phone where the alert sounds and the data can be sent to driver mobile.

Vibrators
The spectacles design consists of micro vibrators, [19] which can help to alert the driver with minimal delay after the drowsiness detection and these vibrator motors were placed on either side of the spectacles, to ensure high efficiency [20] [21]. This invention is a smart spectacle which consists of IR modules, Bluetooth module, microcontroller, and vibrator. This is a solution for the accidents due to the effect of sleep, drowsiness, and also due to the lack of

attention of the driver. This proposed model is the solution for the above type of problems. The basic mechanism is IR sensors count the blinking of eyes per minute [22], and the whole information is monitored by the microcontroller, which is embedded in the spectacles. If the blinking of eyes crosses the threshold value [23], then a notification is sent to the vibrator and to the mobile phone which is connected using Bluetooth [24] to the spectacles then the phone makes some odd loud sounds and the vibrator start vibrating till the person gets into the normal state and he/she needs to turn off the button which is embedded beside the microcontroller. This total mechanism uses energy so it gets charged by a rechargeable battery which is fixed beside the Bluetooth module and can be charged accordingly with the power supply within the vehicle or externally. The advantageous feature of this spectacle is that it can work on 5Volts voltage and can stand up with the battery for a longer time. The smart spectacles and the flow of the commands from the IR sensor detection of the eye blinking rate to the input to the microcontroller and the output of the microcontroller to the external vibrator and the mobile phone connected by Bluetooth if an alert has to be sent to the driver in the procedure of drowsiness detection. The above shown is the circuit diagram of the entire setup with connections of the battery and the other sensors on the macro scale with breadboard connections. This entire setup can be designed on the micro-scale using a printed circuit board so that the reduced circuit can be easily implemented on the spectacle and promote the proper design within the outfit to act as a driver alerting system.

EXPERIMENT AND RESULT

The design of the spectacles in the form of a prototype is shown with all the sensors and other components attached to it.
1. In this position of the spectacle, IR sensors are placed on both sides and will help in quick detection of eye blinking rate.
2. In this position, the microcontroller and battery are placed within the compact size by obtaining the printed circuit design of the microcontroller
3. The Bluetooth module is ensured to place in this position with a compact size printed circuit board by connecting it internally to the microcontroller.
4. The vibrators are placed on either side along the length of the spectacles to have a sleek design and provide comfort to the user while using them.
5. In this way, the design of the spectacles enhances to provide a solution to the drowsiness detection and promote safety feature in driving.

CONCLUSION

In this prototype, the entire spectacle module with different sensors, microcontrollers and other components interfacing with proper code and enhancing built it as a single module will help to develop the solution in preventing the accidents that are caused due to the drowsiness of the driver. Moreover, this solution can make an impact in many ways of providing good efficient output in detecting the rate of eye blinking accurately and intimate the driver as an alert by vibrations and sounds through the Bluetooth communication and acts as an efficient solution for driver drowsiness detection and warning system with higher effective output results.

ACKNOWLEDGEMENTS

REFERENCES

1. Tilley, D.H., Erwin, C.W. and Gianturco, D.T., 1973. Drowsiness and driving: preliminary report of a population survey (No. 730121). SAE Technical Paper.
2. Leechawengwongs, M., Leechawengwongs, E., Sukying, C. and Udomsubpayakul, U., 2006. Role of drowsy driving in traffic accidents: a questionnaire survey of Thai commercial bus/truck drivers. JOURNAL-MEDICAL ASSOCIATION OF THAILAND, 89(11), p.1845.
3. Fuletra, J.D. and Bosamiya, D., 2013. A survey on driver's drowsiness detection techniques. International Journal on Recent and Innovation Trends in Computing and Communication, 1(11), pp.816-819.
4. Ueno, H., Kaneda, M. and Tsukino, M., 1994, August. Development of drowsiness detection system. In Proceedings of VNIS'94-1994 Vehicle Navigation and Information Systems Conference (pp. 15-20). IEEE.
5. Knipling, R.R. and Wang, J.S., 1994. Crashes and fatalities related to driver drowsiness/fatigue. Washington, DC: National Highway Traffic Safety Administration.
6. Sahayadhas, A., Sundaraj, K. and Murugappan, M., 2012. Detecting driver drowsiness based on sensors: a review. Sensors, 12(12), pp.16937-16953.
7. Abtahi, S., Hariri, B. and Shirmohammadi, S., 2011, May. Driver drowsiness monitoring based on yawning detection. In 2011 IEEE International Instrumentation and Measurement Technology Conference (pp. 1-4). IEEE.
8. Ito, T., Mita, S., Kozuka, K., Nakano, T. and Yamamoto, S., 2002, September. Driver blink measurement by the motion picture processing and its application to drowsiness detection. In Proceedings. The IEEE 5th International Conference on Intelligent Transportation Systems (pp. 168-173). IEEE.
9. Sahayadhas, A., Sundaraj, K. and Murugappan, M., 2012. Detecting driver drowsiness based on sensors: a review. Sensors, 12(12), pp.16937-16953.
10. Arcaya-Jordan, A., Pegatoquet, A. and Castagnetti, A., 2019, March. Smart Connected Glasses for Drowsiness Detection: a System-Level Modeling Approach. In 2019 IEEE Sensors Applications Symposium (SAS) (pp. 1-6). IEEE.
11. Ramya, V. and Franklin, R.G., 2019, March. Alert System for Driver's Drowsiness Using Image Processing. In 2019 International Conference on Vision Towards Emerging Trends in Communication and Networking (ViTECoN) (pp. 1-5). IEEE.
12. Yan, J.J., Kuo, H.H., Lin, Y.F. and Liao, T.L., 2016, July. Real-time driver drowsiness detection system based on PERCLOS and grayscale image processing. In 2016 International Symposium on Computer, Consumer and Control (IS3C) (pp. 243-246). IEEE.
13. Assari, M.A. and Rahmati, M., 2011, November. Driver drowsiness detection using face expression recognition. In 2011 IEEE International Conference on Signal and Image Processing Applications (ICSIPA) (pp. 337-341). IEEE.
14. Tabrizi, P.R. and Zoroofi, R.A., 2008, November. Open/closed eye analysis for drowsiness detection. In 2008 first workshops on image processing theory, tools and applications (pp. 1-7). IEEE.
15. Vaisnavi, N.M. and Santhosh, RR, 2010, July. Performance evaluation of statistical approach for drowsiness detection for driver's with and without spectacles. In 2010 Second International conference on Computing, Communication and Networking Technologies (pp. 1-5). IEEE.
16. Johns, M. and Brown, A., Sleep Diagnostics Pty Ltd, 2010. Alertness sensing spectacles. US Patent 7,815,311.
17. Rahman, A., Sirshar, M. and Khan, A., 2015, December. Real time drowsiness detection using eye blink monitoring. In 2015 National Software Engineering Conference (NSEC) (pp. 1-7). IEEE.
18. Yamaguchi, T., Tokyo Parts Ind Co Ltd, 1992. Vibrator motor for wireless silent alerting device. U.S. Patent 5,107,155.
19. Sunaga, S., Tokyo Parts Ind Co Ltd, 1994. Vibrator motor for a wireless silent alerting device. U.S. Patent 5,327,035.
20. Yamaguchi, T. and Koyanagi, N., Tokyo Parts Ind Co Ltd, 1994. Brushless vibrator motor for a wireless silent alerting device. U.S. Patent 5,373,207.

Telugu Maddileti and Jagadeesh Chandra Prasad

21. Ryan, S.B., Detweiler, K.L., Holland, K.H., Hord, M.A. and Bracha, V., 2006. A long-range, wide field-of-view infrared eyeblink detector. Journal of neuroscience methods, 152(1-2), pp.74-82.
22. Praveenkumar, B. and Mahendrakan, K., 2014. Prevention of accident due to Drowsy by using Eye Blink. International Journal of Innovative Research in Science, Engineering and Technology, 3(5), pp.12610-12616.
23. Sakamoto, T., Hino, M., Ohishi, Y., Yamamoto, M., Kikuchi, M. and Watabe, S., Fujitsu Ltd and Honda Access Corp, 2011. Bluetooth communication system for drivers of vehicles. US Patent 7,907,975.

Table 1: Existing system and proposed system

EXISTING SYSTEM	PROPOSED SYSTEM
Detection using camera	Detection using IR rays
Needs high processing power	This model can work with microcontroller based system
Complicated design	Smart design which adds comfort to the user
Consumes more power	Work with less power consumption
Less efficient	Provides much efficiency

Fig.1. Existing Architecture

Fig.2. Eye and eye blink detection using Harcascade Algorithm

Fig.3. The Proposed Architecture of the Smart Sensing Spectacles.

Fig.4. Circuit Design of Working Prototype

Fig.5. Design of the Prototype

48500

Dynamic Voltage and Frequency Scaling (Dvfs) Technique in Cloud Computing Environment

 PDF (https://www.provinciajournal.com/index.php/telematique/article/view/213/204)

Keywords:
Cloud computing, Resource management, Energy efficient solution consolidation, Containerization, Cloud data center, DVFS;

Dr.Arun Kumar Kandru

Associate Professor, Department of CSE, Malla Reddy Engineering College (Autonomous),Secunderabad, Telangana, India-500100

Dr.Kunchala Little Flower

Professor, Department of CSE-AI&ML, Malla Reddy University, Hyderabad, Telangana, India-500100

Mr.Manoj Kumar Vemula

Assistant Professor,Department of Information Technology, Vallurupalli Nageswara Rao Vignana Jyothi Institute of Engineering &Technology, Hyderabad,Telangana, India 500090

Dr.Neeraj Sharma

Associate Professor, Department of CSE, VPPCOE & VA,Mumbai-22,

Abstract

Because of falling hardware, software, and maintenance costs, cloud computing's hosted application and service model has been more popular in recent years. Users of cloud-based services have access to a shared pool of virtual resources housed in huge data centres, which might be useful for a wide range of information and communication services with highly varying resource needs. Cloud data centres have a big carbon footprint and a high electric cost since they use so much power. It's no surprise that effective resource management in cloud systems has become a top priority for cloud providers, which in turn has piqued the attention of academics in developing new methods of conserving energy without sacrificing performance. The primary goals of this work are to (1) offer a fresh, comprehensive taxonomy for energy-efficient cloud resource management systems, (2) assess and categorise

current methodologies in light of our proposed taxonomy, and (3) identify new avenues for research in this field. To cut down on power waste and premature server consolidation methods, the dynamic voltage frequency scaling (DVFS) method may modify the operating voltage and frequency of servers depending on current workload. Here, we present dynamic voltage and frequency scaling (DVFS) approaches as a means to dynamically minimise chip power consumption in accordance with the specific performance needs of the application at hand

Issue
Vol 21, No 1 (2022) (https://www.provinciajournal.com/index.php/telematique/issue/view/44)

Section
Articles

Important Links

Home (http://provinciajournal.com/index.php/telematique)

Aims and Scope (http://provinciajournal.com/index.php/telematique/aims_and_scope)

Call for Papers (http://provinciajournal.com/index.php/telematique/call_for_papers)

Instructions for Authors (http://provinciajournal.com/index.php/telematique/instructions_for_authors)

Editorial Board (http://provinciajournal.com/index.php/telematique/about/editorialTeam)

Archive (http://provinciajournal.com/index.php/telematique/issue/archive)

Download (http://provinciajournal.com/index.php/telematique/downloads)

Ethics & Policies (http://provinciajournal.com/index.php/telematique/ethics_and_policies)

Publication Ethics and Publication Malpractice Statement (http://provinciajournal.com/index.php/telematique/publication_ethics)

Peer Review Policy (http://provinciajournal.com/index.php/telematique/peer_review_policy)

Plagiarism Policy (http://provinciajournal.com/index.php/telematique/plagiarism_policy)

Copyright, Grants and Ownership Declaration (http://provinciajournal.com/index.php/telematique/copyright_grants_ownership_declaration)

Refund Policy (http://provinciajournal.com/index.php/telematique/refund_policy)

Open Access Overview (http://provinciajournal.com/index.php/telematique/open_access_overview)

Open Access License (http://provinciajournal.com/index.php/telematique/open_access_license)

Permissions (http://provinciajournal.com/index.php/telematique/permissions)

Downloads

Copyright Transfer Form (http://provinciajournal.com/downloads/copyright_form.pdf)

Paper Template (http://provinciajournal.com/downloads/paper_template.docx)

Language

English (https://www.provinciajournal.com/index.php/telematique/user/setLocale/en_US?source=%2Findex.php%2Ftelematique%2Farticle%2Fview%2F213)

Español (España)
(https://www.provinciajournal.com/index.php/telematique/user/setLocale/es_ES?
source=%2Findex.php%2Ftelematique%2Farticle%2Fview%2F213)

Review on chemical constituents of Bauhinia species

Mopur Vijaya Bhaskar Reddy◆

Chemistry Department, Malla Reddy Engineering College (Autonomous), Maisammaguda, Dhulapally Road, Kompally, Secunderabad-500100, Telangana, India

Article Info

Abstract

The genus *Bauhinia* which belongs to the subfamily, Caesalpinioideae of the main family Leguminosae, consists about 300 species of which 9 species occur in India. Majority of Bauhinia species are unarmed erect trees, or climbing shrubs with circinate tendrils. Several members of this genus are extensively used in indigenous medicine, in the treatment of the skin diseases, throat troubles, diarrhea, ulcers, dyspepsia, piles, leprosy, asthma, wounds, tumours, snake-bite, vermifuge, antipyretic and dysentric. This review of literature including phytochemical investigations on naturally occurring compounds of flavonoids, like flavones, flavonols, dihydroflavones, dihydroflavonols, chalcones, dihydrochalcones, flavans and catechins, stilbenes, stereoids, terpenes, fatty acids, alcohols and ester derivatives, lignans and miscellaneous chemical constituents from Bauhinia species.

1. Introduction

Bauhinia is a large genus of flowering plants which in the subfamily, Caesalpinioideae of the main family Leguminosae consists about 300 species of which 9 species occur in India (Gamble *et al.*, 1956). Majority of *Bauhinia* species are unarmed erect trees, or climbing shrubs with circinate tendrils. Several members of this genus are extensively used in indigenous medicine (Kitikara*et al.*, 1935; The Wealth of India, 1976; Mathew *et al.*, 1983; Chopra *et al.*, 1956), in the treatment of the skin diseases, throat troubles, diarrhea, ulcers, dyspepsia, piles, leprosy, asthma, wounds, tumours, snake-bite, vermifuge, antipyretic and dysentric.

A survey of the previous phytochemical studies on the genus *Bauhinia* showed that only a few species of a total of more than 300 have so far beenchemically investigated. The major chemical constituents so far reported from *Bauhinia* species include flavonoids, stilbenes and stilbene derived tri-and tetracyclic terpenes, fatty acid esters, lignans *etc.*

2. Flavonoid constituents of *Bauhinia* species

The flavonoid constituent so far isolated from the genus *Bauhinia* can be conveniently grouped into the following types:

(i) Flavones   (Table 1)

(ii) Flavonols (Table 2)

(iii) Dihydroflavones and dihydroflavonols (Table 3)

(iv) Chalcones and dihydrochalcones (Table 4)

(v) Flavans and catechins (Table 5)

Corresponding author: Dr. M. Vijaya Bhaskar Reddy
Chemistry Department, Malla Reddy Engineering College (Autonomous), Maisammaguda, Dhulapally Road, Kompally, Secunderabad-500100, Telangana, India
E-mail: vijaybreddy123@gmail.com
Tel.: +91-8297194349

Table 1: Flavones from different *Bauhinia* species

Compound	Plant source	Reference
1. Chrysin (1)	*B. purpurea*	Kuo *et al.*, 1998
2. 6,8-dimethylchrysin (2)	*B. purpurea*	Kuo *et al.*, 1998
3. Apigenin (3)	*B.variegata*	Wahab *et al.*, 1987
4. Apigenin 7-*O*-β-D-glucopyranoside (4)	*B.variegata*	Wahab *et al.*, 1987
5. Luteolin 5,3'-dimethylether (5)	*B.manca*	Achenbach *et al.*, 1988
6. Luteolin 4'-*O*-β-D-glucopyranoside (6)	*B.tarapotensis*	Braca *et al.*, 2001
7. Chrysoeriol (7)	*B.manca*	Achenbach *et al.*, 1988
8. 5,7,3',4'-Tetramethoxyflavone (8)	*B.championii*	Chin *et al.*, 1984 and 1994
9. 5,7,3',4',5'-Pentamethoxyflavone (9)	*B.championii*	Chin *et al.*, 1984 and 1994
10.5,6,7,3',4'-Pentamethoxyflavone (10)	*B.championii*	Chin *et al.*, 1984 and 1994
11. 5,6,7,3',4',5'-Hexamethoxyflavone (11)	*B.championii*	Chin *et al.*, 1984 and 1994
12.5,6,7,5'-Tetramethoxy-3',4'-methylenedioxyflavone (12)	*B.championii*	Chin *et al.*,1984 and 1994
13.5,7,5'-Trimethoxy-3',4'-methylenedioxyflavone (13)	*B.championii*	Chin *et al.*,1984 and 1994
14. 7-Methoxy-5,6,3',4'-dimethylenedioxyflavone (Bausplendin) (14)	*B.splendens*	Laux *et al.*,1985
15. 5,6-Dihydroxy-7-methoxyflavone-6-*O*-β-D-xylopyranoside (15)	*B.purpurea*	Yadava *et al.*,2000

152

Bausplendin (**14**), a flavone reported from *B.splendens* (Laux *et al.*, 1985), with methylenedioxy substitution in ring-A and ring-B is a rare feature among flavones. C-alkylation among flavones is rare and the isolation of 6,8-dimethylchrysin (**2**) from *B. purpurea* (Kuo *et al.*,1998) constitutes the only of an alkyl substituted flavone from this genus. Different substituted flavones (**1-15**) isolated from *Bauhinia* species are mentioned in Figure 1 and Table 1.

From Table 2, it is evident that all the flavonol glycosides reported from *Bauhinia* species are either kaempferol or quercetin derivatives with the sugar residue attached to the 3-position in the majority of the glycosides. 6,4'-Dihydro-3'-prenyl-3,5,7,5'-tetramethoxy flavone-6-*O*-α-L-rhamnopyranoside (**26**), a flavonol glycoside isolated from *B.purpurea* (Yadava *et al.*, 2001) is the only prenylatedflavonol glycoside occurring in *Bauhinia* species mentioned in Figure 2 and Table 2.
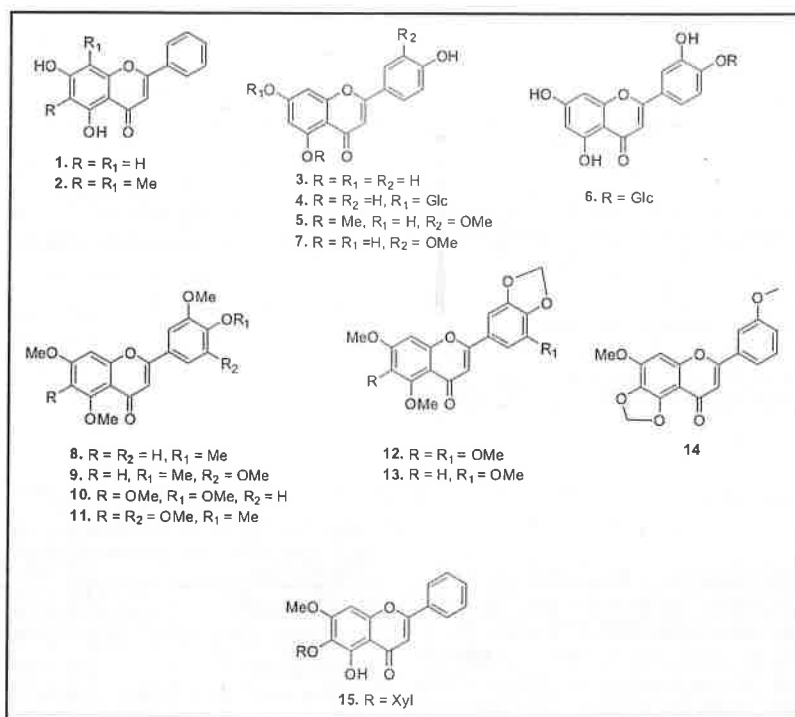

1. R = R$_1$ = H
2. R = R$_1$ = Me

3. R = R$_1$ = R$_2$ = H
4. R = R$_2$ =H, R$_1$ = Glc
5. R = Me, R$_1$ = H, R$_2$ = OMe
7. R = R$_1$ =H, R$_2$ = OMe

6. R = Glc

8. R = R$_2$ = H, R$_1$ = Me
9. R = H, R$_1$ = Me, R$_2$ = OMe
10. R = OMe, R$_1$ = OMe, R$_2$ = H
11. R = R$_2$ = OMe, R$_1$ = Me

12. R = R$_1$ = OMe
13. R = H, R$_1$ = OMe

14

15. R = Xyl

Figure 1: Flavones (1-15).

Table 2: Flavonols isolated from various *Bauhinia* species

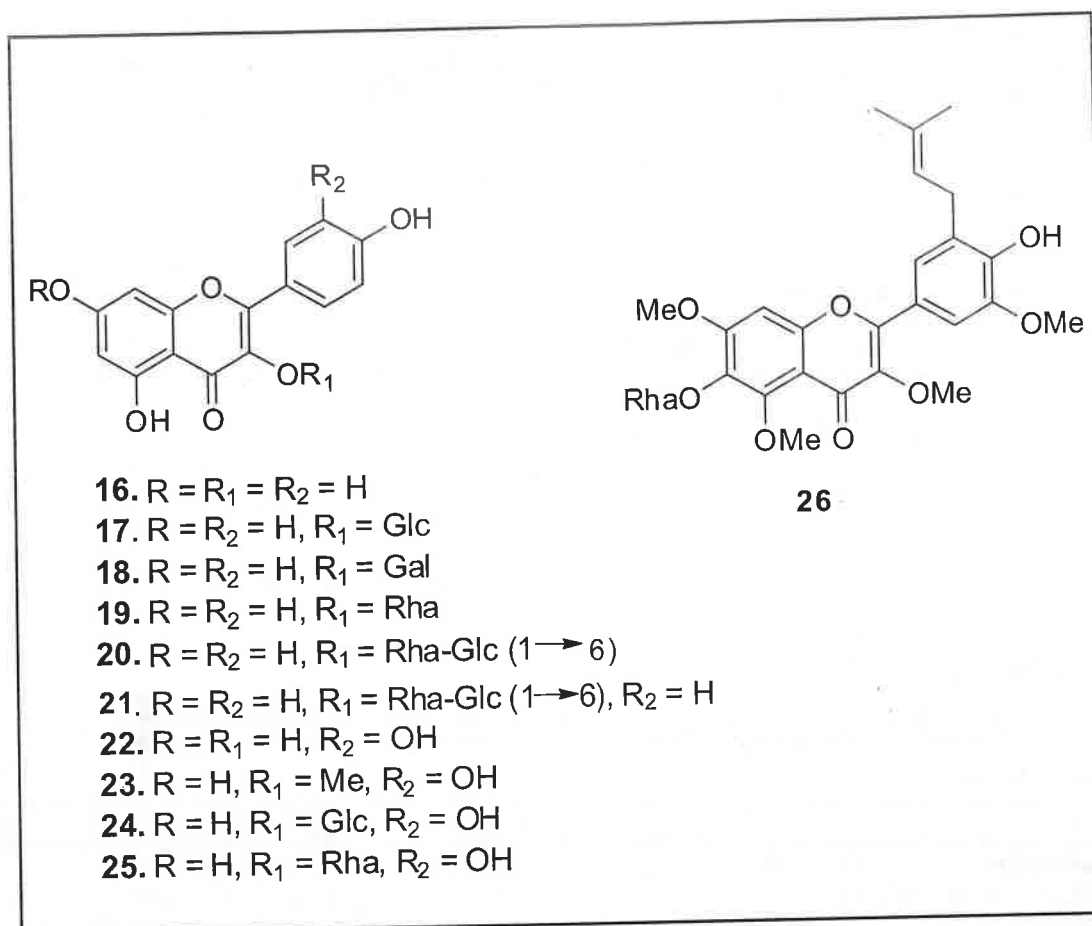| Compound	Plant source	Reference
1. Kaempferol (16)	*B.manca, B.vahlii, B. purpurea*	Achenbach *et al.*, 1988; Sultana *et al.*, 1985; Kuo *et al.*, 1997
2. Kaempferol 3-O-β-D-glucopyranoside (17)	*B.purpurea, B.variegata,*	Ramachandran *et al.*, 1967; Gupta *et al.*, 1984;
3. Kaempferol 3-O-β-D-galactoside (18)	*B.variegata*	Rahman *et al.*, 1985
4. Kaempferol 3-O-α-L-rhamnopyranoside (19)	*B.uruguagensis*	Iribarren *et al.*, 1989
5. Kaempferol 3-O-β-D-rutinoside (20)	*B.variegata, B.candicans, B.tomentosa, B.retusa*	Wahab *et al.*, 1987; Rahman *et al.*, 1985; Iribarren *et al.*, 1983; Row *et al.*, 1954; Tiwari *et al.*, 1978
6. Kaempferol 3-O-β-D-rutinoside-7-O-α-L-rhamnopyranoside (21)	*B.candicans*	Iribarren *et al.*, 1983
7. Quercetin (22)	*B.variegata, B.vahlii, B.purpurea, B.tomentosa*	Wahab *et al.*, 1987; Sultana *et al.*, 1985; Wahab *et al.*, 1987; Ramachandran *et al.*, 1967; Row *et al.*, 1954; Subramanian *et al.*, 1963
8. Quercetin-3-methyl ether (23)	*B.purpurea*	Kuo *et al.*, 1997
9. Quercetin-3-O-β-D-glucopyranoside (Isoquercetin) (24)	*B.vahlii, B.purpurea, B.retusa, B.tomentosa*	Sultana *et al.*, 1985; Ramachandran *et al.*, 1967; Tiwari *et al.*, 1978; Subramanian *et al.*, 1963
10. Quercetin-3-O-α-L-rhamnopyranoside (Quercetrin) (25)	*B.variegata, B.uruguagensis*	Wahab *et al.*, 1987; Iribarren *et al.*, 1989
11. 6,4'-Dihydro-3'-prenyl-3,5,7,5'-tetramethoxyflavone-6-O-α-L-rhamnopyranoside(26)	*B.purpurea*	Yadava *et al.*, 2001

Figure 2: Flavonols and its derivatives (16-26).

16. R = R$_1$ = R$_2$ = H
17. R = R$_2$ = H, R$_1$ = Glc
18. R = R$_2$ = H, R$_1$ = Gal
19. R = R$_2$ = H, R$_1$ = Rha
20. R = R$_2$ = H, R$_1$ = Rha-Glc (1→6)
21. R = R$_2$ = H, R$_1$ = Rha-Glc (1→6), R$_2$ = H
22. R = R$_1$ = H, R$_2$ = OH
23. R = H, R$_1$ = Me, R$_2$ = OH
24. R = H, R$_1$ = Glc, R$_2$ = OH
25. R = H, R$_1$ = Rha, R$_2$ = OH

26

Table 3: Dihydroflavones and dihydroflavonols reported from *Bauhinia* species

Compound	Plant source	Reference
1. Naringenin (27)	*B.manca*	Achenbach *et al.*, 1988
2. Eriodictyol (28)	*B.manca*	Achenbach *et al.*, 1988
3. Liquiritigenin (29)	*B.manca*	Achenbach *et al.*, 1988
4. Liquiritigenin-7-methyl ether (30)	*B.manca*	Achenbach *et al.*, 1988
5. Liquiritigenin-4'-methyl ether (31)	*B.manca*	Achenbach *et al.*, 1988
6. 5,7,4'-Trihydroxyflavanone-4'-O-α-L-rhamnopyranosyl-β-D-glucopyranoside (32)	*B.variegata*	Gupta *et al.*, 1979
7. 4'-Hydroxy-5,7-dimethoxyflavanone-4'-O-α-L-rhamnopyranosyl-β-D-glucopyranoside (33)	*B.variegata*	Gupta *et al.*, 1980
8. Strobopinin (34)	*B.championii*	Chin *et al.*, 1994
9. Taxifolin (35)	*B.hupenhara, B.purpurea*	Xiangui *et al.*, 1992; Kuo *et al.*, 1997
10. 6-(3''-Oxobutyl)taxifolin (36)	*B.purpurea*	Kuo *et al.*, 1998

The compounds **29-31**, occurring in *B.manca* (Achenbach *et al.*, 1988) constitutes the first report of 5-deoxyflavanones from this genus. Strobopinin (**34**), a methylflavanone occurring in *B.championii* (Chin *et al.*, 1994) is the only C-alkyl substituted flavanone reported from *Bauhinia* species. 6-(3''-Oxobutyl) flavanone reported from *Bauhinia* species. 6-(3''-Oxobutyl) taxifolin (**36**) reported from *B.purpurea* (Kuo *et al.*, 1998), is a novel dihydroflavanol with a rare oxobutyl residue at 6-position.Different dihydroflavones and dihydroflavonols reported from *Bauhinia* species are mentioned in Figure 3 and Table 3.
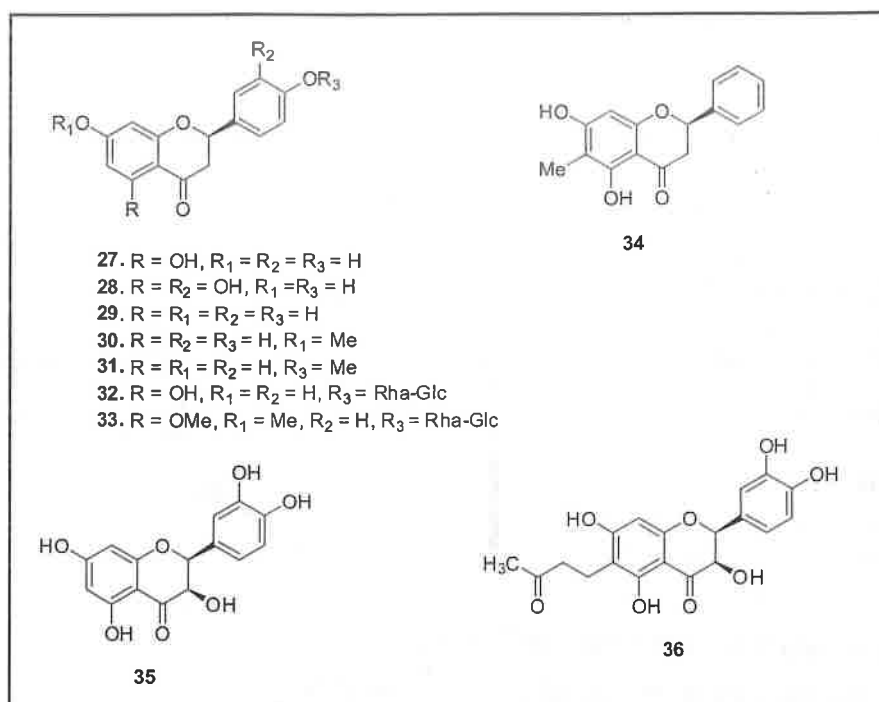
154

Figure 3: Dihydroflavones and dihydroflavonols derivatives (27-36).

Table 4: Chalcones and dihydrochalcones isolated from various *Bauhinia* species

Compound	Plant source	Reference
1. Isoliquiritigenin (37)	*B.manca*	Achenbach *et al.*, 1988
2. Isoliquiritigenin-2'-methyl ether (38)	*B.manca*	Achenbach *et al.*, 1988
3. Isoliquiritigenin-4-methyl ether (39)	*B.manca*	Achenbach *et al.*, 1988; Chin *et al.*, 1994
4. Echinatin (40)	*B.manca*	Achenbach *et al.*, 1988
5. 3,4-Dihydroxychalcone-4-*O*-β-L-arabino-pyranosyl-galac topyranoside (41)	*B.purpurea*	Bhartia *et al.*, 1981
6. 3,4,2',4'-Tetrahydroxychalcone-4'-*O*-β-L- arabinopyranosyl -galactopyranoside (42)	*B.purpurea*	Bhartia *et al.*, 1979
7. 2,4'-Dihydroxy-4-methoxydihydrochalcone (43)	*B.manca*	Achenbach *et al.*, 1988

Compound **41** reported from *B.purpurea* (Bhartia *et al.*, 1981) is achalcone devoid of A-ring oxygenation and is a rare feature among naturally occurring chalconesand dihydrochalcones isolated from various *Bauhinia* species are mentioned in Table 4 and Figure 4.
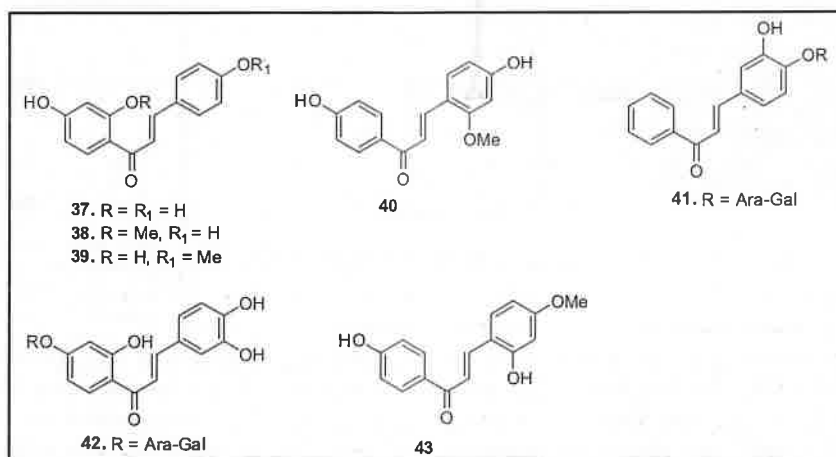

Figure 4: Chalcones and dihydrochalcones derivatives (37-43).

Table 5: Flavans and catechins reported from *Bauhinia* species

Compound	Plant source	Reference
1. 7,4'-Dihydroxyflavan (**44**)	*B. manca*	Achenbach *et al.*, 1988
2. 7,3'-Dimethoxy-4'-hydroxyflavan (**45**)	*B. manca*	Achenbach *et al.*, 1988
3. 4'-Hydroxy-7-methoxyflavan (**46**)	*B. manca*	Achenbach *et al.*, 1988; Viana *et al.*, 1999
4. 3',4'-Dihydroxy-7-methoxyflavan (**47**)	*B. manca*	Achenbach *et al.*, 1988
5. 7,4'-Dihydroxy-3'-methoxyflavan (**48**)	*B. manca*	Achenbach *et al.*, 1988
6. Catechin (**49**)	*B. championii*	Chin *et al.*, 1994
7. 3-*O*-Galloylepicatchin (**50**)	*B. manca*	Achenbach *et al.*, 1988

It is interesting to note that all the five flavan derivatives (**44-48**) occurring in the genus *Bauhinia* was reported from *B.manca* .(Achenbach *et al.*, 1988). The flavans, **45** and **47** reported from

B.manca (Achenbach *et al.*, 1988) showed significant antifungal activity. Flavans and catechinsderivatives arereported from *Bauhinia* species mentioned in Table 5 and Figure 5.
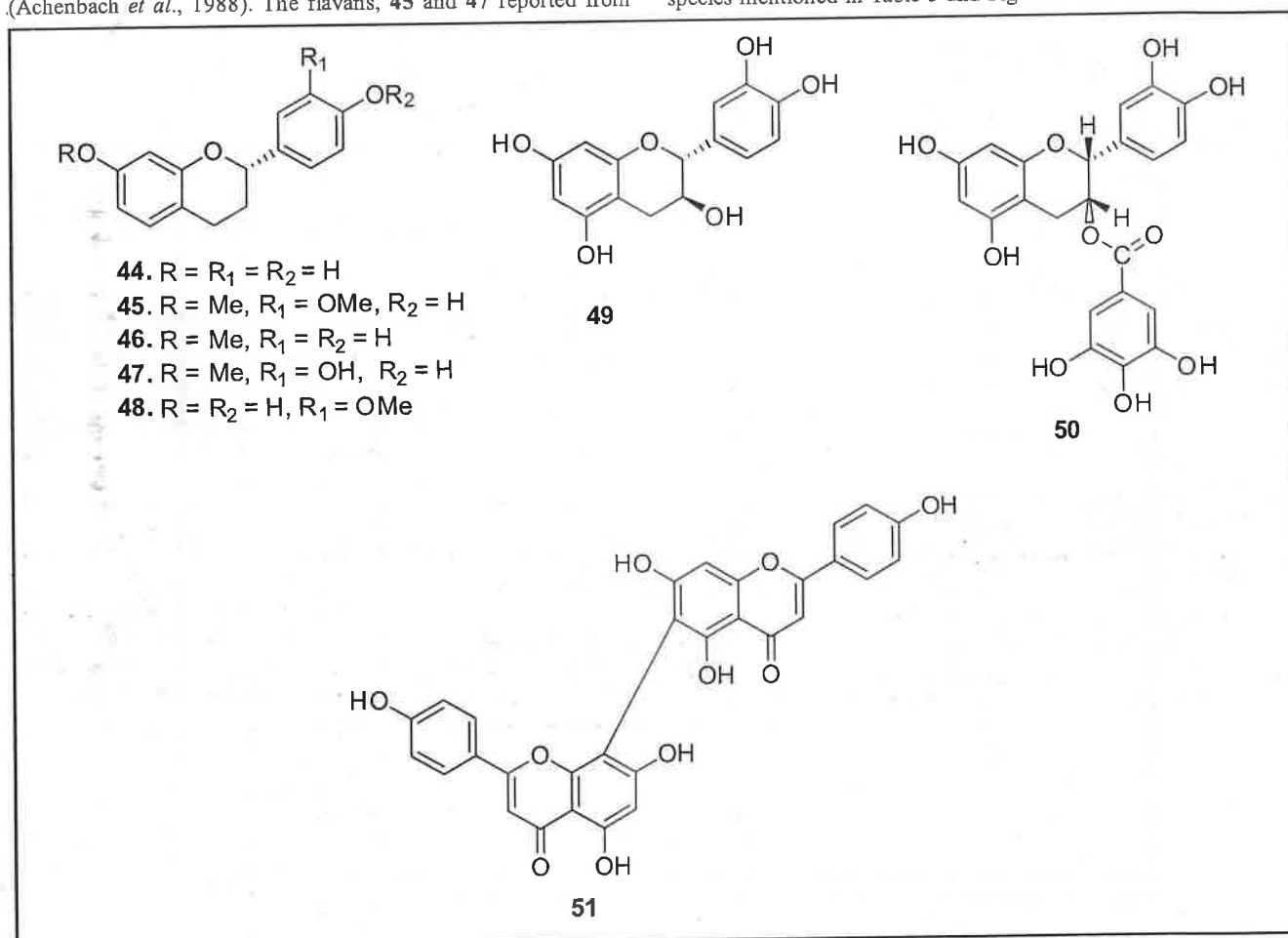

44. R = R$_1$ = R$_2$ = H
45. R = Me, R$_1$ = OMe, R$_2$ = H
46. R = Me, R$_1$ = R$_2$ = H
47. R = Me, R$_1$ = OH, R$_2$ = H
48. R = R$_2$ = H, R$_1$ = OMe

Figure 5: Flavans and catechins derivatives (44-51).

In addition to the flavonoid compounds listed in Tables 1-5, agathisflavone (**51**), a biflavone isolated from as hexamethyl ether from *B.vahlii* (Sultana *et al.*, 1985) is the first report and the only report of biflavonoid in the genus *Bauhinia*. Resveratrol, a natural polyphenol potent antioxidant, antinflammatory agent obtained from stilbenes. *In vitro* studies of resveratrol shows decreased production of TNF-α, IL-1β in monocytes / macrophages (Paramitha *et al.*, 2021)

3. Stilbenes and the stilbene derived tricyclic and tetracyclic phenols

The stilbene and stilbene derived tricyclic and tetracyclic phenolic compounds occurring in the genus *Bauhinia* are presented in Table 6 and Figure 6.

Table 6 : Stilbenes and the stilbene derived phenolic compounds from *Bauhinia* species

| Compound	Plant source	Reference
1. Resveratrol (52)	*B. racemosa*	Anjanneyulu *et al.*, 1984
2. Preracemosol A (53)	*B. malabarica*	Kittikoop *et al.*, 2000
3. Preracemosol B (54)	*B. malabarica*	Kittikoop *et al.*, 2000
4. Racemosol (55)	*B. racemosa, B.malabarica*	Anjanneyulu *et al.*, 1986; Kittikoop *et al.*, 2000
5. De-O-methylracemosol (56)	*B. rufescens, B.racemosa, B. malabarica*	Maillard *et al.*,1991; Prabhakar *et al.*, 1994; Kittikoop *et al.*, 2000
6. 3-Hydroxy-de-O-methylracemosol (57)	*B. racemosa*	Jain *et al.*, 2002
7. 1,7,8,12b-Tetrahydro-2,2,4-trimethyl-2*H*-benzo [6,7]cyclohepta[1,2,3-dc]benzopyran-5,10,11-triol (58)	*B. rufescens*	Maillard *et al.,1991*
8. 5,6-Dihydro-11-methoxy-2,2,12-trimethyl-2*H*-naphtho [1,2,-*f*][1]benzopyran-8,9-diol (59)	*B.rufescens*	Maillard *et al.*,1991
9. 11-Methoxy-2,2,12-trimethyl-2*H*-naphtho[1,2,-*f*][1] benzopyran-8,9-diol (60)	*B.rufescens*	Maillard *et al.*,1991
10. 1,7-Dihydroxy-3-methoxy-2-methyl-dibenzo[b,f]oxepin (Pacharin) (61)	*B.racemosa*	Anjanneyulu *et al.*, 1984
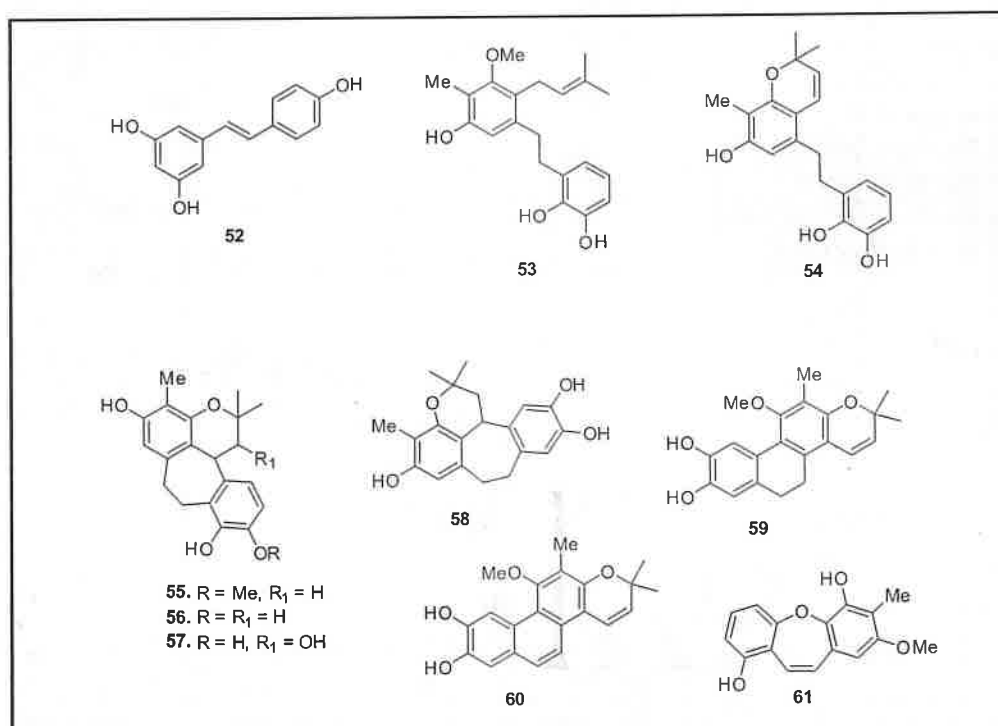
Figure 6: Stilbenes and the stilbene derived phenolic compounds (52-61).

The occurrence of preracemosol A (53) and preracemosol B (54) from *B.malabarica* (Kittikoop *et al.*, 2000) constitute the first report of bibenzyl derivatives in this genus. These two bibenzyl derivatives exhibited moderate antimalarial activity. The isolation of racemosol (55) from *B.malabarica* (Anjanneyulu *et al.*, 1986) constitutes the first report of a new and novel tetracyclic phenolic compound from the genus *Bauhinia*.

Maillard *et al.* (1991) have postulated that the four new antifungal tetracyclic phenolic compounds (56,58-60) occurring in *B.rufescens*

might have obtained biogeneticallyfrom a common stilbene precursor (62) (Scheme-I). Intramolecular cyclization of 62 to the chroman (or chromene) ring and oxidative cyclization at C-6 or C-1'' would lead to compounds 56, 58 and 59 (Scheme 1). Compound 60 could be an oxidation product of 59. The presence of preracemosol A (53) and preracemosol B (54) in *B.malabarica* (Kittikoop *et al.*, 2000) supported Maillard and coworkers's postulation that the stilbene derivative, 62 should be the common precursor for all the tetracyclic stilbene derivatives (55-60).

Scheme-I. Postulated Biosynthetic pathway for compounds **56, 58-60**
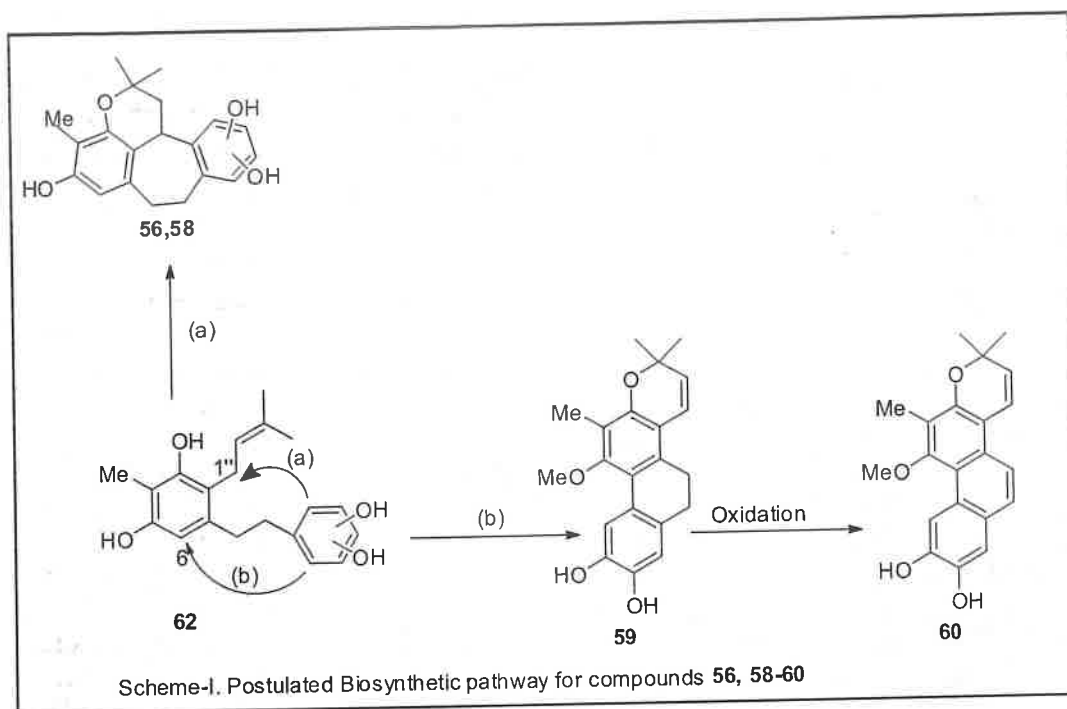
The isolation of pacharin (**61**) from *B.malabarica* by Anjaneyulu *et al.* (1984) constitutes the first report of a naturally occurring dibenzo[b,f] oxepin derivative. The structure of pacharin was established as 1,7-dihydroxy-3-methoxy-2-methyl-dibenzo [b,f]oxepin (**61**) by spectral and X-ray analysis as well as by synthesis (Comber *et al.*, 1980). Anjaneyulu *et al.* (1984) have postulated that pacharin (**61**) might have derived biogenetically

from the corresponding stilbene derivative by ring closure. It is therefore significant to note the occurrence of resveratrol (**52**) in the same plant.

4. Steroids

The steroids occurring in the genus *Bauhinia* are presented in Table 7 and Figure 7.

Table 7: Steroids compounds isolated from various *Bauhinia* species

| Compound	Plant source	Reference
1. Cheolesterol (**63**)	*B.candicans*	Iribarren *et al.*, 1983
2. Campesterol (**64**)	*B.candicans, B.vahlii*	Iribarren *et al.*, 1983; Sultana *et al.*, 1985
3. Stigmasterol (**65**)	*B.candicans, B.vahlii*	
	B.guianensis, B.purpurea	Iribarren *et al.*, 1983; Sultana *et al.*, 1985 Viana *et al.*, 1999; Kuo*et al.*, 1997
4. Stigmast-3,5-dien-7-one (**66**)	*B.candicans*	Iribarren *et al.*, 1983
5. 3β-Hdroxystigmast-5-en-7-one (**67**)	*B.purpurea*	Kuo *et al.*, 1997
6. 3-O-β-D-Glucopyranosyl-stigmast-5,22-diene (**68**)	*B.guianensis*	Viana *et al.*, 1999
7. β-Sitosterol (**69**)	*B.candicans, B.vahlii, B.racemosa, B.guianensis*	Iribarren *et al.*, 1983, Sultana *et al.*, 1985 Anjanneyulu *et al.*, 1984; Jain *et al.*, 2002; Bhartia *et al.*, 1981
8. Sitosterol-3-O-β-D-Glucopyranoside (**70**)	*B.candicans*	Iribarren *et al.*, 1983
9. Sitosterol-3-O-β-D-riburonofuranoside (**71**)	*B.guianensis*	Viana *et al.*, 1999
10. Sitosterol-3-O-β-D-Xylopyranoside (**72**)	*B.candicans*	Comber *et al.*, 1990
11. β-Sitosterylhexadecanote (**73**)	*B.candicans*	Iribarren *et al.*, 1984
12. β-Sitosteryloctadecanote (**74**)	*B.purpurea*	Kuo *et al.*, 1997
13. 6'-(β- Sitosteryl-3-O-β-Glucopyranosidyl) hexadecanoate (**75**)	*B.purpurea*	Kuo *et al.*, 1997
14. 6'-(β- Sitosteryl-3-O-β-Glucopyranosidyl) tetraeicosanoate (**76**)	*B.purpurea*	Kuo *et al.*, 1997
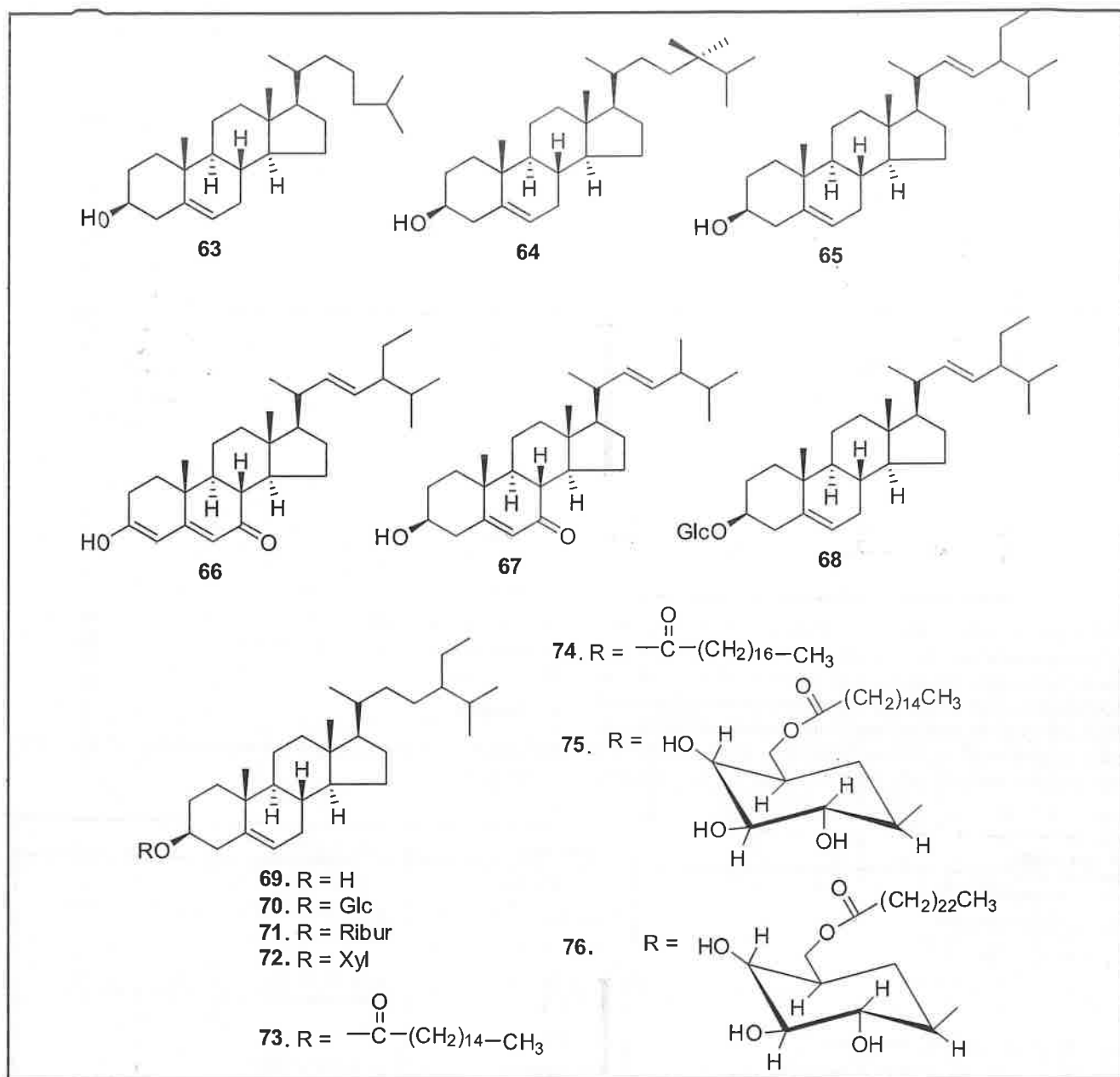
Figure 7: Steroids and its derivative (63-76).

5. Terpenes

All the terpenoid constituents reported from *Bauhinia* species belong to the triterpene class and are presented in Table 8 and Figure 8.

Table 8: Terpenes reported from various *Bauhinia* species

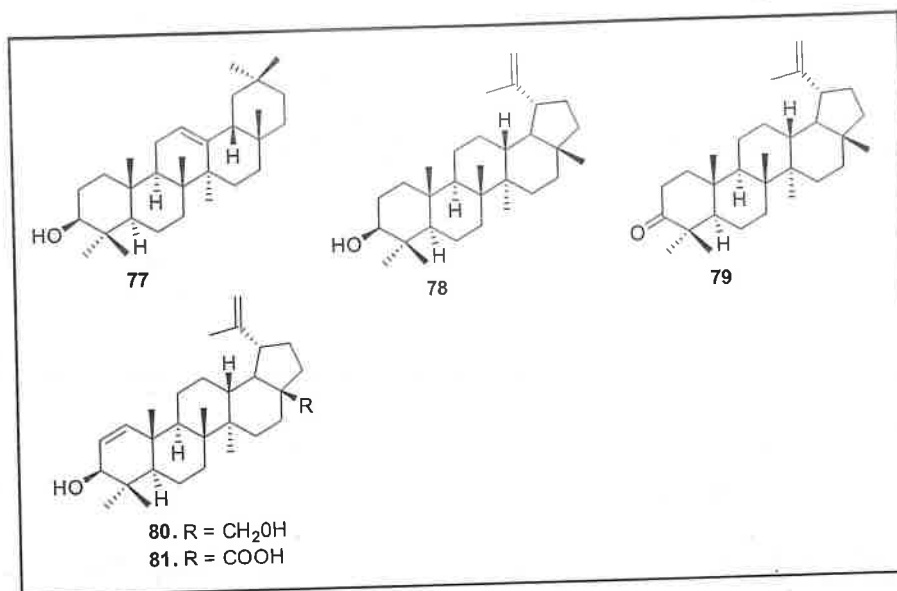| Compound	Plant source	Reference
1. β-Amyrin (77)	*B. racemosa*	Anjanneyulu *et al.*, 1984
2. Lupeol (78)	*B. racemosa*	Kuo *et al.*, 1997; Jain *et al.*, 2002
3. Lupenone (79)	*B. racemosa*	Kuo *et al.*, 1997
4. Betulin (80)	*B. racemosa*	Jain *et al.*, 2002
5. Betulinic acid (81)	*B. vahlii*	Sultana *et al.*, 1985

**Figure 8**: Triterpenoids and its derivatives (77-81).

6. Fatty acids, alcohols and ester derivatives

Bauhinia purpurea is the only species which is reported to fatty acids, alcohols and ester derivatives and these are listed in Table 9 and Figure 9.

Table 9: Fatty acids, alcohols and ester derivatives reported from *Bauhinia* species

| Compound	Plant source	Reference
1. Hexadecanoic acid (82)	*B. purpurea*	Kuo *et al.*, 1997
2. 1-Tetracosonol (83)	*B. purpurea*	Kuo *et al.*, 1997
3. 1-Hexacosonol (84)	*B. purpurea*	Kuo *et al.*, 1997
4. 1-Octacosonol (85)	*B. purpurea*	Kuo *et al.*, 1997
5. Glycerol (86)	*B. purpurea*	Kuo *et al.*, 1997
6. 2,3-Dihydroxypropyl hexadecanoate (87)	*B. purpurea*	Kuo *et al.*, 1997
7. 2,3-Dihydroxypropyl octadecanoate (88)	*B. purpurea*	Kuo *et al.*, 1997
8. 2,3-Dihydroxypropyl oleate (89)	*B. purpurea*	Kuo *et al.*, 1998
9. 2,3-Dihydroxypropyl linoleate (90)	*B. purpurea*	Kuo *et al.*, 1998
10. Methyl hexadecanoate (91)	*B. purpurea*	Kuo *et al.*, 1997
11. Methyl octadecanoate (92)	*B. purpurea*	Kuo *et al.*, 1997
12. 3-(3,4-Dihydroxyphenyl)prop-2-enoyl ester of 2,3,4-trihydroxy-3-hydroxy-methylbutyric acid (93)	*B. tarapotensis*	Braca *et al.*, 2001
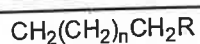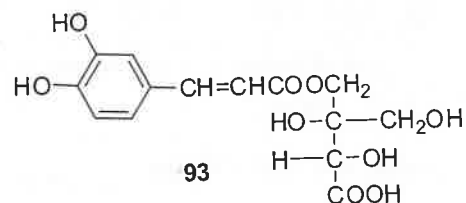
Figure 9: Fatty acids, alcohols and ester derivatives (82-93).

7. Lignans

The lignans reported from *Bauhinia* species are listed in Table 10 and Figure 10.

8. The miscellaneous chemical constituents isolated and reported from the *Bauhinia* species are presented in Table 11 and Figure 11.

The caffeoyl ester of apionic acid (93) and the cyclohexenone derivative (97) reported from *B.tarapotensis* showed significant antioxidant activity. Vijaya Bhaskar Reddy *et al.* (2003) reported a new dihydrodibenzoxepin derivative, namely; as 1,7-dihydroxy-3,4-dimethoxy-2-methyl-5,6-dihydroxyoxepin(b,f)oxepin (110) and a new flavanone, 5,7-dimethoxy-3,4-methylenedioxyflavanone (111) from *B.variegata*. The phytochemical screening of extracts of *Bauhinia purpurea* leaves, showed presence of flavonoids, glycosides, polyphenols, saponin and steroids. These were established preliminary by color tests (Susmita *et al.*, 2020). Evaluation of the in *vitro* antioxidant potential *Bauhinia variegate* plant extract using DPPH (2, 2-diphenyl-1-picrylhydrazyl) and nitric oxide scavenging methods along with phytochemical analysis through thin layer chromatography (Punit *et al.*, 2019).

Table 10: Lignans isolated from various *Bauhinia* species

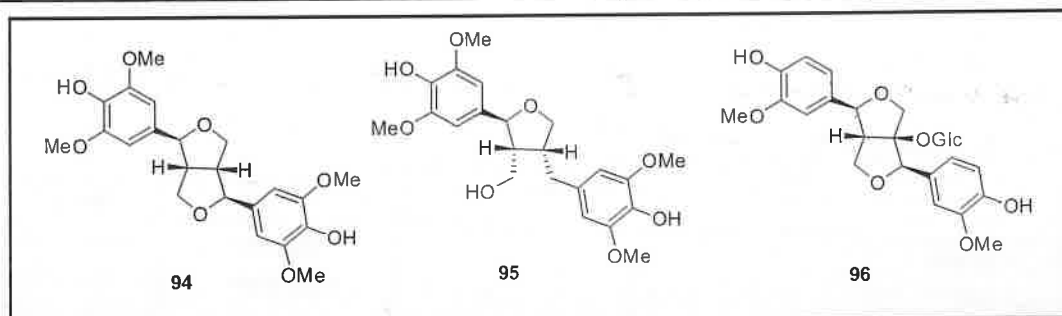| Compound	Plant source	Reference
1. Syringaresinol (94)	*B.manca*	Achenbach *et al.*, 1988
2. (7S, 8R, 8'R)-5,5'-Dimethoxylariciresinol (95)	*B.manca*	Achenbach *et al.*, 1988
3. (+)-l-Hydroxypinoresinol-1-O-â-D-glucopyranoside (96)	*B.tarapotensis*	Braca *et al.*, 2001

Figure 10: Fatty acids, alcohols and ester derivatives (94-96).

Table 11: Miscellaneous chemical constituents reported from *Bauhinia* species

Compound	Plant source	Reference
1. *Cis*-2,4-Dihydroxy-2(2-hydroxyethyl)cyclohex -5en-1-one (97)	*B.tarapotensis*	Braca *et al.*, 2001
2. Lapachol(98)	*B.guianensis*	Viana *et al.*, 1999
3. 5,7-Dihydroxychromone (99)	*B.purpurea*	Kuo *et al.*, 1997
4. Gallic acid (100)	*B.manca*	Achenbach *et al.*, 1988
	B.championii	Chen *et al.*, 1985
5. Vanillic acid (101)	*B.purpurea*	Kuo *et al.*, 1997
6. Isotachioside (102)	*B.purpurea*	Kuo *et al.*, 1997
7. (-) Isolariciresinol-3-á-O-â-D-glucopyranoside (103)	*B.tarapotensis*	Braca *et al.*, 2001
8. Isoaceteoside (104)	*B.tarapotensis*	Braca *et al.*, 2001
9. Indole-3-carboxylic acid (105)	*B.tarapotensis*	Braca *et al.*, 2001
10. D-Pinitol (106)	*B.candicans*	Iribarren *et al.*, 1983
11. Bornesitol (107)	*B.purpurea*	Kuo *et al.*, 1997
12. Bauhinin (108)	*B.championii*	Chen *et al.*, 1985
13. Ω-Hydroxypropioguaiacone (109)	*B.manca*	Achenbach *et al.*, 1988
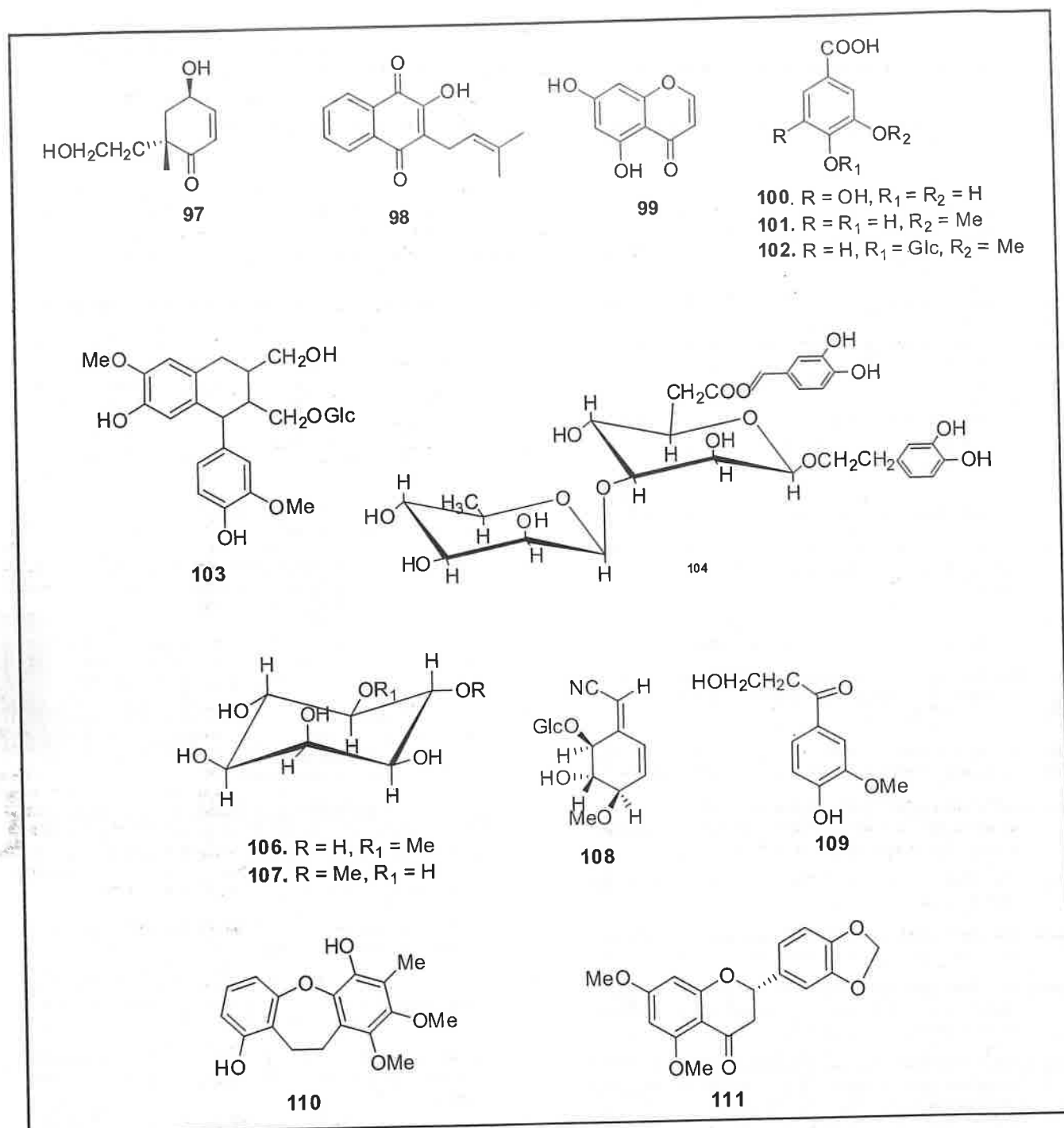
Figure 11: Miscellaneous chemical constituents (97-111).

9. Conclusion

This review of literature including phytochemical investigations on naturally occurring chemical compounds like flavones, flavonols, dihydroflavones, dihydroflavonols, chalcones, dihydrochalcones, flavans and catechins, stilbenes, stereoids, terpenes, fatty acids, alcohols and ester derivatives, lignans and miscellaneous chemical constituents reported from *Bauhinia* species will help researchers and scientists in locating the detailed information and address the continuous development in the phytochemistry and the therapeutic applications. Biosynthetic pathway of pacharin was established through the synthesis and X-ray analysis.

162

Conflict of interest

The author declares no conflicts of interest relevant to this article.

References

Achenbach, H.; Stocker, M. and Constenla, M.A. (1988). Flavonoid and other constituents of *Bauhinia manca*. Phytochemistry, 27(6): 1835-1841.

Anjanneyulu, A.S.R.; Raghava Reddy, A.V.; Reddy, D.S.K.; Cameron, T.S. and Roe,S.P. (1986).Racemosol: A new tetracyclic phenol from *Bauhinia racemosa* Lamk. Tetrahedron,42:2417-2420.

Bhartia, H.P. and Gupta, P.C. (1981). A chalcone glycoside from the seeds of *Bauhinia purpurea*. Phytochemistry, 20:2051-2052.

Bhartin, H.P.; Dubey, P.; Katiyar, S.B. and Gupta, P.C. (1979). A new chalcone glycoside from *Bauhinia purpurea*.Phytochemistry, 18:689-690.

Braca, A.; Tomasi, N.D.; Bari, L.D.; Pizza, C.; Politi, M. and Morelli, I. (2001). Antioxidant principles from *Bauhinia tarapotensis*. J. Nat. Prod., 64(7):892-895.

Cameron, T.S. (1984). Pacharin: a new dibenzo(2,3-6,7)oxepin derivative from *Bauhinia racemosa* Lamk. Tetrahedron, 40:4245-4252.

Chen, C.C.; Chen, Y.P.; Hsu, H.Y.; Lee, K.H. and Tani, S. (1985). Bauhinin, a new nitrile glucoside from *Bauhinia championii*. J. Nat. Prod., 48:933-939.

Chopra, R.N.; Nayer, S.L. and Chopra, I.C. (1956). "Glossary of Indian Medicinal Plants", pp: 34, CSIR, New Delhi.

Chien-Chin, C.; Yuh-Pan, C.; Yuh-Lin, C. and Hong-Yen, H. (1984).*New* Flavones from Bauhinia championii (Benth).Chem.Pharm. Bull., 32(1):166-169.

Chin, C.C.; Lin, H.Y.; Chin, O.J. and Chin.C. (1994).Constituents of the stem of *Bauhinia championii*. Pharm. J. (Taipei), 46:485-489.

Comber, M.F. and Sargent, M.V. J. (1990).The synthesis of pacharin: A dibenzoxepine from the heartwood of *Bauhinia racemosa* Lamk. Chem., Soc. Perkin Trans., 1:1371-1373.

Gamble, J.S. (1956). "Flora of the Presidency of Madras", Vol. II: pp:404, BSI, Calcutta.

Gupta, A.K. and Chauhan, J.S. (1984). Constituents from the stem of *Bauhinia variegate*. Natl. Acad. Sci. Lett. (India), 7:15-16.

Gupta, A.K.; Vidhyapati, T.J. and Chauhan, J.S. (1979).5, 7- Dihydroxy flavanone-4-O-Z- L- rhamnopyranosyl-c-D-glucopyranoside from *Bauhinia variegata*. Indian J. Chem., 18B: 85-86.

Gupta, A.K.; Vidhyapati, T.J. and Chauhan, J.S. (1980). Chemical examination of the stem of *Bauhinia variegata*.Planta Med., 38:174-176.

Iribarren, A.M. and Pomilio, A.B. (1989). Steroidal glycosides, flavonoids, and other components of *Bauhinia uruguayensis*. An Assoc, Quin (Argent), 77:461-466.

Iribarren, A.M. and Pomilio, A.B. (1983).Components of *Bauhinia candicans*. J. Nat. Prod., 46:752-753.

Iribarren, A.M. and Pomillio, A.B. (1985).Sitostero-3-O-â-D-riburonofuranoside from *Bauhinia candicans*. Phytochemistry, 24(2):360-361.

Iribarren, A.M.; Pomillio, A.B. (1984).Sitostero-3-O-â-D-xylopyranoside from *Bauhinia candicans*.Phytochemistry, 23(9):2087-2088.

Jain, R.; Alam, S. and Saxena, U. (2002). A new tetracyclic phenol and other constituents from the roots of *Bauhinia racemosa*. Indian J. Chem., 41B(6):1321-1322.

Kirtikar, K.R. and Basu, B.D.(1935)."Indian Medicinal Plants", Vol. II, pp: 891, Periodical Experts, New Delhi.

Kittikoop, P.; Kirtikara, K.; Tanticharoen, M. and Thebtaranonth,Y. (2000). Antimalarial Preracemosols A and B, possible biogenetic precursors of racemosol from *Bauhinia malabarica* Roxb. Phytochemistry, 55(4):348-352.

Kuo, Y.H.; Chu, P.H. and Chang, C.I. (1998). Chemical studies of the bark of *Bauhinia purpurea*. Chem. Pharm. Bull., 46:1630-1631.

Kuo, Y.H. and Yeh, M.H. (1997). Chemical constituents of heartwood of *Bauhinia purpurea*. J. Chin, Chem, Soc., 44:379-383.

Kuo, Y.H.; Yeh, M.H. and Haung, S.L. (1998). A novel 6-butyl-3-hydroxyflavanone from heartwood of *Bauhinia purpurea*. Phytochemistry, 49:2529-2530.

Laux, D.O.; Stefani, G.M. and Gottlieb, O.R. (1985).Bausplendina dimethylenedioxyflavone from *Bauhinia splendens*. Phytochemistry, 24(5):1081-1084.

Matthew, K.M. (1983). "The flora of the Tamil Nadu and Carnatic", Part III, pp:484, Dioceran, Madras.

Maillard, M.P.; Iglesias, M.C.R.; Saadou, M.; Evans, H.S. andHostettmann, K. (1991). Novel antifungal tetracyclic compounds from *Bauhinia rufescens* Lam. Hel.Chi, Acta, 74(4):791-799.

Paramita, D.; Likhitha, C.; Anjali, N.; Ashwini, A. and Padmavathi. P. (2021). Fundamental of a comparative treatment in rheumatoid arthritis: A brief review. Ann Phytomed. 10(1):23-32.

Prabhakar, P.; Gandhidasan, R.; Venkateswara Raman, P.; Krishnasamy, N.R. and Nanduri, S. (1994). de-O-methylracemosol: A tetracyclic 2,2-dimethylchroman from the roots of *Bauhinia racemosa*. Phytochemistry, 36(3):817-818

Punit, R.; Bhatt, Urvesh, D.; Patel, C.; Modi, M.; Kajal, B.; Pandya and Harshad B. (2019). Thin-layer chromatography and *in vitro* free radical scavenging activity of few medicinal plants from the surroundings of Junagadh, Gujarat, India.Anna. Phytomed., 8(1):45-55.

Ramachandran, R. and Joshi, B.C. (1967).Chemical examination of.*Bauhinia purpurea* flowers. Curr. Sci., 36:574-575.

Rahman, W. and Begum, S.J. (1985). Flower pigments: Flavonoids from the white flowers of *Bauhinia variegata* Linn. Naturwissenschaften, 53:385-387.

Row, L.R. and Viswanatham, N. (1954).Coloring matter of the flower petals of *Bauhinia tomentosa*. Proc. Indian Acad. Sci., 39A:240-242.

Reddy, M.V.B.; Reddy, M.K.; Gunasekar, D.; Caux, C. and Bodo, B. (2003).A flavanone and a dihydrodibenzoxepin from *Bauhinia variegate*. Phytochemistry, 64(4):879-882.

Susmita, G; Karishma, R.; Himanshu, D. and Usha, M. (2020).Screening of selected plants for their effectiveness in the treatment of kidney stone. Ann. Phytomed., 9(1):213-217.

Sultana, S.; Iiyas, Kamil, M. and Shaida, W.A. (1985). Chemical investigation of *Bauhinia vahlii*. J. Indian Chem. Soc., 62:337-338.

Subramanian, S.S. and Nair, A.G.R. (1963). Flavonoids from *Bauhinia tomentosa*.Indian J. Chem., 1:450-452.

Tiwari, K.P.; Masood, M, and Rathore, Y.K.S. (1978). Flavonoid glycoside isolated from *Bauhinia retusa*. Proc. Natl, Acad. Scic., India, Section A: Physical Sciences. 48A:183-186.

The Wealth of India (1976). "A dictionary of Indian Raw Materials and Industrial Products", Vol.I, pp:160, CSIR, New Delhi.

Viana, E.P.; Santa-Rosa, R.S.; Almeida, S.S.M.S. and Santos, L.S. (1999). Constituents of the stem bark of *Bauhinia guianensis*. Fitoterapia, 70:111-112.

Wahab, S.M.A.E.; Wassel, G.M.; Ammar, N.M. and Hanna, T.(1987). Flavonoid constituents in the different organs of selected *Bauhinia*

species and their effect on blood glucose. Herba. Hung., 26 (1):27-31.

Xiangui, T.;Chunping, Y.;Zhihou, Z. and Mohua, Z. (1992). Taxifolin isolated from *B.hupenhara*. Zhongguo .Zhongyao Zazhi, 17:613-615.

Yadava, R.N. and Tripathi, P. (2000).A novel flavone glycoside from the stem of *Bauhinia purpurea*. Fitoterapia,71(1):88-90.

Yadava, R.N. and Sodhi, S.(2001). A Novel flavone glycoside 6,4'-Dihydro-3'-prenyl-3,5,7,5'-tetramethoxyflavone-6-O-$\dot{a}$-L-rhamnopyranoside from the seeds of *Bauhinia purpurea*. Asian J. Chem., 13(2):529-533.

Bioassay guided fractionation, isolation and synthesis of potent antimicrobial agents from *Alpinia galanga* (L.) Willd.

Mopur Vijaya Bhaskar Reddy◆

Chemistry Department, Malla Reddy Engineering College (Autonomous), Maisammaguda, Dhulapally Road, Kompally, Secunderabad-500100, Telangana, India

Article Info

Abstract

The air-dried and powdered methanol solvent extraction of the rhizomes of *Alpinia galanga* (L.) Willd. is subjected to bioassay guided fractionation and isolation yielded two compounds, namely; p-coumaryl diacetate (1) and 1'-S-1'-acetoxychavicol acetate (2). The isolated known compounds have been identified based on the physical, spectral data of IR, 1H, 13C NMR and mass spectroscopy and comparison with an authentic sample. Finally, the isolated p-coumaryl diacetate (1) and 1'-S-1'-acetoxychavicol acetate (2) were confirmed by synthesis. The crude methanol extract, identified known compounds 1 and 2 were tested for antimicrobial property against *Malassezia furfur*, which were exhibited with MIC values 1000, 62.5 and 7.81 μg/ml, respectively.

1. Introduction

Common dandruff is measured by excessive formation of scales of white greyish color, depositing on the scalp area and is common problem for most of the population ethnicity and both genders. The nature and origin of dandruff has been consistently controversial (Shemer *et al.*, 2000). *Pityrodporium ovale* is strongly suspected to play important role in the manifestation of the seborrheic dermatitis (De Angelis *et al.*, 2005: Ro *et al.*, 2005). Clinically, white greyish flakes of scalp skin are very often visible on the hair and shoulders. The remaining indication of dandruff is itching with scalp soreness. Commonly three major etiological factors are causing for dandruff like Malassezia fungi, sebaceous secretions and individual sensitivity (De Angelis *et al.*, 2005: Ro *et al.*, 2005). The genus Malassezia is mainly belongs to Basiodiomycetous yeast and is classified in the Malasseziales (Gueho *et al.*, 1996 : Chang *et al.*, 1998). These are generally identified in the places of rich source in sebaceous glands mainly these are lipid dependent. The *Malassezia furfur* is one of the important microorganisms of dandruff and it is a member of normal fungal flora on the human skin scalp, because it may be isolated from the scalp (Kurtzma *et al.*, 1998). For growth of *M. furfur* is mainly requires essential lipids and proteins, responsible for dermal inflammation and tissue damage (Boekhout *et al.*, 2003). As fungal resistance to synthetic antibiotics is in rise (Mathew *et al.*, 2017), an alternative in the way of herbal medicine in controlling the same is the need of the hour. The current study was an attempt to pick out the potential antimicrobial components from *A. galanga* is an alternative strategy. Earlier reports on this plant showed various biological properties, such as antiviral (Mehrotra *et al.*, 2020), antibacterial, antidiabetic, antiprotozoal, antioxidant, antifungal, immunomodulatory, DNA binding studies (Rekha *et al.*, 2019) antiplatelet and hypolipidemic (De-pooter *et al.*, 1985; Kiuchi *et al.*, 2002). Our main interest on the isolation of biologically active molecules from medicinal plants for antimicrobial agents and we have undertaken the air-dried rhizomes of *A.galanga* and synthesis of isolated known compounds for its antimicrobial action against *M. furfur*.

2. Materials and Methods

2.1 General experimental procedures

IR spectra were recorded on a Bruker IFS-66/S FT-IR spectrometer. NMR spectra were recorded on a Bruker 300 NMR spectrometer operating at 300 MHz (^{1}H) and 75 MHz (^{13}C) with chemical shifts given in ppm (Ä). Silica gel (Merck, 100-200 mesh and 230-400 mesh) was used for column chromatography. The packing material for molecular sieve column chromatography was Sephadex LH-20 (Pharmacia Co.). TLC was performed using Merck pre-coated silica gel F$_{254}$ plates. Spots were detected on TLC under UV light or by heating after spraying with 10% H_2SO_4 in C_2H_5OH (v/v).

2.2 Plant materials

The air-dried rhizomes of *Alpinia galanga* (L.) Willd. (Family: Zingiberaceae) (1.0 kg) were purchased from market in Hyderabad, Telangana, India in December 2019. A voucher specimen (AG-001) of this plant was deposited in the Department of Chemistry, Sri Venkateswara University, Tirupati, Andhra Pradesh, India.

Corresponding author: Dr. M. Vijaya Bhaskar Reddy
Chemistry Department, Malla Reddy Engineering College (Autonomous), Maisammaguda, Dhulapally Road, Kompally, Secunderabad-500100, Telangana, India
E-mail: vijaybreddy123@gmail.com
Tel.: +91-8297194349

664

Figure 1: *A. galanga* rhizomes.

2.3 Extraction and isolation

The air-dried and powdered rhizomes of *A. galanga* (0.8 kg) was extracted with methanol (3 × 3.0 liter) by using Soxhlet apparatus. The filtrate of the solvent was concentrated vacuum distillation under reduced pressure by rotary evaporator at 35°C to yield 40 g. It is represented as methanol crude extract. The crude methanol extract was submitted antimicrobial activity and it showed significant antimicrobial activity against *M. furfur* - MTCC 1374 with MIC 1000 μg/ml. Portion of the methanol extract (25 g) was dissolved in minimum amount of methanol (MeOH) and adsorbed over silica gel (60 g, 100-200 mesh, Merck). 250 g of silica gel (100-200 mesh) was taken in silica gel column and on the top of column crude material was loaded. Initially, column was eluted with direct step gradient mixtures as eluents like hexane: chloroform (1:1, 1:2, 1:3 and 1:4), chloroform and finally with the mixtures of CHCl₃: EtOAc (9:1) collected ten fractions. Based on the TLC pattern, similar fractions are combined it and made into three fractions; Fr.1 (4.52 g), Fr. 2 (10.85 g), and Fr.3 (2.14 g). The separated three fractions (1-3) were submitted for antimicrobial activity against *M. furfur*. Fractions 1 and 2 were showed more potent against antimicrobial activity against *M. furfur* with the MIC 250 μg/ml. Fraction 1 (3.0 g) was further purified by using silica gel column chromatography eluted with hexane/ ethyl acetate (8:2) to give p-coumaryl diacetate (1, 1.2 g). In the TLC analysis, Fraction 2 was showing one major compound and some minor pigments appeared. This was further purified by small silica gel column chromatography using the direct solvent mixture like hexane: chloroform (7:3) yielded a compound 2 as colorless oil (3.5 g). The isolated pure compounds were characterized by various spectral data and it was exactly matched with reported literature of p-coumaryl diacetate (1) and 1'S-1'-acetoxychavicol acetate (2) (Noro et al., 1988). Finally, isolated and known compounds 1 and 2 were confirmed by synthesis. Compounds 1 and 2 have been submitted for antimicrobial activity against *M. furfur* exhibited with the MIC values 62.5 and 7.81 μg/ml.

P-Coumaryl diacetate (1)

1'-S-1'-Acetoxychavicol acetate (2)
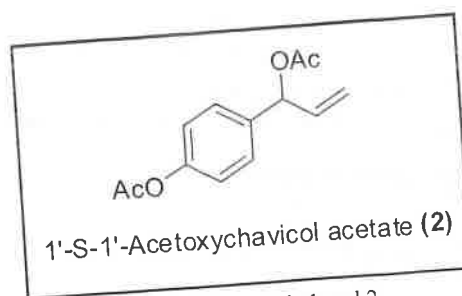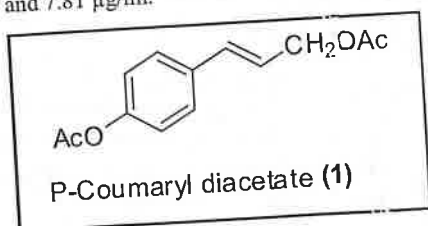
Structures of compounds 1 and 2

2.4 p-coumaryl diacetate (1)

Compound 1 is a pale yellow oil, calculated for $C_{13}H_{14}O_4$, 234.2397; IR (CCl₄) v max, cm⁻¹: 1759, 1651, 1238.¹H NMR (CDCl3, 300 MHz) δ 7.31 (2H, d, J = 8.2 Hz), 7.01 (2H, d, J = 8.2 Hz), 6.58 (1H, d, J = 16.5 Hz), 6.19 (1H, dt, J = 16.5, 6.1 Hz), 4.71 (2H, dd, J = 6.1, 1.3 Hz), 2.31 (3H, s), 2.12 (3H, s); ¹³C NMR (CDCl3, 75 MHz) δ 170.4, 169.2, 150.8, 134.3, 132.8, 127.7, 122.7, 120.7, 64.7, 21.3, 21.0. NMR data were identical to the literature values (Noro et al., 1988 : Khalijah et al., 2010).

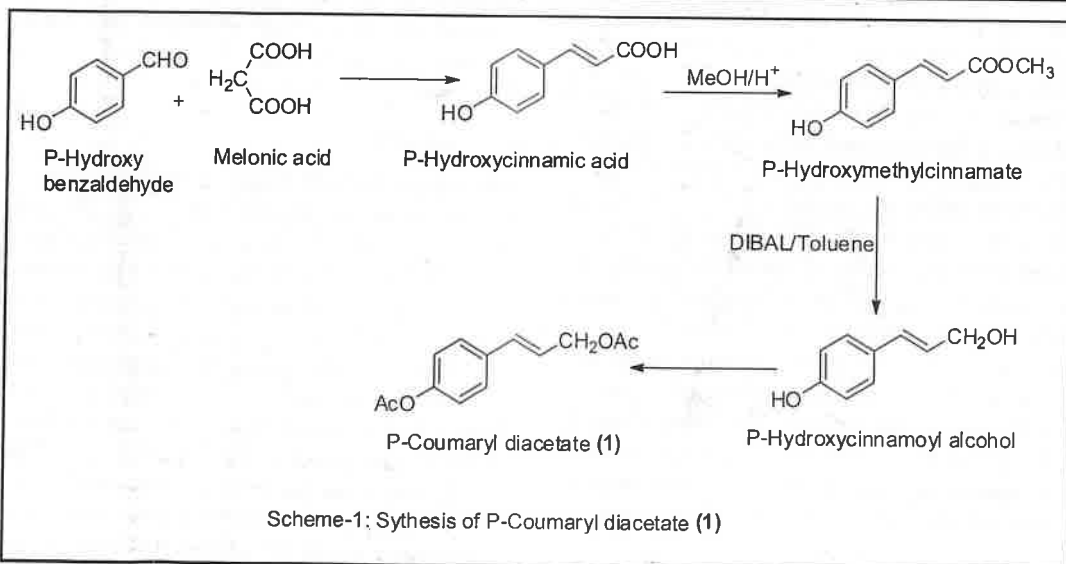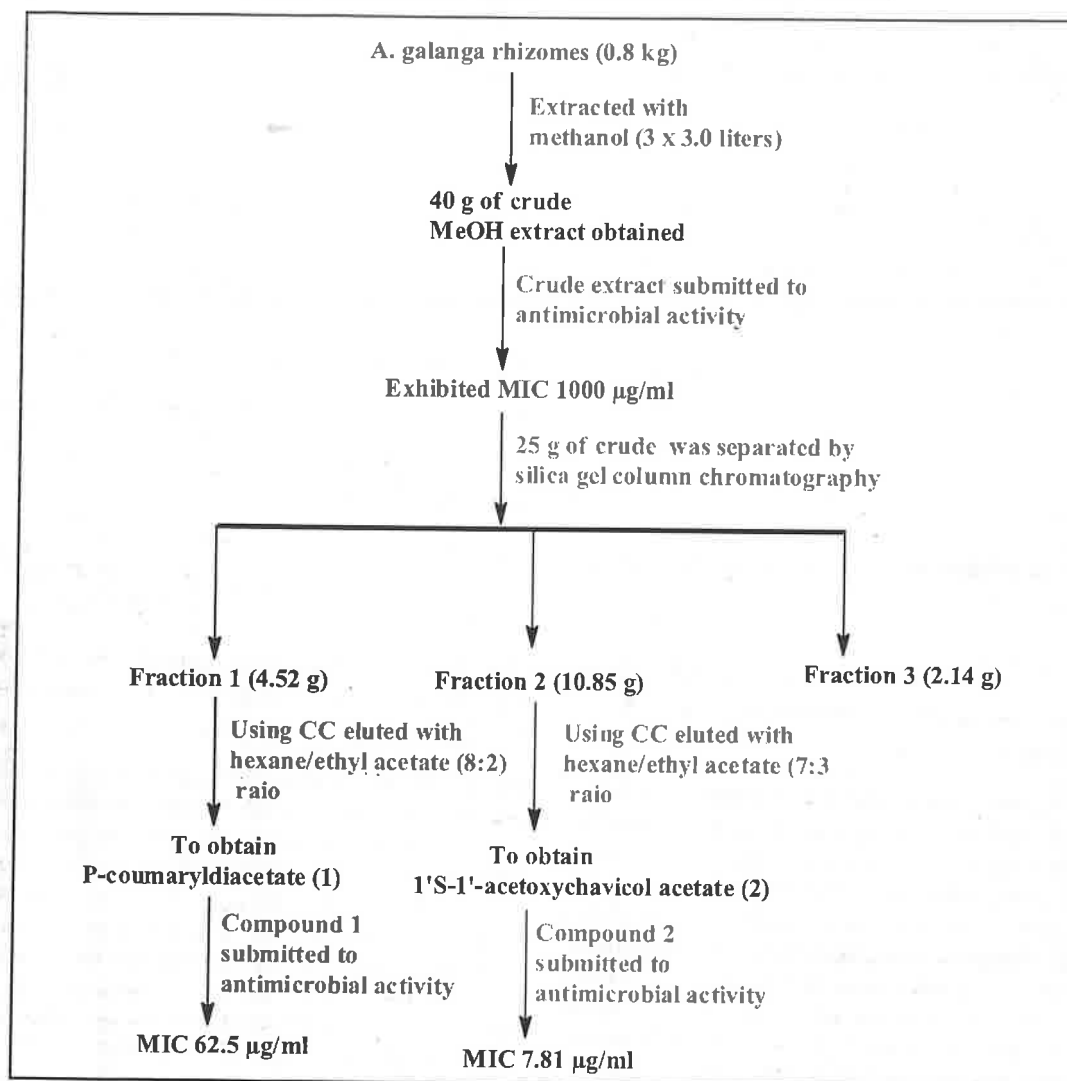### 2.5 1'S-1'-acetoxychavicol acetate (2)

Compound 2 is a colorless oil, calculated for $C_{13}H_{14}O_4$, 234.2479; Found 234, 192, 150, 149, 132, 77, 42. IR (CCl₄) v max, cm⁻¹: 1761, 1645, 1234.¹ H (CD₃OD, 300 MHz): δ 7.35 (2H, d, J = 8.5 Hz), 7.06 (2H, d, J = 8.5 Hz), 6.25 (1H, d, J = 6.1 Hz), 6.01 (1H, ddd, J = 16.2, 10.4, 6.1 Hz), 5.27 (1H, dd, J = 16.2, 1.3 Hz), 5.21 (1H, d, J = 10.4, 1.3 Hz), 2.25 (3H, s), 2.07 (3H, s); ¹³C (CD₃OD, 75 MHz): δ 170.1, 169.4, 150.2, 136.4, 135.2, 126.9, 122.5, 114.9, 75.2, 19.2, 19.3.

2.6 Synthesis of p-coumaryl diacetate (1)

Take p-hydroxybenzaldehyde (61 gm, 0.5 moles) and malonic acid (104 gm, 1 mole) in pyridine solvent (75 ml) at room temperature and added 1.6 ml of piperidine as catalyst. The total solution was refluxed at 105-110°C for 6 h in oil bath. After usual work up to obtain crude solid as P-hydroxycinnamic acid in 58 g, 71 % yield. In the second step, take P-hydroxycinnamic acid (16.4 g, 0.1 moles) in MeOH (250 ml) and added concentrated sulfuric acid (2.0 ml) and reflux at 90-100°C for 4-5 h. After completion of reaction, the solution was cooled down to room temperature and poured in to crushed ice in a beaker to obtain white precipitate. The white precipitate was filtered and washed with cold water thoroughly to obtain P-hydroxymethylcinnamate as color less solid 15.42 g, 87 % yield. Taken P-hydroxymethylcinnamate (1.78 g, 0.01 mole), in freshly distilled toluene (50 ml) in 100 ml RB flask, cooled in ice cold water bath (-5 to 0°C) and added 40 ml of 1.0 M DIBAL (0.04 moles) in toluene solution by syringe over the period of 10 min). The reaction mixture was continued for another one hour and maintained the same temperature. The reaction mixture was quenched with ethanol (5 ml) and the solvent was partially removed in *vacuo* at 40°C and about 50 ml of water was added and the aq. layer was extracted with ethyl acetate (thrice). The combined extract was dried over MgSO₄ and concentrated under vacuum to obtain as buff colored P-hydroxycinnamoyl alcohol (1.28 g, 85%). The obtained P-hydroxycinnamyl alcohol (85 g, 0.566 moles) and Ac₂O (231 ml, 4 eq) was taken in 1 lit. Round bottom flask and added 50 ml pyridine at room temp. The reaction mixture was refluxed for 4 h and then cooled to room temp. The reaction mixture was added to crush ice water in a 2 lit.conical flask to obtain white waxy type solid. This

was further filtered and the resulting solid was dried in *vacuo* to obtain crude and purified by vacuum liquid chromatography (VLC) using hexane: EtOAc (8:2) as solvent system to obtain *p*-coumaryl diacetate (1) in 118 g, 89% yield).

A. galanga rhizomes (0.8 kg)

Extracted with
methanol (3 x 3.0 liters)

40 g of crude
MeOH extract obtained

Crude extract submitted to
antimicrobial activity

Exhibited MIC 1000 μg/ml

25 g of crude was separated by
silica gel column chromatography

Fraction 1 (4.52 g)   Fraction 2 (10.85 g)   Fraction 3 (2.14 g)

Using CC eluted with
hexane/ethyl acetate (8:2)
raio

Using CC eluted with
hexane/ethyl acetate (7:3
raio

To obtain
P-coumaryldiacetate (1)

To obtain
1'S-1'-acetoxychavicol acetate (2)

Compound 1
submitted to
antimicrobial activity

Compound 2
submitted to
antimicrobial activity

MIC 62.5 μg/ml   MIC 7.81 μg/ml

Scheme-1: Sythesis of P-Coumaryl diacetate (1)

2.7 Synthesis of 1'S-1'-acetoxychavicol acetate (2)

The target compound P-coumaryl diacetate was completed in four steps. In the 1st step, P-hydroxycinnamic acid was prepared from P-hydroxybenzaldehyde and malonic acid. Second step, the P-hydroxycinnamic acid was converted to its methyl ester by MeOH and H_2SO_4 and the resulting P-hydroxy methylcinnamate was reduced with DIBAL to obtain P-coumaryl alcohol. This was further acetylation with Ac_2O to obtain P-coumaryl diacetate. Take 188 g of p-hydroxybenzaldehyde in round bottom (RB) flask, added 306 g of acetic anhydride, and 300 ml of pyridine. The reaction mixture was refluxed up to 100-105 °C for 5 h. Reaction mixture progress was observed by TLC (thin layer chromatography) for every one hour. After completion of the reaction, this was cool down to room temperature and poured in to ice cold water. The mixture was extracted with ethyl acetate to get P-acetoxybenzaldehyde as colorless oil, 228 g, yield is 90%. Taken P-acetoxybenzaldehyde (4.0 g, 0.024 mol) in 250 ml of two necked RB flask and add 20 ml of THF. Then, the flaks was cooled to below 0°C by using ice-salt mixture, then added drop wise of vinyl magnesium bromide 1 M solution in THF (30 ml, 0.03 mol) and stirred at same temp for 15 min. Temperature has been raised slowly to room temperature, and the reaction mixture was stirred for another 5 h. Reaction progress was monitored by TLC and quenched with 0.5 M HCl and extracted with ethyl acetate (EtOAc). The ethyl acetate extract was concentrated under reduced pressure and acetylated with acetic anhydride to get colorless liquid compound (2), 1'-acetoxy chavicol acetate and this was exactly matched with isolated compound by TLC.

Scheme-1: Sythesis of 1'-S-1'-Acetoxychavicol acetate (2)
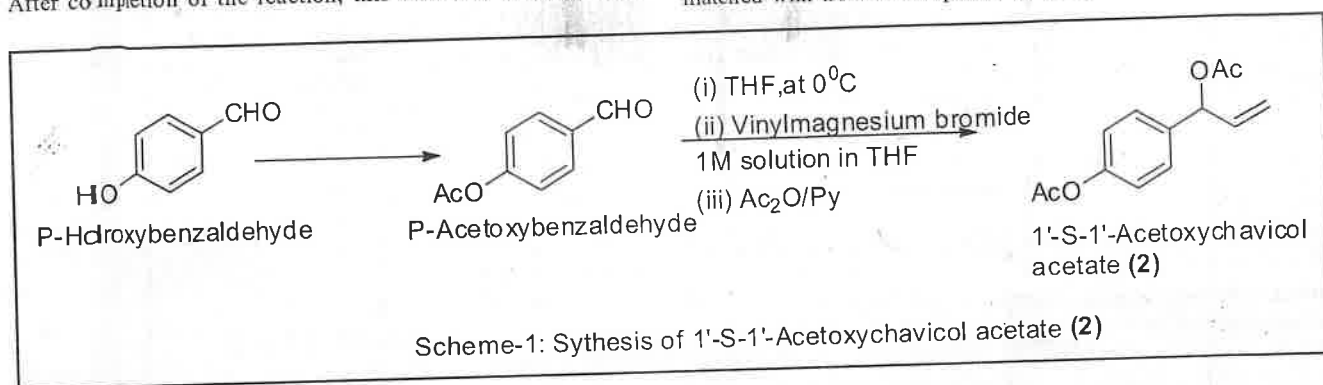
3. Discussion

The antimicrobial assay (antidandruff) was conducted based on the reported method which was done previously (Rao et al., 2012). The cell culture of M. furfur MTCC-1374 was collected from Gene Bank, Institute of Microbial Technology, Sector 39-A, chandigarh, India. Bacterial and yeast cell culture was nourished by Tryptone soya agar (TSA) and sabouraud dextrose agar (SDA), respectively. Stock solution preparation: The antimicrobial stock solution was prepared concentrations at least 1,000 mg /ml or ten times the higher concentration whichever is greater. A sample weighing 15 mg was dissolved in 500 ml of dimethyl sulfoxide (DMSO) and it was further diffused in 1 ml of propylene glycol. The total solution was makeup to 15 ml with tryptone soy broth and vortex for about a minute. The control was used as without any test sample. Preparation of bacterial inoculum: Three to five well isolated colonies of the same morphological type of the fresh stock cell culture was picked on solid agar and transferred into a tube consist of 5 ml of tryptone soy broth (TSB). The broth culture was incubated at 37°C on overnight. The turbidity of the grown stock culture was monitored by spectrophotometer at 600 nm wavelength. Approximately, the culture suspension was adjusted to get with the cell concentration of about 108 cfu/ml. Yeast cultures: Fresh grown stock culture was on solid agar, at least three to five well-isolated colonies of the same morphological type were picked and transferred into a tube containing 5 ml of sabouraud dextrose broth (SDB). The broth culture was incubated at 32°C overnight. The turbidity of the grown culture was measured by a spectrophotometer at 600 nm. Approximately, the culture suspension was adjusted to get with the cell concentration of 106 cfu/ml.

3.1 Macro tube dilution method

The sample stock solution of 500 ml was serially diluted in tubes containing 500 microliters of TSB until concentration of 0.488 mg/ml was reached. 500 microliter of cell suspension was transferred into aseptically test tube and incubated at 37°C for 24 h. The sterile tube containing TSB without sample was inoculated with 500 microliters of cell suspension and used as a positive control. Similarly, a sterile TSB tube containing a sample without cell suspension was used as sample control. After 24 h of incubation, an aliquot was taken from each test tube on tryptone soy agar plates and incubated at 37°C for 48 h to validate the growth. The MIC (minimum inhibitory concentration) was calculated from the lower concentration of the sample that completely inhibits the growth of tested organisms. A similar assay was conducted for yeast with SDB and incubated at 32°C for 72 h.

4. Conclusion

Bioassay guided fractionation and isolation of A. galanga obtained two known compounds identified as, p-coumaryl diacetate (1) and 1'-S-1'-acetoxychavicol acetate (2). The known compounds 1 and 2 were exhibited potent antimicrobial activity against M. furfur with MIC 62.5 and 7.81 µg/ml. This is the first time reported antidandruff activity from this plant. The isolated compounds 1 and 2 were confirmed by synthetic methods. Compounds 1 and 2 are having two acetyl groups, trans C=C double bond in 1 and exocyclic double bond in 2. In compound 1 one of the acetyl groups was attached to methylene carbon and in 2 the acetyl group was attached methine carbon atom. Based on the above information, compound 2 is more potent than 1 due to double bond nature and acetyl group attached carbon play a crucial role antimicrobial activity against M. furfur.

Acknowledgments

The author gratefully acknowledge the Department of Chemistry, Sri Venkateswara University, Tirupathi, Andhra Pradesh, India, for their constant support during this research work for isolation work and evaluation of antidandruff studies.

Conflict of interest

The authors declare no conflicts of interest relevant to this article.

References

Boekhout, T. and Gueho, E. (2003). Basidiomycetous yeasts. In: Pathogenic Fungi in Humans and Animals (Howard, D.H., Ed.), 2 edn, Marcel Dekker, Inc., New York, USA. pp:537-542.

Chang, H.J.; Miller, H.L.; Watkins, N.; Arduino, M.J.; Ashford, D.A.; Midgley, G.; Aguero, S.M.; Pinto-Powell, R.; Von Reyn, C.F.; Edwards, W.; McNeil, M.M. and Jarvis, W.R. (1998). An epidemic of Malassezia pachydermatis in an intensive care nursery associated with colonization of health care workers' pet dogs. N. Engl. J. Med., 338 (11):706-711.

De-Pooter, H.L.; Omar, M.N.; Coolsaet, B.A. and Schamp, N.M. (1985). The essential oil of greater galanga (*Alpinia galanga*) from Malaysia. Phytochemistry, 24(1):93-96.

De Angelis, Y.M.; Gemmer, C.M.; Kaczvinsky, J.R.; Kenneally, D.C.; Schwartz, J.R. and Dawson, T.L. (2005). Three etiologic facets of dandruff and seborrheic dermatitis: Malassezia fungi, sebaceous lipids, and individual sensitivity. J. Investig. Dermatol. Symp. Proc., 10(3): 295-297.

Gueho, E.; Midgley, G. and Guillot, J. (1996). The genus Malassezia with description of four new species. Antonie Van Leeuwenhoek, 69(4): 337-355.

Khalijah, Awang.; Mohamad, Nurul Azmi.; Lionel, In Lian Aun.; Ahmad, Nazif Aziz.; Halijah, Ibrahim. and Noor, Hasima Nagoor. (2010). The apoptotic effect of 1'S-1'-acetoxychavicol acetate from *Alpinia conchigera* on human cancer cells. Molecules, 15(11):8048-8059.

Kurtzman, C.P. and Fell, J.W. (1998). The Yeasts: A Taxonomic Study, 4th edn. Elsevier, Amsterdam, the Netherlands. pp:7-102.

Kiuchi, F.; Keniji, M.; Itano, Y.; Ito, M.; Honda, G. and Qui, T.K. (2002). Screening of natural medicines used in Vietnam for trypanocidal activity. Nat. Med., 56(2):64-68.

Matthew, J.; Cheesman, Aishwarya Ilanko.; Baxter, Blonk. and Ian, E. Cock. (2017). Developing new antimicrobial Therapies: Are synergistic combinations of plant extracts/compounds with conventional antibiotics the solution. Pharmacogn. Rev, 11(22):57-72.

Nupur Mehrotra (2020). Medicinal plants, aromatic herbs and spices as potent immunity defenders: Antiviral (COVID-19) perspectives. Ann. of Phytomed., 9(2):30-49.

Noro, T.; Sekia, T.; Katoh, M.; Oda, Y.; Miyase, T.; Kuruyanagi, M.; Ueno, A. and Ukishima, S. (1988). Inhibitors of xanthine oxidase from *Alpinia galanga*. Chemical and Pharmaceutical Bulletin, 36(1):244-248.

Rao, G.V.; Kavitha, K.; Gopalakrishnan, M. and Mukhopadhyay, T. (2012). Isolation and characterization of a potent antimicrobial compound from *Aerva sanguinolenta* Blume.: An alternative source of Bakuchiol. Journal of Pharmacy Research, 5(1):174-176.

Rekha, R.; Geeta, J. and Arunkumar. A.N. (2019). DNA fingerprinting in industrially important medicinal trees. Ann Phytomed., 8(1):19-35.

Ro, B.I. and Dawson, T.L. (2005). The role of sebaceous gland activity and scalp microfloral metabolism in the etiology of seborrheic dermatitis and dandruff. J. Investig. Dermatol. Symp. Proc., 10(3):194-197.

Shemer, A.; Nathansohn, N.; Kaplan, B.; Weiss, G. and Newman N, T. H. (2000). Treatment of scalp seborrheic dermatitis and psoriasis with an ointment of 40% urea and 1% bifonazole. Int. J. Dermatol., 39(7): 532-534.

Isolation, characterization and structure elucidation of flavonoids from the root bark of *Bauhinia variegata* L.

Mopur Vijaya Bhaskar Reddy◆

Chemistry Department, Malla Reddy Engineering College (Autonomous), Maisammaguda, Dhulapally Road, Kompally, Secunderabad-500100, Telangana, India

Abstract

Three known flavonoids, quercetin-7-O-methyl ether (1), kaempferol-7, 4'-dimethyl ether 3-O-β-D-glucopyranoside (2) and kaempferol 3-O-β-D-glucopyranoside (3) were isolated from the root bark of *Bauhinia variegata* L., and the structures of the all known compounds were mainly established by extensive spectroscopic analysis, including 1D (^{1}H & ^{13}C NMR), 2D NMR (HMBC, HSQC and NOESY) and chemical studies. In the chemical analysis, compounds 2 and 3 were hydrolysis under acidic conditions to obtain their aglycones and these were identified as kaempferol-7, 4'-dimethyl ether (4) and kaempferol (5), respectively.

1. Introduction

Bauhinia variegata L. (Leguminosae) is a medium sized deciduous tree, found on the rocky hills of Circars, Deccan and Carnatic regions of South India (Gamble *et al.*, 1956). An infusion from its bark is used as an astringent, alterative tonic and useful in scrofula, skin diseases and ulcers. The decoction of the roots is used in dyspepsia and as an antidote to snake bites (Tammanna *et al.*, 2000). Previous phytochemical studies on the stems (Guptal *et al.*, 1980, 1984 and 1979), flowers (Wahab *et al.*, 1987; Rahman *et al.*, 1985), root bark (Vijaya Bhaskar Reddy *et al.*, 2003) and seeds (Yadava *et al.*, 2001) of this species have led to the isolation of several flavonoids and their sugar derivatives. Evaluation of the *in vitro* antioxidant potential activity of *B.variegata* plant extract using DPPH (2, 2-diphenyl-1-picrylhydrazyl), and nitric oxide scavenging methods along with phytochemical analysis through thin layer chromatography (Punit *et al.*, 2019). The present work on root bark has resulted in the isolation, characterization and structure elucidation of three known flavonoids, namely; as quercetin-7-O-methyl ether (1), kaempferol-7, 4'-dimethyl ether 3-O-β-D-glucopyranoside (2) and kaempferol 3-O-β-D-glucopyranoside (3). The isolated known compounds were extensively established by various 1D and 2D NMR, mass spectral data and chemical studies. Compounds 1 and 2 were reported first time from the root bark of *B. variegata*.

Corresponding author: **Dr. M. Vijaya Bhaskar Reddy**
Professor, Chemistry Department, Malla Reddy Engineering College (Autonomous), Maisammaguda, Dhulapally Road, Kompally, Secunderabad-500100, Telangana, India
E-mail: vijaybreddy123@gmail.com
Tel.: +91-8297194349

2. Materials and Methods

2.1 General experimental procedures

Melting points were measured on a kofler hot-stage apparatus and are uncorrected. Optical rotations were measured in MeOH at 25°C on a Perkin-Elmer241 polarimeter. ^{1}H and ^{13}C NMR spectra were determined on brukeravance 400 and bruker AC 300 spectrometer using DMSO-d_6 and CDCl$_3$ with TMS as internal standard. (^{1}H-^{1}H COSY, HSQC, HMBC and phase sensitive NOESY (with 500 ms mixing time) spectra were recorded using the standard pulse sequences. ESITOFMS and ESI-MS/MS were recorded in positive ion mode on an API Q- STAR PULSA of applied bio-system. Column chromatography was performed on acme silica gel finer than 200 mesh (0.08 mm). TLC was performed using Merck pre-coated silica gel F$_{254}$ plates. Spots were detected on TLC under UV light or by heating after spraying with 10% H$_2$SO$_4$ in C$_2$H$_5$OH (*v/v*).

2.2 Plant materials

The root bark of *B. variegata* was collected in December 2019 from Tirumala Hills, Andhra Pradesh, South India. A voucher specimen (BR 005) was deposited in the herbarium of the Department of Botany, Sri Venkateswara University, Tirupati, Andhra Pradesh, India.

2.3 Extraction and isolation

Air-dried and powdered root bark of *B.variegata* (1.0 kg) was successively extracted with acetone (Me$_2$CO) (3 × 2.5 liter) and

MeOH (3 × 2.5 liter) by using Soxhlet apparatus. The filtrate of the solvents were concentrated vacuum distillation under reduced pressure by rotary evaporator at 35°C to yield 15 g and 6 g, respectively. Portion of the acetone extract (10 g) was dissolved in a minimum amount of methanol (MeOH) and adsorbed over silica gel (20 g, 100-200 mesh, Merck) 60 g of silica gel (100-200 mesh) was taken in silica gel column and on the top of column crude material was loaded. Initially, column was eluted with direct step gradient mixtures as eluents like n-hexane: ethyl acetate in the ratios 9:1, 8:2, 7:3, 1:1 and 3:7 collected ten fractions. Based on the TLC pattern, similar fractions are combined it and made into two fractions; Fr.1 (3.58 g) and Fr. 2 (4.50 g). Fraction 1 (2.5 g) was further purified by using silica gel column chromatography eluted with hexane/ethyl acetate (8:2) to give compound 1 as yellow crystalline solid 650 mg). In the TLC analysis Fraction 2 was showing one major compound and some minor pigments appeared.

This was further purified by small silica gel column chromatography using the direct solvent mixture like n-hexane: ethyl acetate (2:8) yielded a compound 2 as yellow solid (985 mg). The isolated pure compounds were characterized by using various extensive spectral data and established as quercetin-7-O-methyl ether (1) and kaempferol-7, 4'-dimethyl ether 3-O-β-D-glucopyranoside (2). In the TLC analysis of crude methanol extract showed one major compound. Portion of the crude methanol extract (4 g) was dissolved in minimum amount of methanol (MeOH) and adsorbed over silica gel (10 g, 100-200 mesh, Merck). 40 g of silica gel (100-200 mesh) was taken in silica gel column and on the top of column crude material was loaded. Initially column was eluted with direct solvent like EtOAc and step gradient mixture as EtOAc: MeOH (9:1) to obtain compound 3 (545 mg). The isolated pure compound was established as kaempferol 3-O-β-D-glucopyranoside (3) (Scheme 1).

Scheme 1: Extraction and isolation procedure of *Bauhinia variegata*
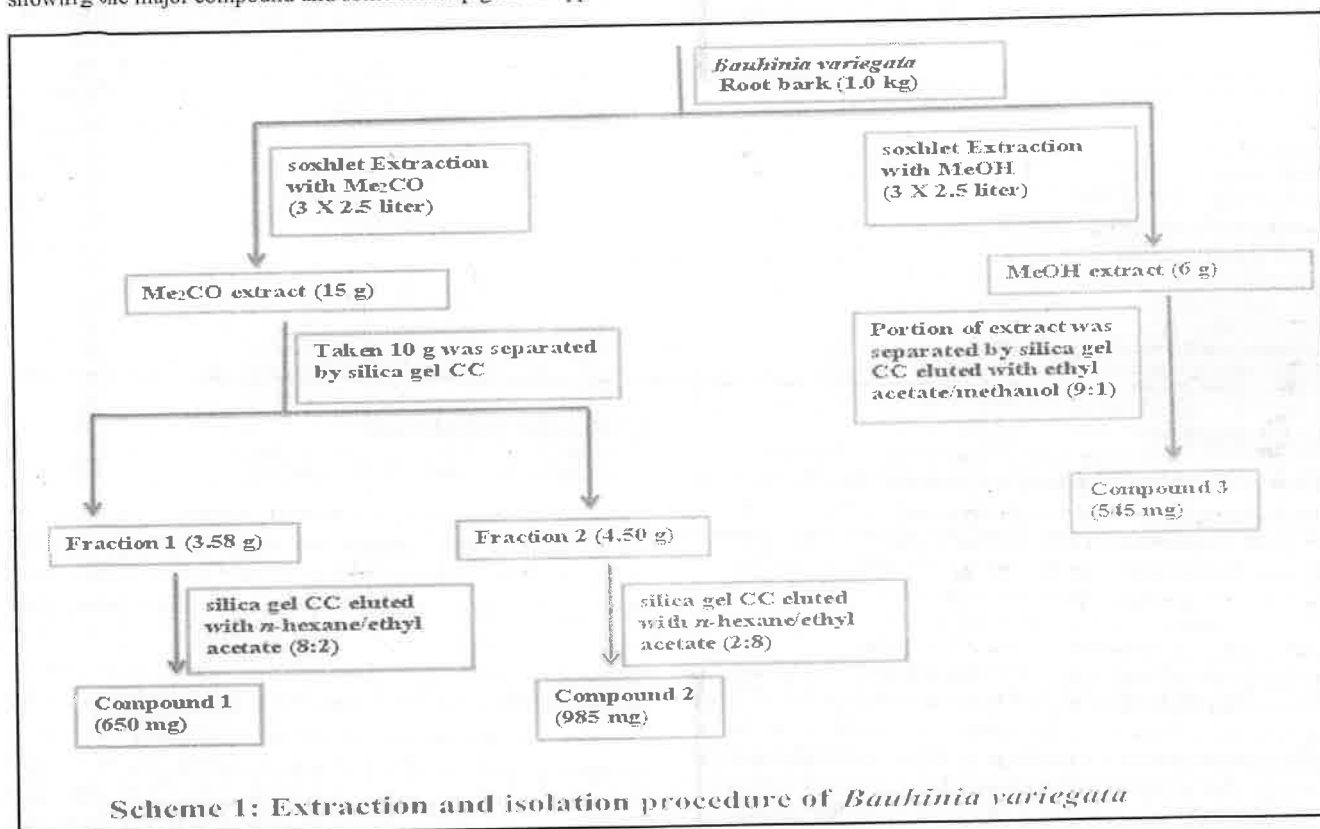
3. Results and Discussion

Compound 1 was obtained as yellow crystalline solid (650 mg) from acetone extract, mp 212-214°C. It gave a green color with alcoholic ferric chloride and an orange red color with magnesium-hydrochloric acid. It was yellow under UV and UV/NH$_3$. It was analyzed for C$_{16}$H$_{12}$O$_7$, which is consistent with the presence of [M+H]$^+$ ion at m/z 317.0480 and [M+Na]$^+$ ion at m/z 339.0309 in the positive ESITOFMS (Electrospray ionization time-of-flight mass spectrometry) spectrum and was corroborated by the presence of sixteen carbon signals in the ^{13}C NMR spectrum. The color reactions together with the UV absorption maxima at 256, 295 (sh), 371 nm suggested compound 1 to be a flavonol derivative (Mabry et al., 1970). UV spectral shifts in the presence of diagnostic reagents

indicated free hydroxyl groups at 3, 5, 3' and 4' positions. The IR spectrum showed two strong absorption bands at 3447 and 1654 cm^{-1} due to hydroxyl and chelated carbonyl functions, respectively.

The ^{1}H NMR spectrum of compound 1 showed a D$_2$O exchangeable downfield signal at δ 12.79 and was attributed to a chelated hydroxyl at C-5 position. It also exhibited signals for three additional phenolic hydroxyl groups at δ 9.40 (1H) and δ 8.20 (2H), and a methoxyl group at δ 3.85. Two *meta*-coupled doublets (J = 2.0 Hz) at δ 6.23 and 6.47, each integrating for one proton, were assigned to H-6 and H-8, respectively. The methoxyl group at δ 3.85 was placed at C-7 position in compound 1 did not show any bathochromic shift with sodium acetate in the UV spectrum. The three aromatic protons

of ring-B were shown up as typical ABX system at δ 7.69, 7.56 and 7.0 and were assigned to 2', 6' and 5' protons, respectively. Thus, the structure of compound 1 (Figure 1) was established as quercetin-7-O-methyl ether and reported first time from the root bark of *B. variegata* as its spectral data agreed well with literature values (Barbera *et al.*, 1986).
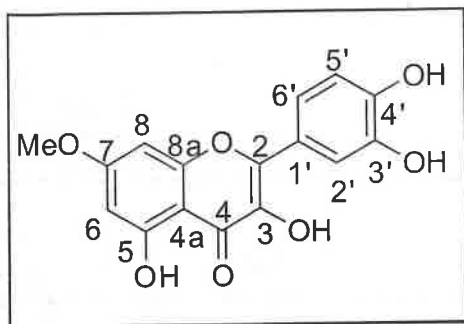

Figure 1: Quercetin-7-O-methyl ether (1).

Compound 2 was crystallized from methanol as yellow solid (985 mg), mp 140-142°C. It had $[\alpha]_D^{25}$-40.7° (c 0.1, MeOH). The $[M+H]^+$ and $[M+Na]^+$ peaks at m/z 477.1376 and 499.0950 in the positive ESITOFMS spectrum suggested the molecular formula $C_{23}H_{24}O_{11}$ for compound 2. This was corroborated by ^{13}C NMR spectrum which showed signals for all the twenty three carbons of the molecule. Positive Molisch's test, the UV absorption maxima in methanol at 266 and 345 nm, the color reactions and the chromatographic behavior suggested compound 2 to be a flavonol-O-glycoside (Mabry *et al.*, 1970).The addition of sodium methoxide and sodium acetate did not cause any shift in the UV absorption maxima, indicating the absence of free hydroxyl groups at C-4' and C-7 positions, respectively. A bathochromic shift of 55 nm in band I of the aluminium chloride and aluminium chloride-hydrochloric acid spectrum compared to methanol spectrum showed the presence of a free hydroxyl group at 5-position. The IR spectrum showed two strong absorption bands at 3400 and 1650 cm^{-1} due to hydroxyl and chelated carbonyl functions, respectively.

The ^1H NMR spectrum of compound 2 exhibited a D$_2$O exchangeable downfield signal at δ 12.55 and was ascribed to C-5 hydroxyl as it showed HMBC correlations with C-5 (δ160.9), C-6 (δ97.9) and C-4a (δ105.0). It also showed signals for two methoxyl groups at δ 3.84 and 3.85. Two *meta*-coupled doublets at δ 6.37 and 6.74 which correlated to carbons at δ 97.9 and 92.3, respectively in the HSQC spectrum, were assigned to C-6 and C-8 protons. The methoxyl group at δ 3.85 was placed at C-7, as these protons showed ^3J correlation with this carbon at δ 165.1 in its HMBC spectrum and showed two strong NOE correlations with H-6 (δ 6.37) and H-8 (δ 6.74) in the NOESY spectrum. The ^1H NMR spectrum of compound 2 also showed the presence of typical A$_2$B$_2$ doublets of ring-B at δ 8.15 (2H, J = 9.0 Hz) and 7.07 (2H, J = 9.0 Hz) and were assigned to H-2', 6' and H-3', 5', respectively. The methoxyl group at δ 3.84 was placed at C-4' as these protons showed HMBC correlation with this carbon at δ 161.3, and a strong NOE correlation with H-3' and 5' (δ 7.07). The chemical shift positions of all the protons and carbons were unambiguously assigned by HSQC (Table 1), HMBC (Table 2) and ^1H-^1H COSY (Table 3). An anomeric proton signal at δ 5.50 (d, J = 7.3 Hz) and a significant mass fragment at m/z 315.1 corresponding to [M+H-162]$^+$ in the ESI-MS/MS spectrum of [M+H]$^+$

ion at m/z 477.1 suggested the presence of a hexose sugar residue with β-configuration.

Acid hydrolysis of compound 2 with 2 N HCl afforded D-glucose and an aglycone identified as kaempferol-7, 4'-dimethyl ether (2a) (Figure 3): (Rossi *et al.*, 1997; Nawwar *et al.*, 1985) indicating that the glucosyl moiety in compound 2 was linked to C-3 position. The attachment of glucosyl residue at C-3 was also evidenced by the presence of a cross peak between H-1'' (δ 5.50) of glucosyl moiety and C-3 (δ133.7) in the HMBC spectrum.Thus, the structure of compound 2 was characterized as kaempferol-7, 4'-dimethyl ether 3-O-β-glycopyranoside and reported first time from the root bark of *B.variegata*.
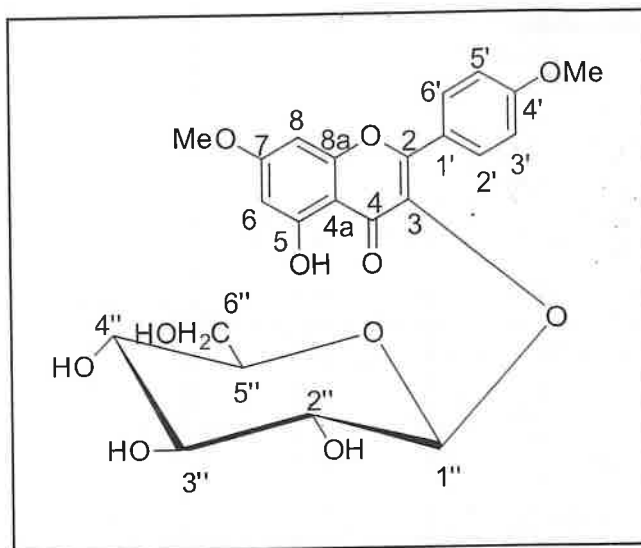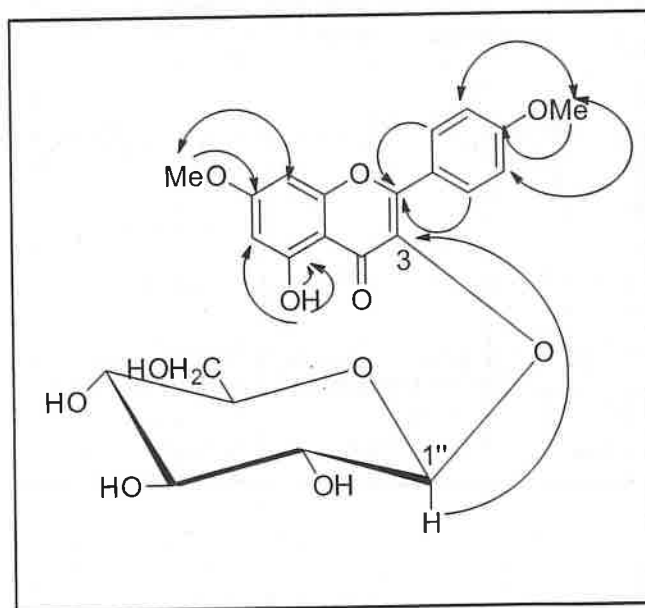

Figure 2(a): kaempferol-7, 4'-dimethyl ether .

Figure 2(b): Significant HMBC (→) and 3-O-β-D-glycopyranoside (2) NOESY (↔) correlations (2).
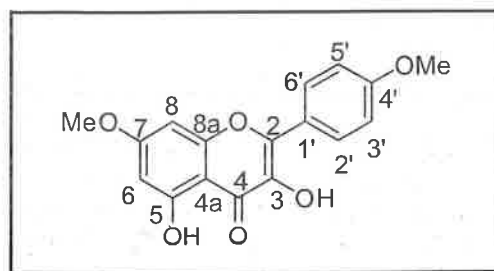
Figure 3: Kaempferol-7, 4' dimethyl ether (2a).

6.74 (H-8)	92.3	C-8
6.37 (H-6)	97.9	C-6
5.50 (H-1")	100.7	C-1"
3.85 (OMe-7)	56.1	OMe-7
3.84 (OMe-4')	55.4	OMe-4'
3.56 (H-6"a)	60.8	C-6"
3.32 (H-6"b)	60.8	C-6"
3.22 (H-5")	76.4	C-5"
3.18 (H-3")	75.5	C-3"
3.07 (H-4")	69.9	C-4"
3.06 (H-2")	74.2	C-2"

Table 2: HMBC ($^{2-3}J_{CH}$) correlations of compound 2

Proton	Chemical shift (δ)	Correlated carbon (s)
OH-5	12.55	C-4a, C-5, C-6
H-2' and 6'	8.15	C-2, C-1', C-4'
H-3' and 5'	7.07	C-1', C-4'
H-8	6.74	C-4a, C-6, C-7, C-8a
H-6	6.37	C-4a, C-5, C-7, C-8
H-1"	5.50	C-3
OMe-7	3.85	OMe-7
OMe-4'	3.84	OMe-4'

Table 3: ^{1}H-^{1}H COSY data of compound 2

Chemical shift of coupled protons (δ)	Type of coupling	Assignment
8.15 and 7.07	*ortho*	H-2' and H-3'
8.15 and 7.07	*ortho*	H-6' and H-5'
6.74 and 6.37	*meta*	H-8 and H-6
5.50 and 3.06	*vicinal*	H-1" and H-2"
3.18 and		

Compound 3 was isolated as yellow needles (545 mg) from methanol, mp 177-178°C. It gave a positive Molisch's test, greenish brown color with alcoholic ferric chloride and an orange color with magnesium-hydrochloric acid. It was purple under UV and yellow under UV/NH₃. The color reactions, positive Molisch's test and UV absorption maxima at 267 and 350 nm suggested the compound to be a flavonol glycoside (Mabry *et al.*, 1970). The IR spectrum showed two strong absorption bands at 3420 and 1657 cm⁻¹ due to hydroxyl and carbonyl functions. Acid hydrolysis of compound 3 yielded an aglycone characterized as kaempferol (3a) and a sugar identified as D-glucose. The purple fluorescence of the glycoside compared to yellow of its aglycone under UV suggested that site of glycosylation at 3-OH, which was supported by a hypsochromic shift of 10 nm in band I of the glycoside compared to its free aglycone (Mabry *et al.*, 1970) in methanol. UV spectral data with diagnostic shift reagents revealed the presence of free hydrolysis at 5,7 and 4'-positions, and blocked hydroxyl at 3-position. From the foregoing observations coupled with the identification of the aglycone as kaempferol (3a). Compound 3 could be assigned the structure kaempferol 3-O-β-glucoside (Figure 4). Conformation of the structure kaempferol 3-O-β-glucoside was provided by the ^{1}H NMR spectral data which showed the presence of four aromatic protons of ring B as typical A₂B₂ doublets at δ 8.03 (2H, *J* = 8.9 Hz, H-2', 6') and 6.87 (2H, *J* = 8.9 Hz, H-3', 5'). A pair of *meta*-coupled doublets at δ 6.19 and 6.42 was ascribed to H-6 and H-8, respectively. An anomeric proton doublet at δ 5.45 with a coupling constant of 7.3 Hz was ascribed to H-1" of the α-glucosyl residue. A complex multiplet over the range δ 2.90-3.57 integrating for 6 protons were assigned to the remaining ix protons of the glucosyl residue.

Upon comparison of ^{13}C NMR spectrum of Compound 3 with its aglycone, kaempferol (3a) (Figure 4a) (Agarwal *et al.*, 1989) (Table 4), it was observed that the C-3 signal of Compound 3 showed an up fieldshift of δ 2.4, and the C-2 and C-4 signals showed downfield shifts of δ 6.4 and 1.6, respectively from that of kaemperol showing the location of the glucose residue at C-3 position (Agarwal *et al.*, 1989; Markham *et al.*, 1978). Finally compound 3 was characterized as kaempferol 3-O-β-D-glucopyranoside. Final confirmation of compound 3 as kaempferol 3-O-β-D-glucopyranoside was by direct comparison with an authentic sample isolated previously from *Tephrosia calophylla* (Kishore *et al.*, 2003).
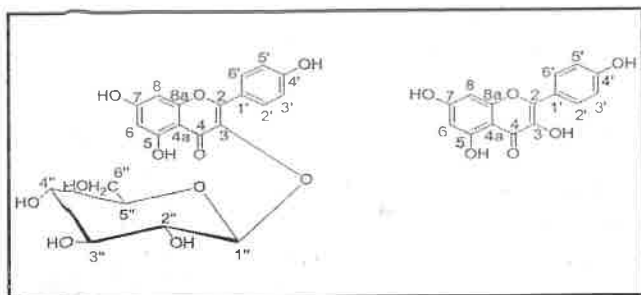
Figure 4: kaempferol-3-O-β-D-glucopyranoside (3).

Table 4: Comparison of ¹³CNMR data in (δ) of compound 3 with its aglycone, kaempferol (3a)

Carbon	Compound 3	Kaempferol (3a)
2	156.2	146.8
3	133.2	135.6
4	177.5	175.9
4a	104.0	103.9
5	161.2	160.7
6	98.7	98.2
7	164.3	163.9
8	93.7	93.5
8a	156.4	156.2
1'	120.9	121.7
2'	130.9	129.5
3'	115.1	115.4
4'	160.0	159.2
5'	115.1	115.4
6'	130.9	129.5
1"	100.9	-
2"	74.2	-
3"	77.5	-
4"	69.9	-
5"	76.4	-
6"	60.9	-

3.1 Quercetin-7-O-methyl ether (1)

Isolated as yellow crystals (650 mg) from acetone, mp 212-214°C; [M + H]⁺ 317.0480 ($C_{16}H_{12}O_7$+H requires 317.0660). UV: λmax (MeOH) (log ε) 256 (4.05), 295 (sh), 371 nm; +NaOMe: 260, 432 nm; +NaOAc: 262, 372 nm; +NaOAc/H_3BO_3:260, 389 nm; +AlCl₃: 273, 451 nm; +AlCl₃/HCl: 268, 423 nm. IR: ν max (KBr) 3447 (-OH), (s), 2910 (OMe) (s), 1654 (>C=O), 1480, 1400, 1210, 1025, 750, 700 cm⁻¹.¹H NMR (400 MHz, Me₂CO-d_6): δ 12.79 (1H, s, OH-5), 9.40 (1H, s, OH-3), 8.20 (2H, s, OH-3', 4'), 7.69 (1H, d, J = 2.1 Hz, H-2'), 7.56 (1H, dd, J = 8.1, 2.1 Hz, H-6'), 6.47 (1H, s, d, J = 2.0 Hz, H-8), 6.23 (1H, s, d, J = 2.0 Hz, H-6), 3.85 (3H, s,

OMe-7).¹³C NMR (75 MHz, Me₂CO-d_6): δ 179.4 (C-4), 164.8 (C-7), 163.1 (C-5), 157.7 (C-8a), 156.6 (C-2), 149.0 (C-3'), 145.8 (C-4'), 139.2 (C-3), 122.9 (C-1'), 122.0 (C-6'), 116.2 (C-5'), 115.9 (C-2'), 105.8 (C-4a), 99.3 (C-6), 94.3 (C-8), 56.6 (OMe-7). ESITOFMS: (positive mode) m/z (rel. int. %) 655.0787 [2M+Na]⁺ (43), 633..995 [2M+H]⁺ (3), 339.0309 [M+Na]⁺ (96), 317.0480 [M+H]⁺ (100) ($C_{16}H_{12}O_7$+H requires 317.0660).ESI-MS/MS: (positive mode) m/z (rel. int. %) 317.0 [M+H]⁺ (56), 302.0 [M+H-CH₃]⁺ (70), 301.0 [M+H-CH₃-H]⁺ (100), 285.0 [M+H-CH₃OH]⁺ (11), 274.0 [M+H-CH₃-CO]⁺ (21), 257.0 [M+H-CH₃OH-CO]⁺ (9), 256.0 [M+H-CH₃-CO-H₂O]⁺ (3), 245.0 [M+H-2CO-H]⁺ (13), 229.0 [M+H-CH₃OH-2CO]⁺ (10), 167.0 (¹,³A⁻) (1), 137.0 (¹,³A⁺-OCH₃+H)(Ma et al., 1997)or (⁰,²B⁺) (2).

3.2 Kaempferol-7, 4'-dimethyl ether 3-O-β-D-glycopyranoside (2)

Compound 2was isolated and crystallized from methanol as yellow crystalline solid (985 mg), mp 140-142°C. It had [λ]$_D^{25}$-40.7° (c 0.1, MeOH); [M+H]⁺ 477.1019 ($C_{23}H_{24}O_{11}$+H 477.1396).UV: λ max (MeOH) (log ε) 266 (4.28), 345 (4.20) nm; +NaOMe: 267, 354 nm;+NaOAc: 268, 343 nm; +AlCl₃: 270, 400 nm. IR: ν max (KBr) 3400 (-OH) (s), 2840 (OMe) (s), 1650 (>C=O) (s), 1600, 1580, 1500, 1450, 1220, 1200, 1150, 1110 cm⁻¹.¹H NMR (400 MHz, DMSO-d_6): δ 12.55 (1H, s, 5-OH), 8.15 (2H, d, J = 9.0 Hz, H-2', 6'), 7.07 (2H, d, J = 9.0 Hz, H-3', 5'), 6.74 (1H, d, J = 2.1 Hz, H-8), 6.37 (1H, d, J = 2.1 Hz, H-6), 5.50 (1H, d, J = 7.3 Hz, H-1"), 3.85 (3H, s, OMe-7), 3.84 (3H, s, OMe-4'), 3.56 (1H, br d, J = 12.0 Hz, H-6"a), 3.32 (1H, br d, J = 12.0 Hz, H-6"b), 3.22 (1H, ddd, J = 9.0, 9.0, 9.0 Hz, H-5"), 3.18 (1H, dd, J = 9.0, 9.0, H-3"), 3.07 (1H, dd, J = 9.0, 9.0 Hz, H-4"), 3.06 (1H, dd, J = 9.0, 9.0 Hz, H-2").¹³C NMR (75 MHz, DMSO-d_6): δ 177.6 (C-4), 165.1 (C-7), 161.3 (C-4'), 160.9 (C-5), 156.3 (C-2), 156.1 (C-8a), 133.7 (C-3), 130.8 (C-2', 6'), 122.4 (C-1'), 113.7 (C-3', 5'), 105.0 (C-4a), 100.7 (C-1"), 97.9 (C-6), 92.3 (C-8), 76.4 (C-5"), 75.5 (C-3"), 74.2 (C-2"), 69.9 (C-4"), 60.8 (C-6"), 56.1 (OMe-7), 55.4 (OMe-4').ESITOFMS: (positive mode) m/z (rel. int. %) 975.1946 [2M+Na]⁺ (27), 499.0950 [M+Na]⁺ (33), 477.1376 [M+H]⁺ (100) ($C_{23}H_{24}O_{11}$+H requires 477.1396). ESI-MS/MS: (positive mode) m/z (rel. int. %) 477.1 [M+H]⁺ (3), 315.1 [M+H-162]⁺ (98), 300.1 [M+H-162-Me]⁺ (56), 273.1 [M+H-162-C₂H₂O]⁺ (18), 272.1 [M+H-162-Me-CO]⁺ (100), 244.1 [M+H-162-Me-2CO]⁺ (70), 229.0 [M+H-162-2Me-2CO]⁺ (33).

3.2.1 Acid hydrolysis of kaempferol-7, 4'-dimethyl ether 3-O-β-D-glycopyranoside (2)

A solution of compound 2 (10 mg) in 4 ml of 2N HCl in MeOH (1:1) was heated under reflux for 2h on a water bath, cooled and MeOH distilled off. The yellow precipitate separated was filtered and recrystallized from MeOH to give yellow needles (4 mg) mp 204-206°C. UV: λ max (MeOH) (log) 268 (4.10), 340 (3.80) nm; +NaOMe: 268, 341 nm; +NaOAc: 270, 342 nm; +AlCl₃: 270, 395 nm; +AlCl₃/HCl: 270, 395 nm. IR: ν max (KBr) 3390 (-OH), 2950 (-OMe), 1654 (>C=O), 1594, 1500, 1245, 1190, 950, 820, 795 cm⁻¹.¹H NMR (200 MHz, CDCl₃): δ 11.35 (1H, s, OH-5),9.40 (1H, s, OH-3), 8.05 (2H, d, J = 8.0 Hz, H-2', 6'), 7.01 (2H, d, J = 8.0 Hz, H-3', 5'), 6.42 (1H, d, J = 2.0 Hz, H-8), 6.25 (1H, d, J = 2.0 Hz, H-6), 3.85 (6H, s, OMe-7, 4').Finally the aglycone was characterized as kaempferol 7,4'-dimethy ether (2a) as its spectral data well agreed with literature data(Rossi et al., 1997 and Nawwar et al., 1985).

3.3 Kaempferol 3-*O*-β-D-glucopyranoside (3)

Isolated and crystallized from MeOH as yellow needles (545 mg), mp 177-178°C (found: C: 56.21, H: 4.50 $C_{21}H_{20}O_{11}$ requires C: 56.25, H: 4.46). UV: λ max (MeOH) (log ε) 267, 350 nm; +NaOMe: 275, 325, 402 nm; +NaOAc: 275, 312 (sh), 284 nm; +NaOAc/ H_3BO_3: 265, 357 nm; +AlCl$_3$: 275, 306, 350, 398 nm; +AlCl$_3$/HCl: 278, 304, 358, 398 nm. IR: ν max (KBr) 3420 (br) (-OH), 2924, 1657 (>C=O), 1609, 1507, 1361, 1289, 1205, 1180, 1061, 1013, 968, 732 cm^{-1}.^{1}H NMR (300 MHz, DMSO-d_6): δ 12.60 (1H, s, OH-5), 10.40 (2H, br s, OH-7, 4'), 8.03 (2H, d, J = 8.9 Hz, H-2', 6'), 6.87 (2H, d, J = 8.9 Hz, H-3', 5'),6.42 (1H, d, J = 2.0 Hz, H-8), 6.19 (1H, d, J = 2.0 Hz, H-6), 5.45 (1H, d, J = 7.3 Hz, H-1"), 2.90-3.57 (6H, m, H-2", 3", 4", 5", CH$_2$-6").^{13}C NMR (75 MHz, DMSO-d_6): δ177.5 (C-4), 164.3 (C-7), 161.2 (C-5), 160.0 (C-4'), 156.4 (C-8a), 156.2 (C-2), 133.2 (C-3), 130.9 (C-2', 6'), 120.9 (C-1'), 115.1 (C-3', 5'), 104.0 (C-4a), 100.9 (C-1"), 98.7 (C-6), 93.7 (C-8), 77.5 (C-3"), 76.4 (C-5"), 74.2 (C-2"), 69.9 (C-4"), 60.9 (C-6"). CIMS (Positive ion mode, CH4) *m/z* (rel. int. %): 449 [M+H]$^+$(16), 287 [M+H-162]$^+$ (100), 180 (54), 162 (9), 145 (4), 121 (2). EIMS (70 eV, DI) *m/z* (rel. int. %): 286 [M-glucosyl]$^+$(100).

3.3.1 Acid hydrolysis of kaempferol 3-*O*-β-D-glucopyranoside (3)

Acid hydrolysis of compound 3(10 mg) with 2N HCl in MeOH (1:1) (13 ml) as described under compound 3gave a solid which on crystallization from MeOH afforded yellow needles (4 mg), mp 274-75°C. It gave a green color with alcoholic Fe^{+3}, pink with Mg-HCl and yellow with Na$_2$CO$_3$ and NaOH. It was yellow under UV and UV/NH$_3$. UV: λ max (MeOH) (log ε) 262, 325 (sh), 364 nm; +NaOMe: 255 (sh), 275, 315 nm; +NaOAc: 274, 301 nm; +AlCl$_3$: 272, 305, 350, 426 nm; +AlCl$_3$/HCl: 272, 305 (sh), 348, 422 nm. IR: ν max (KBr) 3323 (s) (-OH), 1660 (>C=O), 1615, 1520, 1246, 1215, 1093, 1024, 823 cm^{-1}.^{1}H NMR (300 MHz, Me$_2$CO-d_6): δ 12.15 (2H, s, OH-5, OH-3), 9.70 (1H, br s, OH-7), 9.10 70 (1H, br s, OH-4'), 8.14 (2H, d, J = 9.0 Hz, H-2', 6'), 7.0 (2H, d, J = 9.0 Hz, H-3', 5'), 6.52 (1H, d, J = 2.1 Hz, H-8), 6.26 (1H, d, J = 2.1 Hz, H-6).^{13}C NMR (75 MHz, DMSO-d_6): See Table 4:EIMS (70 eV, DI) *m/z* (rel. int. %): 286 [M]$^+$, 285 [M-1]$^-$ (13), 257 [M-29]$^+$ (5), 153 [A$_1$+H]$^+$ (11), 149 (77), 43 (100). Finally the aglycone3awas characterized as kaempferol.

4. Conclusion

Quercetin 7-O-methyl ether (1), kaempferol-7, 4'-dimethyl ether 3-O-β-D-glucopyranoside (2) and kaempferol 3-O-β-glucopyrano-side (3) flavonoids were isolated from the root bark of *B. variegata*, and the structures of all known compounds were mainly established by extensive spectroscopic analysis, including 1D (^{1}H &^{13}C NMR), 2D NMR (HMBC, HSQC & NOESY) and chemical studies. In the chemical analysis, compounds 2 and 3 were hydrolysis under acidic conditions to obtain their aglycones and these were identified as kaempferol-7, 4'-dimethyl ether (4) and kaempferol (5), respectively and these compounds were characterized by ESITOFMS spectroscopy.

References

Agarwal, P.K. (1989). Carbon-13 NMR of flavonoids, Elsevier, Amsterdam. pp:152.

Agarwal, P.K. (1989). Carbon-13 NMR of flavonoids, Elsevier, Amsterdam. pp:292.

Barbera, O.; Sanz, J.F.; Parareda, J.S. and Macro, J.A. (1986). Phytochemistry, further flavonol glycosides from *Anthyllisono brychiodes*, 25: 2361-2365.

Gamble, J.S.(1956). Flora of the Presidency of Madras, Vol. II: pp: 47, BSI, Calcutta.

Gupta, A.K. and Chauhan, J.S. (1984). Constituents from the stem of *Bauhinia variegate*. Natl. Acad. Sci. Lett. (India), 7:15-16.

Gupta, A.K.; Vidhyapati, T.J. and Chauhan, J.S. (1979).5, 7- Dihydroxy flavanone-4-O-Z-L-rhamnopyranosyl-e-D-glucopyranoside from *Bauhinia variegata*. Indian J. Chem., 18B:85-86.

Gupta, A.K.; Vidhyapati, T.J. and Chauhan, J.S. (1980).Chemical examination of the stem of *Bauhinia variegata*.Planta Med., 38:174-176.

Hari Kishore, P.; Reddy, M.V.B.; Gunasekar, D.; Murthy, M.M.; Caux, C. and Bodo, B. (2003).A new coumestan from Tephrosiacalophylla. Chem. Pharm. Bull. 51:194-196.

Mabry, T.J.; Markham, K.R. and Thomas, M.B. (1970). The systematic identification of flavonoids, Springer-Verlag, New York, pp:41.

Mabry, T.J.; Markham, K.R. and Thomas, M.B. (1970). The systematic identification of flavonoids, Springer-Verlag, New York, pp:41& 44.

Markham, K.R.; Turner, B.; Stanley, H.; Geiger, T.J. and Mabry, T.J. (1978).Carbon-13 NMR studies of flavonoids-III, naturally are occurring flavonoid glycosides and their acylated derivatives. Tetrahedron, 34:1389-1397.

Ma, Y.L.; Li, Q.M.; VandenHeuvel, H. and Claeys, M. (1997).Characterization of flavone and flavonolaglycones by collision-induced dissociation tandem mass spectrometry. Rapid.Commun. Mass. Spectrom. 11: 1357-1364.

Nawwar, M.A.M.; Souleman, M.A.; Buddrus, J. and Linscheid, M. (1985). Flavonoids of the flowers of *Tamarix nilotica*. Phytochemistry, 23:2347-2349.

Punit, R.; Bhatt, Urvesh, D.; Patel, C.; Modi, M.; Kajal, B.; Pandya and Harshad B. (2019). Thin-layer chromatography and *in vitro* free radical scavenging activity of few medicinal plants from the surroundings of Junagadh, Gujarat, India. Ann. Phytomed., 8(1):45-55.

Rahman, W. and Begum, S.J. (1985). Flower pigments: Flavonoids from the white flowers of *Bauhinia variegata* Linn. Naturwissenschaften, 53:385-387.

Reddy, M.V.B.; Reddy, M.K.; Gunasekar, D.; Caux, C. and Bodo, B. (2003).A flavanone and a dihydrodibenzoxepin from *Bauhinia variegate.* Phytochemistry, 64(4):879-882.

Rossi, M.H.; Yoshida, M. and Maia, J.G.S. (1997).Neolignans, styrylpyrones and flavonoids from an *Aniba* species. Phytochemistry, 45:1263-1269.

Tammanna, K.; Narayana Rao, K. and Madhava Chetty, K. (2000). "Angios permic Wealth of Tirumala", TTD press; Tirupati, pp:27.

Wahab, S.M.A.E.; Wassel, G.M.; Ammar, N.M. and Hanna, T.(1987). Flavonoid constituents in the different organs of selected *Bauhinia* species and their effect on blood glucose.Herba. Hung., 26(1):27-28.

Yadava, R.N. and Reddy, V.M.S. (2001). A New Flavone Glycoside, 5-Hydroxy 7,32 ,42 ,52 -Tetra-Methoxyflavone 5-O-á-D-Xylopyranosyl-(1'!2)-á-L-Rhamnopyranoside from *Bauhinia Variegata* Linn. J. Asian Nat. Prod. Res., 3:341-346.

A Study on Inside Views of Cloud Computing Tools

[1]Dr. A. Ramaswami Reddy, Professor, Department of CSE, Malla Reddy Engineering College(Autonomous), Secunderabad, Telangana, India-500100

[2]Dr. Arun Kumar Kandru, Associate Professor, Department of CSE ,Malla Reddy Engineering College(Autonomous), Secunderabad, Telangana, India-500100

[3]Dr. Vasavi Bande, Associate Professor, Department of CSE-AIML, Siddhartha Institute of Engineering and Technology, Ibrahimpatnam, Hyderabad, Telangana, India-501506

Email: [1]ramaswamyreddymail@gmail.com, [2]kandruarun002@gmail.com, [3]Vasavi.bande@gmail.com

ABSTRACT

Distributed computing instruments can be isolated into different classifications as demonstrated by their features. Around here, we have made a broad examination with different classes based on the accompanying boundaries like expanding, connection and characterization. In this study, we compare and evaluate many notable open-source Cloud devices for greater efficiency. Particularly helpful would be the development of new calculations for all customers related with the various cycles and its design, which would allow for the improvement of codes in the finer details. Different test frameworks, such as the five open-source Cloud registration apparatuses (CloudSim, Cloud Analyst, Cloud Reports, , iCanCloud, EMUSIM, GroudSim, DCSim and Green Cloud), have different engineering configurations, showing components, reproduction processes, execution measures, and degrees of adaptability. The commercial vendors of these products often advertise them as having standard characteristics, notably with regards to layout, diagrams of components, and the method of multiplication. Some of the key characteristics that may be utilised to zero in on the benefits of these tools include a laser-like focus on a variety of layers and the ability to make accurate predictions about how well they will perform. A few gaming tools have been developed with distributed computing in mind. Simulation develops a virtual environment for testing and validating research trials in quest of effective and superior application-specific solutions. Making a model or real-time system is a scientific approach. As a result, it removes the requirement for and cost of computational facilities for performance assessment and modelling of the research solution. The Cloud Sim simulation is the primary emphasis of this guidebook instrument and its advantages for researchers.

Keywords: CloudAnalyst, CloudReports, CloudExp, GreenCloud, and iCanCloud, CloudSim.

1 INTRODUCTION

Because of its amazing advantages, distributed computing is firmly establishing itself. Expert companies providing distributed computing should regularly evaluate their services. Continuous and certifiable assessment can end up being expensive and unreasonable, so re-enactment offers a path of least resistance. In this piece, we take a look at the various distributed computing testing frameworks available as open source software.

The current value of the Indian server ranch reallocating market is estimated at near to $2billion, and by the end of the fiscal year 2023-24 [1], it is expected to have reached $5 billion, representing a CAGR of 25%. This is why the freshly termed "Cloud Computing strategy" is so important. There are several free and open-source Cloud Processing tools available now, such as CloudSim, Cloud Analyst, Cloud Reports, Cloudsched, and Green Cloud. Our investigation seeks to thoroughly examine the construction plan of every device, stage, programming model, accessibility, realistic support, genuine model, energy usage, reenactment time, memory space needed, etc. Comprehensive, real-world study on all fronts is certainly challenging since it necessitates writers to think about the global organised system as a whole,

which may be beyond their control. It is also impossible to predict or regulate the states of a framework. It's frustrating to try and evaluate consistently how well Cloud provisioning calculations and outstanding major task models are implemented. With this in mind, Cloud-based testing frameworks are designed to spot and use cutting-edge, enterprise-grade Cloud management tools. Here, we showcase five tools for simulating Cloud processing that are available under open source licences.

One of the most recent developments in data innovation is the advent of endlessly dispersed computing. End users are offered access to the company's IT infrastructure and applications as a service, with the accompanying typical cost-based payment model. Recent developments in fields like as virtualization, network processing, Web registration, utility figuring, and related advancements have contributed to distributed computing's rapid spread. Distributed computing via the Internet is useful if you require low-cost access to high-performance computing (HPC) and storage infrastructure. A portion of the vital qualities of distributed computing are: on-request access, flexibility, cost-viability, versatility, insignificant framework the board and area freedom. Trillions of dollars are being put resources into distributed computing today.

Real cloud infrastructure that allows for continuous testing and execution of new computations and strategies is inconceivable for frameworks chiefs, cloud subject matter experts, and even specialists. First-measure execution is crucial before continuous execution, and all potential security risks should be carefully considered. Reenacting and displaying technological advances is the saviour of these problems. The requirement for a distributed computing test system emerges to observe an execution situation progressively. When it comes to optimising the underlying infrastructure, executing new algorithms, detecting security issues, and measuring the system's overall quality and performance, testing environments on the cloud play a significant role.

It is important for researchers, framework administrators, cloud specialists, and board chairs to be able to accurately predict how distributed systems will perform, hence a number of test systems are being developed to aid with this. Finding the appropriate tool for the job at hand or learning about the features available on various gadgets may be a time-consuming and confusing process.

Some of the testing platforms are commercial, while others are open source and free to use. The trend is to explicitly deal with these test systems for a broad variety of complex and actual difficulties of distributed computing, since free and open source test systems foster in-depth learning and trial-and-error.

The critical benefits of utilizing a reenactment based structure in distributed computing are recorded underneath:

Test systems work with dynamic and adaptable arrangement and improvement conditions. They empower specialists cum framework overseers to learn and make the continuous cloud climate more adaptable and solid.

Test systems give simple to-utilize order/graphical points of interaction with loads of customisation choices that assist specialists with envisioning genuine situations, in this way keeping away from a wide range of ongoing issues.

Test systems are the most practical answer for true execution, as they are first planned, then grew, appropriately tried and whenever required, even overhauled, reconstructed and retested. Doing this in reality is very difficult regarding cost and time.

Through the use of test equipment, specialists may create their own display, security, and other provisioning calculations to replicate cloud settings.

This article provides an overview of some of the most useful open-source and free distributed computing testing frameworks currently available.

Our first efforts have focused on reducing response times [2], [4] on the Cloud in order to better serve the customer. The multiple quality limits of Cloud climate have also been studied, and their implementation is discussed in [3]. Next, we used Cloud Reports [5] [7] to analyse a number of different power models that save energy, and we used Green Cloud to study a number of different job schedulers that conserve energy. [6]. However, we have also invested much in the development of the Edge Cloud system [8]. Gridsim, developed by the authors in [9], is a Grid processing device

primarily used for solving asset distribution challenges on the Grid. As shown in [10], developers have amassed a Cloudsim toolkit for doing Cloud-based asset provisioning calculations. Cloud Analyst was created by the author in [11] as a tool for use in a Distributed Computing Environment on a grand scale. Cloud Reports, developed by Thaigo Teixeira Sa et al. in [12], is a graphical user interface (GUI) based recreation tool designed to keep Cloud environments low-energy. FlexCloud is a system developed by Minxian Xu et al. [13].

2. ARCHITECTURE OF VARIOUS CLOUD SIMULATION TOOLS

2.1 Cloud Analyst

The GUI-based testing platform CloudAnalyst, acquired from CloudSim, has certain extended features and capabilities. At the University of Melbourne, Australia's Department of Computer Science and Software Engineering's CLOUDS Laboratory, Bhathiya Wickremasinghe and Rajkumar Buyya proposed CloudAnalyst. [18][15][11]. The test bed's setup lets us gauge the effectiveness of different server farms and user bases around the world. The modeller may generate circle-by-circle replicas and guide a series of reenactments with little modifications to the boundaries, which can be utilised to determine the behaviour of large-scale Internet applications housed in the cloud.

When it comes to providing always-on server farms, CloudAnalyst is a sophisticated replication framework for keeping tabs on load balancing, cloud group monitoring, and the consistent outflow of data. Users may now save their game configurations in XML files and export their live results to PDF format.

See below for a rundown of CloudAnalyst's best features.

Simple graphical user interface for configuring and reviewing the outcomes of various distributed computing experiments.

Reproduction definition through a serious level of setup and adaptability: CloudAnalyst is furnished with modelers that have a serious level of command over the examination by demonstrating elements, for example, server farms, virtual machines, memory, stockpiling and data transfer capacity.

Explore circling: CloudAnalyst can save recreation situations and circle them over and over by means of reenactment varieties. Both XML and PDF versions of the results may be stored.

In addition to a wealth of information, CloudAnalyst generates visual output like tables and graphs to show what went into the reproduction process.
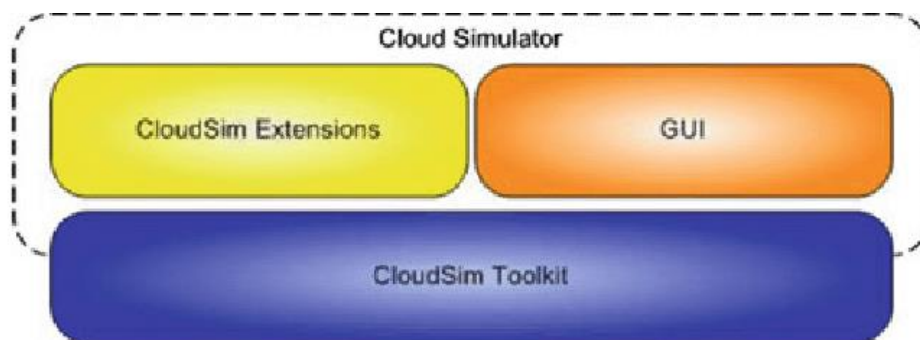

Figure 1. Architecture of Cloud Analyst Simulator

2.2 GreenCloud

GreenCloud gives a recreation climate to energy-mindful distributed computing server farms. For energy-efficient distributed computing server farms with an emphasis on cloud connections, this is the most advanced parcel-level test system currently available. It provides a detailed breakdown of how much power is used by the servers, switches, and other electronics in a data centre.

University of Luxembourg scholar Dzmitry Kliazovich (Project Leader) and his colleagues created the GreenCloud assessment platform. This pilot programme is used to cultivate cutting-edge arrangements in areas such as accounting, asset allocation, responsibility booking, and even communication norms, product development, and organisational underpinnings.

To further develop the NS-2 parcel level organisation test system, GreenCloud was developed. It classifies energy use into three distinct types: those associated with data registration and transmission, data communication, and the physical infrastructure of a server farm. The most recent variant of GreenCloud is 2.1.2.

Many of the supplementary recreation scripts are invoked by the GreenCloud test system.

setup_params.tcl: Comprises the whole configuration of the server, including switches, commitments, checks, and motion.

toplogy.tcl: Produces the topology for a data center's server farm.

dc.tcl: Produces physical and virtual machines for a data center's server farm.

user.tcl: Sets the standards for how cloud users should behave.

record.tcl: Methods for notifying outcomes during execution are set up.

finish.tcl: Measures the reenactment and presents the results.

Here are the parts of the GreenCloud testing system:

The test system primarily centers around the cloud organization and, especially, energy utilization observing in distributed computing advances.

It upholds reproduction of CPU, memory, stockpiling and systems administration assets.

Upholds analysts in investigating techniques to limit power utilization by further developing power the board, as well as progressively overseeing and designing the power-mindful capacity of the framework's gadgets.
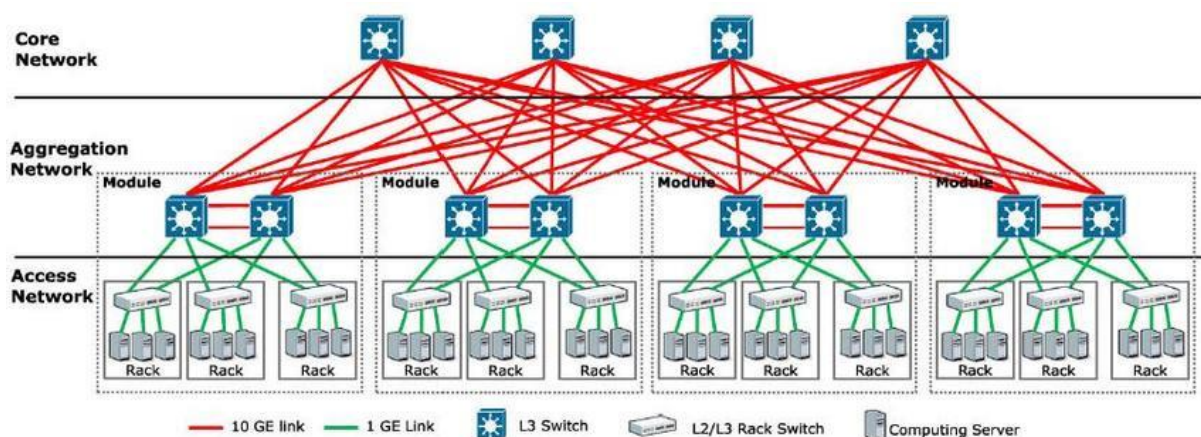
Has an easy to use GUI and is open source.

Figure 2. Architecture of GreenCloud Simulator (3Tier)

2.3 iCanCloud

Based on SIMCAN, iCanCloud is a distributed computing emulation platform that helps you play out scenarios involving massive storage facilities. Predicting the trade-offs between cost and execution of a certain arrangement of uses performed in unambiguous equipment is the goal of this study. A. Nunez and J.L. Vazquez-Poletti developed the

iCanCloud reproduction structure. After that, the beta system will provide customers with information on those costs. Originally developed to enhance cloud services' flexibility, accuracy, execution, and diversity, iCanCloud is now a formidable test system for designing, implementing, and analysing a broad variety of cloud architectures.

The iCanCloud infrastructure is currently being built using the OMNeT++ platform. The newest release, 1.0, calls for OMNeT++ 4.6 and INET 2.5. It's possible to implement it on all flavours of Ubuntu and MAC OS.

Below is a list of iCanCloud's features:

Proof-of-concept and replication are possible for both proven and theoretical distributed computing architectures.

With an adjustable cloud hypervisor module, it's easy to try out new cloud facilitation methods while still using the ones you know and love.

Virtual machines that may be modified are useful for quickly simulating both single- and multi-center architectures.

iCanCloud gives many setups for capacity frameworks, which incorporate models for neighborhood capacity frameworks, distant capacity frameworks like NFS, and equal capacity frameworks (like equal document frameworks and RAID frameworks).

iCanCloud gives an easy to use GUI that makes it more straightforward to create and tweak enormous disseminated models. This graphical user interface (GUI) is helpful for managing a stockpile of preconfigured virtual machines (VMs), a granary of predetermined examinations, and a stockpile of preset cloud frameworks to start tests straight from the GUI and create visible results.

For presenting and simulating applications, iCanCloud provides a POSIX-based API and a take on the MPI library. Additionally, iCanCloud supports many approaches to showing apps, including creating new applications directly in the reproduction stage, using indications of real applications, and using a status chart.

In order to increase iCanCloud's utility, new components may be uploaded to the archive.
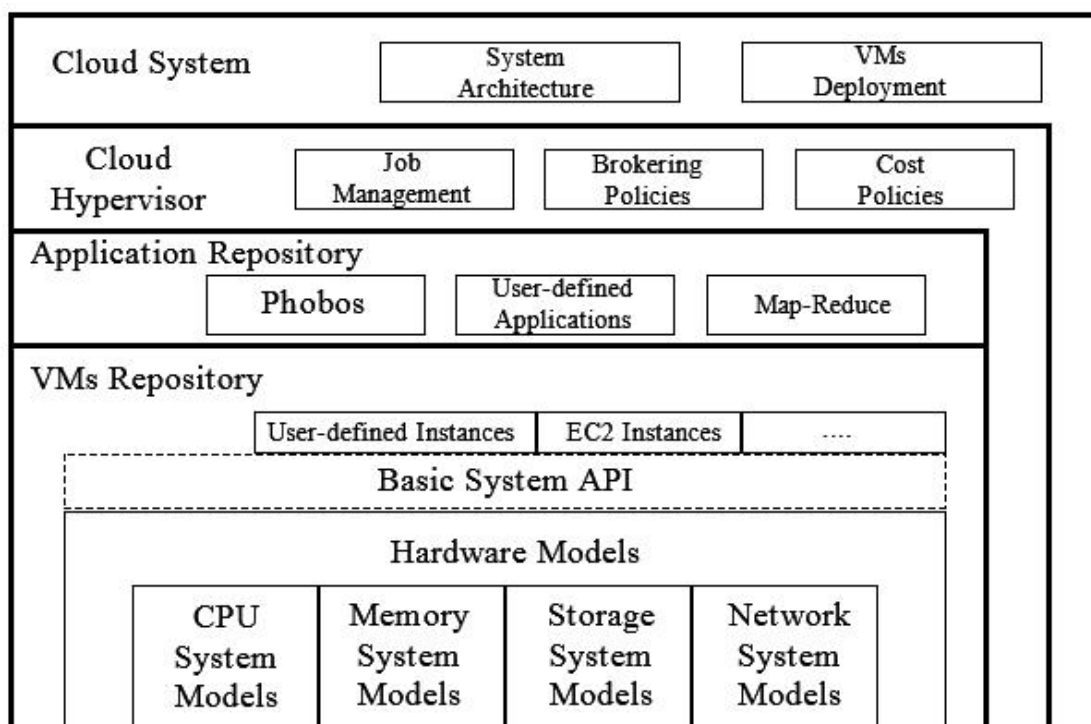

Figure 3. iCanCloud Architecture

2.4 EMUSIM

The abbreviation EMUSIM refers to the practise of merging actual hardware with virtual environments for educational purposes. It combines copying (AEF-Automated Emulation Framework) and simulation to allow more realistic models of programming artefacts to be employed during reproductions (CloudSim). The Cloud Computing and Distributed Systems (CLOUDS) Laboratory at the University of Melbourne's Department of Computing and Information Systems is responsible for the creation of EMUSIM[17].

As a result, EMUSIM employs copying to learn about how applications behave, and then uses that knowledge to create a reproduction model. When the analyst has no idea how the product will be presented under the changed degrees of simultaneousness and parallelism that prevent reenactment, the EMUSIM test system is invaluable. Such alternatives may be used in place of in-person examinations if the latter need resources that are either out of reach of the analyst or too expensive to provide in the cloud. According to the GNU General Public License, EMUSIM is free software.

In August of 2010, version 1.3 of the Advanced Execution Format (AEF) was released.

Below are some of EMUSIM's most notable features:

To assess the impact of asset migration, this article provides instances of request for cloud-based software as well as the means to create virtual copies of the original.

Accurately simulates application behaviour in order to provide information about runtime behaviour.

Decreases the expense of running cloud based reenactment, on the grounds that as opposed to nearby and restricted framework utilization, variable pricing based on actual expenses The evaluation makes use of the public cloud.

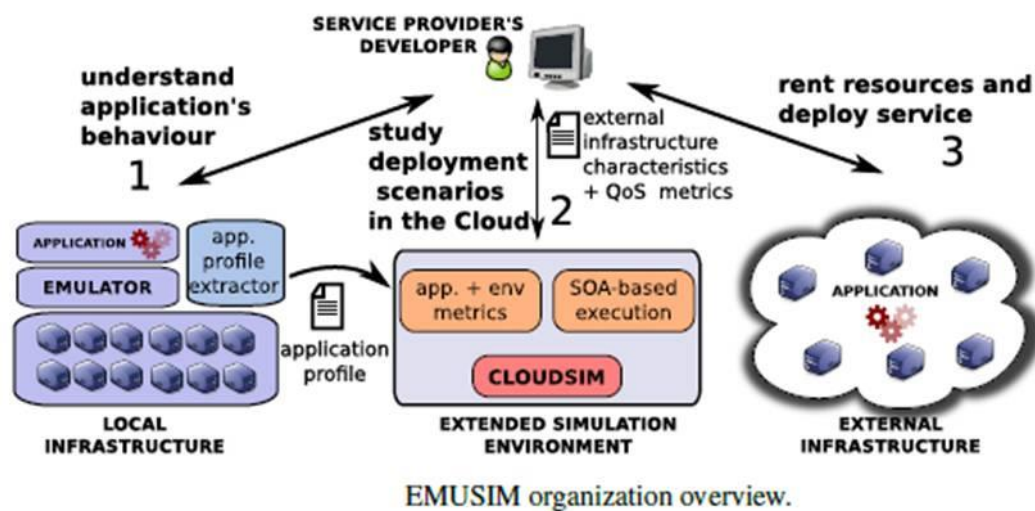Allows for CPU-intensive programmes with loose coupling to be run.

EMUSIM organization overview.

Figure 4. ENUMSIM Architecture

2.5 GroudSim

For logical applications in the cloud or on a grid, we provide GroudSim (Gr-Grid oud-Cloud), an event-based testing solution. There is just one reenactment string needed. The work of S. Ostermann, K. Plankensteiner, and D. Bodner, GroudSim provides a framework and cloud recreation tool compartment for logical applications based on a flexible reproduction free discrete-occasion centre.

GroudSim offers a full suite of tools for complex reenactment scenarios, from simple job executions on rented registered equipment to detailed calculations of expenses and foundation strain on assets. GroudSim is at its best when used to the IaaS subset of distributed computing. SaaS and PaaS models are examples of distributed computing that may benefit from this method of expansion.

The core GroudSim class, SimEngine, is responsible for keeping track of the chemicals that have been registered for use in following time, keeping a clock, and listing upcoming events. Many of the Groud bundle's typical utilities can be found in the framework and cloud assets classes, and these classes should be used instead of Groud's specialised behaviour.

Below are some of GroudSim's most notable features:

It is a robust collection of Java-based simulation tools for use in simulations of logical processes.

It incorporates both cloud and matrix architectures and is supported by a compartmentalised set of tools for occasional reproduction.

Contrast ad hoc execution to process-based methods across various testing environments.

May be successfully enlarged by using probability appropriation bundles.

GroundEntity, the most original part of GroudSim, defines error behaviour in its own unique way. The customer has the option to cancel the contract at any time.
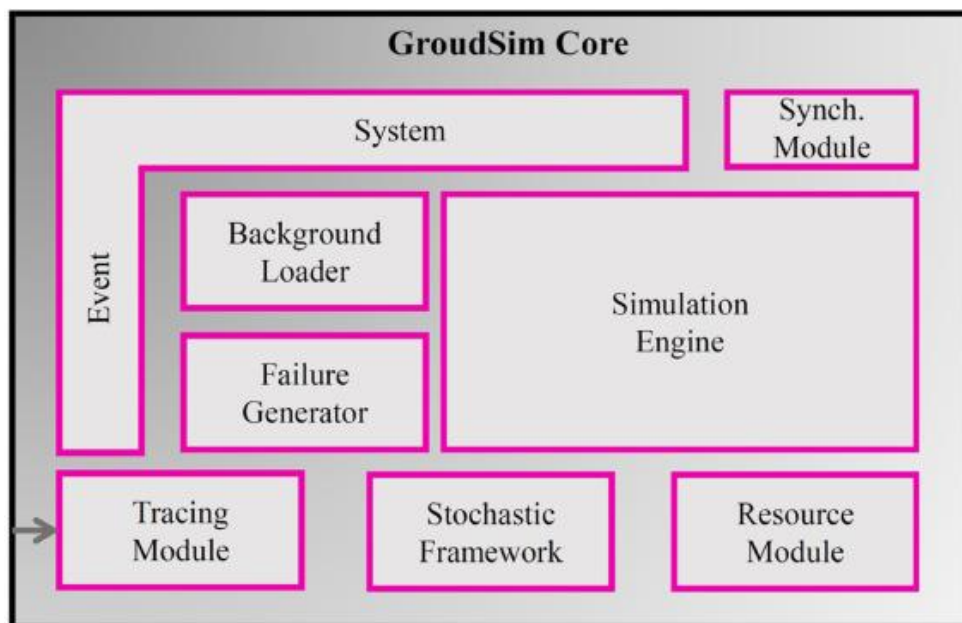

Figure 5. GroundSim core

2.6 DCSim (Data Center Simulation)

DCSim is a Java-based test system for server farms that can be easily expanded. It gives a steady and simple structure for creating and performing very good quality investigations on server farm the board strategies and calculations. DCSim, being an occasion driven test system, recreates a server farm IaaS proposing to various clients.

The ability to display replicated VMs is a new feature in DCSim, allowing the separation of activities and conditions across VMs that is essential for a multi-layered application.

The following are the components of DCSim:

Integrated with a multi-tiered application approach that allows VMs to "play out" scenarios with one another.

Works with quick turn of events, assessment and criticism on server farm the executives approaches and calculations.
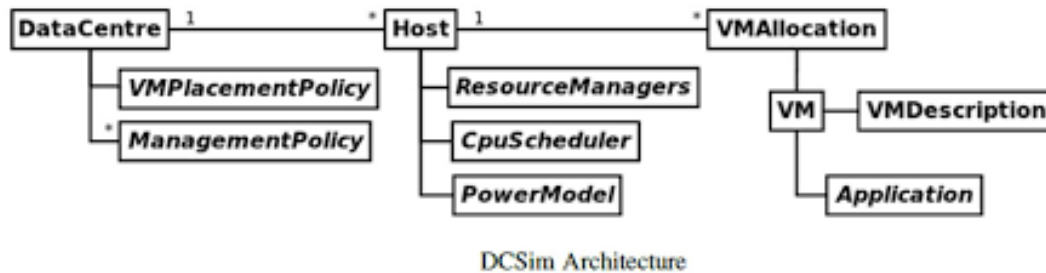

Figure 6. DCSim Architecture

2.7 CloudSim

CloudSim's [9] multidimensional design engineering is seen in Fig. 1. Users' needs for VMs and their dynamically constructed states are the primary emphasis of the client code layer. The Cloud provider may fairly weigh the merits of several approaches at this tier by developing the core VM to provide comfort. User Code monitors the top layer's focus substances for has and via expanding parts. Associating with the application allows planners to anticipate outcomes based on a cloud model's state at any one time, as well as the results of a mix of reasoning, configuration, and expected outcomes. User code, the CloudSim layer, and the CloudSim recreation motor layer make up the three tiers of the CloudSim's engineering.

CloudSim is an innovative, comprehensive, and modular set of Java-based simulation tools that may be used to simulate any real-world scenario. It maintains many essential features, including event lining and handling, the construction of CloudSim components, matching of parts and timekeeping administration in a game. It was developed by Professor (Dr.) Rajkumar Buyya of the University of Melbourne, Australia's Department of Computer Science and Software Engineering at their CLOUDS Laboratory to simulate cloud environments. In the realm of remote computing and application management, this toolbox enables consistent showing, reenactment, and trial and error. A possible label is "demonstrating an environment in which the apparatus is accepted as a starting point for creativity," with an emphasis on the need of paying close attention to the nuances of the new ideas being explored.

The main features of CloudSim are the basic classes for inferring server farms, Everything from virtual machines to apps to clients to computational resources to the policies and procedures used to book and furnish such resources. It uses strategies for application provisioning that are both scalable and resilient.

The CloudSim test system model is presented, which shows the birth of a single-host data centre, each of which operates a single cloudlet.The most recent variant of CloudSim is 4.0. Its highlights are recorded underneath:

Allows for the presentation and replication of massive, distributed computing server farms.

Supports a variety of techniques for feeding host resources to virtual machines, as well as the presentation and replication of virtual server components.

Allows for easy usage of regenerative features, breaks, and restarts.

Makes available client-defined procedures for VM host allocation (VMs).

Allows for the creation of distributed data centres with a wide range of possible network configurations, message-passing applications, and low-power servers.

Capable of simulating a hybrid cloud environment consisting of resources from both public and private networks. In-depth research on torrents and automated application scaling requires this fundamental piece of equipment.
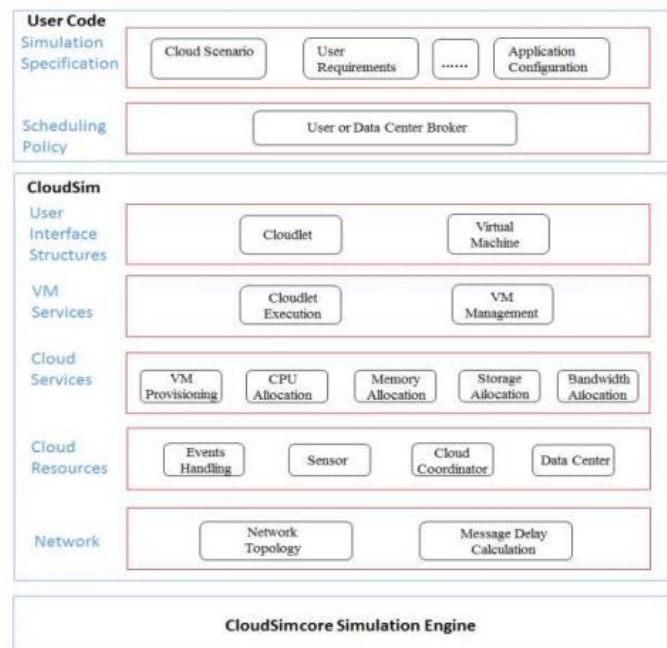
Figure 7. Architecture of CloudSim

2.8 Cloud Reports

Cloud Reports' architecture is seen in Fig. 4. The Cloud Reports coders want to implement a schedule like the one shown in Fig. 5. Presently, there are five mandatory modules and one extension module. The graphical user interface (GUI), report manager, simulation administrator, supplementary modules, and fundamental parts all belong to the business layer. Meanwhile, the Cloud Reports application is now being built on top of the CloudSim game engine and the Java virtual machine (JVM). The Cloud Reports service makes use of a SQLite database. The reports manager is responsible for compiling, analysing, and formatting restoration data gleaned from database archives to provide entertainment reports. The reports are constructed using HTML and raw data. The HTML files aggregate overall and per-user control use statistics from Cloud server farms and clients. Using all available game data, the report manager draws out charts that are included in the HTML report files. Raw data files have redundant information in a standardised format that can be fed into programmes like MATLAB and Octave.
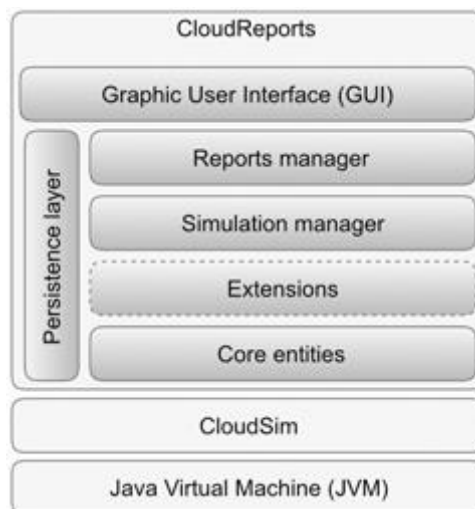

Figure 8. Architecture of Cloud Report

3. CONCLUSSION

This study explains the fundamental distinctions between five distinct Cloud-based simulators—CloudSim, Cloud Analyst, Cloud Reports, Cloudsched, and Green Cloud. These test environments may simulate real-world conditions encountered in a cloud server farm at many design levels. We provide comprehensive correlations based on the structures, component displays, recreation process, execution metrics, and outputs of these test systems. Research and analysis of the system's complexity and traffic demands simulators as vital instruments. It is obvious that none of them is ideal from every angle and configuration, as there is still much work to be done to demonstrate different Cloud layers, high extensibility that can enable new modules to be sent effectively in the devices, simplicity of use, and, finally, consideration of the client's need.

REFERENCES

1. "Data Centre Business Picks up Pace in India", Oct. 22, 2019. Accessed on Jan. 07, 2020. [Online]. Available: https://tech.economictimes.indiatimes.com/news/internet/data-centre-business-picks-up-pace-in-india/71641333.

2. Soumya Ranjan Jena, and Zulfikhar Ahmad, "Response Time Minimization of Different Load Balancing Algorithms in Cloud Computing Environment", IJCA, Vol 69, No. 17, Pages 22-27, May 2013.

3. Soumya Ranjan Jena, and Bhushan Dewan, "Improving Quality-of-Service Constraints of Cloud Data Centers", IEEE, 2nd International Conference on Computing for Sustainable Global Development, BVICM, New Delhi ,2015.

4. Soumya Ranjan Jena, Sudarshan Padhy, and Balendra Kumar Garg, "Performance Evaluation of Load Balancing Algorithms on Cloud Data Centers", IJSER, Vol 5, 3, Pages 1137-1145, 2014.

5. Soumya Ranjan Jena, V. Vijayaraja, and Aditya Kumar Sahoo, "Performance Evaluation of Energy Efficient Power Models for Digital Cloud", INDJST, Vol 9, 48, Pages 1-7, 2016.

6. Soumya Ranjan Jena, and L.Shridhara Rao," A Study on Energy Efficient Task Scheduler over Three-Tier Cloud Architecture using Green Cloud", JARDCS, Vol 9, 18, 2017.

7. Soumya Ranjan Jena, Sukant Kishoro Bisoy and Bhushan Dewan, "Performance Evaluation of Energy Efficient Power Models for Differnent Scheduling Algorithms in Cloud using Cloud Reports", IEEE, GUCON 2019, International Conference on Computing, Power and Communication Technologies, pages. 880-891, Galgotias University, Greater Noida, U.P, India.

8. Soumya Ranjan Jena, Raju Shanmugam, Rajesh Kumar Dhanaraj, Kavita Saini, "Recent Advances and Future Research Directions in Edge Cloud Framework", IJEAT, Volume 9, Issue 2, Pages. 439-444, December 2019.

9. R. Buyya and M. Murshed, "GridSim: A Toolkit for the Modeling and Simulation of Distributed Resource Management and Scheduling for Grid Computing", Concurrency and Computation: Practice and Experience, 14(13-15), Wiley Press, Nov.-Dec., 2002.

10. Rodrigo N. Calheiros, Rajiv Ranjan, Anton Beloglazov, C´esar A. F. De Rose, and Rajkumar Buyya, "CloudSim: A Toolkit for Modeling and Simulation of Cloud Computing Environments and Evaluation of Resource Provisioning Algorithms", John Wiley & Sons, Software– Practice and Experience, 41, Pages 23–50, 2011.

11. Bhathiya Wickremasinghe, "CloudAnalyst: A CloudSim based Tool for Modelling and Analysis of Large Scale Cloud Computing Environments" MEDC project report, 433-659 Distributed Computing project, CSSE department., University of Melbourne, 2009.

12. Thaigo Teixeira Sa, Rodrigo N Calheiros and Danielo G Gomes, "CloudReports: An Extensible Simulation Tool for Energy-Aware Cloud Computing Environments" , Springer International Publishing: Chapter 6, Cloud Computing- Challenges, Limitations and R & D Solutions. 2014 21st Oct (Book); pages. 127-42,. ISBN: 978-3-319-10529-1.

13. Minxian Xu, Wenhong Tian, Xinyang Wang, and Qin Xiong, "FlexCloud: A Flexible and Extendable Simulator for Performance Evaluation of Virtual Machine Allocation", 2015 IEEE International Conference on Smart City/SocialCom/SustainCom (SmartCity), 19-21 Dec. 2015, Chengdu, China.

14. Beloglazov A. Department of Computing and Information Systems, The University of Melbourne: "Energy-efficient Management of Virtual Machines in Data Centers for Cloud Computing", Doctor of Philosophy (PhD Thesis), 2013 February.

15. Rajkumar Buyya, Rajiv Ranjan, Rodrigo N. Calheiros, "Modeling and Simulation of Scalable Cloud Computing Environments and the CloudSim Toolkit: Challenges and Opportunities", 2009 International Conference on High Performance Computing & Simulation, Leipzig, Germany, 21-24 June 2009.

16. Wenhong Tian, Yong Zhao, Minxian Xu, Yuanliang Zhong, Xiashuang Sun, "A Toolkit For Modeling and Simulation of Real-time Virtual Machine Allocation in a Cloud Data Center", IEEE Transactions on Automation Science and Engineering, Volume: 12 , Issue: 1 , Jan. 2015.

17. Thiago Teixeira Sá, Rodrigo N. Calheiros and Danielo G. Gomes, " Chapter 6: CloudReports: An Extensible Simulation Tool for EnergyAware Cloud Computing Environments", Springer International Publishing Switzerland, Cloud Computing, Computer Communications and Networks, page 127-141, 2014.

18. R.Buyya, C. S. Yeo, S. Venugopal, J. Broberg, and I. Brandic, "Cloud Computing and Emerging IT Platforms: Vision, Hype, and Reality for Delivering Computing as the 5th Utility. Future Generation Computer Systems", 25(6): 599-616, Elsevier Science, Amsterdam, The Netherlands, June 2009.